

Co-registered Multimodal Endoscope for Early Ovarian Cancer

by

David Vega

Copyright © David Vega 2021

A Dissertation Submitted to the Faculty of the

WYANT COLLEGE OF OPTICAL SCIENCES

In Partial Fulfillment of the Requirements

For the Degree of

DOCTOR OF PHILOSOPHY

In the Graduate College

THE UNIVERSITY OF ARIZONA

2021

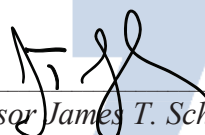
THE UNIVERSITY OF ARIZONA
GRADUATE COLLEGE

As members of the Dissertation Committee, we certify that we have read the dissertation prepared by **David Vega**, titled ***Coregistered Multimodal Endoscope for Early Ovarian Cancer Detection*** and recommend that it be accepted as fulfilling the dissertation requirement for the Degree of Doctor of Philosophy.



Professor Jennifer Kehlet Barton

Date: 05/14/2021



Professor James T. Schwiegerling

Date: 5/14/21



Professor Rongguang Liang

Date: 05/14/2021

Final approval and acceptance of this dissertation is contingent upon the candidate's submission of the final copies of the dissertation to the Graduate College.

I hereby certify that I have read this dissertation prepared under my direction and recommend that it be accepted as fulfilling the dissertation requirement.



Professor Jennifer Kehlet Barton
Dissertation Committee Chair
Wyant College of Optical Sciences

Date: 05/14/2021



ARIZONA

STATEMENT BY AUTHOR

This dissertation has been submitted in partial fulfillment of the requirements for an advanced degree at the University of Arizona and is deposited in the University Library to be made available to borrowers under rules of the Library.

Brief quotations from this dissertation are allowable without special permission, provided that an accurate acknowledgement of the source is made. Requests for permission for extended quotation from or reproduction of this manuscript in whole or in part may be granted by the head of the major department or the Dean of the Graduate College when in his or her judgment the proposed use of the material is in the interests of scholarship. In all other instances, however, permission must be obtained from the author.

SIGNED: David Vega

DEDICATION

A mi familia.

To my family.

Table of Contents

ABSTRACT	9
CHAPTER 1: INTRODUCTION	11
1.1 MOTIVATION	11
1.1.1. OVARIAN CANCER	12
1.1.2. DIAGNOSTIC IMAGING USED FOR OVARIAN CANCER DETECTION.	13
1.1.3. OVARIAN TISSUE ACCESS	13
1.2 ENDOSCOPES WITH VARYING FOV (MAGNIFICATION)	15
1.3 OPTICAL COHERENCE TOMOGRAPHY (OCT)	17
1.3.1 OPTICAL COHERENCE TOMOGRAPHY (OCT) AND OPTICAL COHERENCE MICROSCOPY (OCM)	17
1.3.2 TIME DOMAIN OCT (TD-OCT)	21
1.3.3 SPECTRAL DOMAIN OCT (SD-OCT)	26
1.3.4 OCT MECHANISM OF CONTRASTS IN TISSUE	34
1.4 MULTI-PHOTON MICROSCOPY (MPM)	36
1.4.1 MULTI-PHOTON MICROSCOPY (MPM) PRINCIPLES	36
1.4.2 MPM MECHANISMS OF CONTRAST IN TISSUE	38
1.5 NARROW-BAND REFLECTANCE IMAGING	45
1.5.1 REFLECTANCE MECHANISMS OF CONTRAST	45
1.5.2 HEMOGLOBIN ABSORPTION TO IDENTIFY AREAS OF INCREASED VASCULARITY	46
CHAPTER 2: PRESENT STUDY	48
2.1 ENABLING MULTIPLE OPTICAL PATHS FOR CO-REGISTERED IMAGING	48
2.2 CO-REGISTERED PROXIMAL SYSTEM	51
2.3 EN-FACE TRIPLE MODALITY CO-REGISTERED ENDOSCOPE (SALPINGOSCOPE)	53
CHAPTER 3: FUTURE WORK	56
4.1 MULTIPLE OPTICAL PATHS FOR CO-REGISTERED IMAGING FUTURE WORK	56
4.2 CO-REGISTERED PROXIMAL SYSTEM FUTURE WORK	56
4.3 EN-FACE TRIPLE MODALITY CO-REGISTERED ENDOSCOPE (SALPINGOSCOPE) FUTURE WORK	57
REFERENCES	59
APPENDIX A: USE OF EMBEDDED AND PATTERNED DICHROIC SURFACES WITH REFLECTIVE OPTICAL POWER TO ENABLE MULTIPLE OPTICAL PATHS IN A MICRO-OBJECTIVE	63
A.1 ACCEPTED MANUSCRIPT: USE OF EMBEDDED AND PATTERNED DICHROIC SURFACES WITH REFLECTIVE OPTICAL POWER TO ENABLE MULTIPLE OPTICAL PATHS IN A MICRO-OBJECTIVE	63

A.1.1 FILES STORAGE AND CONTRAST DATA	85
A.1.2 NON-SEQUENTIAL MODELING OF NON-CONVENTIONAL COMPONENTS	87
A.2 ACCEPTED ABSTRACT: MODEL AND EVALUATION OF FACE FORWARD ILLUMINATION FOR MULTIMODAL ENDOSCOPIC PROBES	94
A.2.1 REFLECTANCE MODALITY STRAY LIGHT STUDY	100
A.3 GENERATING VISUALIZATION OF SCANNING SYSTEMS WITH OPTICSTUDIO	114

APPENDIX B: PROXIMAL SUPPORTING SYSTEM FOR CO-REGISTERED MULTIMODAL IMAGING DESIGNED FOR REFLECTANCE, MULTIPHOTON, AND OPTICAL COHERENCE MICROSCOPY. **118**

B.1 ACCEPTED MANUSCRIPT: A CO-REGISTERED MULTIMODAL IMAGING SYSTEM FOR REFLECTANCE, MULTIPHOTON, AND OPTICAL COHERENCE MICROSCOPY.	118
B.1.1 FILES STORAGE LOCATION	141
B.2 ELECTRONICS FOR SYSTEMS WITH MULTIPLE PHOTOMULTIPLIER TUBES	142
B.3 STANDARD OPERATING PROCEDURE B02-021B: ALIGNMENT & ASSEMBLY PROCEDURE OF OPTICAL COMPONENTS FOR THE MULTIPHOTON MICROSCOPE	145
B.4 STANDARD OPERATING PROCEDURE B02-022: SALPINGOSCOPE SPECTROMETER ALIGNMENT	172

APPENDIX C: TRIPLE MODALITY CO-REGISTERED ENDOSCOPE. **181**

C.1 MANUSCRIPT: TRIPLE-MODALITY CO-REGISTERED ENDOSCOPE FEATURING WIDE-FIELD REFLECTANCE IMAGING, AND HIGH-RESOLUTION MULTIPHOTON AND OPTICAL COHERENCE MICROSCOPY.	181
C.1.1 FILES STORAGE LOCATION	215
C.2 STANDARD OPERATING PROCEDURE B16-011: SALPINGOSCOPE FIBER GLUING	216
C.3 STANDARD OPERATING PROCEDURE B02-024: SALPINGOSCOPE STOP-OBJECTIVE LENS GLUING	227
C.4 STANDARD OPERATING PROCEDURE B16-014: SALPINGOSCOPE FERRULE CONSTRUCTION	234
C.5 STANDARD OPERATING PROCEDURE B16-012: SALPINGOSCOPE HANDLE ASSEMBLY	253
C.6 STANDARD OPERATING PROCEDURE B02-023: CONNECTORIZING THE SALPINGOSCOPE	273
C.7 STANDARD OPERATING PROCEDURE B02-017A: SALPINGOSCOPE CLEANING - STERILIZATION	284
C.8 STANDARD OPERATING PROCEDURE B02-027: MULTIMODAL MICROSCOPE AND SALPINGOSCOPE OCT SPECTROMETER CALIBRATION AND ALIGNMENT	286

LIST OF FIGURES

Figure 1. (Left) A-scan of backscattered light intensity vs axial position. (Right) B-scan where adjacent A-scans are taken at different locations of a transverse scan of the sample.....	17
Figure 2. (Left) A low NA imaging system providing a large DOF several times larger than the coherence length. (Right) A high NA imaging system providing a DOF of about one coherence length.....	20
Figure 3. Time Domain OCT basic diagram.....	21
Figure 4. Diagram of a balanced detection system in a TD-OCT configuration.	22
Figure 5. Interferogram showing the carrier in blue and the envelope in red.....	23
Figure 6. Representation of multiple scatterers along the axial direction.....	24
Figure 7. Full I_{det} is shown in blue. Envelope shown in red.	25
Figure 8. A-line extracted from the multiple scatterers.	26
Figure 9. Spectral Domain OCT basic diagram.....	27
Figure 10. Ophthalmic Spectral Domain OCT system diagram.	28
Figure 11. Gaussian shaped spectrum as a function of wavenumber $S(k)$	28
Figure 12. Different frequency modulations produced by the echo delay between z_R and z_{Sn} where $z_{Sn'}$ has a larger delay than z_{Sn} . The frequency modulation is imposed in a Gaussian shaped spectrum.....	29
Figure 13. Representation of multiple scatterers along the axial direction using a delta function scaled by their respective reflectivity.	29
Figure 14. Representation of I_{det} at the detector plane. Cross-correlation terms and auto-correlation terms are present.....	31
Figure 15. Representation of I_{det} after spectrum DC term subtraction.....	31
Figure 16. Fourier transform showing the positive and the negative sides. The red side of the graph is usually not used.....	33
Figure 17. Fourier transform showing only the positive side with a threshold filter.....	34
Figure 18. Jablonski diagram for 1-photon absorption fluorescence excitation. Left axis represents the energy and bottom axis represents time. Blue squiggly arrow represents a high energy photon that is absorbed by the molecule. Blue arrow represents the transition of the electron to a possible excited electronic state. Green arrow represents energy dissipation between vibrational states. Red arrow represents the transition of the molecule to a ground electronic state where the energy is dissipated through electromagnetic emission represented with the red squiggly arrow. If the molecule does not come back to the true ground state after electromagnetic emission decay, it can further decay through energy dissipation until ground state is reached. ..	37
Figure 19. Jablonski diagram for 2-photon absorption fluorescence excitation. Left axis represents the energy and bottom axis represents time. Dark red squiggly arrow represents a high energy photon that is absorbed by the molecule that transition the electron to a possible excited	

state. The molecule can then relax through non-radiative relaxation (green arrow) until it decays by emitting electromagnetic radiation (light red squiggly arrow). 39

Figure 20. Jablonski diagram for 3-photon absorption fluorescence excitation. Dark red squiggly arrow represents a high energy photon that is absorbed by the molecule that transition the electron to a possible excited state. The molecule can then relax through non-radiative relaxation (green arrow) until it decays by emitting electromagnetic radiation (green squiggly arrow). 41

Figure 21. Jablonski diagram for SHG. Dark red squiggly arrow represents a high energy photon that is absorbed by the molecule that transition the electron to a virtual excited state. The molecule can only return to the ground state by emitting electromagnetic radiation (yellow squiggly arrow). 42

Figure 22. Molecular dependance of SHG. If molecules emit SHG off-phase, SHG from the different molecules can interact destructively annihilating SHG. If molecules emit SHG in-phase, the emitted SHG interacts constructively. 43

Figure 23. Jablonski diagram for THG. Dark red squiggly arrow represents a low energy photon that is absorbed by the molecule. An electron is transitioned to a virtual excited state. The molecule can only return to the ground state by emitting electromagnetic radiation (blue squiggly arrow). 44

Figure 24. Hemoglobin and Oxyhemoglobin molar extinction coefficient as a function of wavelength. Data reproduced from [52] 47

LIST OF TABLES

Table 1. Hallmarks of cancer [1]..... 11

Table 2. Optical system requirements and measured performance..... 50

ABSTRACT

Ovarian cancer (OC) has the highest mortality rate of all gynecological cancers, affecting 22,000 patients and causing 14,000 deaths a year in the United States alone. The lack of non-invasive technology to detect OC and lack of specific OC symptoms results in late diagnosis and motivates the development of new methods to detect OC at early stages. A successful early detection technique can improve the survival rate from 17% to 90% if OC is detected at stage 1. High-grade serous carcinomas are considered to originate in the distal fallopian tube and then migrate to the ovary. Therefore, successful early detection of OC must incorporate the ability to detect the distal serous tubal intraepithelial carcinoma (STIC) at the fallopian tubes as well as to detect early stage OC at the ovaries. This work demonstrates the feasibility of a triple multimodality imaging endoscope (salpingoscope) that is minimally invasive and could be used as a screening method for various cancers in the future, especially OC. The endoscope incorporates optical imaging, irrigation, and biopsy accessory channels. The optical modalities are narrowband reflectance, optical coherence microscopy (OCM), and multiphoton microscopy (MPM). Narrowband reflectance enables the identification of regions with increased vascularity. OCM provides depth-resolved, micron-scale resolution images of tissue microstructure, and MPM provides high-resolution non-linear imaging of fluorescent molecules such as lipopigments and porphyrins that are known to be altered in cancerous tissue.

The work is presented in three sections. The first validates a novel dual-path optical system through modeling and testing of the optical assembly. The system's dual path allows co-registration of the images from the different imaging technologies. Patterned dichroic surfaces

embedded within the optical system provide reflective optical power and enable the wavelength-dependent two optical paths. The different optical paths are used to accommodate multiple imaging technologies by selecting the proper illumination wavelength.

The second section describes a combined proximal system, whose components can be used for reflectance, OCM, and MPM imaging, including light sources, fibers, detectors, data acquisition, software, and actuator control for either a scanning endoscope (such as the salpingoscope) or a tabletop scanning microscope. The light sources and photonic components are selected to be compatible with the dual-path co-registered optical system described in section 1. Feasibility images are included of *ex-vivo* ovine ovarian tissue taken with a tabletop microscope.

The third section presents the design and feasibility testing of a co-registered endoscope using the optical assembly from section 1, the proximal system from section 2, a quartered-piezo scanning assembly with a cantilevered fiber, and optomechanical components of an approximately 3.5 mm diameter endoscope. The common component of all the systems is a dual-clad fiber that provides illumination and collection mechanisms for the optical imaging modalities.

CHAPTER 1: INTRODUCTION

1.1 Motivation

Cancer is a multistage disease that researchers are still working to comprehend. It develops through a series of genetic mutations, and at the early stages, it is localized and usually most responsive to treatment. Also, at early stages, cancer lacks specific symptoms, and its size is at the microscopic scale. Therefore, detecting cancer at early stages is challenging in nature.

While there are different types of cancer, they all have some typical hallmarks [1] listed in Table 1. Each of these landmarks comes with an accompanying signature. Examples of these signatures are the cell size and structure changes by evading growth suppressors or changes in the cell's molecular composition when deregulating cellular processes. These early signatures can be detected utilizing different methods such as imaging.

Table 1. Hallmarks of cancer [1].

Hallmarks of cancer
Resisting cell death
Evading growth suppressors
Inducing angiogenesis
Deregulating cellular energetics
Avoiding immune destruction
Sustaining proliferative signaling
Activating invasion and metastasis
enabling replicative immortality
Genome instability and mutation
Tumor promoting inflammation

This work focuses on developing and integrating multiple imaging techniques into an endoscope intended for ovarian cancer screening utilizing a novel dual-path optical system to co-register the images from the different imaging technologies. The techniques used are narrow-band reflectance, optical coherence microscopy (OCM), and multiphoton microscopy (MPM).

Narrow-band reflectance used with a wide field of view (FOV) provides a modality that can

identify suspicious areas while navigating the endoscope. OCM, used with a narrow FOV, provides high-resolution depth and lateral images of the tissue layering. Additionally, MPM provides high-resolution non-linear imaging of fluorophores related to the early signatures produced by the changes caused by the genetic mutations in cancer cells.

1.1.1. Ovarian Cancer

Ovarian cancer (OC) is the deadliest gynecological cancer [2]. It is estimated that OC accounts for more than 22,000 new diagnoses of cancer annually [2–4], and it causes more deaths than any other cancer of the female reproductive system accounting for about 14,000 deaths per year [3,4]. The statistics suggest that OC has a very low survival rate [2] primarily due to late diagnosis. Proper early diagnosis is often delayed due to several reasons, including the lack of non-invasive technology to diagnose OC at the point of care, the non-specific symptoms such as bloating or pelvic pain, and the desire to avoid invasive laparoscopy procedures used to detect OC in high-risk patients. There has been limited success in developing a screening method for OC, motivating the development of new methods to detect OC at early stages. A successful early detection technique can improve the survival rate of affected patients since stage 1 is 90%, whereas the rate at stage 3 is only 38%, with its lowest at stage 4 of 17% [3].

The early detection of OC must consider the ability to visualize the distal fallopian tube for serous tubal intraepithelial carcinoma (STIC) as well as the ovary for early stage cancer as many high grade serous carcinomas are considered to originate in the distal fallopian tube and then migrate to the ovary [5–7]. OC screening methods such as palpation, CA-125 blood test, or transvaginal ultrasound have poor sensitivity and specificity, and patients at high risk are recommended to undergo risk-reducing Salpingo-Oophorectomy (RRSO), often in childbearing

years [8]. Early RRSO comes with consequences such as the abrupt onset of menopause [9]. Therefore, a reliable method to detect early ovarian cancer is needed to avoid unnecessary surgeries and improve the outcome of affected patients.

1.1.2. Diagnostic Imaging Used for Ovarian Cancer Detection.

Optical imaging techniques including reflectance, fluorescence, confocal microscopy, multiphoton microscopy (MPM), and optical coherence tomography (OCT) have proven to be a sensitive and specific way to detect OC in ovaries and fallopian tubes [10–15]. These imaging modalities detect either the morphological changes or molecular/physiological changes of the disease. Additionally, multiple imaging modalities such as fluorescence imaging and optical coherence tomography, when combined, may improve classification accuracy [16]. Several dual multimodal endoscopes have been developed to detect OC featuring OCT and other imaging modalities such as fluorescence wide-field imaging [17–20].

1.1.3. Ovarian Tissue Access

A major challenge with OC screening is access to the tissue of interest. Potential routes of access to the ovary and fallopian tubes include laparoscopic, falloposcopic, or transvaginal.

Laparoscopy is the most straightforward, utilizing rigid endoscopes up to several mm in diameter, typically with distention of the abdomen and the presence of white-light imaging and grasper tools to facilitate imaging of all sides of the ovary. Laparoscopes have been used in vivo for confocal and optical coherence tomography imaging of the ovary [10,21]. However, the lumen of the fallopian tube is difficult to image due to the unfavorable entrance angle and potentially large diameter of the endoscope. An articulating tip of a confocal microscope was developed to mitigate some of these issues [22]. Also, laparoscopy is a surgery requiring general

anesthesia, increasing risks and procedural costs, thus making adoption of laparoscopy as a screening method unlikely.

Fallopscopy utilizes the natural orifice of the vagina, uterus, and fallopian tube to access the ovaries, typically with the assistance of a hysteroscope and an introducing catheter. Advantages of falloposcopic access are no tissue cutting- allowing this minimally invasive procedure to be performed in an office or outpatient setting, and the ability to visualize the fallopian tube lumen along the entire path from the ostium to the fimbria. Disadvantages include the requirement for extremely small (sub-mm) diameter, high flexibility, and inability to see the entire surface of the ovary. In vivo white light fallopscopy was first demonstrated in the early 1990s for fertility examinations [23], and a high-resolution white light falloposcope was recently demonstrated [23–27]. The small size, however, limits the resolution and scanning capabilities of the endoscope.

Transvaginal access is where a small incision in the vagina wall is made to provide access to the peritoneal cavity and thus to the ovaries and fallopian tubes. Generally, a rigid endoscope is utilized. The advantages of this method include reduced invasiveness compared to laparoscopy enabling an office or outpatient procedure option to use an endoscope with several mm diameter and a favorable entrance angle for examining the distal lumen of the fallopian tube.

Disadvantages include the inability to examine the entire fallopian tube and concern about rectal puncture, which is small and can be avoided by pelvic examination or ultrasound. Transvaginal access has been used for transvaginal hydrolaparoscopy, enabling diagnosis and treatment of endometriosis and polycystic ovary syndrome, and examining of the patency and health of fallopian tubes with the FDA-approved Fertiloscope from Fertility Focus [28–30].

1.2 Endoscopes with Varying FOV (magnification)

Typically, separate optical systems are used to combine wide-field white light imaging and microscopic techniques. Endoscopes with several optical systems are not common but introducing a separate endoscope through the instrument channels of a bigger endoscope allows separate optical systems to be guided and utilized. This technique increases the required size of the host endoscope and carries the challenge of accurately co-registering images. There are few endoscopes commercially available that provide adjustable levels of magnification (zoom). For example, the EndocytoTM, made by Olympus (Tokyo, Japan), and the EC-760Z-VM/VL, made by Fujifilm (Tokyo, Japan). These two endoscopes are 9.7 mm and 12.8 mm in diameter, respectively, and provide 520x and 145x zoom. Both of these commercially available endoscopes are limited to white-light imaging.

Other research groups have developed smaller zoom endoscopes with diameters of > 4.5 mm [31–37]. There are three main techniques used by these groups that allow the design of endoscopes with zoom capabilities. The first is to use conventional lenses driven by direct linear actuators [31]. These mechanical zoom systems require relatively complex and bulky optomechanical assemblies. Even when some of these systems feature lenses with diameters of ~ 2 mm, the outer diameter of the device is ~ 6 mm or more [31,32]. The second is to use liquid tunable lenses [33,34]. These lenses consist of liquid optical materials enclosed in a chamber. The optical materials can change their shape when the chamber experiences a voltage change. A varioptic lens made by Corning Inc. (NY, USA) is an example of such lenses. The complexity of the lenses requires a large assembly around the chamber. Therefore, these lenses also do not provide small diameters for atraumatic endoscopes. The third is to use liquid crystal tunable

lenses [36,37]. These lenses can adjust their refractive index by changing the orientation of the liquid crystal molecules utilizing electric fields. These are also bulky and often require other optical components such as polarizers that reduce the light collection efficiency of the system.

An alternative to these main techniques is to use patterned dichroic coatings to generate low magnification and high magnification optical paths in the same lens system. This technique has been demonstrated in a 5 mm outer diameter endoscope [38]. Using this technique helps to implement a compact optical system and does not need any moving parts or assemblies around the lenses. Therefore, the entire diameter of the lens can be used to increase its clear optical aperture providing assemblies that feature smaller diameters. Changing the illumination wavelengths selects the zoom by utilizing a different optical path. The dichroic surfaces are designed in such a way that wavelengths at a specific band do not interact with the surfaces and pass optically unaffected, and other wavelengths outside of this band reflect at the surfaces. This technique results in two different optical paths in the same optical system.

1.3 Optical Coherence Tomography (OCT)

1.3.1 Optical Coherence Tomography (OCT) and Optical Coherence Microscopy (OCM)

OCT is an interferometric technique that obtains its contrast from the backscattered light intensity of the sample and can perform high-resolution cross-sectional and 3D volumetric imaging of a tissue's internal structure [39,40]. This backscattered intensity is measured as a function of depth along the optical axis (A-scan, 1D). Due to the OCT scanning nature, successive A-lines need to be measured while performing a transverse scan before a cross-sectional image can be constructed (B-scan, 2D). Then, adjacent cross-sectional images can be stitched together to create a volumetric reconstruction of the object being imaged (C-scan, 3D). Figure 1 shows a representation of the A and B scans used in OCT [39].

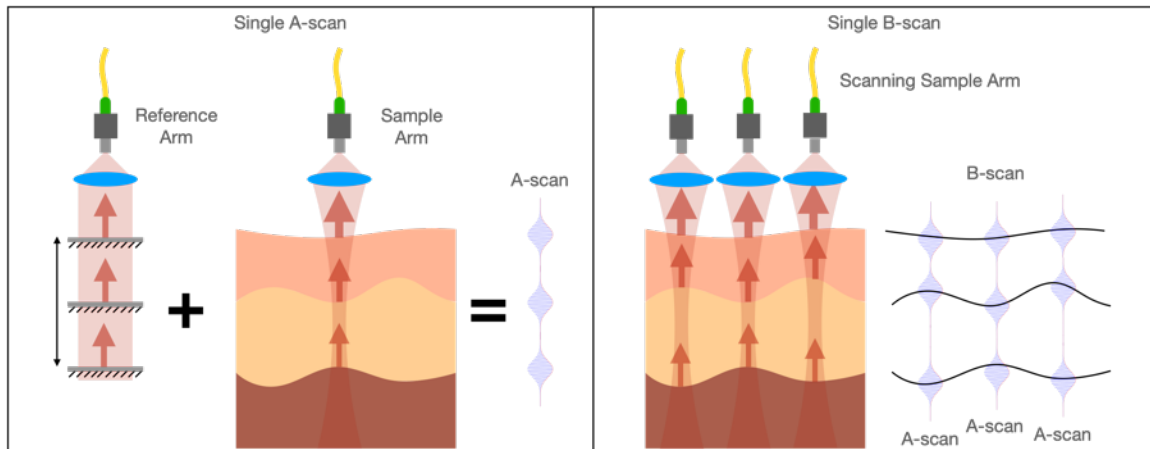


Figure 1. (Left) A-scan of backscattered light intensity vs axial position. (Right) B-scan where adjacent A-scans are taken at different locations of a transverse scan of the sample.

A C-scan provides OCT's ability to generate a volumetric structural map displayed similarly to MR or CT images. These maps (2D and 3D) are often referred to as optical biopsies in the medical community since they provide similar pathological information to histopathology techniques. OCT has an advantage over histopathology since it is nondestructive and can access

the tissue *in vivo* when OCT is integrated into medical instruments such as catheters or endoscopes.

Time Domain OCT (TD-OCT) is first described in order to provide a comprehensive understanding of the OCT technique. TD-OCT uses a low-coherence interferometry technique known as white light interferometry to detect optical echoes representing where the light is being back-scattered or back-reflected along the optical axis (A-scan direction). This interferometric technique performs correlating measurements between the light that has reached the sample and light sent towards a reference arm. A low-coherence (broad bandwidth) light source is used to detect optical echoes since the interference is only observed when the reference and sample arms are matched within the light source's coherence length [39]. The coherence length is inversely proportional to the source's bandwidth. Therefore, axial resolution along the A-scan axis is improved by reducing the coherence length (increasing the bandwidth), allowing detecting the echo's location more precisely. The foundation of optical coherence tomography is based on the ability to detect these echoes as a function of the reference arm location. The echo interferometric amplitude is a function of the reflected light amplitude. The reference arm's location is matched to the location where the echo originated at the sample (adjusted by the sample's index of refraction). Combining this information, we can reconstruct a map defining where light is reflected and its intensity.

A unique aspect of OCT is that the lateral resolution is decoupled from the axial resolution. The lateral resolution depends on the lens used to scan the sample, while the axial resolution depends on the light source being used [40]. OCT can be seen as a confocal technique since the illumination and light collection happens within the same lens system. OCT's lateral resolution

has been shown [41,42] to be slightly different from the Rayleigh resolution criterium since it is often used with a Gaussian beam and is defined as

$$\Delta x = \Delta y = \frac{4\lambda f}{\pi D_x} \approx \frac{2\lambda}{\pi NA_{obj}}$$

D_x is the diameter of the exit pupil that is fully illuminated by a Gaussian beam, λ is the illumination wavelength, f is the focal length, and NA_{obj} is the object space NA of the system in the paraxial approximation. As explained above, the axial resolution depends on the resolution for the echo time delay, and this resolution depends on the source being used to perform OCT. The axial resolution is given by the autocorrelation function of the source bandwidth [39]. For a spectrum with a Gaussian shape, the axial resolution is:

$$\Delta z = \Delta l_c = \frac{2\ln(2)\lambda^2}{\pi n \Delta \lambda}$$

Δz is the full-width-at-half-maximum of the autocorrelation function, $\Delta \lambda$ is the full-width-at-half-maximum of the power spectrum, Δl_c is the coherence length, and λ is the center wavelength of the light source. The FOV can be arbitrary for some endoscopes and catheters since they can take a very long cross-sectional image using OCT and moving the whole instrument while acquiring data. In scanning systems where scanning devices are used, such as galvanometers, the FOV is less arbitrary and can be approximated by

$$FOV_{x,y} = \frac{f \tan(\theta)}{2}$$

θ is twice the angular deviation of the scanning mirror [40]. Due to the confocal nature of OCT, the depth of field (DOF) is coupled with the lateral resolution through the confocal parameter b , which is two times the Rayleigh range and is defined as

$$b = \frac{\pi \Delta x^2}{\lambda} = \frac{4\lambda}{\pi NA_{obj}^2}$$

In the literature, OCT's DOF is described in different ways [39,40], but all definitions have a $\lambda \times \text{NA}^{-2}$ dependency. The pre-factors vary from definition to definition, but the result is the same since the DOF and lateral resolution are coupled by λ and the system's NA. Therefore, there is always a compromise between DOF and lateral resolution in OCT systems. The better lateral resolution, the smaller the DOF. This effect can be seen in Figure 2.

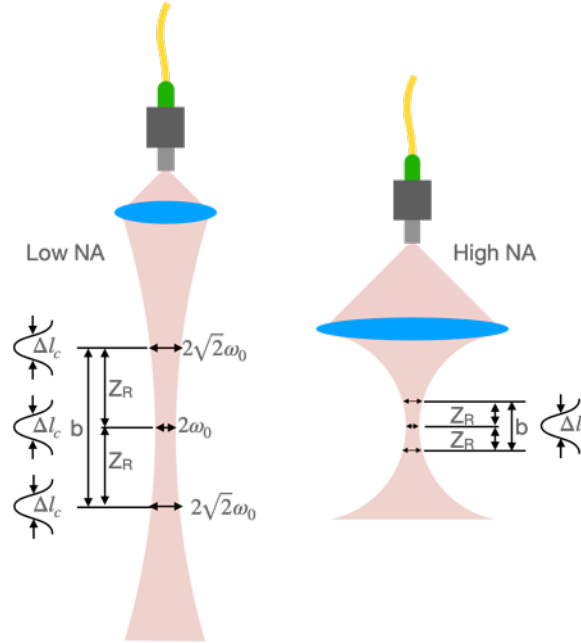


Figure 2. (Left) A low NA imaging system providing a large DOF several times larger than the coherence length. (Right) A high NA imaging system providing a DOF of about one coherence length.

The most common OCT implementations are:

- Time Domain OCT (TD-OCT)
- Spectral Domain OCT (SD-OCT)
- Swept-Source OCT (SS-OCT)

In the next sections, a brief description of TD-OCT and SD-OCT will be given, and SS-OCT will be left to the reader since it is not included in the subject of this work.

1.3.2 Time Domain OCT (TD-OCT)

TD-OCT is the most basic implementation to perform OCT imaging. This setup was employed in early OCT research due to its simplicity. TD-OCT relies on the combination of a broadband light source, a Michelson-type interferometer, and a mechanical scanning of the reference arm, as seen in Figure 3.

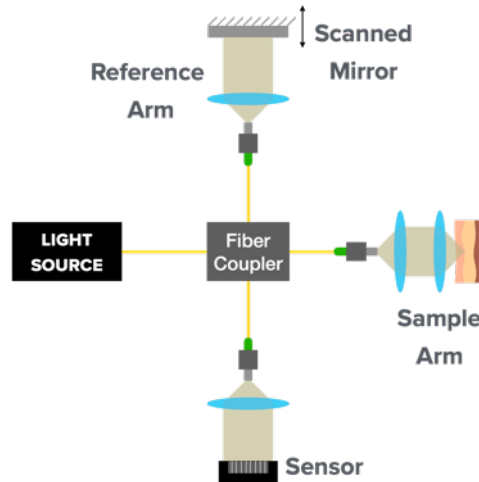


Figure 3. Time Domain OCT basic diagram.

In practice, TD-OCT is usually performed using optical fibers, and the complexity of a TD-OCT imaging system is higher than the one shown in Figure 3. Figure 4 is more presentative of a practical TD-OCT system. Low coherence light is sent to a circulator to be then split 50%/50% among the reference arm and the OCT probe. The OCT probe illuminates the sample and collects the reflected light that will interfere with light from the reference arm. The reference arm is usually built with polarization control to maximize the electric field interference at the detector side and a high speed delay scanner or galvo. This scanner oscillates a mirror along the optical axis. This oscillation allows the scanning at different optical path lengths. When light is coupled back to the fibers and recombined at the 50%/50% splitter, part of the light goes back to the light source arm while the rest of the light goes directly to the detector. The circulator allows the

recovery of the light in the source arm and delivers it to a balanced detector to be subtracted from the direct detection arm. By subtracting the signals, the desired interference adds the amplitude in both arms while the relative intensity noise (RIN) from the light source is canceled [39].

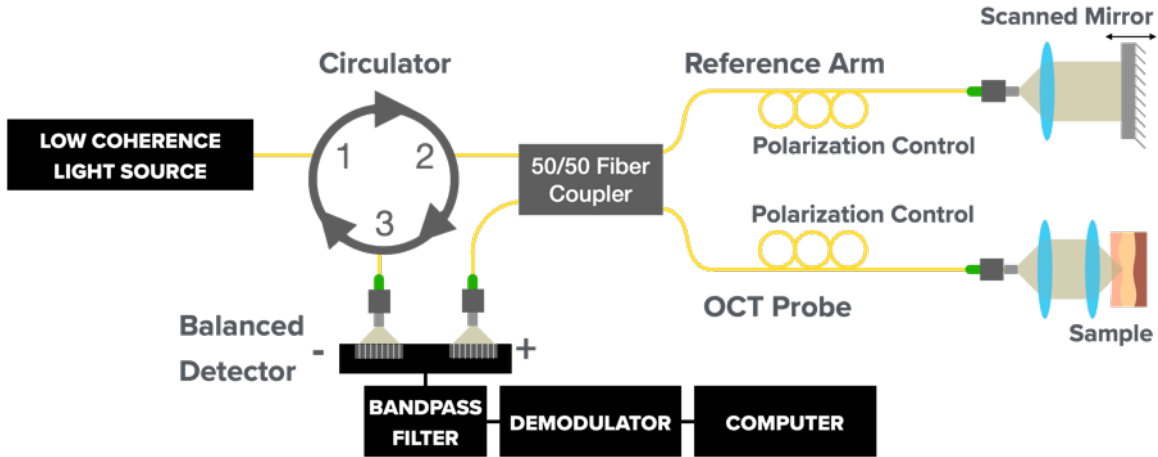


Figure 4. Diagram of a balanced detection system in a TD-OCT configuration.

The system shown in Figure 4 can measure the temporal delay between light sent to the sample and light sent to the reference high speed delay scanner mirror as a function of depth [40]. For simplicity, let us examine the case of a single scatterer in the sample arm. Let the scatterer at the sample arm have reflectivity $R_s = |r_s|^2$, and it is located at depth z_s . Let the reference arm have reflectivity $R_r = |r_r|^2$, and it is located at z_r . z_r is moving at a constant velocity v_r , and therefore $z_r = v_r t$ [40]. In this case, the delay τ is given by [40]

$$\tau(t) = \frac{2[v_r t - z_s]}{c}$$

c is the speed of light. The intensity at the detector as a function of $\tau(t)$ becomes [40]

$$I_{det}(t) = \alpha \beta I_0 \left[\underbrace{R_R + R_S}_{DC} + \underbrace{2\sqrt{R_R R_S} \times \cos(2k_0 v_r t - \phi) \times \exp\left(-16 \ln(2) \left[\frac{v_r t - z_s}{c \tau_c}\right]^2\right)}_{AC} \right]$$

α and β are the fractions of light sent to each arm, I_0 is the source intensity, k_0 is the source center wavelength k number, τ_c is the source's coherence time, and the ϕ is the phase difference given by

$$\phi = \frac{2\omega_0 z_S}{c}$$

$I_{\text{det}}(t)$, plotted in Figure 5 in blue, can be separated on a DC and an AC term. The DC term does not carry any information about the scatterer. The information is enclosed in the AC term. The echo interferometric amplitude given by [39]

$$A_{\text{int}} = \alpha\beta I_0 [\sqrt{R_R R_S}]$$

is related to the reflected light intensity that reaches the detector. In TD-OCT, the envelope plotted in red carries the spatial information about the sample reflectivity and the location [39].

A_{int} is scaled by r_s and shifted in time by z_s/v_r . The time axis can be scaled to represent the physical distance along the A-scan axis using the velocity of the reference arm mirror v_r .

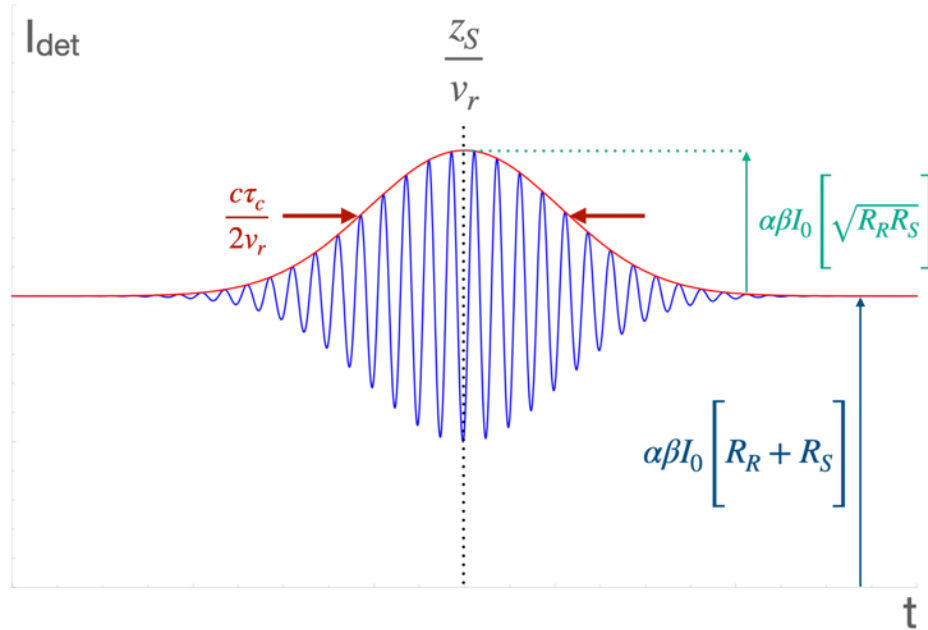


Figure 5. Interferogram showing the carrier in blue and the envelope in red.

For multiple scatterers as shown in Figure 6 the sample can be represented as a collection of N scatterers located at depths z_{Sn} such that

$$r_s(z) = \sum_{n=1}^N r_{Sn} \delta(z - z_{Sn})$$

where r_{Sn} is the reflectivity of the N th scatterer at the axial location z_{Sn} [40].

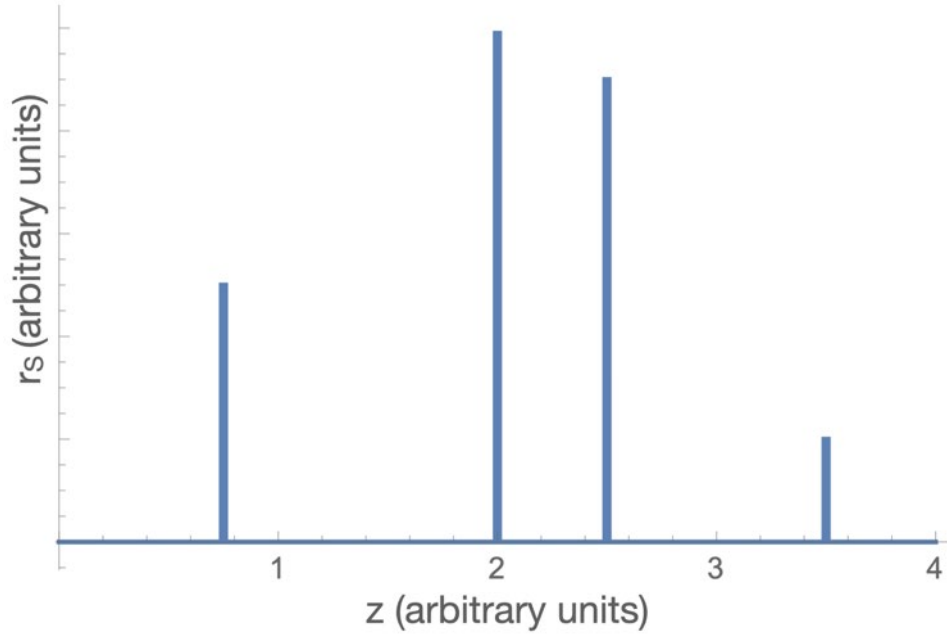


Figure 6. Representation of multiple scatterers along the axial direction.

Then the photocurrent at the detector becomes [40]

$$I_{det}(t) = \alpha \beta I_0 \left[\underbrace{R_R + \sum_{n=1}^N R_{Sn}}_{DC} + 2r_R \sum_{n=1}^N r_{Sn} \times \underbrace{\cos(2k_0 v_r t - \phi_n)}_{Carrier} \times \underbrace{\exp\left(-16 \ln(2) \left[\frac{v_r t - z_{Sn}}{c \tau_c}\right]^2\right)}_{Envelope} \right]$$

where ϕ_n is the phase that depends on the n th scatterer position z_{Sn} given by

$$\phi_n = \frac{4\pi z_{Sn}}{\lambda_0}$$

The DC is usually filtered using an electronic high pass filter to increase the detector dynamic range. This result is not different than the equation for a single scatterer with the exception that it is a superposition of the interferogram given by the multiple scatterers. Therefore, by rectifying I_{det} , after the DC term filtering, only the envelop remains. Figure 7 shows I_{det} and its envelope showing the location of the scatterers in Figure 6.

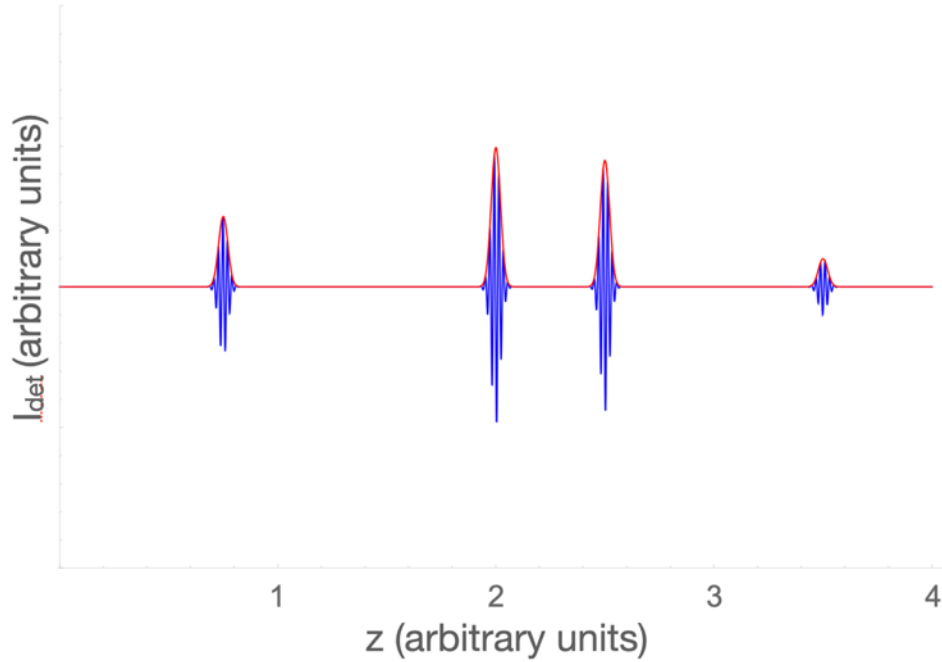


Figure 7. Full I_{det} is shown in blue. Envelope shown in red.

After filtering the DC term and the carrier I_{det} becomes proportional to

$$I_{det}(t) \propto \left[2r_R \sum_{n=1}^N r_{Sn} \times \exp \left(-16 \ln(2) \left[\frac{z - z_{Sn}}{l_c} \right]^2 \right) \right]$$

which is the function usually graphed as the A-scan in an TD-OCT system such as the one shown in Figure 8.

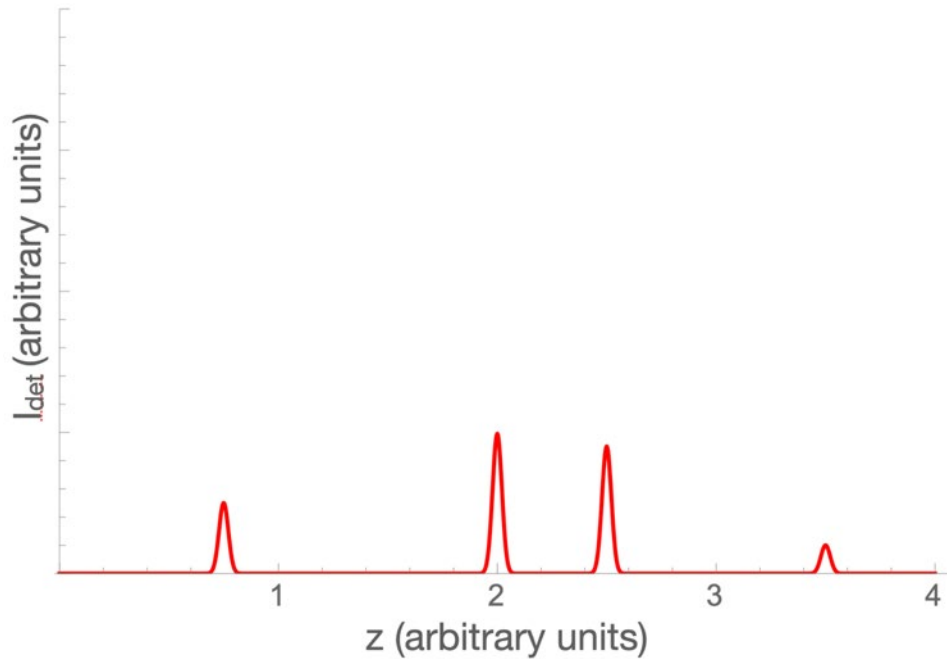


Figure 8. A-line extracted from the multiple scatterers.

1.3.3 Spectral Domain OCT (SD-OCT)

SD-OCT is an advanced OCT implementation where a spectrometer is used to analyze the interfered light from the reference and sample arms. This implementation uses the spectrometer to detect the interference pattern using a line scan CCD array [39,40]. Figure 9 shows the basic diagram of a SD-OCT implementation where the Michelson interferometer acts as a periodic frequency filter that depends on the optical path difference between the sample and reference arms. In this setup, the reference arm mirror is fixed, the simpler source used in these setups is a broadband short coherence super luminescent diode (SLD), and a spectrometer is used to acquire the interferometric data as a function of wavenumber k .

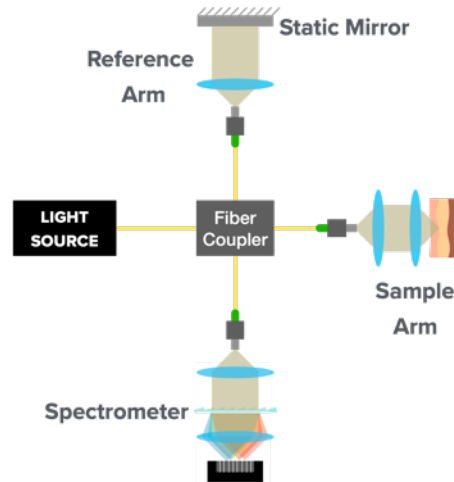


Figure 9. Spectral Domain OCT basic diagram.

Figure 10 shows a diagram of a typical SD-OCT instrument. The low coherence light source is delivered through a fiber coupler that splits the light between the reference and the sample arm. The reference arm has a fixed delay, and it is not scanned. The diagram belongs to an ophthalmic OCT system and includes the ophthalmic user interface. After the light propagates through the reference arm and the sample arm, the reflected light is directed towards the spectrometer CCD camera. A computer reads the line CCD array, rescales the data from wavelength to wavenumber, and performs a Fourier transform to generate A-scans. In this setup, the reference arm has a glass block and density filter to match the reference mirror dispersion and dim the light to appropriate levels to maximize fringe contrast.

SD-OCT has the advantage that it simultaneously detects light reflected from all delays in the sample arm [39]. SD-OCT relies heavily on the power spectral dependence of the light source [39]. For a comprehensive understanding, we will consider a Gaussian shaped spectrum as a function of wavenumber $S(k)$ shown in Figure 11. The interference of the two beams will

show the Gaussian shaped spectrum modulated with a periodicity that is inversely proportional to the echo time delay given by the location of the scatterer reflecting light.

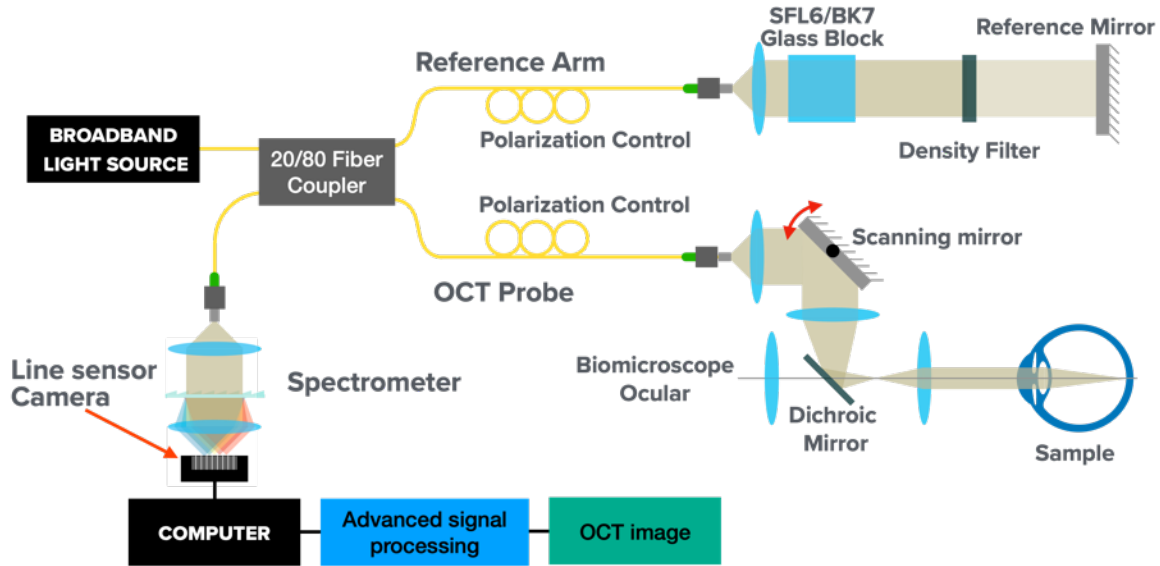


Figure 10. Ophthalmic Spectral Domain OCT system diagram.

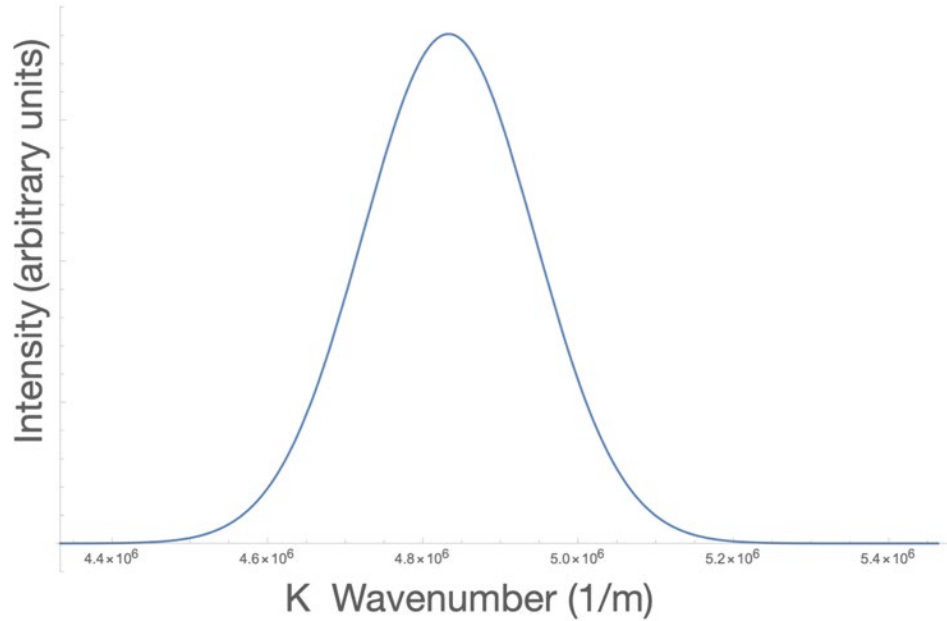


Figure 11. Gaussian shaped spectrum as a function of wavenumber $S(k)$

Due to the inverse relationship, different optical delays will generate different frequency modulations over-imposed in the Gaussian shaped spectrum, as shown in Figure 12.

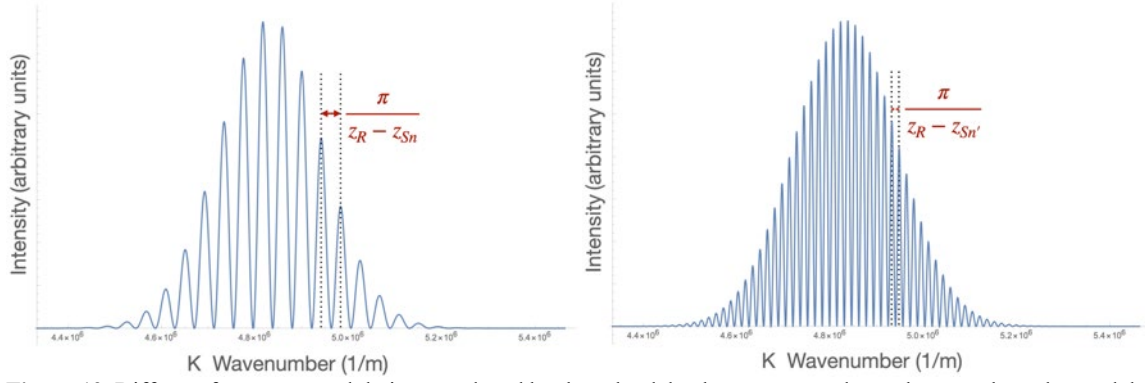


Figure 12. Different frequency modulations produced by the echo delay between z_R and z_{S_n} where $z_{S_{n'}}$ has a larger delay than z_{S_n} . The frequency modulation is imposed in a Gaussian shaped spectrum.

For an example, let's consider multiple scatterers as shown in Figure 13 the sample can be represented as a collection of N scatterers located at depths z_{S_n} such that

$$r_s(z) = \sum_{n=1}^N r_{S_n} \delta(z - z_{S_n})$$

where z_{S_n} is the reflectivity of the N th scatterer at the axial location z_{S_n} [40].

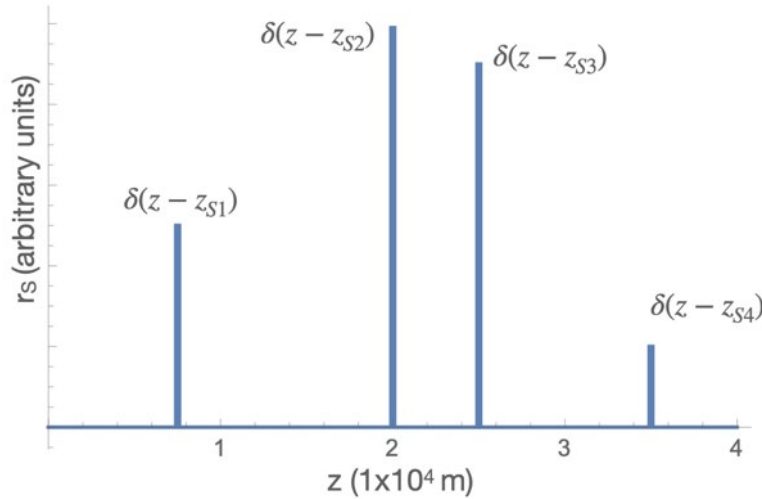


Figure 13. Representation of multiple scatterers along the axial direction using a delta function scaled by their respective reflectivity.

When this mathematical representation of the sample is introduced in the OCT theory, it can be shown that the intensity as a function of the wavenumber at the detector plane is [39]

$$I_{det}(k) \propto S(k) \left[\underbrace{\frac{1}{4} \left(R_R + \sum_{n=1}^N R_{Sn} \right)}_{DC} + \underbrace{\frac{1}{2} \sum_{n=1}^N \sqrt{R_R R_{Sn}} \times \cos(2k(z_R - z_{Sn}))}_{Cross-CorrelationTerms} + \underbrace{\frac{1}{4} \sum_{m \neq n=1}^N \sqrt{R_{Sm} R_{Sn}} \times \cos(2k(z_{Sm} - z_{Sn}))}_{Auto-CorrelationTerms} \right]$$

I_{det} shows three distinct terms that depend on the source spectrum and reflectors:

1. A DC term composed of the addition of all reflections independent of optical path.
2. A cross-correlation term that includes a cosine frequency for each reflector in the sample that depends on the optical path difference between the sample's reflectors and the reference arm. This is the desired component for OCT imaging since it encodes $r_s(z)$.
3. An auto-correlation term for each combination in between the reflectors in the sample that will appear as artifacts in the final OCT image.

Note that the spectrum is modulated by multiple cosine terms, each having a different frequency and amplitude that depends on the position of the reflector and the reflection efficiency. An example of the Gaussian spectrum modulated by the reflectors shown in Figure 13 is shown in Figure 14. Note that the cosine terms can add constructively or destructively along the spectrum.

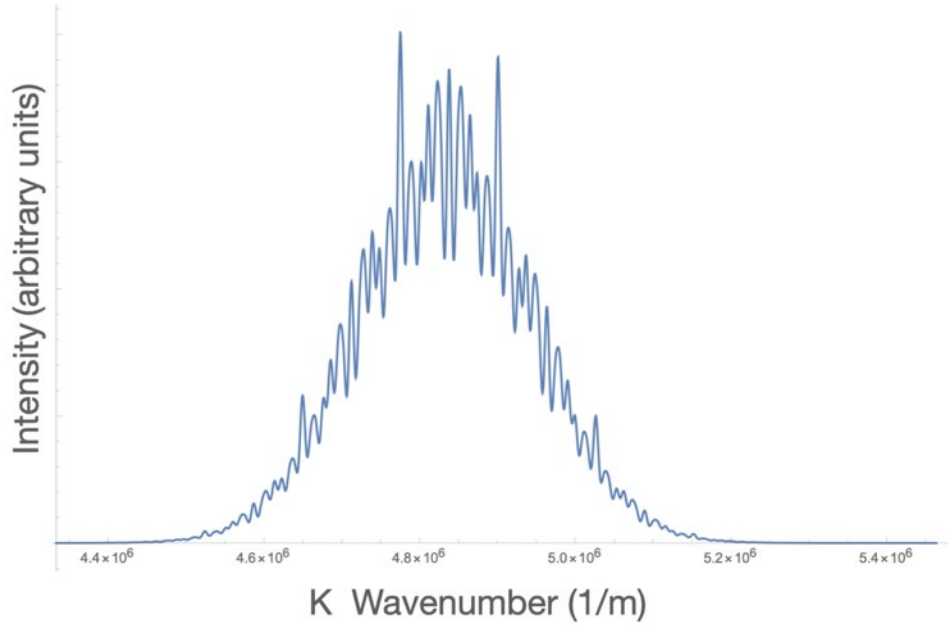


Figure 14. Representation of I_{det} at the detector plane. Cross-correlation terms and auto-correlation terms are present.

Often, the DC term is dominated by R_R . Therefore, having knowledge of the spectrum, the DC term can be subtracted almost entirely. After an ideal subtraction of the DC term, the interferogram oscillates along the axis, but note that an envelope provided by the spectrum is still present, as seen in Figure 15.

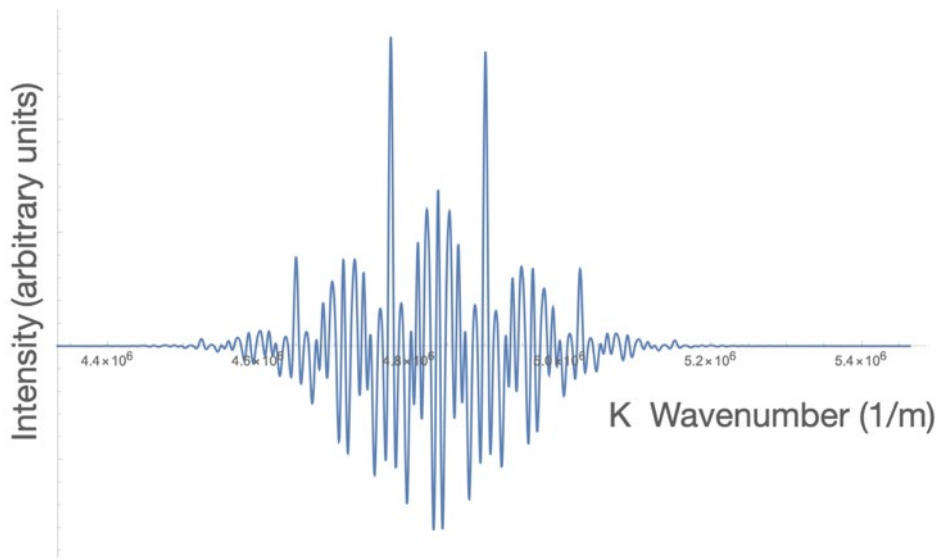


Figure 15. Representation of I_{det} after spectrum DC term subtraction.

The I_{det} function shown in Figure 15 can be expressed using

$$I_{det}(k) \propto S(k) \left[\underbrace{\frac{1}{2} \sum_{n=1}^N \sqrt{R_R R_{Sn}} \times \cos(2k(z_R - z_{Sn}))}_{\text{Cross-CorrelationTerms}} + \underbrace{\frac{1}{4} \sum_{m \neq n=1}^N \sqrt{R_{Sm} R_{Sn}} \times \cos(2k(z_{Sm} - z_{Sn}))}_{\text{Auto-CorrelationTerms}} \right]$$

I_{det} encodes $r_S(z)$ in the cross-correlation cosine terms. The auto-correlation terms and amplitude modulation given by $S(k)$ appear as artifacts in the reconstruction of $r_S(z)$. When using Fourier analysis to process I_{det} , the Fourier transform of the used spectrum $\gamma(z)$ called the “coherence function” dominates the axial (A-scan direction) point spread function as it broadens the delta functions shown in Figure 13 [39]. Making use of the convolution theorem, the Fourier transform pair $.5(\delta(z+z_0)+\delta(z-z_0)) \Leftrightarrow \cos(k z_0)$, and the sifting property of the delta function, we can obtain the Fourier transform of I_{det} that is used as the A-scan in OCT [39]. The result is in the form of

$$\mathfrak{F}\{I_{det}(k)\}_{k \rightarrow z} \propto \underbrace{\gamma(z)}_{\text{BlurTerm}} \left[\underbrace{\frac{1}{4} \sum_{n=1}^N \sqrt{R_R R_{Sn}} (\delta[2(z_R - z_{Sn})] + \delta[2(z_R - z_{Sn})])}_{\text{Cross-CorrelationTermscontain}r_S(z)} + \underbrace{\frac{1}{8} \sum_{m \neq n=1}^N \sqrt{R_{Sm} R_{Sn}} (\delta[2(z_{Sm} - z_{Sn})] + \delta[2(z_{Sm} - z_{Sn})])}_{\text{Auto-CorrelationTerms}} \right]$$

Note that $r_S(z) = \sum_{n=1}^N r_{Sn} \delta(z - z_{Sn})$ is reproduced in the cross-correlation terms with the following modifications: $r_S(z)$ is blurred by the coherence function $\gamma(z)$, it is scaled by $1/4$ r

that acts as a gain factor, the reference coordinate is z_R , and the apparent displacement of each sample reflector from the reference position is doubled due to the interferometer roundtrip. To simplify the representation z_R is set to z and $\mathfrak{F}\{I_{det}(k)\}_{t \rightarrow z}$ is scaled so $z_{Sn}=0.5z_{Sn}'$. By doing this, we obtain the function shown in Figure 16 that includes the negative complex conjugate artifact due to the Hermitian nature of the inverse Fourier transform. Both the negative complex conjugate and the positive conjugate must be real and identical since they are Hermitian [41].

The OCT reconstruction only needs the cross-correlation terms. Often, a blur, a median, or a threshold filter is used to eliminate or flatten the autocorrelation terms. Then, $\mathfrak{F}\{I_{det}(k)\}_{t \rightarrow z}$'s positive side is plotted as the A-scan for OCT image resulting in Figure 17. Figure 17 shows the scaled and blurred cross-correlation terms with a threshold filter where everything below the threshold is shown as black in the OCT image.

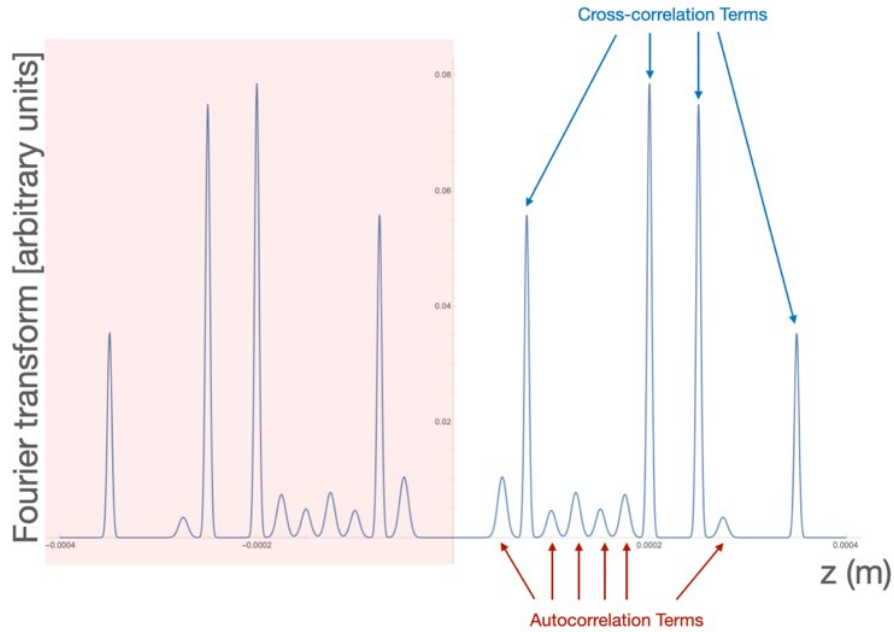


Figure 16. Fourier transform showing the positive and the negative sides. The red side of the graph is usually not used.

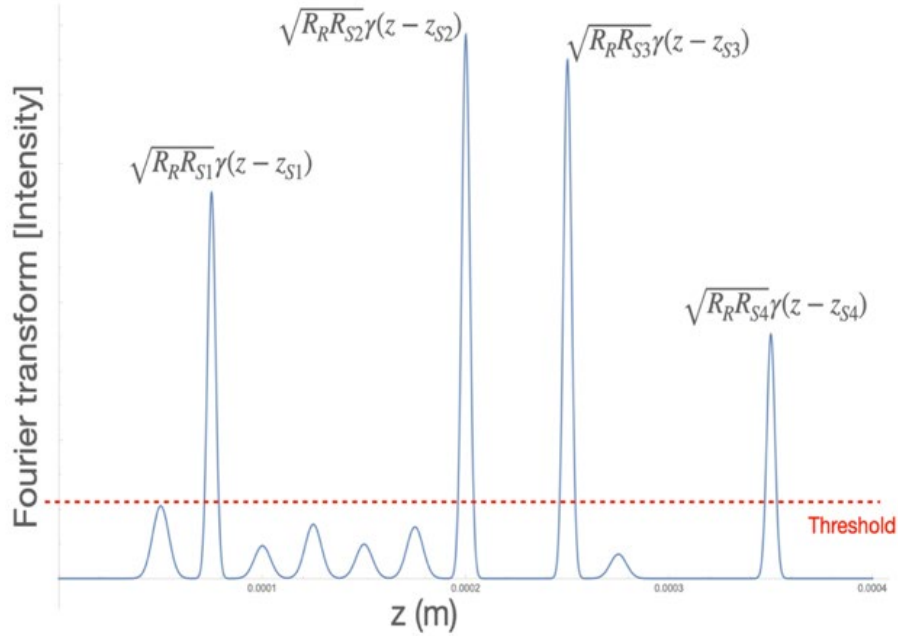


Figure 17. Fourier transform showing only the positive side with a threshold filter.

A similar implementation to SD-OCT is the Swept Source OCT (SS-OCT), also known as frequency domain interferometry (OFDI). SS-OCT uses an interferometer with a frequency swept narrow-band light source [39] that depends on time. While the method differs, the mathematical representation is equivalent. The difference is that I_{det} depends on time instead of wavenumber. The Fourier transform also recovers a blurred $rs(z)$.

1.3.4 OCT Mechanism of Contrasts in Tissue

OCT signal originates from the back-reflected or backscattered light from the sample that is captured by the OCT sample arm optics [39,40]. Back-reflections happen at interfaces in between two layers of different mediums with different indices of refraction, with the amount of back-reflected light dependent upon the index of refraction difference. In the special case of a single surface and light with normal incidence, the back-reflections can be calculated by

$$\rho = \left[\frac{n_2 - n_1}{n_2 + n_1} \right]^2$$

The largest index of refraction mismatch normally encountered is at an air-tissue interface. Since the average index of refraction of tissue is about 1.4, this will lead to a 2.8% back-reflection.

Smaller back-reflections can occur at other types of interfaces.

Because tissue is extremely complex, with components from the nanometer to meter scale, multiple indices of refraction mismatches occur within an OCT focal volume. Therefore, contrast is often said to come from back-scattering due to a summation of back-reflection events. The denser the number and scale of index mismatches, the stronger the backscattering, and the higher the OCT signal appears from that region of tissue. An example of an image region that would appear bright is a cell-rich tissue layer since cells are high back-scatterers due to their membranes, nuclei and sub-cellular components. On the other end, regions that lack scatterers, such as clear fluid-filled cavities, appear dark. The light remitted from the tissue and collected by the sample arm optics interferes with the light returning from the OCT reference arm, and the depth location of the backscattering is extracted by processing the interferometric data.

Variants of OCT exploit alternative mechanisms of contrast. For example, polarization sensitive OCT obtains its contrast through sensitivity to changes in the polarization of the incident light, due to tissue birefringence and retardance. Doppler OCT (DOCT) obtains contrast by sensitivity to phase changes in the incident light, caused by interaction with moving scatterers such as red blood cells in capillaries or other blood vessels. Spectroscopic OCT obtains its contrast from measuring relative changes in the amplitude as a function of wavelength of the incident light, due to the wavelength-dependent absorption coefficient of the medium.

1.4 Multi-Photon Microscopy (MPM)

1.4.1 Multi-Photon Microscopy (MPM) Principles

Multi-photon microscopy (MPM) is an imaging technique based on the molecules' ability to absorb two or more low-energy photons. This technique can produce at least four signals of biological interest: 2-Photon Excited Fluorescence (2PEF), 3-Photon Excited Fluorescence (3PEF), Second Harmonic Generation (SHG), and Third Harmonic Generation (THG). The absorption of the photon energy excites the molecules to a higher electronic state, and the molecules decay to the ground state by emitting a single higher-energy photon. The higher electronic state is a virtual state when SHG and THG are produced, and an allowed electronic state when 2PEF and 3PEF are generated. The molecules that experience the latter transition and radiometric decay are commonly named fluorophores.

The main difference between 1-photon fluorescence and multi-photon fluorescence is the number of photons absorbed. In 1-photon fluorescence, a high-energy photon is absorbed, and a photon with slightly less energy is emitted. Since the excitation light photon energy should match the molecule's energy gap, the excitation spectrum often partially overlaps with the emission spectrum making the detection of fluorescent light difficult. A useful representation of the fluorescence effect is shown in Figure 18. Multi-photon fluorescence adds the energy of the photons being absorbed. Therefore, the main advantage of two and three photons fluorescence is that a significantly different excitation wavelength can excite the molecule allowing the definite differentiation between the excitation and emission wavelengths [43]. Another significant advantage of multi-photon in life sciences is the use of incident light in the near infrared since it allows deeper tissue penetration and causes less photobleaching and heating of tissue.

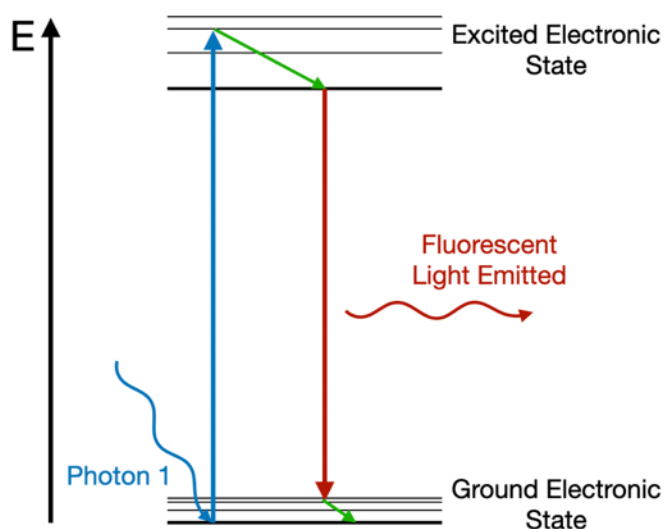


Figure 18. Jablonski diagram for 1-photon absorption fluorescence excitation. Left axis represents the energy and bottom axis represents time. Blue squiggly arrow represents a high energy photon that is absorbed by the molecule. Blue arrow represents the transition of the electron to a possible excited electronic state. Green arrow represents energy dissipation between vibrational states. Red arrow represents the transition of the molecule to a ground electronic state where the energy is dissipated through electromagnetic emission represented with the red squiggly arrow. If the molecule does not come back to the true ground state after electromagnetic emission decay, it can further decay through energy dissipation until ground state is reached.

Unfortunately, multi-photon effects require at least two photons delivered in a very short period of time in the order of a femtosecond rendering a small probability of a multi-photon event happening [40]. Therefore, to generate multi-photon effects, very high power must be used to increase the photon flux and increase the probability of two photons interacting with a molecule in such short times. This necessity has been fulfilled using high NA optical systems that compact the photon flux into a very small volume and recent advances in laser technology. These lasers provide high average power with short laser pulse duration at high repetition rates.

In tissue, multi-photon effects can be obtained using endogenous tissue fluorophores and exogenous fluorophores used as contrast agents. Collagen, elastin, NADH, and flavins are major endogenous fluorophores in tissue that can be excited to produce 1-photon fluorescence with wavelengths in the 200 to 500 nm range and detected in a bandwidth that spans from 300 to 600

nm [40]. Exogenous fluorophores such as cyanine dyes (e.g., Cy5.5, indocyanine green) have excitation wavelengths in the 600 to 800 nm range and emission in the 700 to 900 nm range. An ideal multi-photon excitation laser for these fluorophores should exhibit a center wavelength between 1200 and 1500 nm, which is the overlap between the two-photon excitation of exogenous fluorophores in the 1200-1600 nm range, and the three-photon excitation of endogenous fluorophores between 600-1500 nm.

1.4.2 MPM Mechanisms of Contrast in Tissue

1.4.2.1 Two and Three Photon Excited Fluorescence (2PEF, and 3PEF)

Several different molecules generate 2-Photon Excited Fluorescence (2PEF) and 3-Photon Excited Fluorescence (3PEF) in tissue, including NADH, NADPH, and FAD, known to be up-regulated in cancerous cells [44]. As described before, 2PEF is generated in molecules that can absorb two photons nearly simultaneously, taking the molecule to an excited electronic state to decay emitting light with a shorter wavelength than the excitation light.

2PEF is akin to traditional fluorescent because it is considered an isotropic phenomenon due to the random rotation of the molecule dipole [40]. Since 2PEF is an inelastic transition, some energy is lost in the non-radiative relaxation of the molecule, and the emitted wavelengths for 2-PEF are usually a spectrum of longer wavelength than the two-photon energy equivalent wavelength. This shift in wavelength is known as the Stokes shift [40]. The effect is illustrated in Figure 19.

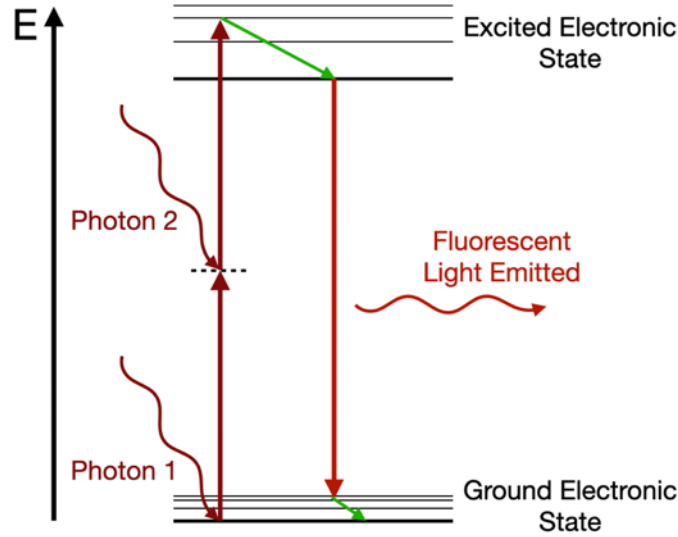


Figure 19. Jablonski diagram for 2-photon absorption fluorescence excitation. Left axis represents the energy and bottom axis represents time. Dark red squiggly arrow represents a high energy photon that is absorbed by the molecule that transition the electron to a possible excited state. The molecule can then relax through non-radiative relaxation (green arrow) until it decays by emitting electromagnetic radiation (light red squiggly arrow).

For the 2-PEF, all of the traditional fluorescence effects happen and therefore the relationships between the incident power and radiated power are virtually the same [40]. The differences are the way that the cross-section of the sample is calculated and the quantum efficiency of the sample. The 2PEF emitted power can be calculated by using the following equation [40],

$$P_f^{2PEF} = \eta^{2PEF} \sigma_a^{2PEF} \frac{\nu_f}{2\nu_i} E_i^2$$

where P_f^{2PEF} is the two photons fluorescent power, η^{2PEF} is the 2PEF quantum yield of the material, σ_a^{2PEF} is the 2PEF cross-section, ν is the fluorescent and the illumination wavelength frequencies, E_i is the irradiance in W/m^2 .

The power relationship P_f^{2PEF} is for a single wavelength, and therefore, the need to integrate P_f^{2PEF} over the range of wavelengths with the energy of $E_{min}=h\nu_i$ to $E_{max}=2 h\nu_i$. The final florescent power for this range of wavelengths can be calculated by

$$P_{f-Total}^{2PEF} = \int_{\nu_{min}}^{\nu_{max}} \eta^{2PEF} \sigma_a^{2PEF} \frac{\nu}{2\nu_i} E_i^2 d\nu$$

2PEF signal is typically very weak. An efficient way to increase 2PEF signal without increasing linear absorption is to confine the laser energy in high energy pulses instead of using continuous wave illumination. In order to account for the time dependency of the illumination P_f^{2PEF} can be expressed in terms of the laser irradiance

$$P_f^{2PEF}(t) = \eta^{2PEF} \sigma_a^{2PEF} \frac{\nu_f}{2\nu_i} E_i^2(t) = \sigma_f^{2PEF} E_i^2(t)$$

Therefore, by multiplying P_f^{2PEF} by $\langle E_i(t) \rangle^2 / \langle E_i(t) \rangle^2 = 1$, the average emitted power becomes

$$\langle P_f^{2PEF}(t) \rangle = \sigma_f^{2PEF} \langle E_i^2(t) \rangle = \sigma_f^{2PEF} \langle E_i(t) \rangle^2 \frac{\langle E_i^2(t) \rangle}{\langle E_i(t) \rangle^2}$$

Note that $\langle E_i(t) \rangle^2$ is the average irradiance of the pulsed laser (E_{ave}), and the last term

$\langle E_i^2(t) \rangle / \langle E_i(t) \rangle^2$ is the degree of second-order coherence of the laser being used that can be expressed such that

$$\langle P_f^{2PEF}(t) \rangle = \sigma_f^{2PEF} E_{ave}^2 \frac{g_p}{\tau_p f}$$

where g_p is the pulse shape factor (rectangular $g_p=1$, Gaussian $g_p=.664$), τ_p is the pulse duration and f is the laser repetition rate. Therefore, by decreasing either τ_p or f , or increasing E_{ave} the average emitted power can be increased.

3-Photon Excited Fluorescence (3PEF) is generated by a similar process as 2PEF, and it is also generated by upregulated endogenous fluorophores. 3PEF can confirm the presence of NADH and FAD [45]. The effect is illustrated in Figure 20. 3PEF elevates the electron to a higher energy state. Therefore, when it decays emitting electromagnetic radiation, the molecule emits a higher energy photon.

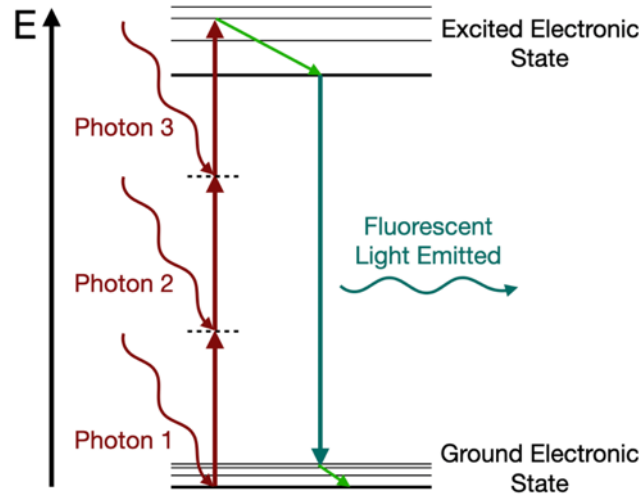


Figure 20. Jablonski diagram for 3-photon absorption fluorescence excitation. Dark red squiggly arrow represents a high energy photon that is absorbed by the molecule that transition the electron to a possible excited state. The molecule can then relax through non-radiative relaxation (green arrow) until it decays by emitting electromagnetic radiation (green squiggly arrow).

1.4.2.2 Second Harmonic Generation (SHG) and Third Harmonic Generation (THG)

SHG and THG are processes that are instantaneous, coherent, and preserve polarization [40].

These processes involve the absorption of two or more photons at the same time. SHG, THG, and higher harmonics that happen during light interactions are described by the simplified polarization density [40]

$$\rho = [\varepsilon_0 X^{(1)} \rho + \varepsilon_0 X^{(2)} \rho^2 + \varepsilon_0 X^{(3)} \rho^3 + \dots],$$

where ε_0 is the permittivity of free space, $X^{(n)}$ is the nth- susceptibility, and ρ is the electric field (E) phasor term equal to $.5[Ee^{-i\omega t} + E^*e^{i\omega t}]$. Note that the nth- susceptibility factors are dependent on the sample. Additionally, the arrangement of the molecules contributes to the signal enhancing or annihilating through constructive or destructive interference due to the coherent nature of SHG. For all MPM signals described here, phase matched conditions and confinement of photons are necessary to achieve the type of field strengths required by the technique. This is

usually accomplished by using a high-power pulsed laser to obtain large electric field amplitude and a large NA_{obj} to confine photons into a small volume. These requirements allow us to specify the laser to be used in the system.

Second Harmonic Generation (SHG) is generated when non-centrosymmetric molecule arrangements absorb two photons simultaneously, taking the molecule to a virtual excited state to later decay by emitting light of exactly half the wavelength than the excitation light. These molecules are called harmonophores since they can generate optical harmonics under illumination from an intense optical field (akin to a fluorophore for fluorescent emission). It is described by the second term of the polarization density that depends on $X^{(2)}$. Figure 21 illustrates SHG using a Jablonski diagram. SHG is strongly generated by healthy organized collagen molecules that are disrupted by cancerous lesions [46].

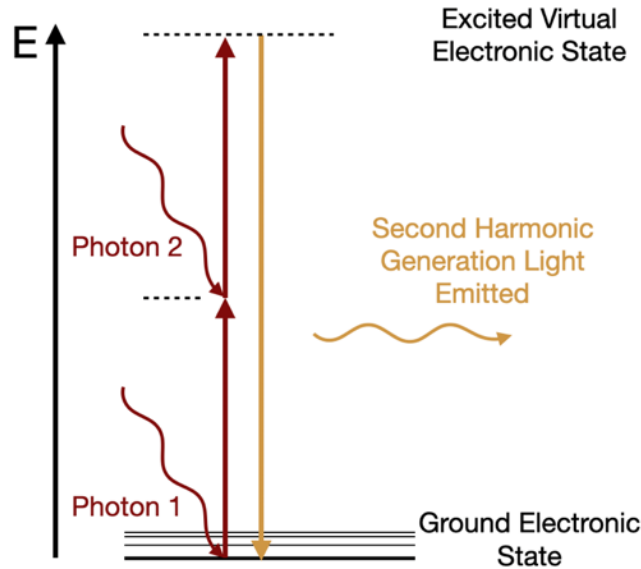


Figure 21. Jablonski diagram for SHG. Dark red squiggly arrow represents a high energy photon that is absorbed by the molecule that transition the electron to a virtual excited state. The molecule can only return to the ground state by emitting electromagnetic radiation (yellow squiggly arrow).

SHG is an $X^{(2)}$ process described by the second-order polarization density, which is the second term in the polarization density equation.

$$P^{(2)} = \epsilon_0 X^{(2)} \rho^2$$

SHG depends on the molecular orientation. Since SHG is a coherent process, the molecules can enhance or annihilate the signal through constructive or destructive interference [40]. Figure 22 illustrates this process. For focused Gaussian beams, the SHG power generated is

$$P_{SHG} = \frac{13\pi^2 d_{eff}^2 L}{\epsilon_0 c n_F^2 \lambda_F^3} P_F$$

where d_{eff} is the d coefficient defined as $.5 X^{(2)}$, L is the interaction length, n, λ , and P_F are the fundamental index, wavelength, and power.

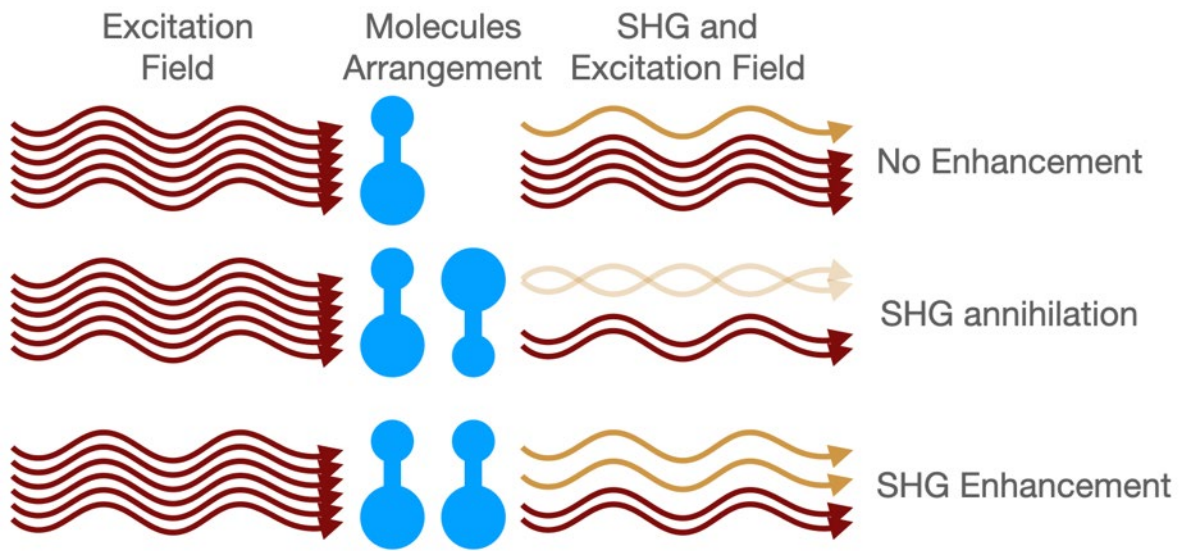


Figure 22. Molecular dependence of SHG. If molecules emit SHG off-phase, SHG from the different molecules can interact destructively annihilating SHG. If molecules emit SHG in-phase, the emitted SHG interacts constructively.

Third Harmonic Generation (THG) is similar to SHG. In the case of THG, a molecule absorbs three photons simultaneously, taking the molecule to a virtual state with higher energy than SHG. Since the atom is in a virtual state, the atom must decay by emitting light of exactly one third the wavelength of the excitation light, as shown in Figure 23.

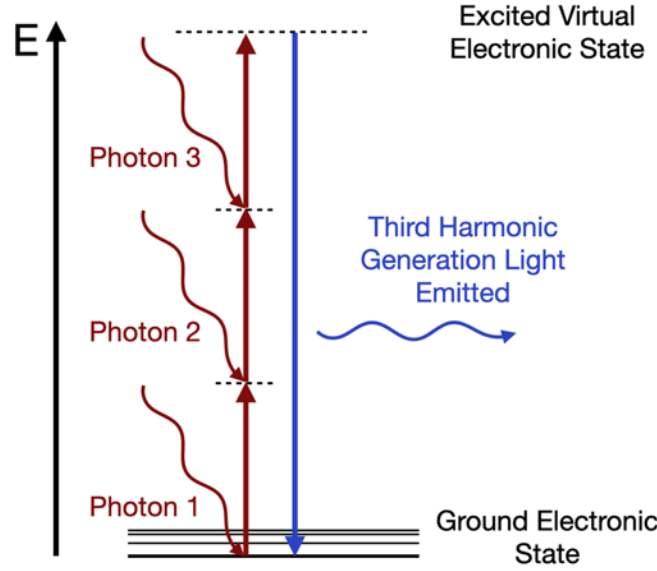


Figure 23. Jablonski diagram for THG. Dark red squiggly arrow represents a low energy photon that is absorbed by the molecule. An electron is transitioned to a virtual excited state. The molecule can only return to the ground state by emitting electromagnetic radiation (blue squiggly arrow).

THG is generated at a sharp index of refraction discontinuities where the discontinuity allows for the harmonic generation of light without destructive interference caused by the Gouy phase shift [46,47]. If this condition is not met, any THG generated just before the focus interferes destructively with THG generated just after [48]. By considering a high energy laser beam propagating in the z direction with a Gaussian profile, the third harmonic power generated is [49]

$$P_{THG} = k_{3\omega} k_{\omega}^3 \left(\frac{4\pi}{n_{3\omega} n_{\omega}^2 c} \right)^2 P_w^3 \left| \int_{z'_L}^{z'_R} \frac{X^{(3)} e^{i(k_{3\omega} - 3k_{\omega})(k_{\omega} \omega_0^2)z'}}{(1 + iz')^2} dz' \right|^2$$

where $X^{(3)}$ is the third order susceptibility, z' normalized coordinate along the optical axis measured from the beam waist position, k_{ω} and n_{ω} the fundamental wave number and index of refraction respectively, $k_{3\omega}$ and $n_{3\omega}$ are the third harmonic wave number and index of refraction respectively, ω_0 is the beam waist radius, and P_{ω} is the excitation laser power. z'_L and z'_R are normalized input and output places coordinates. In general, THG is useful to observe muscle fibers, cell membranes, and fatty connective tissue that are boundaries between the aqueous interstitial fluids and large protein aggregates or lipid structures.

1.5 Narrow-Band Reflectance Imaging

1.5.1 Reflectance Mechanisms of Contrast

Light incident upon a boundary between two media with different indices of refractions may be reflected, absorbed, or transmitted. The properties of the material, the directional properties of the incident light, and the wavelength can affect the amount of light that goes to each process [50]. Reflected light can be diffuse or specular and is differentiated by its directional behavior. The specular reflection is described by the law of reflection where the incident light angle with the normal of the boundary is the negative of the specular reflected light angle ($\theta_i = -\theta_r$) [51]. In contrast, diffuse reflection is light incident upon the two media boundary that reflects towards the same hemisphere containing the incident light but is scattered at many angles rather than just one such as the specular light. Scattered light can have a preferred directionality defined by the wavelength and the directionality of the incoming light as well as the properties of the material. A perfectly specular reflection and a perfectly diffuse reflection (Lambertian profile) are the two extreme profiles that describe the reflection material properties, but most non-ideal materials do not reach these limits.

Spectral reflectance $\rho(\lambda)$, which is the ratio of the reflected spectral flux to the incident spectral flux [50], plays an essential role in narrow-band reflectance imaging since it is the primary mechanism of contrast. Some materials or samples have a higher efficiency reflecting some wavelengths while acting as an absorber or transmitter to other wavelengths, defining the final perceived color of the material. For example, an object made of a material that highly reflects the blue wavelengths in the visible spectrum ($\sim 360\text{-}460\text{ nm}$) but absorbs green and red wavelengths ($\sim 460\text{ to }780\text{ nm}$) will be perceived as a blue object. If this object is illuminated

with a narrow band light (e.g., 635 nm diode), it will appear black since it mostly will absorb this wavelength. However, if the object is illuminated with a blue light (e.g., 445 nm diode), the object will appear bright.

Scanning reflectance imaging uses the apparent brightness of an object to generate an image. This technique scans a focused or collimated laser onto the scene and collects light that reflects diffusely at objects' surfaces point by point. Most reflectance systems use diffuse reflected light as the primary signal to generate an image. Therefore, depending on the target properties, reflectance systems can suffer saturation (whiteout) if the light collecting mechanism captures a specular reflection since most specular reflections carry a more significant radiant intensity (W/sr) than the diffuse reflected light.

1.5.2 Hemoglobin Absorption to Identify Areas of Increased Vascularity

One advantage of using reflectance in endoscopes is that it obtains contrast from tissue scatterers and absorbers, particularly hemoglobin (Hb) and oxyhemoglobin (HbO₂). Narrow-band illumination in the blue side of the visible spectrum (~380-600 nm) enables the identification of regions with increased vascularity which is a hallmark of cancer [1]. As seen in Figure 24, wavelengths in the ~400-425 nm range would be the most absorbed by Hb and HbO₂ [52], providing higher contrast than other wavelengths, but these short wavelengths are not optimum for endoscopy reflectance since laser standards such as the ANSI Z136.1 restricts the irradiance used to illuminate a small spot on the tissue. The restricted irradiance decreases the radiant intensity that can be captured and detected by the scanning optical system.

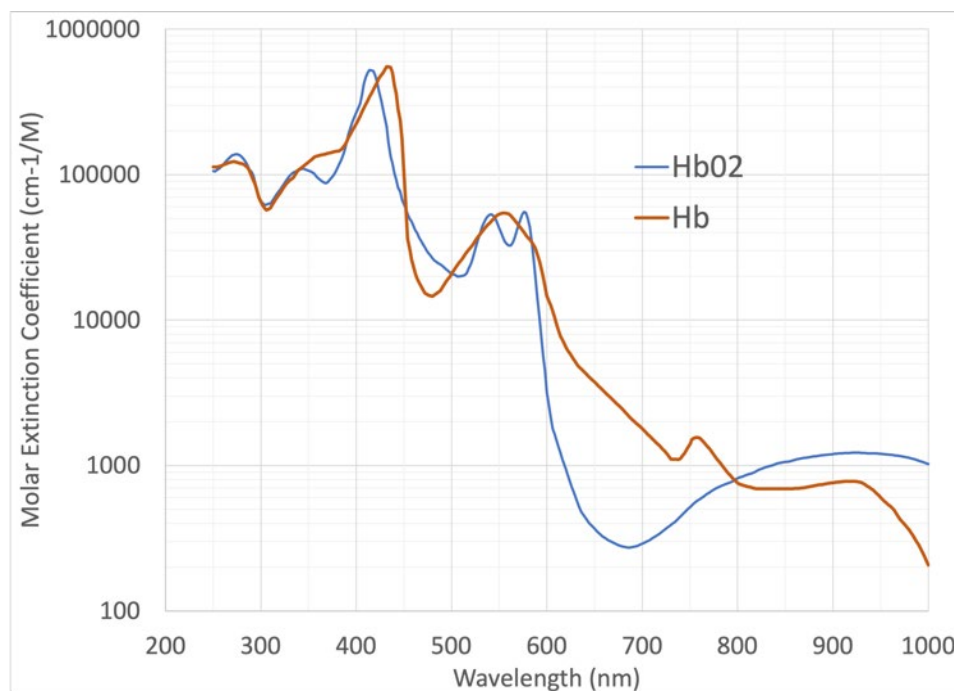


Figure 24. Hemoglobin and Oxyhemoglobin molar extinction coefficient as a function of wavelength. Data reproduced from [52] .

A laser with a center wavelength in the ~520-690 nm can provide contrast with higher irradiance at the illuminated spot while easing detection by increasing the radiant intensity while still in compliance with laser standards.

CHAPTER 2: PRESENT STUDY

The present study demonstrates the design and feasibility of a multimodal co-registered endoscope using a dual optical path lens system. My work enhances the field of optical engineering for biomedical applications with the following contributions:

1. The design, modeling, and testing of a dual optical path lens system featuring embedded and patterned dichroic surfaces that enables co-registered imaging.
2. The development and validation of a proximal system containing the subsystems to support co-registered OCT, MPM, and reflectance imaging.
3. The design and feasibility testing of an endoscope to perform OCT, MPM, and reflectance co-registered imaging.

The appendices include a comprehensive summary of my contributions with manuscripts, supporting documentation, and standard operating procedures developed as part of this work.

2.1 Enabling Multiple Optical Paths for Co-Registered Imaging

While dual optical path objectives were previously reported [38], a similar miniaturized optical system for endoscopic applications was not developed. Therefore, my work demonstrates the use of an optical system that is miniaturized and suited for endoscopic applications. This optical system's design uses stacked lenses for easy alignment, reduces the total length of the optical system by bending the optical path, and provides lenses with diameters considered acceptable for an atraumatic endoscope. Additionally, patterned dichroic surfaces with reflective optical power

enables the endoscopic system to accommodate multiple imaging technologies by providing multiple optical paths.

This work focuses on the design, modeling, and testing of the lenses with the dichroic surfaces. The optical path selection is enabled by choosing the proper illumination wavelengths. The wavelengths in the 470 - 900 nm band transmit through the dichroic surfaces optically unaffected and are only affected by the lenses' optical power. The result is a low NA optical path focused at ~5 mm from the endoscope cover glass. The wavelengths in the 950 - 1450 nm band are reflected in the curved dichroic surfaces arranged in a telescope-like configuration providing additional optical power. A high NA optical path results from this configuration and focuses at ~50 μm from the endoscope cover glass. The curved dichroic surfaces providing the additional optical power are embedded in between lenses cemented together, forming a triplet.

The triplet offers three main practical advantages:

2. The use of a folded optical path decreases the length of the optical system, enabling a compact design and the possibility to use the optical system with flexible endoscopes.
3. The ability to vary the materials (index of refraction and Abbe number), thicknesses, and the radii of curvature in the three elements of the triplet helps correct color aberrations and flatten the field for the high NA optical path.
4. The embedding of the dichroic surfaces protects from mechanical damage such as scratches and detachment of the patterned dichroic surfaces.

Before manufacturing, the model of the optical system was used for several studies to estimate its viability. Such studies included performance analysis, stray light analysis, optical efficiency modeling, and validation of requirements to perform OCM, MPM, and reflectance imaging.

After viability was confirmed, the different elements were manufactured by several vendors:

- The cover glass was manufactured by Bern Optics, Inc. (Westfield, MA, USA).
- The aspheric objective was manufactured by the Precision Freeform Optics Design, Fabrication and Testing Facility at The University of Arizona, and Micro-Lam, Inc (Portage, MI, USA).
- The triplet and its embedded dichroic surfaces were manufactured by Optics Technology, Inc (Pittsford, NY, USA) and Blue Ridge Optics (Bedford, VA, USA).

The elements testing was conducted as part of this work, and Appendix A includes the results in detail. The high NA and low NA optical requirements and measured performance are summarized in Table 2.

Table 2. Optical system requirements and measured performance.

Optical requirements			
Requirement	Specification	Measurement	Pass or Fail
Low NA Optical Path			
Full Field of View	$> 45^\circ$	70°	Pass
Working Distance	6-12 mm	5-22 mm	Pass
RNS Radius Spot Size/Resolution	50 μm	13.9 μm - 54.1 μm	Pass
Design Wavelength	450-900 nm	561 nm	Pass
High NA Optical Path			
Full Field of View	$> 100 \mu\text{m}$	$\sim 100 \mu\text{m}$	Pass
Working Distance	$\sim 50 \mu\text{m}$	$\sim 50 \mu\text{m}$	Pass
RNS Radius Spot Size/Resolution	$< 2 \mu\text{m}$	1.95 μm	Pass
Design Wavelength	1350 nm	1350 nm	Pass

This work presented a versatile, compact lens system capable of imaging modalities such as white-light navigation, narrowband reflectance, fluorescence, OCM, MPM, and CM, among other imaging techniques.

2.2 Co-Registered Proximal System

The work described in this section focuses on the development and validation of a proximal system containing the components to support OCT, MPM, and reflectance imaging based on previous work [53]. This system works in tandem with a scanning endoscope or a scanning microscope. The project aims to address the challenge in multimodal imaging systems to provide co-registered images. Often, the different images are obtained with separate instruments, making it challenging to precisely image the same tissue area or co-register the images computationally. The development of this proximal system allows obtaining images from precisely the same tissue location with OCT, MPM, and reflectance.

A dual-clad fiber (DCF) is the co-registration mechanism integrated into a scanning endoscope or a scanning microscope. The DCF allows using the same fiber to illuminate or excite the sample through the single-mode core and collect signals using either its single-mode core or the multimode first cladding. For example, in the current implementation, a 1300 nm super luminescent diode, a custom femtosecond 1400 nm fiber laser, and a continuous wave 561 nm laser are coupled into the single-mode fiber core to illuminate or excite the sample. The coupling of the different lasers into the DCF is performed passively using a complex arrangement of wavelength division multiplexers (WDM) and a dual clad fiber coupler (DCFC). Once the signal is collected by the microscope or endoscope optics, the WDMs, the DCFC, and a set of dichroic mirrors deliver the different signals to their corresponding detectors. The OCT detector is a

spectrometer built based on previous work [53]. The reflectance detector is a variable gain photodiode, and the MPM detectors are four PMTs arranged to detect SHG, THG, 2PEF, and 3PEF separately. The custom PMT setup was custom-built [53], and PMTs electronics to supply and control power and gain were designed and tested, ensuring proper gain levels [54].

This work was highly collaborative as several lab members, vendors, and research groups provided different components optimized for the desired functionalities. For example, Castor Optics, Inc. (Quebec, Canada) provided a WDM/DCFC customized for high coupling efficiency for both the 1300 nm OCT source and the 1400 nm MPM source. Also, the signal decoupling that directs the MPM signal to the PMTs was improved by their design compared with commercially available DCFC (>90% vs. ~ 60%). Also, the software was developed in collaboration with INTAQ (AZ, USA), and the 1400 nm was provided by The Ultrafast Fiber Lasers and Nonlinear Optics group, led by Professor Khanh Kieu.

To validate the setup, *Ex-vivo* ovine ovary tissue images were obtained using the proximal system with a scanning microscope built as part of this work. The results of this test are included in detail in Appendix B. In brief, the tissue used was free of labeling or contrast agents.

Reflectance and MPM *en face* images have the same ~300 x300 μm FOV, and OCT has a ~300 μm lateral FOV. The reflectance image shows the tissue topology. Most of the signal in the 2PEF image is SHG generated by tissue collagen as limited two-photon autofluorescence would be expected with our 1400nm center wavelength source and tissue sample. However, it was noted that longer wavelength fluorophores such as porphyrin might also contribute to the 2PEF signal. 3PEF images likely show fluorescence emission from various endogenous fluorophores,

including collagen, and may include THG contamination from step index of refraction changes. The OCT image shows the inner tissue morphology along a horizontal line. All images correspond to the same location on the tissue, demonstrating the co-registration of images.

2.3 *En-face* Triple Modality Co-Registered Endoscope (Salpingoscope)

The work summarized in this section is presented in Appendix C and focuses on the design and feasibility testing of a triple modality co-registered endoscope (Salpingoscope). The salpingoscope implements the dual optical path lenses, a quartered piezo scanning assembly, and the co-registered proximal system to perform co-registered OCT, MPM, and reflectance imaging. This project was highly collaborative as well. The quartered-piezo scanning assembly was developed in collaboration with now graduate students Dominique Galvez and Nancy Y. Pham. The scanning assembly is based on previous collaborative work by several former students and myself [55]. The custom ferrule that holds all the optical components, the scanning assembly, and the irrigation and accessory channels tubing was designed in collaboration with Gabriella Romano, a University of Arizona alumni. Gabriella Romano, Ricky Cordova, and I collaborated to design the salpingoscope's handle.

The functional capabilities such as biopsy and irrigation are enabled by the working channels spanning the entire salpingoscope hypotube and handle. The accessory channel allows for the introduction of any commercially available surgical tool such as biopsy forceps (SpyBite, M00546270, Boston Scientific Corporation, Natick, MA, USA) with a diameter of up to 1.22 mm. The irrigation channel is a .86 mm diameter channel that allows for saline or contrast imaging agents to be introduced and delivered at the distal end of the salpingoscope.

The quartered-piezo scanning assembly has a cantilevered DCF with brass fiber mass and operates with a raster scanning pattern. Raster scanning enables easy image reconstruction and allows for slow scanning for OCM and fast scanning for video-rate *en face* navigation and MPM imaging. The optical system allows OCM, MPM, and reflectance by using the dual optical path system combined with the DCF installed in the quartered-piezo scanning assembly. One path features a low numerical aperture and wide field of view to allow reflectance imaging of distant objects. The other path features a high numerical aperture and short working distance to allow microscopy techniques such as OCM and MPM. The multimodal proximal system contains all components needed to operate the imaging modalities and complies with electrical and laser safety requirements (IEC 60601-1 Part 1, third edition, Part 1, section 8.7.3d and ANSI Z136.1). Each imaging modality was tested, verified, and characterized by obtaining images of test targets demonstrating the feasibility of the design.

In summary, the demonstrated novel triple modality co-registered salpingoscope provides several practical advantages such as:

1. Functional capabilities through dedicated channels. (For example, irrigation, and accessory usage).
2. Face forward scanning imaging.
3. Multimodal imaging can be adapted to various imaging modalities with low-resolution and wide field of view or high numerical aperture with high-resolution imaging.
4. The imaging co-registration is provided for both low and high-resolution modalities.

5. Optical coherence microscopy provides depth-resolved, micron-scale resolution images of tissue that can identify modified tissue and cellular microstructure.
6. Reflectance narrow-band imaging provides contrast at tissue places with increased vascularity.
7. Multiphoton microscopy provides insights into present fluorescent molecules that are known to be altered in cancerous tissue (For example, altered collagen structure and changes in biomolecule concentration).
8. A potential minimally invasive imaging salpingoscope that could be used as an optical screening method for various cancers in the future, especially ovarian cancer.

CHAPTER 3: FUTURE WORK

4.1 Multiple Optical Paths for Co-Registered Imaging Future Work

The optical system dichroic filter obscuration causes significant losses for the OCM and MPM. Together with other system losses, the power on the sample is lower than optimum. A higher efficiency optical system can be designed to build upon this work. An alternative could be to increase the power sources to improve the overall signal to noise for these modalities.

Additionally, Major technological advances need to enable better patterned dichroic surfaces as the current technologies cannot achieve straight or circular patterns in curved surfaces with satisfactory repeatability. The technique implemented by the provider for the surfaces used in this project was a proof of concept, but it needs to be more robust to increase repeatability. Due to this technological limitation, the dichroic surfaces are more efficient in some angles than in others, degrading image quality and causing unexpected stray light and uneven vignetting across the field.

4.2 Co-Registered Proximal System Future Work

The multimodal imaging proximal system is functional and has been demonstrated using a scanning microscope and a scanning endoscope. The proximal system still needs some calibration and performance adjustments to improve imaging quality. Future work includes enabling *en-face* 3D OCM imaging in the scanning microscope. The current limitation is the software controlling the scanning galvos as it lacks the ability to control bi-directional scanning in OCT mode. The spectrometer used in this system does lack sufficient lateral resolution to provide a lower roll-off and increased sensitivity for deeper imaging. Therefore, an improved spectrometer is included in the future timeline of this project. A better spectrometer can provide

better contrast and lower roll-off, enabling deeper axial imaging if sufficient resolution is achieved. The software can be improved to allow for simultaneous acquisition of OCM and MPM images, ensuring their co-registration. No hardware limitation prevents the implementation of this simultaneous acquisition.

4.3 *En-face* Triple Modality Co-Registered Endoscope (Salpingoscope) Future Work

Recent technology has allowed for the miniaturization of complementary metal-oxide semiconductor (CMOS) imaging sensors. Smaller chip-on-tip designs can be achieved using these miniaturized CMOS sensors. CMOS sensors are convenient due to their simplicity and practicality for non-scanning imaging modalities, but endoscopes based on scanning mechanisms provide an unmatched versatility compared to chip-on-tip technologies when it comes to multimodal imaging endoscopes. The use of a double-clad fiber (DCF) as a co-registration mechanism offers significant advantages for multimodal endoscopes as it provides the ability to use the DCF single-mode core and its first cladding for illumination and collection. For instance, the triple modality co-registered endoscope (salpingoscope) could be a quad or even a quint multimodal imaging endoscope by changing and adding components to the proximal system. For example, the addition of a UV source, a filter wheel, and a PMT can permit one photon fluorescence imaging. With such changes, the salpingoscope can provide narrowband reflectance and one photon fluorescence imaging that works in the wide-field low-NA optical path. OCT could also be performed in the low-NA optical path by using a superluminescent diode in the ~ 800 nm range, providing a larger FOV, better depth of focus, but lower lateral resolution than OCM. The fiber components will need to be replaced for components that can accommodate these changes, but no technological limitation prevents this enhancement.

The salpingoscope was successfully demonstrated in a laboratory mode, providing proof of concept. The salpingoscope still needs to be fully packaged and sterilized to be ready for clinical pilot studies. Imaging of ovarian and fallopian tube tissue in an ewe model and human volunteers will demonstrate its use for clinical applications. However, the system and imaging processing still need calibration and performance adjustments. For example, image calibration is still needed due to the sinusoidal motion of the piezo since the current images have less sampling on the center of the field than at the edges. Images with more pixels can be obtained by raster scanning at higher frequencies. For example, using the first and fourth resonance, a higher pixel density in the slow axis (rows in the image) could be achieved. The quartered piezo tubes also would need to have tighter tolerances to provide a more consistent behavior. The asymmetric quartered piezo provided by the current manufacturers degrade the scanning trajectory and cause severe stable whirling issues that can interfere with the proper scanning trajectories.

REFERENCES

1. D. Hanahan and R. A. Weinberg, "Hallmarks of Cancer: The Next Generation," *Cell* **144**, 646–674 (2011).
2. K. A. Cronin, A. J. Lake, S. Scott, R. L. Sherman, A.-M. Noone, N. Howlader, S. J. Henley, R. N. Anderson, A. U. Firth, J. Ma, B. A. Kohler, and A. Jemal, "Annual Report to the Nation on the Status of Cancer, part I: National cancer statistics: Annual Report National Cancer Statistics," *Cancer* **124**, 2785–2800 (2018).
3. L. A. Torre, B. Trabert, C. E. DeSantis, K. D. Miller, G. Samimi, C. D. Runowicz, M. M. Gaudet, A. Jemal, and R. L. Siegel, "Ovarian cancer statistics, 2018: Ovarian Cancer Statistics, 2018," *CA. Cancer J. Clin.* **68**, 284–296 (2018).
4. F. Bray, J. Ferlay, I. Soerjomataram, R. L. Siegel, L. A. Torre, and A. Jemal, "Global cancer statistics 2018: GLOBOCAN estimates of incidence and mortality worldwide for 36 cancers in 185 countries," *CA. Cancer J. Clin.* **68**, 394–424 (2018).
5. R. J. Kurman and I.-M. Shih, "The Origin and Pathogenesis of Epithelial Ovarian Cancer: A Proposed Unifying Theory," *Am. J. Surg. Pathol.* **34**, 433–443 (2010).
6. R. S. Tuma, "Origin of Ovarian Cancer May Have Implications for Screening," *JNCI J. Natl. Cancer Inst.* **102**, 11–13 (2010).
7. C. P. Crum, R. Drapkin, D. Kindelberger, F. Medeiros, A. Miron, and Y. Lee, "Lessons from BRCA: The Tubal Fimbria Emerges as an Origin for Pelvic Serous Cancer," *Clin. Med. Res.* **5**, 35–44 (2007).
8. P. I. Stanciu, T. E. J. Ind, D. P. J. Barton, J. B. Butler, K. M. Vroobel, A. D. Attygalle, and M. A. E. Nobbenhuis, "Development of Peritoneal Carcinoma in women diagnosed with Serous Tubal Intraepithelial Carcinoma (STIC) following Risk-Reducing Salpingo-Oophorectomy (RRSO)," *J. Ovarian Res.* **12**, 50 (2019).
9. J. L. Shifren, R. Nahum, and N. A. Mazer, "Incidence of Sexual Dysfunction in Surgically Menopausal Women," *Menopause N. Y. N* **5**, 189–189 (1998).
10. L. P. Hariri, G. T. Bonnema, K. Schmidt, A. M. Winkler, V. Korde, K. D. Hatch, J. R. Davis, M. A. Brewer, and J. K. Barton, "Laparoscopic optical coherence tomography imaging of human ovarian cancer," *Gynecol. Oncol.* **114**, 188–194 (2009).
11. Nathaniel D Kirkpatrick, Molly A Brewer, and Urs Utzinger, "Endogenous Optical Biomarkers of Ovarian Cancer Evaluated with Multiphoton Microscopy," *Cancer Epidemiol. Biomarkers Prev.* **16**, 2048–2057 (2007).
12. T. Wang, M. Brewer, and Q. Zhu, "An overview of optical coherence tomography for ovarian tissue imaging and characterization: An overview of optical coherence tomography," *Wiley Interdiscip. Rev. Nanomed. Nanobiotechnol.* **7**, 1–16 (2015).
13. R. M. Williams, A. Flesken-Nikitin, L. H. Ellenson, D. C. Connolly, T. C. Hamilton, A. Y. Nikitin, and W. R. Zipfel, "Strategies for High Resolution Imaging of Epithelial Ovarian Cancer by Laparoscopic Nonlinear Microscopy," *Transl. Oncol.* **3**, 181–194 (2010).
14. E. C. Rentchler, K. L. Gant, R. Drapkin, M. Patankar, and P. J Campagnola, "Imaging Collagen Alterations in STICs and High Grade Ovarian Cancers in the Fallopian Tubes by Second Harmonic Generation Microscopy," *Cancers* **11**, 1805- (2019).
15. T. H. Tate, B. Baggett, P. F. S. Rice, J. W. Koevary, G. V. Orsinger, A. C. Nymeyer, W. A. Welge, K. Saboda, D. J. Roe, K. D. Hatch, S. K. Chambers, U. Utzinger, and J. K. Barton, "Multispectral fluorescence imaging of human ovarian and fallopian tube tissue for early-stage cancer detection," *J. Biomed. Opt.* **21**, 056005–056005 (2016).

16. T. W. Sawyer, J. W. Koevary, C. C. Howard, O. J. Austin, P. F. S. Rice, G. V. Hutchens, S. K. Chambers, D. C. Connolly, and J. K. Barton, "Fluorescence and Multiphoton Imaging for Tissue Characterization of a Model of Postmenopausal Ovarian Cancer," *Lasers Surg. Med.* **52**, 993–1009 (2020).
17. A. R. Tumlinson, B. Považay, L. P. Hariri, J. B. McNally, A. Unterhuber, B. M. Hermann, H. Sattmann, W. Drexler, and J. K. Barton, "In vivo ultrahigh-resolution optical coherence tomography of mouse colon with an achromatized endoscope," *J. Biomed. Opt.* **11**, 064003 (2006).
18. Y. Li, J. Jing, J. Yu, B. Zhang, T. Huo, Q. Yang, and Z. Chen, "Multimodality endoscopic optical coherence tomography and fluorescence imaging technology for visualization of layered architecture and subsurface microvasculature," *Opt. Lett.* **43**, 2074 (2018).
19. D. Lorensen, B. C. Quirk, M. Auger, W.-J. Madore, R. W. Kirk, N. Godbout, D. D. Sampson, C. Boudoux, and R. A. McLaughlin, "Dual-modality needle probe for combined fluorescence imaging and three-dimensional optical coherence tomography," *Opt. Lett.* **38**, 266–268 (2013).
20. H. Yoo, J. W. Kim, M. Shishkov, E. Namati, T. Morse, R. Shubochkin, J. R. McCarthy, V. Ntziachristos, B. E. Bouma, F. A. Jaffer, and G. J. Tearney, "Intra-arterial catheter for simultaneous microstructural and molecular imaging in vivo," *Nat. Med.* **17**, 1680–1684 (2011).
21. A. A. Tanbakuchi, J. A. Udovich, A. R. Rouse, K. D. Hatch, and A. F. Gmitro, "In vivo imaging of ovarian tissue using a novel confocal microlaparoscope," *Am. J. Obstet. Gynecol.* **202**, 90.e1-90.e9 (2010).
22. A. R. Rouse, A. Kano, J. A. Udovich, S. M. Kroto, and A. F. Gmitro, "Design and demonstration of a miniature catheter for a confocal microendoscope," *Appl. Opt.* **43**, 5763–5771 (2004).
23. J. Kerin, L. Daykhovskiy, J. Segalowitz, E. Surrey, R. Anderson, A. Stein, M. Wade, and W. Grundfest, "Falloscopy: A microendoscopic technique for visual exploration of the human fallopian tube from the uterotubal ostium to the fimbria using a transvaginal approach," *Int. J. Gynecol. Obstet.* **35**, 292–293 (1991).
24. C. J. Engelbrecht, R. S. Johnston, E. J. Seibel, and F. Helmchen, "Ultra-compact fiber-optic two-photon microscope for functional fluorescence imaging in vivo," *Opt. Express* **16**, 5556–5564 (2008).
25. M. Keenan, T. H. Tate, K. Kieu, J. F. Black, U. Utzinger, and J. K. Barton, "Design and characterization of a combined OCT and wide field imaging falloscope for ovarian cancer detection," *Biomed. Opt. Express* **8**, 124 (2017).
26. T. H. Tate, M. Keenan, J. Black, U. Utzinger, and J. K. Barton, "Ultraminiature optical design for multispectral fluorescence imaging endoscopes," *J. Biomed. Opt.* **22**, 036013 (2017).
27. K. C. Kiekens, G. Romano, D. Galvez, R. Cordova, J. Heusinkveld, K. Hatch, W. Drake, Z. Kmeid, and J. K. Barton, "Reengineering a falloscope imaging system for clinical use," *Transl. Biophotonics* **2**, n/a (2020).
28. R. Campo, S. Gordts, and I. Brosens, "Minimally invasive exploration of the female reproductive tract in infertility," *Reprod. Biomed. Online* **4**, 40–45 (2002).
29. R. Campo and C. R. Molinas, "Modern endoscopic-based exploration of the female reproductive tract: a model for developing countries?," *ESHRE Monogr.* **2008**, 54–59 (2008).

30. A. Watrelot, "Place of transvaginal fertiloscopy in the management of tubal factor disease," *Reprod. Biomed. Online* **15**, 389–395 (2007).
31. Y. Zou, F. S. Chau, and G. Zhou, "Ultra-compact optical zoom endoscope using solid tunable lenses," *Opt. Express* **25**, 20675–20688 (2017).
32. R. D. G. Daweke, M. Kelp, H. Lehr, O. Monnich, and P. Osiak, "Electromagnetic direct linear drives for medical endoscopes," in (IEEE, 2014), pp. 245–251.
33. S. W. Seo, S. Han, J. H. Seo, Y. M. Kim, M. S. Kang, N. K. Min, W. B. Choi, and M. Y. Sung, "Microelectromechanical-System-Based Variable-Focus Liquid Lens for Capsule Endoscopes," *Jpn. J. Appl. Phys.* **48**, 52404- (2009).
34. S. Kuiper, "Electrowetting-based liquid lenses for endoscopy," in (SPIE, 2011), Vol. 7930, pp. 793008–793008.
35. X. Chen, Z. Chen, X. Li, L. Shan, W. Sun, X. Wang, T. Xie, and S. Dong, "A spiral motion piezoelectric micromotor for autofocus and auto zoom in a medical endoscope," *Appl. Phys. Lett.* **108**, 052902 (2016).
36. M.-S. Chen, P.-J. Chen, M. Chen, and Y.-H. Lin, "An electrically tunable imaging system with separable focus and zoom functions using composite liquid crystal lenses," *Opt. Express* **22**, 11427–11435 (2014).
37. H.-S. Chen and Y.-H. Lin, "An endoscopic system adopting a liquid crystal lens with an electrically tunable depth-of-field," *Opt. Express* **21**, 18079–18088 (2013).
38. D. G. Ouzounov, D. R. Rivera, W. O. Williams, J. A. Stupinski, T. L. Southard, K. H. Hume, J. Bentley, R. S. Weiss, W. W. Webb, and C. Xu, "Dual modality endomicroscope with optical zoom capability," *Biomed. Opt. Express* **4**, 1494–1503 (2013).
39. W. Drexler and J. G. Fujimoto, *Optical Coherence Tomography: Technology and Applications* (Springer Science & Business Media, 2008).
40. C. Boudoux, *Fundamentals of Biomedical Optics: From Light Interactions with Cells to Complex Imaging Systems* (Pollux, 2018).
41. J. G. Fujimoto, C. Pitris, S. A. Boppart, and M. E. Brezinski, "Optical Coherence Tomography: An Emerging Technology for Biomedical Imaging and Optical Biopsy," *Neoplasia* **2**, 9–25 (2000).
42. P. Tsai, N. Nishimura, E. Yoder, E. Dolnick, G. Allen White, and D. Kleinfeld, "Principles, Design, and Construction of a Two-Photon Laser-Scanning Microscope for In Vitro and In Vivo Brain Imaging," in *In Vivo Optical Imaging of Brain Function*, R. Frostig, ed., Frontiers in Neuroscience (CRC Press, 2002), Vol. 20024445.
43. T. S. Tkaczyk, *Field Guide to Microscopy* (SPIE, 2004).
44. Warren R Zipfel, Rebecca M Williams, Richard Christie, Alexander Yu Nikitin, Bradley T Hyman, and Watt W Webb, "Live Tissue Intrinsic Emission Microscopy Using Multiphoton-Excited Native Fluorescence and Second Harmonic Generation," *Proc. Natl. Acad. Sci. - PNAS* **100**, 7075–7080 (2003).
45. D. M. Huland, K. Charan, D. G. Ouzounov, J. S. Jones, N. Nishimura, and C. Xu, "Three-photon excited fluorescence imaging of unstained tissue using a GRIN lens endoscope," *Biomed. Opt. Express* **4**, 652 (2013).
46. P. E. Powers, *Field Guide to Nonlinear Optics* (Society of Photo-Optical Instrumentation Engineers SPIE, 2013).
47. D. Yelin and Y. Silberberg, "Laser scanning third-harmonic-generation microscopy in biology," *Opt. Express* **5**, 169–175 (1999).

48. Y. Barad, H. Eisenberg, M. Horowitz, and Y. Silberberg, "Nonlinear scanning laser microscopy by third harmonic generation," *Appl. Phys. Lett.* **70**, 922–924 (1997).
49. R. W. Boyd, *Nonlinear Optics*, Fourth edition. (Academic Press is an imprint of Elsevier, 2020).
50. B. Grant, *Field Guide to Radiometry* (SPIE, 1995).
51. J. E. Greivenkamp, *Field Guide to Geometrical Optics* (SPIE, 2004).
52. P. Scott, "Optical Absorption of Hemoglobin," <https://omlc.org/spectra/hemoglobin/>.
53. K. C. Kiekens, O. Talarico, and J. K. Barton, "Proximal design for a multimodality endoscope with multiphoton microscopy, optical coherence microscopy and visual modalities," in (SPIE, 2018), Vol. 10501, pp. 1050119-1050119–14.
54. D. Vega, J. K. Barton, D. B. Galvez, S. P. Santaniello, Z. Adams, N. Y. Pham, K. Kiekens, R. Cordova, and J. Montague, "A coregistered multimodal imaging system for reflectance, multiphoton, and optical coherence microscopy," in *Multimodal Biomedical Imaging XVI*, F. S. Azar, X. Intes, and Q. Fang, eds. (SPIE, 2021), p. 24.
55. K. Kiekens, D. Vega, H. Thurgood, D. Galvez, D. McGregor, T. Sawyer, and J. Barton, "Effect of an Added Mass On the Vibration Characteristics for Raster Scanning of a Cantilevered Optical Fiber," *J. Eng. Sci. Med. Diagn. Ther.* (2021).

APPENDIX A: Use of embedded and patterned dichroic surfaces with reflective optical power to enable multiple optical paths in a micro-objective

This appendix includes all supplemental material for the optical design phase of the project, including a paper submitted and accepted by the Applied Optics Journal – OSA Publishing, an accepted and presented abstract in the OSA Biophotonics: Optics in the Life Sciences 2019 conference, and a brief description on how to analyze an optical system in non-sequential ray trace utilizing the OpticStudio Application Programming Interface (API).

A.1 Accepted Manuscript: Use of embedded and patterned dichroic surfaces with reflective optical power to enable multiple optical paths in a micro-objective

The following manuscript was published August 1, 2020 by the Applied Optics Journal – OSA Publishing.

<https://doi.org/10.1364/AO.391654>

David Vega, Travis W. Sawyer, Nancy Y. Pham, and Jennifer K. Barton, "Use of embedded and patterned dichroic surfaces with reflective optical power to enable multiple optical paths in a micro-objective," Appl. Opt. 59, G71-G78 (2020)

Use of embedded and patterned dichroic surfaces with reflective optical power to enable multiple optical paths in a micro-objective

DAVID VEGA^{1,*}, Travis W. Sawyer¹, Nancy Y. Pham², AND JENNIFER K. BARTON^{1,2}

¹The University of Arizona, The James C Wyant College of Optical Sciences, The University of Arizona, Tucson, AZ, USA, 85721

²University of Arizona, Biomedical Engineering, The University of Arizona, Tucson, AZ, USA, 85721

* dvega@email.arizona.edu

Abstract:

We demonstrate the use of patterned dichroic surfaces with reflective optical power to create multiple optical paths in a single lens system. The application of these surfaces enables a micro-endoscope to accommodate multiple imaging technologies with only one optical system, making the packaging more compact and reliable. The optical paths are spectrally separated using different wavelengths for each path. The dichroic surfaces are designed such that the visible wavelengths transmit through the surfaces optically unaffected, but the near-infrared wavelengths are reflected in a telescope-like configuration with the curved dichroic surfaces providing reflective optical power. We demonstrate wide-field visible monochromatic imaging, and microscopic near-infrared imaging using the same set of lenses. The on-axis measured resolution of the wide-field imaging configuration is approximately 14 μm , and the measured resolution of the microscopic imaging configuration is approximately 2 μm . Wide-field white-light imaging of an object is also demonstrated for a qualitative perspective on the imaging capabilities. Other configurations and applications in fields such as optical metrology are discussed to expand on the versatility of the demonstrated optical system.

1. Introduction

White-light endoscopy is a primary method of screening for cancers in organs with relatively large lumens, including colon and esophagus. Unfortunately, it is challenging to design and engineer optical systems that are small enough to navigate through very small ducts or to be inserted in small openings to access other organs of interest. The human ovary and distal fallopian tube, which is considered the origin of ovarian cancer [1], is an example of tissue that is located deep within the body and is difficult to reach. Three ways of accessing the ovary are laparoscopic, falloposcopic, and trans-vaginal, each with its advantages and disadvantages. Laparoscopic access accommodates larger diameter, rigid endoscopes of 5-10 mm diameter, but is a surgical procedure requiring general anesthesia, so it is not suitable for screening. Falloposcopic access requires flexible sub-millimeter probes due to the ~ 1 mm diameter lumen of the fallopian tube at the ostium before the tube opens to around 1 cm diameter at the fimbriae. The third mode of access, trans-vaginal access (puncture through the vaginal wall) accommodates rigid endoscopes of around 3 mm diameter, has an angle of approach much more favorable than laparoscopes for imaging the distal fallopian tube, and is commonly utilized in outpatient procedures such as oocyte harvesting. Such an endoscope, which we have named a salpingoscope, must at a minimum perform face-forward navigational imaging to reach the tissue of interest. Ideally, it should be capable of multiple advanced optical imaging techniques, which may be used in synergy to improve early cancer detection accuracy [2].

To provide both the ability to navigate to the organ of interest and rapidly assess tissue for areas of concern, then acquire microscopic resolution images of the suspicious area, an endoscope needs to incorporate both a wide-field, long depth of focus modality and a high magnification

modality. Currently, there are a limited number of multi-modality endoscopic systems, and the combination of wide-field and microscopic techniques generally requires separate optical systems, which increases the size and carries the challenge of accurately co-registering images. Endoscopes that provide adjustable levels of magnification are commercially available (e.g. EndocytotM, Olympus, Tokyo, Japan) but these devices are limited to white-light imaging. Also, optical zoom systems are relatively complex and can require bulky optomechanical components, so these systems tend to have ~3mm diameter optics that are packaged in endoscopes with diameters of 6mm or more, restricting their applications [3, 4]. The use of liquid lenses to provide zoom capability is attractive, but limitations for endoscopic studies include relatively large packaged diameters of more than 6 mm [5, 6].

Other dual-modality endoscopes have been employed to address the need for low and high-resolution imaging. Our laboratory has developed a miniature (0.8 mm diameter) dual-modality side-viewing optical coherence tomography (OCT) and forward-viewing fluorescence imaging endoscope [7], but this device utilizes separate optical systems and images different parts of the sample. The extreme miniaturization required for this endoscope impeded the inclusion of a distal scanning mechanism, so the endoscope is manually pulled back to obtain two-dimensional OCT images. Another dual-modality endoscope uses a single lens system with separate delivery fibers for side-viewing OCT and surface magnifying chromoendoscopy [8], but this device has the same limitation of a side-viewing field of view as our miniature endoscope. We and others have developed a variety of side-viewing, co-registered OCT and fluorescence spectroscopy endoscopes [9, 10, 11, 12], but there is a lack of devices that can perform co-registered forward-viewing imaging. Forward-viewing is required for applications where the endoscope must be

navigated through a relatively open space such as the peritoneal cavity, and where the tissue to be viewed is located in front of the endoscope, as in transvaginal approaches to the ovary and fallopian tubes. Forward-viewing OCT and epi-fluorescence endomicroscopy have been demonstrated using a robotic arm for scanning [3], which is not appropriate for applications that require the endoscope to navigate a tortuous route to internal organs. To address the challenges of image co-registration, simplicity, compactness, and the need for forward-viewing high-resolution imaging, we designed and demonstrated a multi-modal system. The beam paths for the different imaging techniques are multiplexed within a single optical system using patterned dichroic surfaces and spectral separation.

Multilayered thin film coatings are widely used and readily available in the field of optics, as this robust technology started its development in the mid-1900s [14, 15, 16]. The deposition of thin optical films can be used to generate edge filters, bandpass filters, anti-reflection coatings, beam splitters, and high-reflectance coatings [17]. The performance of an optical coating may be specified at more than one wavelength, being highly transmissive at some wavelengths and highly reflective at others, creating a dichroic filter [18]. In our application, the dichroic filters are used as a reflective mechanism for long wavelengths to provide reflective optical power (i.e. focusing power) at an internal curved surface of a triplet, while transmitting shorter wavelengths unaltered.

2. Design requirements

Our endoscopic optical system provides two optical paths at two different wavelengths in a single set of optical elements. High resolution, depth-resolved tissue imaging is frequently performed in the near-infrared (NIR) because longer wavelengths provide better tissue

penetration due to lower scattering. Therefore, it was decided to implement an object space high numerical aperture (HNA) optical path with NIR wavelengths, while keeping visible wavelengths for an object space wide-field low numerical aperture (LNA) optical path. As examples of possible imaging modalities, the HNA optical path can be utilized by optical coherence microscopy (OCM), multi-photon microscopy (MPM), and confocal microscopy (CM). The LNA optical path is designed for wide-field white-light, narrow-band, multispectral reflectance/fluorescence imaging, and OCT.

Table 1 summarizes the specifications for the HNA optical system. A lateral resolution of $2\mu\text{m}$ was specified to achieve cellular resolution. The requirement for the full field of view (FFOV) was driven by the practical consideration of having a representative amount of tissue imaged. This requirement was arbitrarily set at a minimum of 10 cell diameters or $>100\mu\text{m}$. The resolution specification is desired over the entire FFOV. The optical system itself does not include the ability to adjust the focal depth, although this capability could be incorporated into other aspects of an endoscope (e.g. mechanics for adjusting endoscope-tissue spacing or fiber/lens spacing [19]). A working distance of $50\mu\text{m}$ from the final optical element was specified, as this fixed depth is appropriate for visualizing the epithelial layer of most organs with acceptable tissue attenuation.

Table 1. High Numerical Aperture (HNA) optical path specifications

Specification	Target Value
HNA Full Field of View	$>100\mu\text{m}$
HNA Working Distance	$\approx 50\mu\text{m}$
HNA RMS radius spot size	$<2\mu\text{m}$
Required design wavelength	1350nm

Based on these tissue imaging specifications, the required object space numerical aperture (NA_{obj}) was calculated. It has been shown [20, 21] that the lateral resolution (beam waist) for a system being illuminated with a Gaussian beam is related to the NA of the system by equation 1.

$$\Delta x = \frac{4\lambda f}{\pi d} \approx \frac{2\lambda}{\pi NA_{obj}} \quad (1)$$

where d is the diameter of the exit pupil that is fully illuminated by a Gaussian beam, λ is the illumination wavelength, f is the focal length, and NA_{obj} is the object space numerical aperture of the system in the paraxial approximation. A sufficiently high NA_{obj} is also required to generate non-linear optical phenomena such as multiphoton processes. For a center wavelength of 1350nm, equation 1 indicates that a $\approx .40 NA_{obj}$ is needed to attain a cellular resolution of $<2\mu m$ at the object space. This NA_{obj} , in our experience, is sufficient for multiphoton processes using high peak power laser systems. Since the NA_{obj} and the spot size are interlaced with each other, during design we used the root mean square (RMS) spot radius as the optical system figure of merit.

Table 2 summarizes the specifications for the LNA optical path. These specifications were driven by the need to provide an adequate field of view and depth of field (DOF) to enable navigation and detection of suspicious areas, over a range of wavelengths appropriate for autofluorescence and/or targeted fluorescent agent imaging. Major endogenous fluorophores in tissue, including collagen, elastin, NADH, and flavins can be excited with light in the range of 200nm to 500nm range and detected in a bandwidth that spans from 300nm to 600nm [22]. However, for ease of compliance with ANSI standards for laser exposure [23], ultraviolet

wavelengths (<400 nm) were excluded. Exogenous fluorophores such as cyanine dyes (e.g. Cy5.5, indocyanine green) have excitation wavelengths in the 600-800 nm range and emission in the 700-900 nm range. A wavelength range of 450-900 nm was specified for the LNA optical path.

For systems without a fixed imaging depth, an angular FFOV is generally specified. A FFOV of 45° is adequate for navigation and avoiding obstacles. A depth of field or working distance from 1 mm to infinity would be desirable, but a range from 6-12 mm was specified as adequate for navigation in the peritoneal cavity. The resolution (RMS spot radius) is driven by the ability to detect features of interest. In our case, serous tubal intraepithelial carcinomas (STICs, putative ovarian cancer precursors) are defined as abnormal clusters of 10 or more cells [24], giving a resolution specification of $50\ \mu\text{m}$. While this resolution would be desirable over the entire FFOV, in practice the center of the field is most critical. Indeed, many successful commercial white-light endoscopes have barrel distortion and uneven illumination, leading to lower contrast and resolution at the edges of the field of view.

Table 2. Low Numerical Aperture LNA optical path specifications

Specification	Target Value
LNA Full Field of View	$>45^\circ$
LNA Working Distance	6-12mm
LNA RMS radius spot size	$\leq 50\ \mu\text{m}$
Required design wavelengths	450-900nm

The maximum optical system diameter was defined by the clinical application and other mechanical aspects of the endoscope. A maximum endoscope diameter of 3mm was deemed acceptable for vaginal puncture. Since a practical salpingoscope needs to integrate other ports for

functions such as biopsy extraction and irrigation, together with the optical system, the available space for optics was limited to 1.5mm in diameter [25]. An optical system of this diameter could be packaged into smaller, less fully functional endoscopes for a variety of minimally invasive applications.

3. Optical design and the use of the dichroic surfaces

Utilizing a single set of lenses for both the HNA and LNA systems places constraints on the ability to independently optimize NAs, FFOVs, and RMS spot sizes for the two systems, with limited modification possible through the use of dichroic coatings on lens surfaces. Because the HNA system requirements were the most challenging to meet, and the most critical for proper optical system operation, during lens design, optimization, and tolerancing using OpticStudio (Zemax LLC, Kirkland, WA), a higher weight was given to the HNA system requirements.

The design of the 5-element optical system is shown in Figure 1 with the tissue to be imaged on the left-hand side, and the light delivery and/or imaging system located on the right. The optical system has three main subcomponents: 1) a flat cover glass (element 1) that ensures an air interface for the subsequent powered surface, provides proper spacing to the tissue, and protects internal elements, 2) an objective (element 2) that focuses the light and has the optical stop on the front surface, and 3) a triplet (elements 3, 4, 5) that contains the embedded dichroic surfaces that provide separate optical paths for visible light (LNA) and NIR light (HNA) systems.

Specific element prescriptions are given in Table 3. The front of an element is defined as the surface on the left-hand side, and the back as the surface on the right. The sign convention is such that directed distances such as radii and thicknesses to the right are positive and to the left

are negative, and radius of curvature is defined as the directed distance from the vertex to the center of curvature [26].

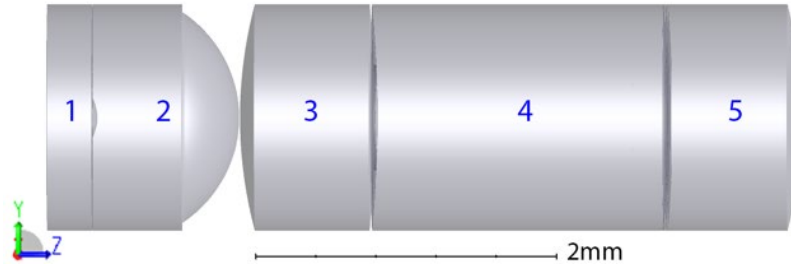


Fig. 1. Elements of the multi-path optical system. 1: Cover plate, 2: Objective, 3-5: Triplet with embedded dichroic surfaces.

Table 3. Prescription of the optical system shown in Fig 1. Radii to the right are positive and to the left are negative. Parameters: C=Back radius conic -0.0498, S= Stop clear aperture radius .132 mm, and D=Coated with dichroic surfaces

Element	Material	Front Radius (mm)	Thickness (mm)	Back Radius (mm)	Parameters
1	Fused Silica	Infinity	.300	Infinity	
2	ZnS broadband	-.287 (Stop)	.944	-.826	C, S
3	S-LAH79	2.90	.900	-7.68	
4	N-BK7	-7.68	1.93	-9.35	D
5	S-LAH58	-9.35	.880	-2.87	

The optical system is designed to create two different beam profiles separated by patterned dichroic surfaces in the triplet. One of the profiles is an object side high numerical aperture ($NA_{obj} = .44$) limited by the stop at the front surface of element 2, and this is enabled by designing the dichroic coatings to be highly reflective in the NIR. Figure 2 illustrates the patterned dichroic surfaces used to achieve the two different beam paths through the triplet. As seen in Figure 2 left, the front surface of element 4 has a centered dot (radius 0.35 mm), and the back surface has a centered ring (clear aperture 0.35 mm) of dichroic coatings. The transmission of the coating is shown in Figure 2 right and is highly transmissive for wavelengths between 470

nm and 900 nm, and highly reflective for wavelengths between 950 nm and 1450 nm. As these dichroic surfaces are curved, they provide optical power to the NIR wavelengths and act as a beam compressor in a configuration that is similar to a telescope. The net effect of the triplet's external powered surfaces and internal beam compressor is that the light beam between the triplet and the objective nearly fills the aperture of element 3, then it is compressed to have an image NA_{img} of 0.12, as shown in Figure 3 left. The second profile is an object side low numerical aperture system ($NA_{obj} = .007$). The light is weakly expanded by the objective and weakly focused through the triplet to converge at the image plane with the same image NA_{img} of .12 as the HNA optical path. The LNA ray trace is shown in Figure 3 right.

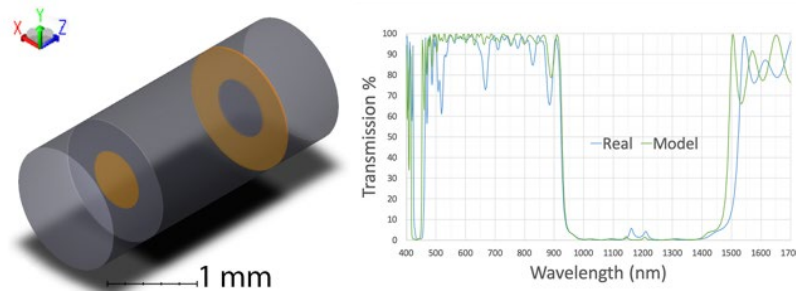


Fig. 2. Left: rendering of triplet formed with elements 3, 4, and 5, with embedded dichroic surfaces shown in orange. The coating radii are .35mm for the centered dot and .35mm to .75mm for the ring. Right: theoretical (green) and measured (blue) transmission curves for the dichroic coating at normal light incidence.

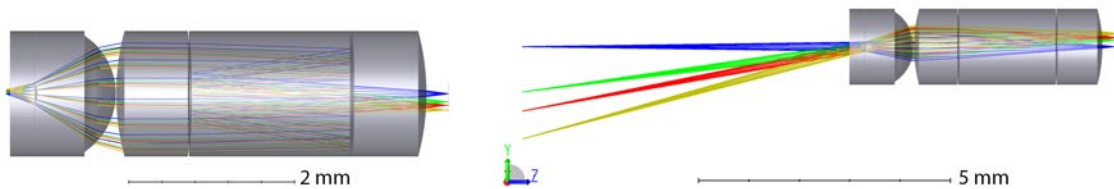


Fig. 3. Ray trace for the HNA optical path (left) and LNA optical path (right). Both configurations show a ray trace for normalized object height of 1, 0.7, 0.5, and 0.

The triplet offers several practical advantages. First, the use of a folded optical path decreases the length of the optical system, enabling a more compact design. Second, the ability to vary the material (index of refraction), thickness, and the radii of curvature in the three elements of the

triplet help to correct color aberrations and flatten the field in the HNA optical path. Third, embedding the dichroic surfaces provides protection from mechanical damage. This concept of using dichroic patterned surfaces to generate two separate beam paths is similar to Ouzounov [27], with differences that their design utilizes lenses that are spaced in air, increasing the total length of the optical system and increasing complexity of assembly, and that their design requires larger diameter optical elements that are not suitable for our miniature design.

4. Predicted performance

After optimization, the theoretical performance of the optical design was compared to the specifications of the system. While there were trade-offs made in the LNA system to prioritize the performance of the HNA system, the theoretical system still met most requirements. As designed, the HNA optical path has an NA_{obj} of 0.44. Using equation 1, this NA corresponds to a spot size of $1.95 \mu\text{m}$, which is equivalent to resolving an image of a square wave of 256 cycles per millimeter. There are many different equations and criteria for resolution, yielding slightly different calculated results. The resolution at the diffraction limit for the optical system is dictated by the Rayleigh resolution criterion. Using equation 2, an ultimate resolution of $1.87 \mu\text{m}$ is calculated, which is equivalent to resolving an image of a square wave of 267 cycles per millimeter.

$$Resolution = 0.61 \frac{\lambda}{NA_{Obj}} \quad (2)$$

The Rayleigh resolution criterion is derived assuming Köhler illumination and matching objective and condenser NAs, which may not occur in practice. Our system is intended to be used primarily with Gaussian beam illumination; therefore, we utilize equation 1 as the dictating equation for resolution.

The modulus of the optical transfer function (MTF) shown in Fig. 4 left, is close to being diffraction-limited up to the effective resolution of 256 cycles per millimeter. At this resolution, the MTF graph indicates that the system will have a contrast of .21. Graphs for the normalized fields $H = 0.0$ (blue), 0.5 (green), 0.707 (red), and 1.0 (yellow) are shown, where H indicates the fraction of the normalized FOV. The dotted lines represent the sagittal MTF, and the solid lines represent the Tangential MTF. The diffraction-limited MTF, calculated with paraxial raytracing, is shown in black but is nearly covered by the blue line. The slope of the diffraction limit has an inflection point at about 135 cycles per millimeter; this is caused by the telescope-like structure of the triplet and its obscuration. The spot diagram shown in Fig. 4 right, shows that the optical system is well corrected for aberrations through the entire FOV since the largest RMS spot radius calculated is $1.2\ \mu\text{m}$ which is smaller than the ultimate resolution determined using equation 2. Table 4 summarizes the results from the model analysis and shows that all requirements for the HNA system were met.

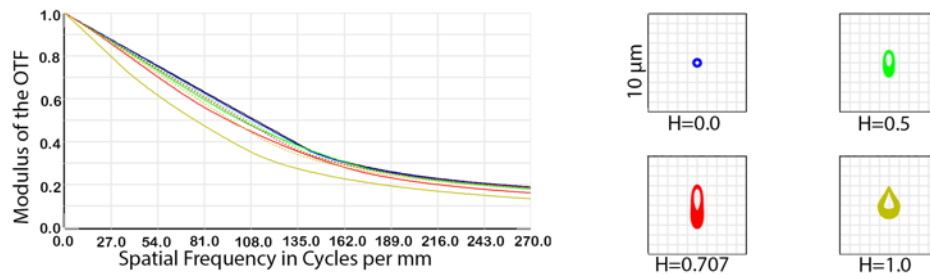


Fig. 4. Left: HNA Fourier transform merit transfer function evaluated at 1350nm for normalized fields $H = 0.0$ (blue), 0.5 (green), 0.707 (red), and 1.0 (yellow). Dotted lines represent the sagittal MTF and solid lines represent the Tangential MTF profiles. The black line represents the diffraction limit. Right: corresponding RMS spot radii of 0.38, 0.83, 1.2, and $1.0\ \mu\text{m}$.

Table 4. HNA theoretical model analysis summary.

Specification	Target Value	Predicted Value
HNA Full Field of View	100 μm	$\approx 110\mu\text{m}$
HNA Working Distance	$\approx 50\mu\text{m}$	$\approx 50\mu\text{m}$
HNA RMS radius spot size	$<2\mu\text{m}$	1.95 μm

The MTF for the LNA system is shown in Fig. 5, with the same color and line conventions as Fig. 4. The MTF of the LNA optical path is close to optimum at the center of the field, but performance degrades towards the edge. The MTF indicates that an image of a square wave at 20 cycles/mm should be resolvable with a contrast of about 0.4 in the center of the field of view, and 0.02 at the edge of the field of view. The contrast at 35.9 cycles/mm reduces to about 0.2 at the center of the field of view. Table 5 summarizes the results from the model analysis for the LNA and shows that the working distance and spot size specifications were met, but the field of view was smaller than desired. The optical system allows for a larger FFOV, but as suggested in Fig. 5, the continuing degradation of spot size with an increasing field of view places that measurement out of specification.

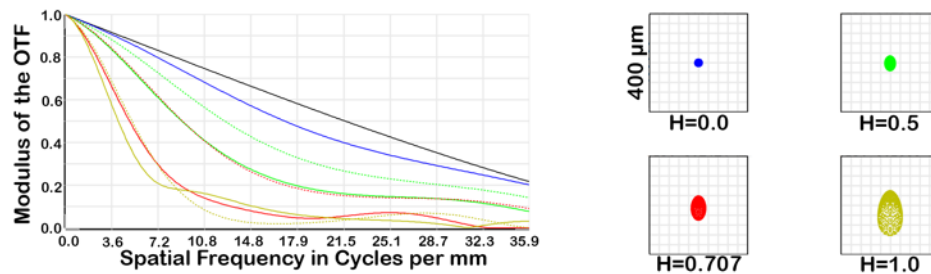


Fig. 5. Left: LNA Fourier transform merit transfer function evaluated at 561nm for normalized fields $H = 0.0$ (blue), 0.5 (green), 0.707 (red), and 1.0 (yellow). Dotted lines represent the sagittal MTF and solid lines represent the Tangential MTF profiles. The black line represents the diffraction limit. Right: corresponding RMS spot radii of 11.0 μm , 19.9, 30.5, and 54.1 μm .

Table 5. LNA design theoretical specifications summary.

Specification	Target Value	Predicted Value
LNA Full Field of View	$>45^\circ$	$\approx 25^\circ$
LNA Working Distance	6-12mm	$\approx 5.0\text{mm}$ to $\approx 22\text{mm}$
LNA RMS radius spot size	$\leq 50\mu\text{m}$	10.98 μm to 54.1 μm

5. Measured optical system performance

Element 1 as specified in Table 3 was custom provided by Bern Optics, Inc. (Westfield, MA, USA). Element 2 was diamond turned at the Precision Freeform Optics Design, Fabrication and Testing Facility at The University of Arizona. Elements 3, 4 and 5 as specified were custom provided by Optics Technology, Inc (Pittsford, NY, USA). Dichroic surfaces were fabricated on individual elements by Blue Ridge Optics (Bedford, VA, USA), and the triplet was cemented by Optics Technology, Inc. The optical stop was provided by Gateway Laser Services (Maryland Heights, MO, USA). The entire lens system was assembled at the University of Arizona into a ferrule fabricated by wire electrical discharge machining (Majer Precision Engineering, Tempe, AZ, USA).

To test the optical performance of this lens system, a microscope consisting of a 20X objective (M Plan Apo 20X, Mitutoyo, Kanagawa, Japan), an $f=100\text{mm}$ lens (KBX064, Newport, Irvine, CA, USA), and an $f=9\text{ mm}$ lens (#32019, Edmund Optics, Barrington, NJ, USA) was built to observe the image plane (right side of element 5) and record it on a near-IR camera (A6260, FLIR Systems, Inc., Wilsonville, OR) or a CMOS sensor camera (0.3M HD CMOS Sensor, TSAAGAN, China). The object utilized was a chrome on glass USAF test target (#58-198, Edmund Optics, Barrington, NJ, USA). The criterion for when an element was resolved was a contrast of .05 or greater, using equation 3 where I is grayscale value. Grayscale values were read from a line traced through all three lines of the respective element. An I_{max} or I_{min} was taken at the inflection points of each fringe, and a contrast value was calculated for each adjacent I_{max} and I_{min} values using equation 3. The contrast values reported are the average of the contrast values obtained for all three fringes. For the HNA configuration, the test target was placed

approximately 50 μ m from the endoscopic lenses and back-illuminated by a superluminescent diode broadband source with ~ 70 nm bandwidth centered at 1350nm (D1300-HP, Superlum, Ireland). Lighting and camera parameters were adjusted so that the image remained just below saturation. Fig. 6 shows an example image obtained from this configuration. Group 8 element 1 was resolved, which is 256 cycles per millimeter or equivalent to a resolution of 1.95 μ m. However, the measured on-axis contrast value is .09 for the horizontal lines and .05 for the vertical lines, below the predicted contrast of 0.21 from the MTF in Fig. 4. The differences in contrast and the exacerbated astigmatism seen in Fig. 6 and 7 may be attributable to the non-optimum alignment of the lenses, non-centration of dichroic coatings, and the added MTF of the microscope system built to visualize the image plane. The image is also dimmer on the edges due to the lack of illumination uniformity of the FOV.

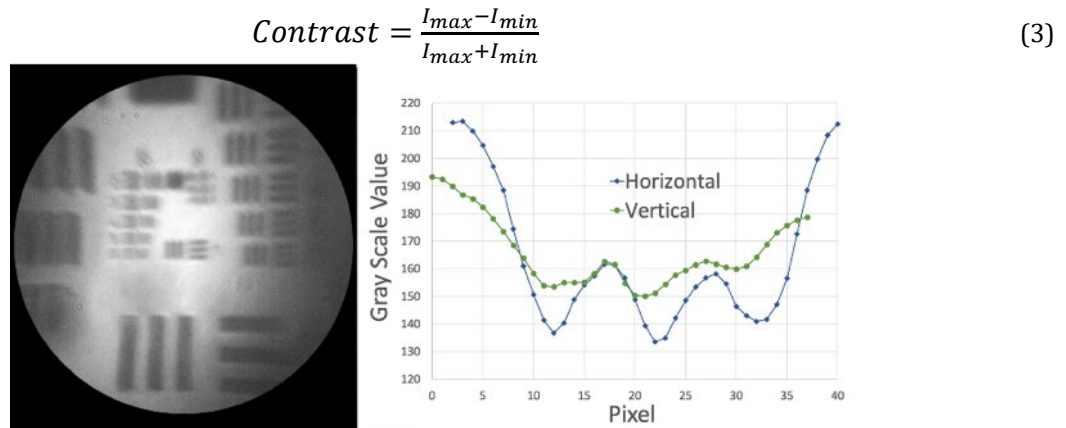


Fig. 6. Left: USAF Target imaging using the HNA configuration. Group 8 Element 1 is resolved. Contrast and exposure were digitally adjusted for clarity. Right: Gray Scale values extracted from lines traced over the horizontal and vertical patterns of Group 8 Element 1.

To test the LNA configuration, the test target was placed at a distance of 8.5mm from the lens system, and back-illuminated by a green laser (L560103SX, LaserGlow Technologies, Toronto, ON, Canada). An example image in this configuration is shown in Fig. 7. Group 5 element 2 is resolved in the center of the field of view, which corresponds to resolving a square wave of 35.9 cycles/mm or a lateral resolution of 13.9 μ m. The contrast values obtained are .05 for the

horizontal lines and .04 for the vertical line. This performance is lower than the prediction of resolving group 5 element 3 at a contrast of $\sim .20$. The degradation is likely due to several factors. First, the long coherence of the illumination laser created circular fringes at the detector cover plate which obscured some elements and lowered the contrast. These circular fringes can be seen in Fig. 7 across the field of view. Second, the performance of the LNA path is highly sensitive to alignment, which may have been imperfect. The resolution value reached, while less than predicted, is at the center of the field of view still within the specification of a 50 μm RMS spot radius.

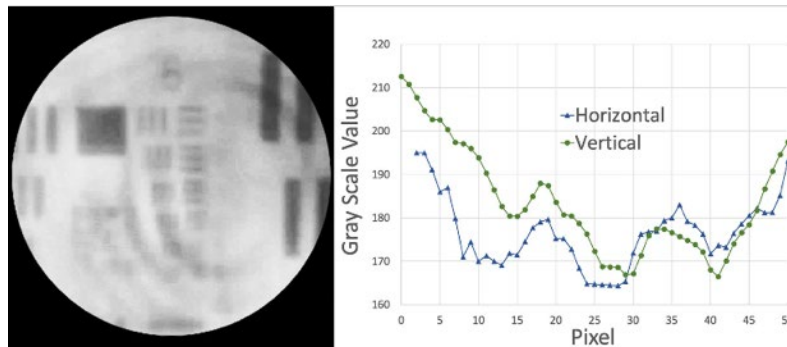


Fig. 7. Left: USAF Target imaging using the LNA configuration. Group 5 Element 2 is fully resolved, and Element 3 is partially resolved. The sagittal component of Element 5 is unresolved due to the system astigmatism. Contrast and exposure were digitally adjusted for clarity. Right: Gray Scale values extracted from lines traced over the horizontal and vertical patterns of Group 5 Element 2.

Additionally, to test the capabilities of the system for white-light imaging and a wider field of view, an image of The University of Arizona logo on white card stock ($\sim 16 \times 16$ mm), front-illuminated with a white LED lamp, was taken at a distance of 12mm. While the system is designed to have a 25 degrees FFOV, in this case, we decreased the magnification of the observing microscope and imaged the largest field of view possible. The system showed a wide FFOV of ~ 70 degrees when fully vignetted. An example image is shown in Fig. 8. This additional test was performed for a qualitative analysis of polychromatic performance. The image shows no significant color degradation, although it shows significant barrel distortion,

suggesting that there is no separation of color nor less performance between the red, green, and blue. The yellow center in the image is the centered dot dichroic coating footprint in the image plane where only wavelengths in the range of 450nm-900nm are transmitted producing a yellowish appearance.

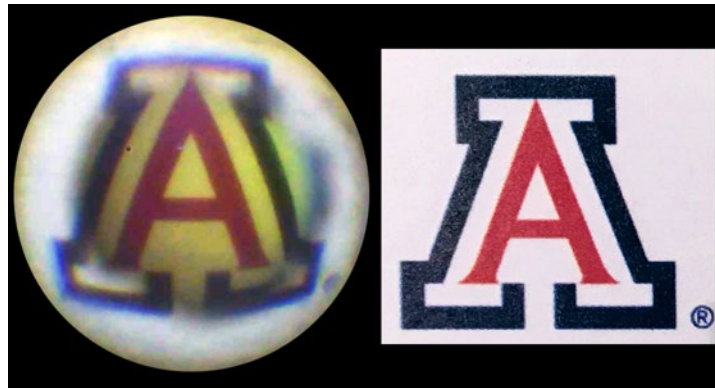


Fig. 8. Left: LNA image of The University of Arizona logo for a qualitative white-light imaging demonstration. Right: Original stock card of The University of Arizona logo that was imaged.

6. Discussion

We presented a versatile, compact lens system capable of both HNA, small FFOV imaging and LNA, large FFOV imaging. This optical system could be used for imaging modalities such as white-light navigation, narrow band, fluorescence, OCM, MPM, and CM, among other imaging types. We intend to use the optical system integrated with a scanning dual clad fiber optic for OCM and MPM as seen in Fig. 9. This scanning fiber optic is enabled by the use of a quartered piezo tube. A proximal dual clad fiber coupler separates the OCT and MPM signals and directs them to appropriate detection systems [28]. The wide field low-resolution imaging configuration is used with the same scanning piezo, but the image is reconstructed by collecting scattered light using multiple large NA fibers placed around the optical system, which are bundled at the proximal end and connected to a sensitive visible detector.

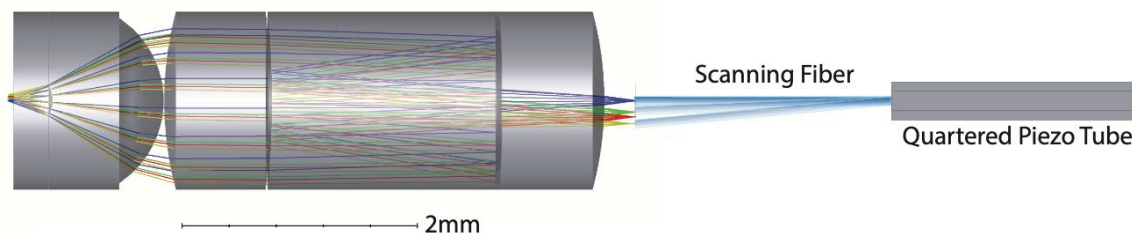


Fig. 9. HNA system configuration suggestion for microscopy using a quartered piezo tube to scan a cantilevered fiber. Illumination is performed using the core of the fiber. If a dual-clad fiber is used, the collection can be done through the first cladding.

Other imaging options are possible. Use of a fiber bundle instead of dual clad fiber optic and scanning system, together with separate illumination fibers can create a multi-pixel imaging system for white-light imaging or multispectral fluorescent Imaging (MFI) in the 450-900 nm wavelength range, although some degradation in imaging bundle performance over the large wavelength range will occur. An example of this configuration is shown in Fig. 10. Dichroic filters at the proximal end may be used to separate multiple wavelength bands to appropriate sensitive cameras. These are two suggested configurations; others are possible.

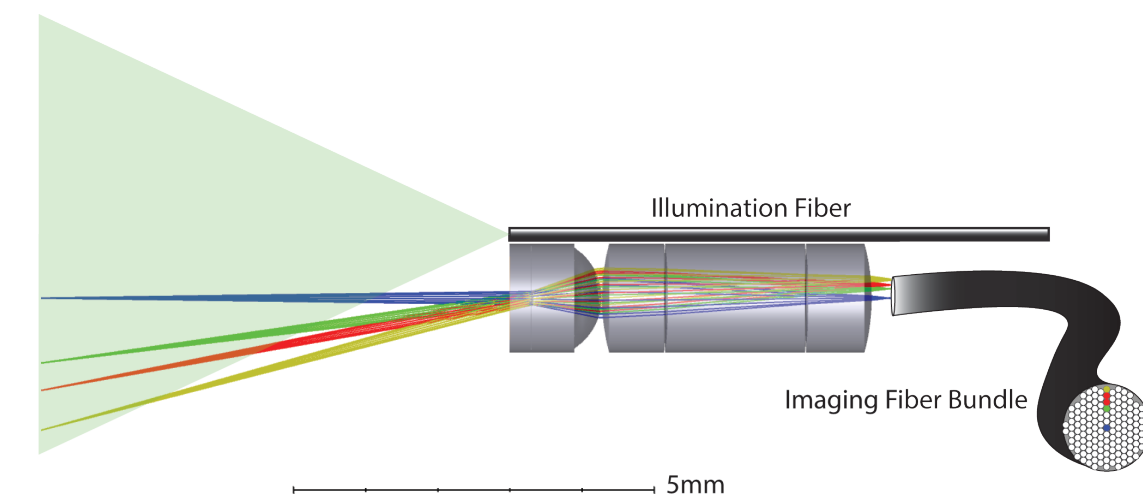


Fig. 10. LNA system configuration suggestion for visible light imaging. A separate fiber carries illumination light to the sample, and a fiber bundle is used to image the sample using the optical system.

While we demonstrate the use of patterned dichroic surfaces with reflective optical power for combining multiple imaging modalities into a single lens system, other technologies can benefit

from the technique of patterned dichroic surfaces. One example is light-based metrology systems, where the use of patterned dichroic surfaces could allow multiple resolutions and testing distances within one instrument. Machine vision product inspection could potentially benefit from the same technology, where the same optical system could be used to inspect different scale features in a product simply by changing the illumination wavelength.

Funding

Research reported in this publication was supported by National Institute of Biomedical Imaging and Bioengineering of the National Institutes of Health under award number 1R01EB020605.

This material is based upon work supported by the National Science Foundation Graduate Research Fellowship Program under Grant No. DGE-1746060 and DGE-1143953. Any opinions, findings, and conclusions or recommendations expressed in this material are those of the author(s) and do not necessarily reflect the views of the National Science Foundation.

Acknowledgments

We would like to extend our gratitude to Sasaan Showghi for allowing us to borrow the FLIR camera to complete the testing of the optics presented in this paper. We also thank John Warda, Walter Siehien and Ben Piatt for their valuable work manufacturing the extremely challenging triplet needed for this project.

Disclosures

The authors declare no conflicts of interest.

References

1. R. J. Kurman and I.-M. Shih, "The origin and pathogenesis of epithelial ovarian cancer: A proposed unifying theory," *The Am. J. Surg. Pathol.* **34**, 433–443 (2010).
2. J. K. Barton, B. Amirsolaimani, P. Rice, K. Hatch, and K. Kieu, "Three-photon imaging of ovarian cancer," in *Photonic Therapeutics and Diagnostics XII*, vol. 9689 H. W. Kang, G. J. T. M.D., K. W. G. M.D., L. Marcu, M. C. Skala, P. J. Campagnola, B. Choi, N. Kollias, H. Zeng, A. Mandelis, B. J. F. W. M.D., and J. F. I. M.D., eds., International Society for Optics and Photonics (SPIE, 2016), pp. 375 – 382.
3. Y. Zou, W. Zhang, F. S. Chau, and G. Zhou, "Miniature adjustable-focus endoscope with a solid electrically tunable lens," *Opt. Express* **23**, 20582 (2015).
4. R. D. genannt Daweke, M. Kelp, H. Lehr, O. Monnich, and P. Osiak, "Electromagnetic direct linear drives for medical endoscopes," in *2014 International Conference on Optimization of Electrical and Electronic Equipment (OPTIM)*, (IEEE, 2014).
5. Corning Incorporated, "Corning varioptic lenses," <https://www.corning.com/worldwide/en/innovation/corning-emerging-innovations/corning-varioptic-lenses/variable-focus-lenses-a-series/varioptic-A-16F.html>.
6. Stemmer Imaging AG, "Stemmer Optotune Fluid Lenses," <https://www.stemmer-imaging.com/en/products/category/focus-tunable-fluid-lenses-2/>.
7. M. Keenan, T. Tate, E. Swan, J. Black, U. Utzinger, and J. Barton, "Optical imaging falloposcope for minimally invasive ovarian cancer detection," *J. Minim. Invasive Gynecol.* **21**, S89 (2014).
8. R. A. Wall and J. K. Barton, "Fluorescence-based surface magnifying chromoendoscopy and optical coherence tomography endoscope," *J. Biomed. Opt.* **17**, 1 – 8 (2012).
9. R. Tumlinson, B. Považay, L. P. Hariri, J. B. McNally, A. Unterhuber, B. M. Hermann, H. Sattmann, W. Drexler, and J. K. Barton, "In vivo ultrahigh-resolution optical coherence tomography of mouse colon with an achromatized endoscope," *J. Biomed. Opt.* **11**, 1 – 8 (2006).
10. Y. Li, J. Jing, J. Yu, B. Zhang, T. Huo, Q. Yang, and Z. Chen, "Multimodality endoscopic optical coherence tomography and fluorescence imaging technology for visualization of layered architecture and subsurface microvasculature," *Opt. Lett.* **43**, 2074–2077 (2018).
11. D. Lorensen, B. C. Quirk, M. Auger, W.-J. Madore, R. W. Kirk, N. Godbout, D. D. Sampson, C. Boudoux, and R. A. McLaughlin, "Dual-modality needle probe for combined fluorescence imaging and three-dimensional optical coherence tomography," *Opt. Lett.* **38**, 266–268 (2013).
12. H. Yoo, J. W. Kim, M. Shishkov, E. Namati, T. Morse, R. Shubochkin, J. R. McCarthy, V. Ntziachristos, B. E. Bouma, F. A. Jaffer, and G. J. Tearney, "Intra-arterial catheter for simultaneous microstructural and molecular imaging in vivo." *Nat. Medicine* **17**, 1680 – 1684 (2011).
13. M. J. Marques, M. R. Hughes, K. Vyas, A. Thrapp, H. Zhang, A. Bradu, G. Gelikonov, P. Giataganas, C. J. Payne, G.-Z. Yang, and A. Podoleanu, "En-face optical coherence tomography/fluorescence endomicroscopy for minimally invasive imaging using a robotic scanner," *J. Biomed. Opt.* **24**, 1 – 15 (2019).

14. O. S. Heavens, *Optical Properties of Thin Solid Films (Dover Books on Physics)* (Dover Publications, 2011).
15. L. Holland and J. Greenspan, "Vacuum deposition of thin films," *J. The Electrochem. Soc.* **104**, 116C (1957).
16. H. Anders, *Thin Films in Optics* (The Focal Press, 1967).
17. H. A. MacLeod, *Thin-Film Optical Filters, Third Edition (Series in Optics and Optoelectronics)* (CRC Press, 2001).
18. D. H. Cushing, *Enhanced Optical Filter Design (SPIE Press Monograph PM201)* (SPIE Press, 2011).
19. R. T. Kester, T. S. Tkaczyk, M. R. Descour, T. Christenson, and R. Richards-Kortum, "High numerical aperture microendoscope objective for a fiber confocal reflectance microscope," *Opt. Express* **15**, 2409–2420 (2007).
20. J. G. Fujimoto, C. Pitris, S. A. Boppart, and M. E. Brezinski, "Optical coherence tomography: An emerging technology for biomedical imaging and optical biopsy," *Neoplasia* **2**, 9 – 25 (2000).
21. P. Tsai, N. Nishimura, E. Yoder, E. Dolnick, G. A. White, and D. Kleinfeld, "Principles, design, and construction of a two-photon laser-scanning microscope for in vitro and in vivo brain imaging," in *In Vivo Optical Imaging of Brain Function*, (CRC Press, 2002).
22. C. Boudoux, *Fundamentals of Biomedical Optics* (Blurb, 2019).
23. S. S. Charschan and B. A. Rockwell, "Update on ANSI z136.1," *J. Laser Appl.* **11**, 243–247 (1999).
24. K. Visvanathan, R. Vang, P. Shaw, A. Gross, R. Soslow, V. Parkash, I.-M. Shih, and R. J. Kurman, "Diagnosis of serous tubal intraepithelial carcinoma based on morphologic and immunohistochemical features," *The Am. J. Surg. Pathol.* **35**, 1766–1775 (2011).
25. D. Vega, K. Kiekens, N. C. Syson, T. Baker, J. K. Barton, and G. Romano, "Full optical model of micro-endoscope with optical coherence microscopy, multiphoton microscopy and visible capabilities," in *Endoscopic Microscopy XIII*, M. J. Suter, G. J. Tearney, and T. D. Wang, eds. (SPIE, 2018).
26. J. E. Greivenkamp, *Field Guide to Geometrical Optics (SPIE Vol. FG01)* (SPIE Publications, 2003),
27. D. G. Ouzounov, D. R. Rivera, W. O. Williams, J. A. Stupinski, T. L. Southard, K. H. Hume, J. Bentley, R. S. Weiss, W. W. Webb, and C. Xu, "Dual modality endomicroscope with optical zoom capability," *Biomed. Opt. Express* **4**, 1494 (2013).
28. K. Kiekens, J. Barton, and O. Talarico, "Proximal design for a multimodality endoscope with multiphoton microscopy, optical coherence microscopy and visual modalities," in *Optical Diagnostics and Sensing XVIII: Toward Point-of-Care Diagnostics*, G. L. Coté, ed. (SPIE, 2018).

A.1.1 Files Storage and Contrast Data

All the files associated with this publication are stored in the following directories:

Research/Barton/Projects/Grants/Salpingoscope/Journal papers files/Salpingoscope optics paper/
OSA published files/

Research/Barton/Projects/Grants/Salpingoscope/Journal papers files/Salpingoscope optics paper/
Visibility/

Within the OSA published files folder, the images included in the original manuscript are available as individual .png, .eps, or .psd files. This folder also includes the OpticStudio model used to fabricate the lenses and produce the analysis figures presented in the manuscript.

The visibility folder includes the raw images (.tif, .jpg, or .png) used for the contrast evaluation published in the manuscript of both the HNA and the LNA optical paths. Within this folder, an excel file named “Visibility Values Master.xlsx” is stored. This file contains the contrast values for all different data sets. The contrast values were obtained using ImageJ using the following method:

A line was traced along the element being evaluated using the straight segmenting tool.

The profile of gray values along the segmentation tool was obtained by the option Analyze\Plot Profile option in the ImageJ menu.

An I_{\max} or I_{\min} was taken at the inflection points of each fringe, and a contrast value was calculated for each adjacent I_{\max} and I_{\min} values using Eq. (3) in the manuscript.

Figure 1 shows an example of the process for the high NA optical path. The same process was applied to the low NA optical path.

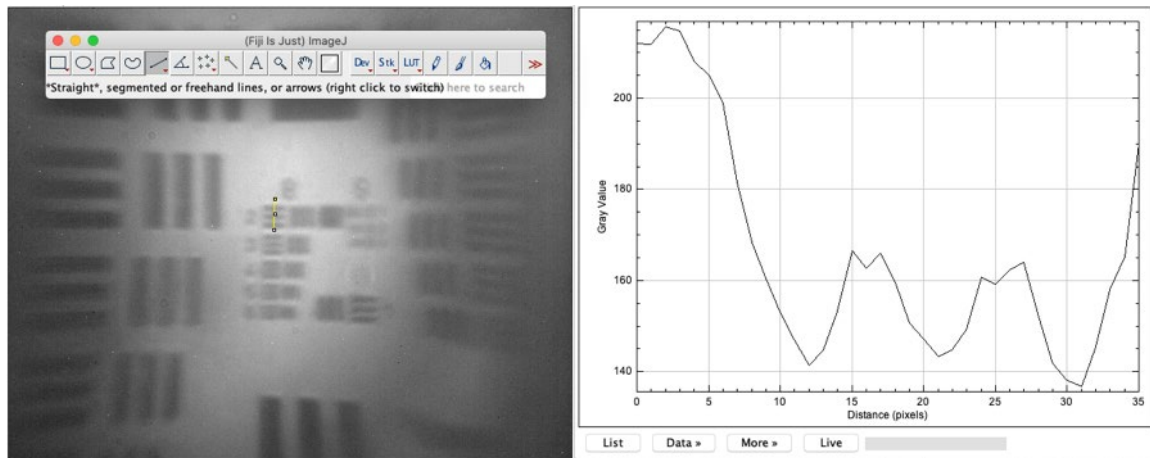


Figure 1 Example of the trace and plot used to calculate contrast.

A.1.2 Non-Sequential Modeling of Non-Conventional Components

A.1.2.1 Non-Sequential Optical Fiber Model

It is helpful to model fiber optics correctly, in order to obtain an accurate representation of the light behavior in the system. Below, a non-sequential optical fiber model is presented. It should be noted that this model is specifically for the initial fiber ordered for the salpingoscope. The initial custom, large NA fiber allowed efficient collection of remitted light in the low NA mode. Unfortunately, this fiber was brittle and unable to sustain constant bending rendering the fiber unreliable. Therefore, the current system uses a reliable .50 NA multimode fiber (FP200URT, Thorlabs, NJ, USA). The model below could be adapted for the new fiber.

The custom ordered fiber is made of Schott 8250 cladding and Schott F2 core. The purpose of the study was to confirm the accuracy of the fiber model to be acceptable for inclusion in the whole system model. The manufacturer specifications are as follow:

- Bare Un-Jacketed Fiber
- NA: 0.66NA
- Overall Diameter: 225 μm +/- 10 μm
- Core Diameter: ~205 μm
- Transmission: 400-900nm
- Ok to use with lengths below 10M to avoid yellowing of transmission
- Core Material: Schott F2 core
- Cladding Material: Schott 8250

The geometrical dimensions were placed in OpticStudio for simulations in the Non-Sequential Ray Trace mode (NSC). This fiber can be made with two standard lens surfaces with no

curvature on the ends. The standard lens surface representing the core should have a higher index (numbers 33 on the first column as shown in Figure 2) than the standard lens surface representing the cladding (numbers 32). The order of the objects is to respect the nesting object rules for OpticStudio. OpticStudio will assume that the object with a higher index precedes the object with the lower index if they overlap.

	Object Type	Comment	Ref Object	Inside Of	X Position	Y Position	Z Position	Tilt About X	Tilt About Y	Tilt About Z	Material
32	Standard Lens ▾	Fiber1 Cladding 8250	0	0	0.90	0.34	4.67 P	180.00	0.00	0.00	SCH8250
33	Standard Lens ▾	Fiber 1 Core F2	32	0	0.00	0.00	0.00	0.00	0.00	0.00	N-F2

Figure 2. OpticStudio non-sequential editor showing the fiber structure. Object with index 32 represents the cladding, and object with index 33 represents the core.

The source was set as a source ellipse with the dimensions of the fiber. The cosine exponent (Cn) was set to 1 to make it Lambertian. According to the OpticStudio help file, the rays are emitted with a distribution of the form

$$I \approx I_0 \cos^{Cn}(\theta)$$

Where I_0 is the source intensity, θ is the ray angle being emitted with respect to the optical axis, and Cn is a user-defined parameter. Note that the larger Cn, the narrower the distribution becomes, but still rotationally symmetric. The Sobol sampling checkmark was removed in the sources options, and a random source was selected to obtain an accurate result without additional sampling. While this may leave gaps between ray angles in the source, $1e7$ rays are traced to minimize the problem. Polarization, ignore errors, split NSC rays, and Scatter NSC rays were selected at the time of raytracing. The detector was set as a detector polar, as seen in Figure 3. This detector will catch any rays that are emitted by the fiber at $\pm 90^\circ$.

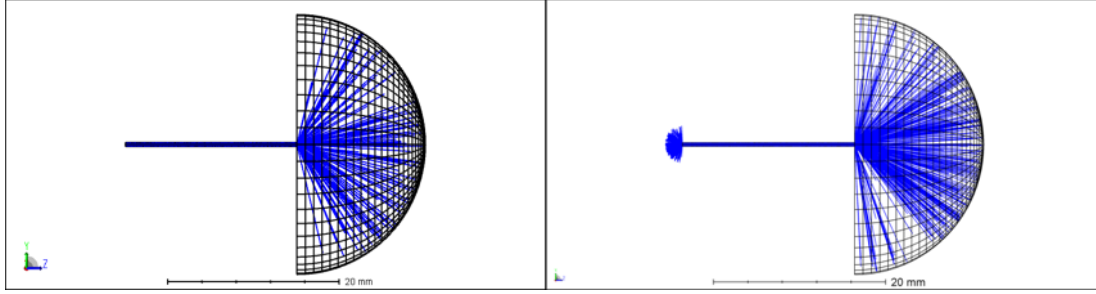


Figure 3. Left. Fiber model with the polar detector and the outgoing rays. The source is placed just outside of the fiber on the left. For clarity, polarization was disabled when this figure was generated. Right. When scattering and splitting are selected, rays are reflected at the air-input face of the fiber. This effect decreases the total power that reaches the detector when compared with the source.

The model suggests that the fiber works with an acceptance/exittance angle of ~ 41 degrees, corresponding to a .66 NA, as shown in Figure 4. Some rays hit the detector at larger angles, but after inspecting the power in the detector, they are shown to be negligible compared to the rays in the acceptance angle cone. These rays come from a ray that hits the boundary between the cladding and air and are remnants of multiple Fresnel reflections. Therefore, the ray suffers Fresnel losses at each intersection, and its energy is negligible by the time it reaches the detector.

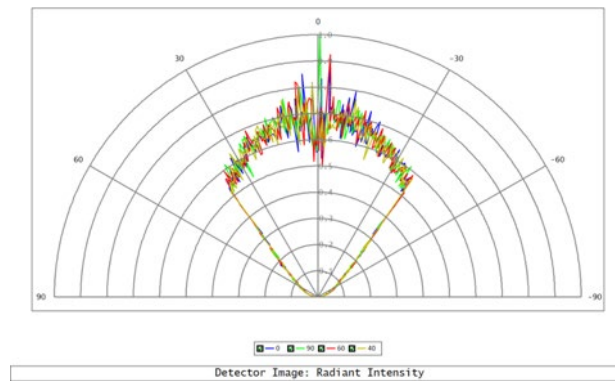


Figure 4. Plot of radiant intensity in polar coordinates taken at 0, 90, 60, and 40 degrees with respect to the tangential plane. No averaging or post-processing of the raw ray data is present.

It is worth noticing that the Schott F2 material properties are in the OpticStudio library, but not the properties for the Schott 8250 glass. Therefore, Schott AG was contacted to obtain the index of refraction data available for a non-specific batch. The provided data is in Table 1. The data was included in the model by using the index fit tool in OpticStudio. This model was initially

inserted in the salpingoscope model to ensure an accurate representation of the fibers and later removed for the .55 NA model.

Table 1. Schott 8250 index of refraction vs wavelength data provided by Schott AG.

Wavelength (nm)	Measured Index
441	1.493
639	1.483
947	1.477
1550	1.469

A.1.2.2 Generating Native Non-Conventional Shapes in OpticStudio

Most optical modeling software includes parametric surfaces that are native to the engine resulting in several advantages such as faster optimization and ray tracing for non-sequential ray trace engines. Unfortunately, objects with shapes that are not supported often need to be included in the model for accurate results. The salpingoscope features one of these non-supported objects. The cover plate is a 300 μm plane-parallel plate and 3.3 mm in diameter. It also has two openings that are used for functional capabilities, such as introducing biopsy forceps. These openings can cause internal reflections that could affect the reflectance imaging modality of the endoscope. Therefore, a stray light analysis was performed to ensure the endoscope functionality, and the endoscope model needed to reflect the instrument's physical characteristics. Therefore, the cover plate, the ferrule, and the hypotube were added to the 3D model to perform this analysis.

While there are many techniques to generate the cover plate shape seen in Figure 5, the cover was modeled with a Boolean native object. The Boolean native objects allow fast ray tracing

since the engine does not have to transform other coordinate systems definitions or shape definitions to versions that OpticStudio can understand.

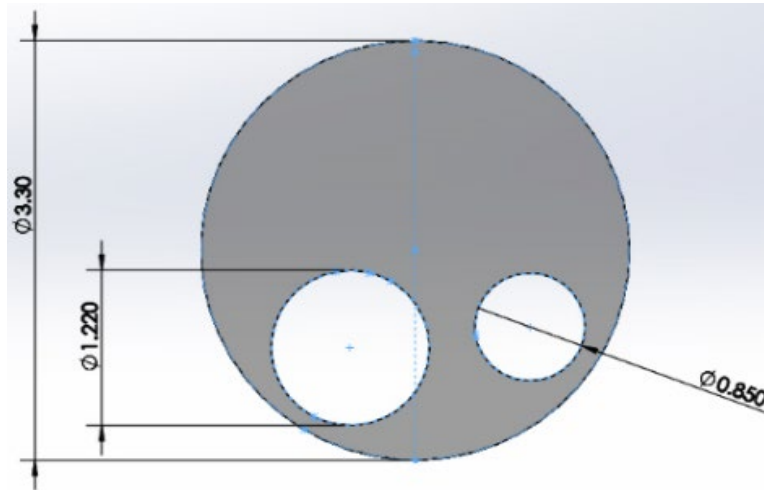


Figure 5. Endoscope cover plate featuring two extruded cut holes that allow functionalities such as irrigation in the endoscope.

A Boolean native object is constructed with known shapes. The base shape, in this case, is a standard lens with no curvature, 3.3 mm in diameter, and 300 μm thickness. Two additional cylinders (standard lens surfaces) need to be included in the model to subtract the “material” from the base object. These two cylinders need to have the correct diameters of .85 mm and 1.22 mm, respectively. The thickness of these two cylinders should be larger than 300 μm to ensure the complete subtraction of the volume. A fourth object will be created using these three objects, called the parent objects. This object is the Boolean that will be the actual cover used in the design for ray tracing and display.

The parent objects used to make the Boolean object can be placed on any part of the 3D space of the file. They do not need to coincide with the final Boolean object in space. Figure 6 shows the Non-Sequential Component Editor parameters that generate this object. First, a cover plate (object A) without holes was set as a standard lens. Then two cylinders (objects B and C) created

with the same standard lens surface type were inserted in the file and located at the proper locations as shown in Figure 7. The comment cell is used to create the Boolean object by typing the equation that generates the object from the parent objects. The cover is created by writing “A-B-C” in the comment cell. This string indicates OpticStudio to subtract the two cylinders from the base cover.

	Object Type	Comment	Ref	Ins	X Position	Y Position	Z Position	Tilt About X	Tilt About Y	Tilt About Z	Material
16	Standard Lens ▾	Cover plate	0	0	0.000000	-0.800000	4.723262	0.000000	0.000000	0.000000	F_SILICA
17	Standard Lens ▾	Cover hole	0	0	-0.500000	-1.570000	4.720000	0.000000	0.000000	0.000000	F_SILICA
18	Standard Lens ▾	Cover hole	0	0	0.880000	-1.400000	4.720000	0.000000	0.000000	0.000000	F_SILICA
19	Boolean Native ▾	A-B-C	0	0	0.000000	-0.800000	4.723262 P	0.000000	0.000000	0.000000	F_SILICA

Figure 6. Final parameters of the OpticStudio lens editor for a Boolean native object.

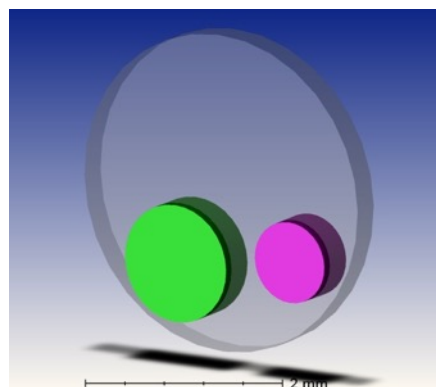


Figure 7. Layout of parent objects to create the Boolean native object.

The resulting Boolean object is shown in Figure 8. Optionally, objects A, B, and C can be hidden and ignored in their surface properties. It is highly recommended to proceed with this step to avoid any ray tracing issues. Figure 9 shows the menu to select the “Ignore and Hide Object” option. The base cover and the two cylinders should not have any materials assigned since the Boolean assigned material overrides the parents’ objects materials.

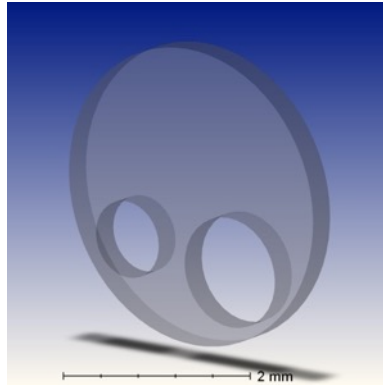


Figure 8. Resulting Boolean native object from the parent objects.

16	Standard Lens ▾	Cover plate	0	0	0.000000	-0.800000	4.723262
17	Standard Lens ▾	Cover hole	0	0	-0.500000	-1.570000	4.720000
18	Standard Lens ▾	<div> Edit Object Consider and Show Object Ignore and Hide Object Copy Cells Paste Cells Create Cell Pickup </div>				-1.400000	4.720000
19	Boolean Native ▾					-0.800000	4.723262
20	Standard Surface ▾					0.000000	4.723000
21	Cylinder Pipe ▾					0.000000	0.299582
22	Annular Volume ▾		workin			-1.570000	4.723262
23	Annular Volume ▾		workin			-1.400000	4.723262

Figure 9. Ignore and hide objects can be set by selecting all the surfaces to be ignored and using right click to set the objects to “Ignore and Hide Object”.

A.2 Accepted Abstract: Model and evaluation of face forward illumination for multimodal endoscopic probes

The following abstract was accepted and presented in the OSA Biophotonics Congress: Optics in the Life Sciences, published on April 17, 2019.

<https://doi.org/10.1364/BODA.2019.DM2B.6>

D. Vega and J. K. Barton, "Model and evaluation of face forward illumination for multimodal endoscopic probes," in *Biophotonics Congress: Optics in the Life Sciences Congress 2019 (BODA,BRAIN,NTM,OMA,OMP)*, OSA Technical Digest (Optical Society of America, 2019), paper DM2B.6.

Model and evaluation of face forward illumination for multimodal endoscopic probes.

David Vega¹, and Dr. Jennifer K. Barton^{1,2}

¹ College of Optical Sciences, ²Biomedical Engineering, The University of Arizona, Tucson, AZ, 85721, USA.
dvega@optics.arizona.edu

Abstract: Multimodal probes with microscopy capabilities can obtain high-resolution images of tissue without additional probes. Initial results of modeling and evaluation of the optical performance predict the possible feasibility of the multimodal system.

1. Introduction

Compact multimodal endoscopes are advantageous for imaging tissues since they can obtain a variety of information using different techniques enclosed in the instrument. Physicians can navigate the probes to a deep organ of interest such as the ovary, and without changing the instrument, obtain images such as Optical Coherence Microscopy (OCM) or even biopsy samples if the endoscope has a working channel to help detecting carcinomas in vivo.

Additionally, by combining all optical modalities in the same optical system the endoscope size can be reduced making it less invasive and preferable to use.

The challenge preventing wide adoption of these probes in the medical community is the difficulty of combining different imaging modalities, since they each require different optical specifications and mechanisms. For example, Multi-Photon Microscopy (MPM) requires a pulsed high-peak-power laser, a high numerical aperture (HNA) and a scanning mechanism since the image is integrated point by point across the full field of view (FFOV). OCM requires a broadband laser, a scanning mechanism, and the numerical aperture can vary for different desired imaging depths. Visible navigation requires a method to obtain video rate imaging, a wide FFOV, and a low numerical aperture (LNA) to obtain long depth of focus imaging. To

design an endoscopic system with all these specifications, several optical and mechanical design techniques have to be used¹. Additionally, modeling to evaluate the performance of the optical system is required to ensure feasibility and identification of possible problems that need to be mitigated before they affect the optical performance. In our study, we model the performance of an endoscope that combines OCM, MPM, and visible light navigation.

2. Scanning mechanism and illumination requirements

A common requirement for both OCM and MPM is the scanning of the FFOV. This system utilizes a technique previously demonstrated for visible navigation². This system uses a quartered piezo tube (QPT) that can oscillate in two orthogonal directions at different frequencies, to create spiral, Lissajous, or raster scanning patterns. This QPT drives a cantilevered fiber typically near resonance.

To accomplish OCM, MPM and Visible navigation different wavelengths have to be used to illuminate the sample. For OCM a broad spectrum of $\pm 100\text{nm}$ centered at around 1350nm is used. For MPM a narrow band high-power pulse centered also near 1350nm is preferred for our application. Finally, a light green laser centered at 561nm is used for navigation.

3. Light collecting mechanisms

A multimodal endoscope rarely uses a single light collecting mechanism for all imaging modalities. This system encloses three different light collecting mechanisms, and the different signals are separated at the proximal end of the system³. The piezo encloses a dual clad fiber, which can be used for both illumination and collection. OCM light propagates through the core of the fiber, and the reflected signal from tissue coupled back into the core returns to interfere with the reference signal and provide the interferogram. The same light source coupled in the

core illuminates for MPM, but the return signal is coupled to the fiber first cladding and routed to a Photo-Multiplier Tube (PMT) assembly to detect two- and three-photon signals. For the visible navigation channel, the green light is also delivered through the core of the fiber, but a set of collection fibers around the optical assembly is used to collect reflected light and computationally construct a contrast image using remitted light from the tissue.

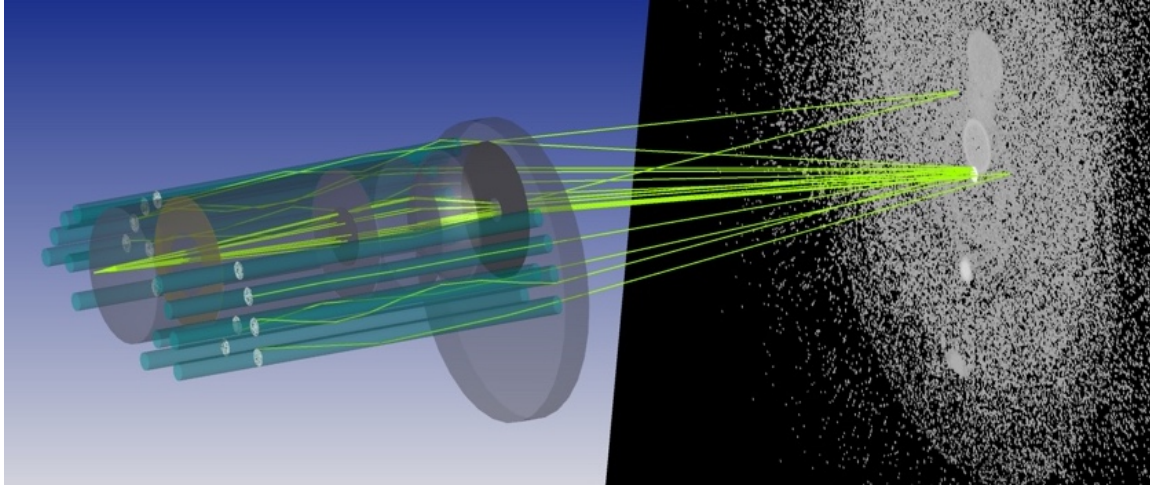


FIGURE 1: A) Visible layout with rays illuminating an object plane. B) Illumination distribution in the plane at a distance of 3mm.

4. Multi-Optical path lens system

Our optical system has been described previously¹. This optical system provides both an HNA needed for microscopy and an LNA needed for navigation separated via illumination wavelength. The system works as a high optical power microscope objective for the purpose of high-resolution microscopy while also providing a low optical power lens system for the navigation feature. This is accomplished by dichroic surfaces embedded in the lens assembly¹. When the multi-optical path system is used in synergy with the scanning fiber, the different illumination wavelengths and the different light collecting mechanisms, it creates a set of combinations that can be used to create the multimodal endoscope. For example, by illuminating the tissue with 561nm, the reflected and scattered light from the tissue can be collected by the

surrounding collection fibers as shown in figure 1-A. The same principle is used for microscopy with a different wavelength to utilize the HNA optical path and collect the signals through the double clad illumination fiber.

5. Stray light and white out for visible navigation

Due the different wavelengths that need to travel within the optical system for illumination and epicollection, an antireflective coating for the exposed surfaces is hard to design and expensive to manufacture. Several unwanted reflections are produced in the optical system and may reach the sample illuminating other areas that are not intended to be illuminated creating noise signal around the intended illuminated spot such as the one shown in Figure 1-B. Therefore, a stray light analysis was performed to evaluate the system signal to noise ratio (SNR) as a function of illumination fiber position. With this analysis we can attempt to account for this noise computationally or identify optical surfaces that may require additional processing for stray light mitigation.

The visible navigation system measures scattered light from the tissue, but there under certain conditions the system visualizes direct specular reflection from the to reach one of the collecting fibers. Specular reflection by epithelial tissues is stronger than the scattered reflection¹, which can cause a condition called “white out” at these scan positions. Noise as seen in Figure 1-B is orders of magnitude lower irradiance than the signal, and preliminary observations suggest that the SNR is above the noise floor across the FOV even without antireflective coatings in the lens system. However, collected specular reflections should be addressed further.

Because of the confocal and non-linear effects which determine the collected OCM and MPM signals, these modalities are less sensitive to stray light. In these cases, stray light primarily manifests as a loss of signal intensity.

6. Summary

In this work we present an approach of integrating three different imaging modalities into a compact endoscope for cancer detection such as ovarian carcinomas. This endoscope model, features OCM, MPM and visible capabilities enclosed in the same optical system. By combining different scanning patterns, wavelengths and collection systems, the endoscope can perform any of the imaging techniques. The novel application of embedded dichroic surfaces allows us to create a multi-optical path lens that separates the longer wavelengths for high resolution microscopy while still using the shorter wavelengths for visible imaging navigation. Trade-offs of the lack of antireflective coatings in the multimode endoscope include reduced efficiency in the HNA channel, and complex stray light leading to higher background noise in the visible navigation channel.

7. References

- [1] David Vega, Kelli C. Kiekens, Nikolas C. Syson, Gabriella Romano, Tressa Baker, Jennifer K. Barton, "Full optical model of micro-endoscope with optical coherence microscopy, multiphoton microscopy and visible capabilities," Proc. SPIE 10470, Endoscopic Microscopy XIII, 104700M (14 February 2018);
- [2] Lee, C. M., Engelbrecht, C. J., Soper, T. D., Helmchen, F., & Seibel, E. J. "Scanning fiber endoscopy with highly flexible, 1-mm catheterscopes for wide-field, full-color imaging," Journal of Biophotonics, 3(5-6), 385–407. (2010).
- [3] Kelli C. Kiekens, Olivia Talarico, Jennifer K. Barton, "Proximal design for a multimodality endoscope with multiphoton microscopy, optical coherence microscopy and visual modalities," Proc. SPIE 10501, Optical Diagnostics and Sensing XVIII: Toward Point-of-Care Diagnostics, 1050119 (20 February 2018);

A.2.1 Reflectance Modality Stray Light Study

While a stray light analysis can be performed for all imaging modalities of the endoscope, the confocal and non-linear effects which determine the collected OCM and MPM signals render these modalities less sensitive to degradation by stray light. In the MPM and OCM cases, stray light primarily manifests as a loss of signal intensity. Therefore, this section only focuses on the reflectance modality since the different surfaces of the system will generate several unwanted reflections that reach the sample and illuminate areas that are not intended to be illuminated. These additional illuminated areas generate noise signals around the intended illuminated spot, potentially blurring the image. This work is the background for the abstract presented in A.2.

A simulation was performed using the assumption that the fiber would move in a raster pattern along a plane. While it is not precisely correct due to the curvature of the actual fiber tip movement, the assumption facilitates the analysis of the system. A map of the points used as a function of fiber deflection is shown in Figure 10

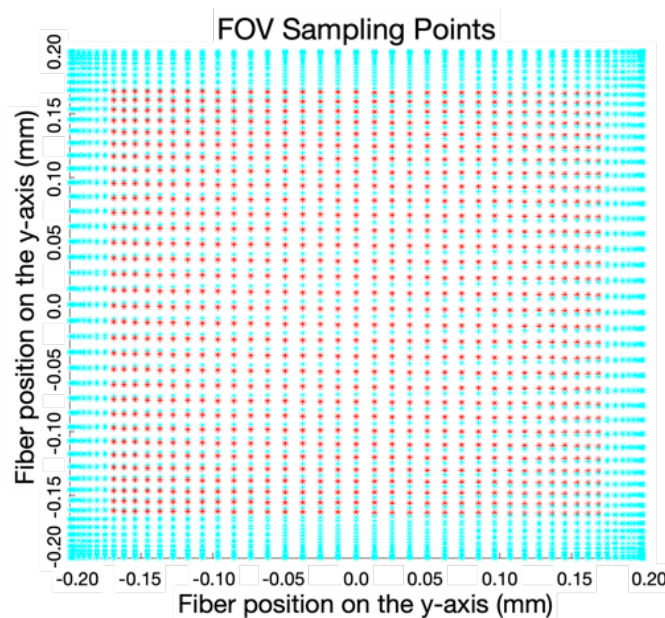


Figure 10. Sampling points used as a function of fiber deflection. Red dots indicate where samples were taken, and blue marks indicate where samples were ignored due to the raster scan sampling. The system is designed to only take data in the most linear part of the sine wave.

A.2.1.1 File Storage

All the files associated with this work are stored in the following directory:

Research/Barton/Projects/Grants/Salpingoscope/Journal papers files/2019 OSA Biophotonics/

Within the 2019 OSA Biophotonics folder, a folder named Salping_NS_SNR_files contains the images included in this section together with the model and MATLAB codes to generate the images. This folder includes the OpticStudio Non-Sequential models used to perform the stray light analysis and generate the visualizations. The visualization model does have invalid settings needed to generate understandable renders of the system and is to be used only for visualization purposes. The model named “all modalities_4_1_19_SNRV1.1.ZDA” can be used to perform analysis.

These files will be explained in the following sections, but in brief: The folder named SNRAnalysis contains the results from the ray tracings performed for this study in a .txt form. .BMP of the system and SNR maps are included in the folder. All relevant figures are stored in MATLAB .fig and .png formats. Two versions of the code used are stored in this folder. The code included in the file “Interactive_Raytrace_readDetectors_moveSource_SNRstrings.m” is used in the OpticStudio Interactive mode (see OpticStudio manual for the latest setup and settings for this mode). The code included in the file “Standalone_Raytrace_readDetectors_moveSource_SNRstrings.m” runs in MATLAB automatically and requires an OpticStudio license present in the computer.

Finally, the file “GenerateVisualizationFrames_Salpingoscope.ZPL” is a macro utilized in OpticStudio to generate frames that later can be used to generate a video to visualize optical ray tracing.

A.2.1.2 OpticStudio and Its Application Programming Interface Setup

The model “all modalities_4_1_19_SNRV1.1.ZDA” was constructed by first transforming the original sequential file utilizing the “Convert to NSC Group” tool in OpticStudio. Figure 11 shows the different objects included in the model. The “Convert to NSC Group” tool will generate the objects in rows 7 to 15. The cover plate from the sequential model was erased and replaced by the cover generated by the methods explained in section A.2.1.2. The optical stop was added after all the optical components to ensure that the stop acts as the aperture by following OpticStudio nesting rules. This nesting rule defines how OpticStudio will behave if a ray strikes more than one object at the same point in space. For example, if the object strikes the optical stop and the cover plate at the cover-stop boundary, the last object listed in the Non-Sequential Editor will determine the properties of the surface or volume at that point. Therefore, the stop precedes all the optical components by placing it last.

The sources generated by the conversion tool were erased, and the source DDL - Fiber.DLL was added in line 1 since this model accurately models a fiber source (See OpticStudio guide for details). A source point was added in line 2 for the case of single ray troubleshooting. The double clad fiber was modeled with a standard lens object. This fiber is for display and stray light analysis purposes only since it does not transport the light from the source. The source is located at the distal end of this dummy clad fiber. Lines 4 and 5 represent the piezo and piezo collar. The

endoscope ferrule is imported using the CAD Part object type. This object type imports a cad file located in the OpticStudio folder for CAD parts (usually located within the “My Documents” folder). Therefore, a copy of the file is saved in this folder. A cylinder pipe object type was used to model the hypotube that encloses the endoscope components, and two annular volumes were used to model the working channel polyimide tubing. Tissue was modeled by a rectangular volume made of seawater in line 28. The properties at the surface of this volume were changed to behave similar to tissue and explained in a later section. Finally, twelve optical fibers were added from line 32 to line 67. These fibers were constructed utilizing the methods presented in section A.2.1.1 and are shown in Figure 12.

	Object Type	Comment	Ref Object	Inside Of	X Position	Y Position	Z Position	Tilt About X	Tilt About Y	Tilt About Z	Material	Radius 1	Conic 1	Clear 1	Edge
1	Source DLL	fiber1.DLL	0	0	0.00	0.00	-0.27	0.00	0.00	0.00	-	10	1E+05	1.00	
2	Source Point		0	0	0.00	0.00	5.07	0.00	0.00	0.00	-	0	0	1.00	
3	Standard Lens	Dummy DoubleCladFiber	0	0	0.00	0.00	-0.27 P	180.00	0.00	0.00	F_SILICA	0.00	0.00	0.13	
4	Standard Lens	piezo	3	0	0.00	0.00	10.00 P	0.00	0.00	0.00	ABSORB	0.00	0.00	0.50	
5	Standard Lens	collar	4	0	0.00	0.00	9.00 P	0.00	0.00	0.00	ABSORB	0.00	0.00	0.75	
6	CAD Part: SolidWorks®	Final Ferrule Design.SLDP...	0	0	0.00	-0.80	4.72	0.00	0.00	0.00	ABSORB	26.00			
7	Standard Lens	Glue LAH58/N-BK7	0	0	0.00	0.00	0.88	0.00	0.00	0.00	N-BAK1	9.35	0.00	0.75	
8	Standard Lens	Glue NBK7/LAH79	0	0	0.00	0.00	2.83	0.00	0.00	0.00	N-BAK1	7.68	0.00	0.75	
9	Standard Lens	Water Medium	0	0	0.00	0.00	5.02	0.00	0.00	0.00	WATER	0.00	0.00	7.00	
10	Standard Lens	LAH58 Lens	0	0	0.00	0.00	0.00	0.00	0.00	0.00	S-LAH58	2.87	0.00	0.75	
11	Standard Lens	N-BK7 lens	0	0	0.00	0.00	0.90	0.00	0.00	0.00	N-BK7	9.35	0.00	0.75	
12	Standard Lens	LAH79 Lens	0	0	0.00	0.00	2.84	0.00	0.00	0.00	S-LAH79	7.68	0.00	0.75	
13	Standard Lens	Dichroic center	12	8	0.00	0.00	-1.00E-02	0.00	0.00	0.00	S-LAH79	7.68	0.00	0.32	
14	Annular Aspheric Lens	Annular Dichroic	11	0	0.00	0.00	-1.00E-02	0.00	0.00	0.00	N-BK7	0.35	0.75	0.35	
15	Standard Lens	Objective Asphere	0	0	0.00	0.00	3.75	0.00	0.00	0.00	ZNS_BRO...	0.83	-0.05	0.70	
16	Standard Lens	Cover plate	0	0	0.00	-0.88	4.72	0.00	0.00	0.00	F_SILICA	0.00	0.00	1.65	
17	Standard Lens	Cover hole	0	0	-0.50	-1.57	4.72	0.00	0.00	0.00	F_SILICA	0.00	0.00	0.61	
18	Standard Lens	Cover hole	0	0	0.88	-1.48	4.72	0.00	0.00	0.00	F_SILICA	0.00	0.00	0.42	
19	Boolean Native	A-B-C	0	0	0.00	-0.80	4.72 P	0.00	0.00	0.00	F_SILICA	0			
20	Standard Surface	Stop	0	0	0.00	0.00	4.72	0.00	0.00	0.00	ABSORB	0.00	0.00	0.75	
21	Cylinder Pipe	Shaft	19	0	0.00	0.00	0.30	180.00	0.00	0.00	MIRROR	1.70	26.33	1.65	
22	Annular Volume	working channel pipe	0	0	-0.50	-1.57	4.72	180.00	0.00	0.00	ABSORB			0.61	
23	Annular Volume	working channel pipe	0	0	0.88	-1.48	4.72	180.00	0.00	0.00	ABSORB			0.42	
24	Null Object	working channel pipe 2	0	0	0.00	0.00	0.00	0.00	0.00	0.00	-				
25	Detector Rectangle	Near tissue	16	0	0.00	0.80 P	0.35	0.00	0.00	0.00		0.07	0.07	101	
26	Detector Surface	OCT Collector	0	0	0.00	0.00	-0.27	0.00	0.00	0.00		0.00	0.00	4.50E-03	
27	Detector Surface	MPM Collection	0	0	0.00	0.00	-0.27	0.00	0.00	0.00		0.00	0.00	0.05	
28	Rectangular Volume	Far skin volume	16	0	0.00	0.80 P	6.00	0.00	0.00	0.00	SEAWATER	7.00	7.00	3.00	
29	Detector Rectangle	far tissue	16	0	0.00	0.80 P	6.00 P	0.00	0.00	0.00		7.00	7.00	1024	
30	Detector Surface	spot detector	16	0	0.00 V	0.00 V	6.00 P	0.00	0.00	0.00		0.00	0.00	0.25	

Figure 11. Non-Sequential Editor showing the objects contained in the model.

	Object Type	Comment	Ref Object	Inside Of	X Position	Y Position	Z Position	Tilt About X	Tilt About Y	Tilt About Z	Material	Par 1(unused)	Par 2(unused)	Par 3(unused)	Par 4(unused)
32	Standard Lens	Fiber1 Cladding 8250	0	0	0.90	0.34	4.67 P	180.00	0.00	0.00	SCH8250	0.00	0.00	0.11	
33	Standard Lens	Fiber 1 Core F2	32	0	0.00	0.00	0.00	0.00	0.00	0.00	N-F2	0.00	0.00	0.10	
34	Detector Surface	Detector Fiber 1	32	0	0.00	0.00	25.98 P	0.00	0.00	0.00	ABSORB	0.00	0.00	0.11 P	
35	Standard Lens	Fiber 2 Cladding 8250	0	0	1.15	0.14	4.67 P	180.00	0.00	0.00	SCH8250	0.00	0.00	0.11	
36	Standard Lens	Fiber 2 Core F2	35	0	0.00	0.00	0.00	0.00	0.00	0.00	N-F2	0.00	0.00	0.10	
37	Detector Surface	Detector Fiber 2	35	0	0.00	0.00	25.98 P	0.00	0.00	0.00	ABSORB	0.00	0.00	0.11 P	
38	Standard Lens	Fiber 3 Cladding 8250	0	0	1.33	-0.14	4.67 P	180.00	0.00	0.00	SCH8250	0.00	0.00	0.11	
39	Standard Lens	Fiber 3 Core F2	38	0	0.00	0.00	0.00	0.00	0.00	0.00	N-F2	0.00	0.00	0.10	
40	Detector Surface	Detector Fiber 3	39	0	0.00	0.00	25.98 P	0.00	0.00	0.00	ABSORB	0.00	0.00	0.11 P	
41	Standard Lens	Fiber 4 Cladding 8250	0	0	1.46	-0.45	4.67 P	180.00	0.00	0.00	SCH8250	0.00	0.00	0.11	
42	Standard Lens	Fiber 4 Core F2	41	0	0.00	0.00	0.00	0.00	0.00	0.00	N-F2	0.00	0.00	0.10	
43	Detector Surface	Detector Fiber 4	41	0	0.00	0.00	25.98 P	0.00	0.00	0.00	ABSORB	0.00	0.00	0.11 P	
44	Standard Lens	Fiber 5 Cladding 8250	0	0	0.97	-0.29	4.67 P	180.00	0.00	0.00	SCH8250	0.00	0.00	0.11	
45	Standard Lens	Fiber 5 Core F2	44	0	0.00	0.00	0.00	0.00	0.00	0.00	N-F2	0.00	0.00	0.10	
46	Detector Surface	Detector Fiber 5	44	0	0.00	0.00	25.98 P	0.00	0.00	0.00	ABSORB	0.00	0.00	0.11 P	
47	Standard Lens	Fiber 6 Cladding 8250	0	0	0.76	-0.66	4.67 P	180.00	0.00	0.00	SCH8250	0.00	0.00	0.11	
48	Standard Lens	Fiber 6 Core F2	47	0	0.00	0.00	0.00	0.00	0.00	0.00	N-F2	0.00	0.00	0.10	
49	Detector Surface	Detector Fiber 6	47	0	0.00	0.00	25.98 P	0.00	0.00	0.00	ABSORB	0.00	0.00	0.11 P	
50	Standard Lens	Fiber 7 Cladding 8250	0	0	-0.90	0.34	4.67 P	180.00	0.00	0.00	SCH8250	0.00	0.00	0.11	
51	Standard Lens	Fiber 7 Core F2	50	0	0.00	0.00	0.00	0.00	0.00	0.00	N-F2	0.00	0.00	0.10	
52	Detector Surface	Detector Fiber 7	50	0	0.00	0.00	25.98 P	0.00	0.00	0.00	ABSORB	0.00	0.00	0.11 P	
53	Standard Lens	Fiber 8 Cladding 8250	0	0	-1.15	0.14	4.67 P	180.00	0.00	0.00	SCH8250	0.00	0.00	0.11	
54	Standard Lens	Fiber 8 Core F2	53	0	0.00	0.00	0.00	0.00	0.00	0.00	N-F2	0.00	0.00	0.10	
55	Detector Surface	Detector Fiber 8	53	0	0.00	0.00	25.98 P	0.00	0.00	0.00	ABSORB	0.00	0.00	0.11 P	
56	Standard Lens	Fiber 9 Cladding 8250	0	0	-1.33	-0.14	4.67 P	180.00	0.00	0.00	SCH8250	0.00	0.00	0.11	
57	Standard Lens	Fiber 9 Core F2	56	0	0.00	0.00	0.00	0.00	0.00	0.00	N-F2	0.00	0.00	0.10	
58	Detector Surface	Detector Fiber 9	56	0	0.00	0.00	25.98 P	0.00	0.00	0.00	ABSORB	0.00	0.00	0.11 P	
59	Standard Lens	Fiber 10 Cladding 8250	0	0	-1.46	-0.45	4.67 P	180.00	0.00	0.00	SCH8250	0.00	0.00	0.11	
60	Standard Lens	Fiber 10 Core F2	59	0	0.00	0.00	0.00	0.00	0.00	0.00	N-F2	0.00	0.00	0.10	
61	Detector Surface	Detector Fiber 10	59	0	0.00	0.00	25.98 P	0.00	0.00	0.00	ABSORB	0.00	0.00	0.11 P	
62	Standard Lens	Fiber 11 Cladding 8250	0	0	-0.97	-0.29	4.67 P	180.00	0.00	0.00	SCH8250	0.00	0.00	0.11	
63	Standard Lens	Fiber 11 Core F2	62	0	0.00	0.00	0.00	0.00	0.00	0.00	N-F2	0.00	0.00	0.10	
64	Detector Surface	Detector Fiber 11	62	0	0.00	0.00	25.98 P	0.00	0.00	0.00	ABSORB	0.00	0.00	0.11 P	
65	Standard Lens	Fiber 12 Cladding 8250	0	0	-0.76	-0.66	4.67 P	180.00	0.00	0.00	SCH8250	0.00	0.00	0.11	
66	Standard Lens	Fiber 12 Core F2	65	0	0.00	0.00	0.00	0.00	0.00	0.00	N-F2	0.00	0.00	0.10	
67	Detector Surface	Detector Fiber 12	65	0	0.00	0.00	25.98 P	0.00	0.00	0.00	ABSORB	0.00	0.00	0.11 P	

Figure 12. Non-Sequential Editor showing the fibers model with their respective detectors.

This model is intended to support the modeling of all optical modalities. Therefore, lines 25 to 27 are detectors used in these other modalities. Detectors in lines 29 and 30 are in the reflectance modality. The detector in line 29 detects the illumination at the tissue surface with low sampling but a larger FOV, while the detector in line 30 is designed to sample the spot illuminated by the on-axis field with high resolution but small FOV.

The hypotube is treated as an infinitely thin cylinder with a reflective inside (aluminum) and an absorbing outside. While the hypotube is not absorbing on the outside, it was set this way to ensure the rays are terminated and not traced after hitting the external surface towards free space, saving computational power.

When a CAD object is imported into an OpticStudio model such as the ferrule, OpticStudio breaks up the CAD file into different “faces,” which are different surfaces in the CAD model.

Each of these surfaces or faces could potentially have different optical properties that make the rays behave differently when an interaction happens. Therefore, the Object Properties/CAD/Surface to Face Mapping options were used to prevent the model from assigning different optical properties in the CAD faces. The menu is shown in Figure 13. An IS scatter function was then assigned to this face in the Object Properties/Coat/Scatter/Select Reflect and Transmit Data options. Since there was no measured IS scatter function in this part, the closest scattering function to the real optical properties is utilized. The menu is seen in Figure 14.

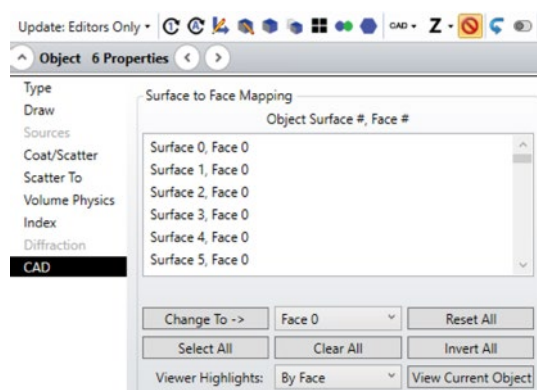


Figure 13. Object Properties/CAD/Surface to Face Mapping options. All faces were set to Face 0 using the “Change to ->” button.

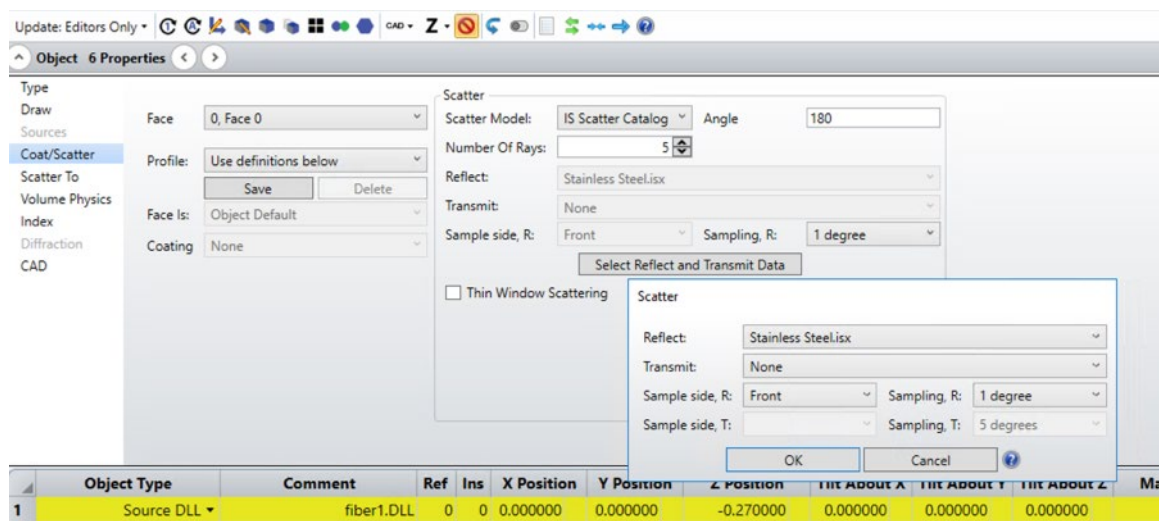


Figure 14. Object Properties/Coat/Scatter/Select Reflect and Transmit Data options utilized to assign the properties of the stainless steel.isx scatter profile to the ferrule.

The tissue scattering model was set using parameters obtained in our lab and presented in the proceeding "Full Optical Model of Micro-endoscope with Optical Coherence Microscopy,

Multiphoton Microscopy, and Visible Capabilities." The specular reflection is $\sim 6\%$, and the scattered fraction of that is .869. The scattered profile is Gaussian with a sigma of 2.3. The settings were input in the Object Properties/Coat/Scatter/ menu, as shown in Figure 15. The final Non-Sequential shaded model can be seen in Figure 16.

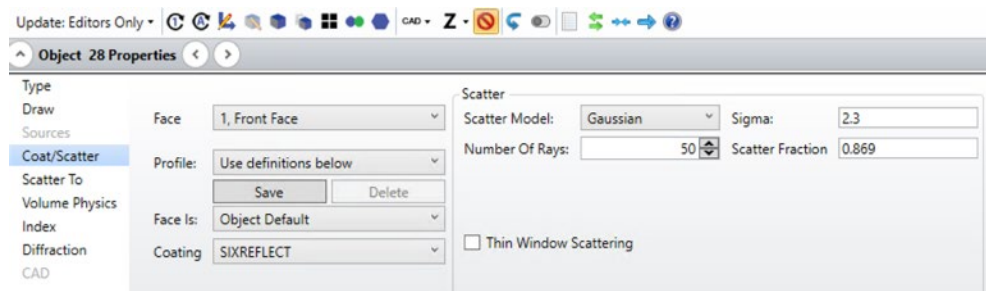


Figure 15. Object Properties/Coat/Scatter/ menu for the object modeling the tissue.

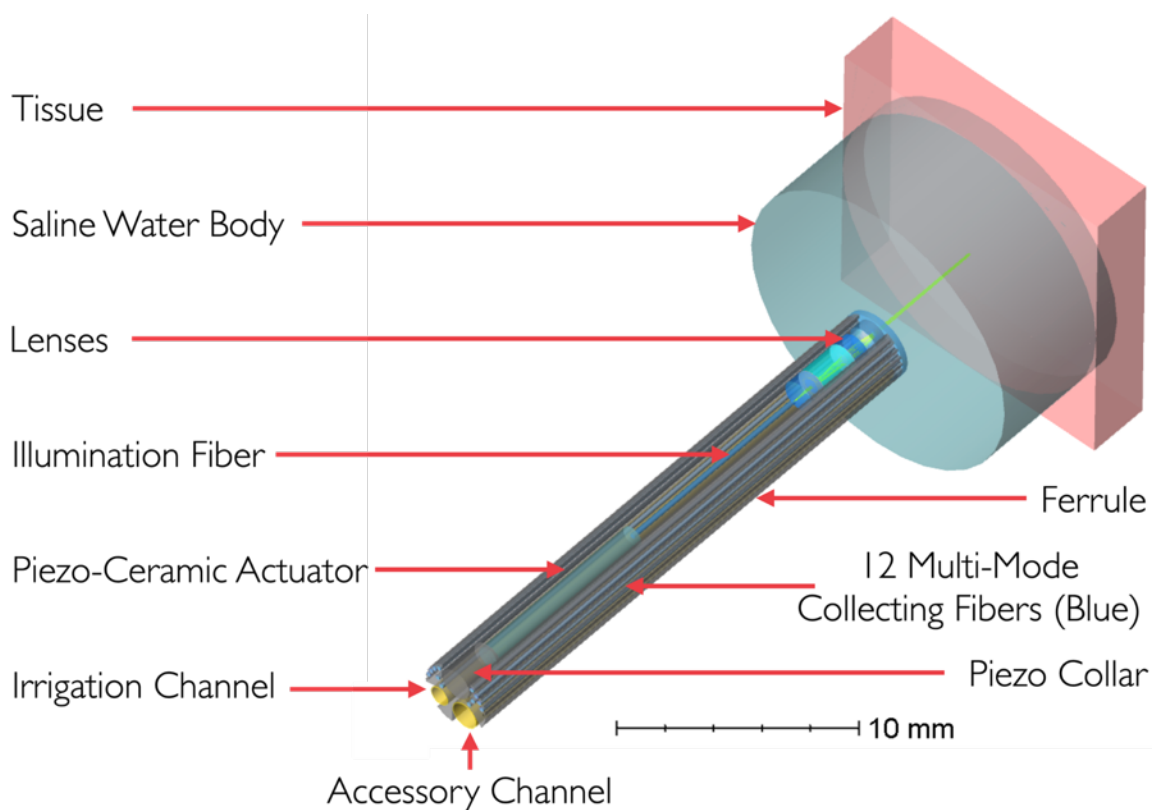


Figure 16. Endoscope shaded model containing all the mechanical and optical elements. The hypotube has been made transparent to generate the render for clarity.

A.2.1.3 Model Convergence Test

The SNR code will run 1089 (33x33) non-sequential ray traces moving the source along the raster scan path of the fiber and calculate the SNR from the rays' data. The ray tracing can be done with a different number of rays. Therefore, the model needs to be set up with settings that ensure repeatability of the simulation is achieved. Ray traces with a different number of rays were performed with the source at the optical axis to test where the ray trace converges and becomes consistent. Each ray trace was performed multiple times to obtain a standard deviation of the power in the detectors behind the collecting fibers. In this study, the consideration for the convergence of the model is that the standard deviation of power in the detectors is two orders of magnitude less than the average power in the detectors for a given number of rays. The code “Interactive_Raytrace_readDetectors_checkConvergenceVsRays.m” runs the described test and provides a graphical output to evaluate convergence visually. The graphs can be seen in Figure 17. The first graph, Energy vs. Number of Rays Traced, shows the obtained energy for each run in blue and the average in red. The standard deviation is then shown in the second graph.

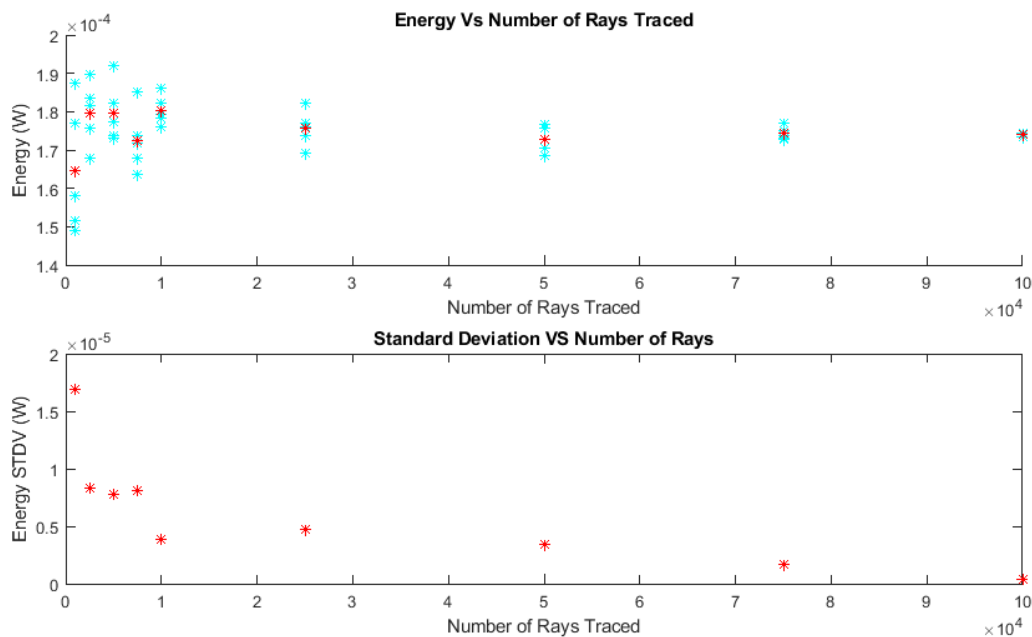


Figure 17. Convergence test graphs. Red dots in Energy vs Number of rays traced are the average for the given number of rays.

Runs with less than $1e4$ rays have a standard deviation of about one order of magnitude below the average. Therefore, ray traces with $1e4$ rays are acceptable for this convergence test. Runs with $7.5e4$ rays can decrease the error in the SNR value since its standard deviation is close to three orders of magnitude below the average. Unfortunately, computational time increases by a factor of five since the time per run is linear with the number of rays. The ray trace using $1e4$ takes 1020 seconds on average (17 mins) compared with a ray trace using $7.5e4$ rays taking 5030 seconds on average (84 mins).

A.2.1.4 Stray Light Analysis

The interactive extension of OpticStudio is used in conjunction with the MATLAB code “Interactive_Raytrace_readDetectors_moveSource_SNRstrings.m”. The code will be introduced in this section. The code utilizes a filter string to separate and save only the rays that hit any of the twelve detectors behind the collecting fibers (See “the filter string” in the OpticStudio help file for a thorough explanation of these filters). Any other rays are discarded, and only the rays saved are utilized for subsequent analysis. In brief, if the filter string is blank, all rays are drawn, saved, or analyzed. Otherwise, only rays that meet the criteria defined by the filter string will be drawn, saved, or analyzed. Filters are composed of a letter and a number. For example, to filter all the rays that hit detector 34 behind one of the collection fibers, the filter string should be “H34”. H informs OpticStudio to include only rays that hit the object 34. Also, strings can have logical operators such as “&” and “|” representing AND and OR, respectively.

The strings defined in this study are the following:

- The saving filter “(H34 | H37 | H40 | H43 | H46 | H49 | H52 | H55 | H58 | H61 | H64 | H67)” saves rays that hit the detectors regardless of their optical path.

- Scattered signal filter “R28 & F28 & (!G6 & !G7 & !G8 & !G9 & !G10 & !G11 & !G12 & !G13 & !G14 & !G15 & !G19)” looks for rays that hits the object 28 (tissue) and scatters (F28) from it. It eliminates any other ray using the ghosting condition !G#.
- Specular reflection filter “R28 & !F28 & (!G6 & !G7 & !G8 & !G9 & !G10 & !G11 & !G12 & !G13 & !G14 & !G15 & !G19)”. The usage of ! before the F28 filters out the rays that scattered from the tissue and leave only the specular rays.
- Tissue noise filter “H28 & (G6 | G7 | G8 | G9 | G10 | G11 | G12 | G13 | G14 | G15 | G19)” filter rays that hit the tissue (28) but did not travel through the main optical path. These rays are ghosted in the optical system but reach the tissue with a modified trajectory. An example of such rays is the ray that reflects at the distal face of the cover plate, then reflects again at the proximal face of the cover plate and reaches the tissue. Therefore, this is the noise coming from the tissue that reaches the detectors.
- Stray light filter “!H28” filter rays that hit the detectors but never exits the endoscope. This light is collected by the internal fibers next to the optical system.

An example of each of these filters, except for the saving filter, can be seen in Figure 18. The scattered signal is the primary signal of interest to generate a reflectance image. The specular signal comes from the intended illuminated spot, but it is not the most desired signal for reflectance imaging since it is based on tissue surface geometry rather than tissue optical properties and can lead to white out. The tissue noise is unwanted light scattered within the optical system that contacts the tissue before being collected by the collection fibers. The stray light is a noise signal caused by light reflecting from optical surfaces and does not leave the optical system.

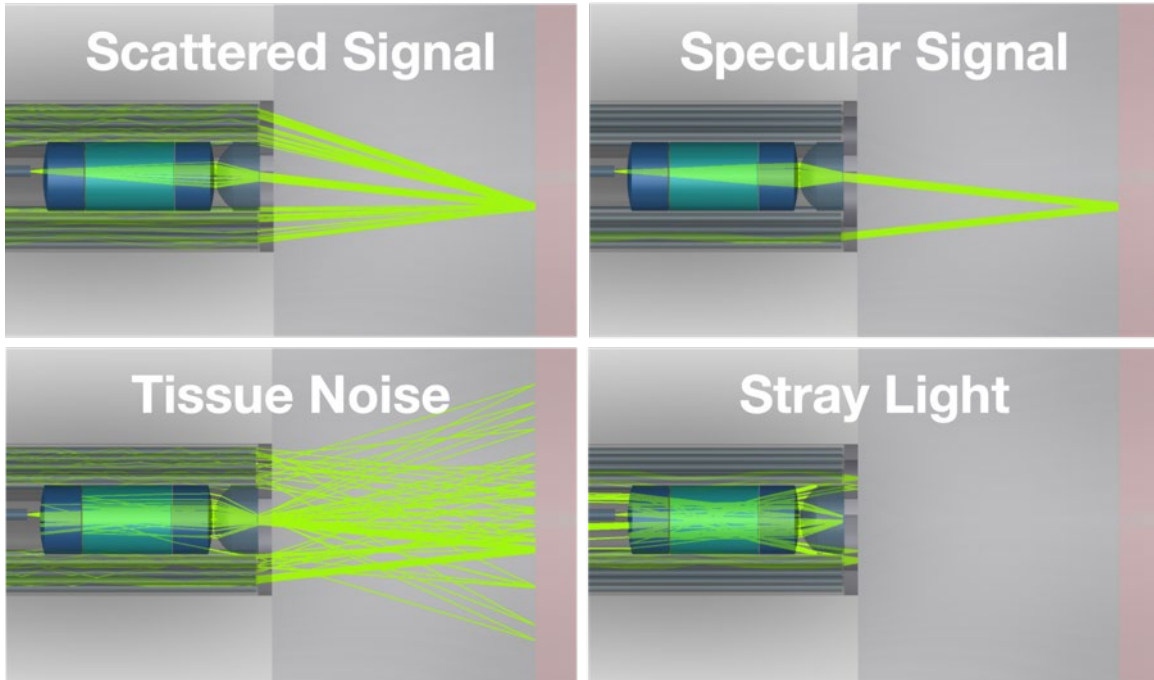


Figure 18. Rays separated by the different strings.

Once the filters were verified, few ray traces were performed to verify the model and compare the total power reaching the detector for each set of filtered rays. An example of these results is given in Table 2. The statistics of three different scenarios are shown in this table. The first scenario is the on-axis ray trace where the source is located at the optical axis, and no specular signal is expected. The second scenario is the specular condition where the light illuminates a specific place in the tissue that reflects light towards one of the collection fibers, as shown in Figure 18 specular signal filter. The source was moved to $x=0.11$ mm and $y=0.01$ mm to generate this scenario. Using this source location, one of the collection fibers receives direct specular reflection. The third scenario is the off-axis ray trace where the source is not at the optical axis, and the specular signal is not expected. The source was moved to $x=0.2$ mm and $y=0.0$ to generate this scenario.

Once the energy in the detector was read, the SNR was calculated using two different equations.

SNR_{SS} treats the specular light as a signal, and SNR_{S0} ignores the specular light and are defined

as

$$SNR_{SS} = \frac{\text{Scattered Signal} + \text{Specular Signal}}{\text{Tissue Noise} + \text{StrayLight}}$$

and

$$SNR_{S0} = \frac{\text{Scattered Signal}}{\text{Tissue Noise} + \text{StrayLight}}$$

Table 2. Reflectance SNR statistics for the on-axis, specular condition, and off-axis ray traces.

Reflectance SNR		
On-Axis Ray Trace		
	Power	% of total power
Scattered signal:	8.16E-05 W	95.98
Specular Signal	0.00E+00 W	0
Tissue Noise	3.07E-06 W	3.62
Stray Light	3.41E-07 W	0.4
Total	8.50E-05 W	
SNR _{S0}	23.9	
SNR _{SS}	23.9	
Specular Condition Ray Trace		
	Power	% of total power
Scattered signal:	7.72E-05 W	2.18
Specular Signal	3.45E-03 W	97.36
Tissue Noise	1.56E-05 W	0.44
Stray Light	6.35E-07 W	0.02
Total	3.54E-03 W	
SNR _{S0}	4.8	
SNR _{SS}	216.9	
Off-Axis and No Specular Condition Ray Trace		
	Power	% of total power
Scattered signal:	7.73E-05 W	96.26
Specular Signal	0.00E+00 W	0
Tissue Noise	2.26E-06 W	2.81
Stray Light	7.42E-07 W	0.92
Total	8.03E-05 W	
SNR _{S0}	25.8	
SNR _{SS}	25.8	

The on-axis and off-axis ray traces show similar SNR indicating a homogeneous SNR across the FOV. In the specular condition, the specular signal dominates the total power collected by the fibers, indicating that the system suffers from whiteout at these field locations when a flat object is being imaged using the reflectance modality.

When “Interactive_Raytrace_readDetectors_moveSource_SNRstrings.m” is executed, it keeps track of the energy reaching the detector by each set of filtered rays. After ray tracing locations, maps of the source location versus the energy deposited by each set of filtered rays are generated. These maps are shown in Figure 19.

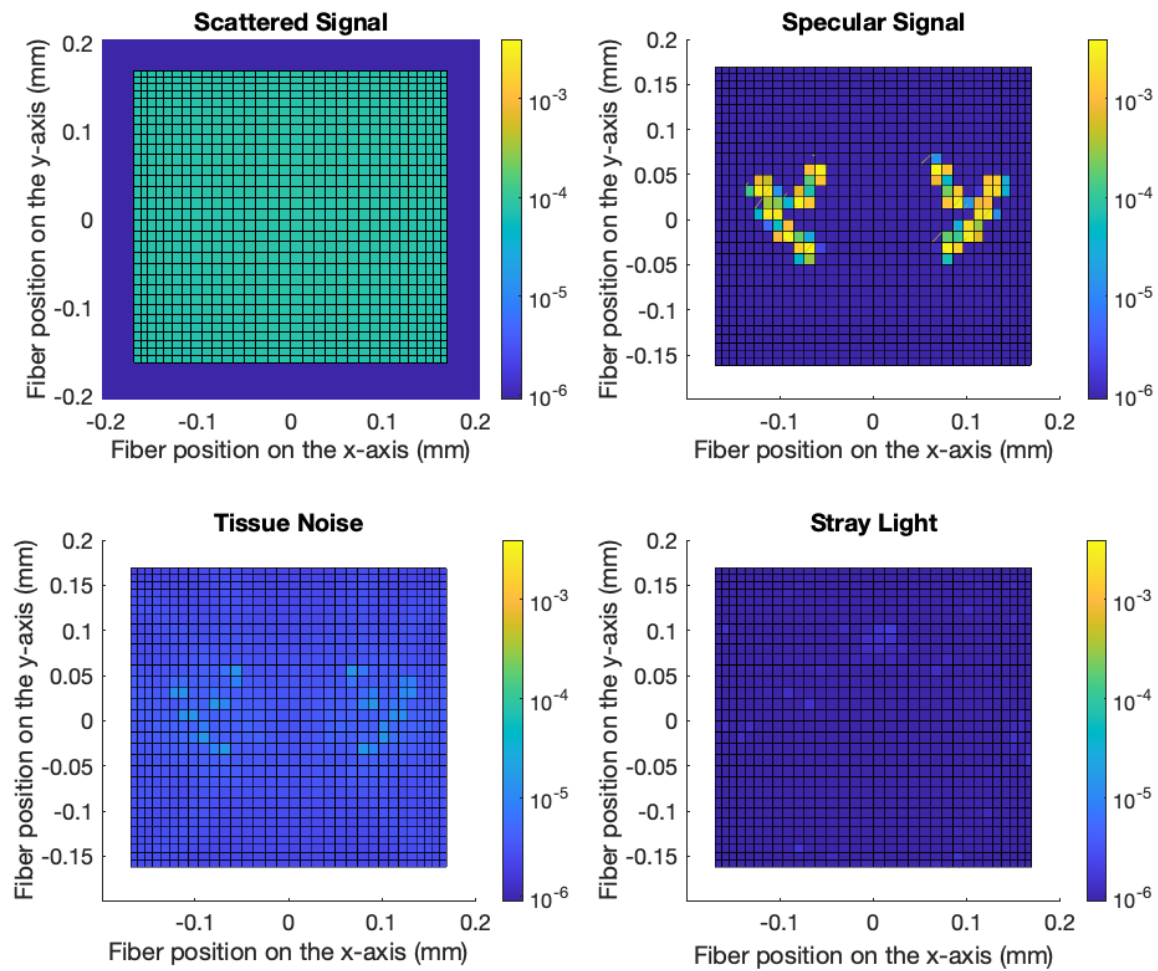


Figure 19. Source location versus the energy deposited by each set of filtered rays.

The scattered signal map confirms the homogeneity across the FOV. This homogeneity causes the SNR_{S0} to be maintained across the FOV. Except at the positions where the specular signal scenario happens. At these locations, the SNR_{S0} decreases, but SNR_{SS} increases considerably.

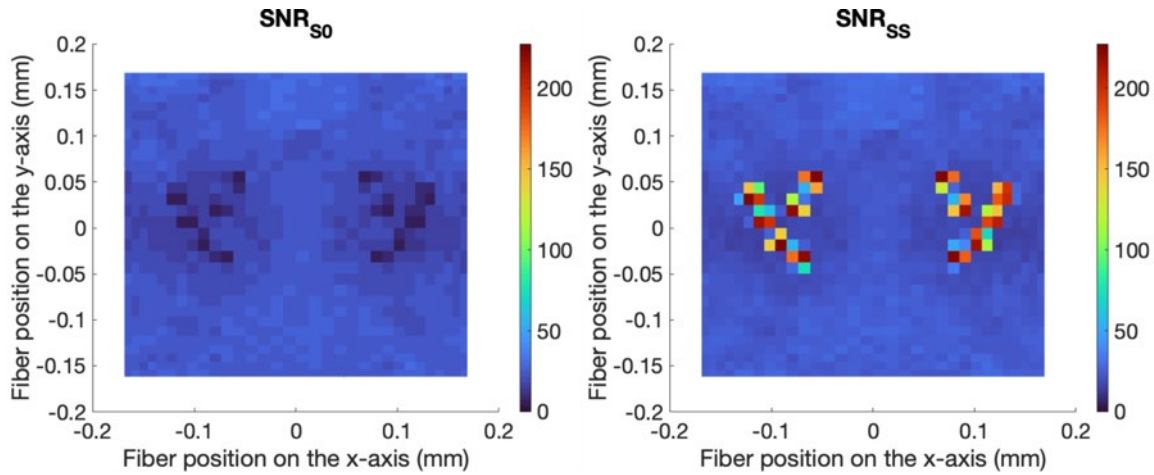


Figure 20. Signal to Noise Ratio (SNR) for both SNR_{S0} and SNR_{SS} .

During this study, the SNR was found to be >4 at any location for both SNR_{S0} and SNR_{SS} .

Therefore, the optical system is deemed to be capable of reflectance imaging. This study provides confidence that the reflectance modality will be successful and identifies the possible problem of whiteout at locations where the specular condition happens.

A.3 Generating visualization of scanning systems with OpticStudio

The endoscope subject of this work features several novel functions, including the dual optical path enabled by dichroic surfaces explained in A.1. The understanding of novel functions is often impaired by the lack of videos showcasing such functions. To facilitate the ability to create such videos, the macro “GenerateVisualizationFrames_Salpingoscope.ZPL” is utilized with OpticStudio to generate frames that later can be used to generate a video to visualize optical ray tracing. In general, the designer needs to follow these steps:

Step 1)

Set up the analysis window (system viewers) in the angle you to see in the video. Let us assume this is window 1 in the OpticStudio environment.

Set up the filter string needed to visualize the rays needed (e.g., FilterString\$=“H15”)

Step 2)

An iterative process is executed until all the frames are generated. This iterative code is in the form of the following pseudocode.

LayoutWindow = 1

FOR i, 0, CyclesToRun, increment

 #Make changes to the optical model

 Print "Processing Frame ", i, " of ", CyclesToRun

 UPDATE LayoutWindow

 FileString3\$="C:\Users\<directory>\Layout_OCT_xz_" + \$STR(i)

 EXPORTBMP LayoutWindow, FileString3\$

 #Extract any desired analysis values

 Rewind

Next

The first line selects the window to be saved. The FOR loop iterates the modification of the optical system, rendering of the next frame, saving of the frame to a specific directory, and potentially extracting results of analyses performed for each iteration.

Step 3)

At the end of the execution, the frames are stored in a directory. The frames need to be further processed to generate a video. Software such as ImageJ can be used to build the video with the saved frames.

Using ImageJ, the steps to build the video are the following:

Open all the frames in ImageJ. Opening all the files at the same time will open the files ordered by name. Therefore, the filenames should identify the frame number for each frame. This is illustrated in Figure 21.

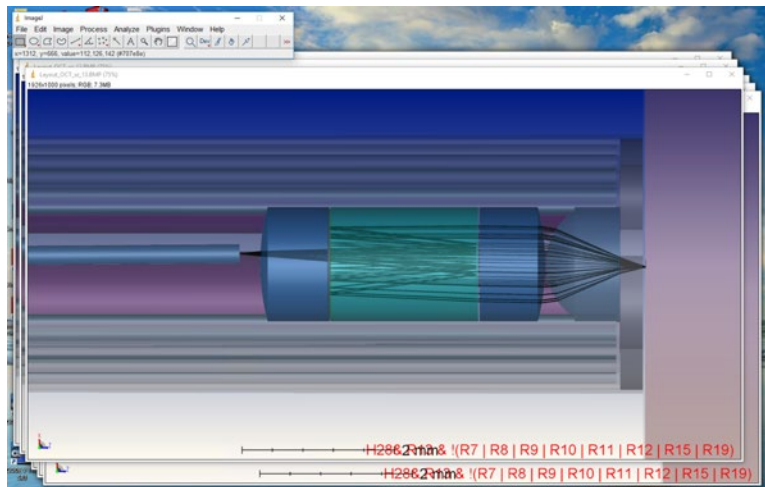


Figure 21. ImageJ with all the frames open.

Use the tool “Image/Stacks/Images to Stack” to create the stack used to build the video. The frame order can be verified using the play button located at the bottom of the stack window. If

there are any frames in the incorrect order, move the frame in the stack to correct the issue. The menu for the “Images to Stack” tool is shown in Figure 22.

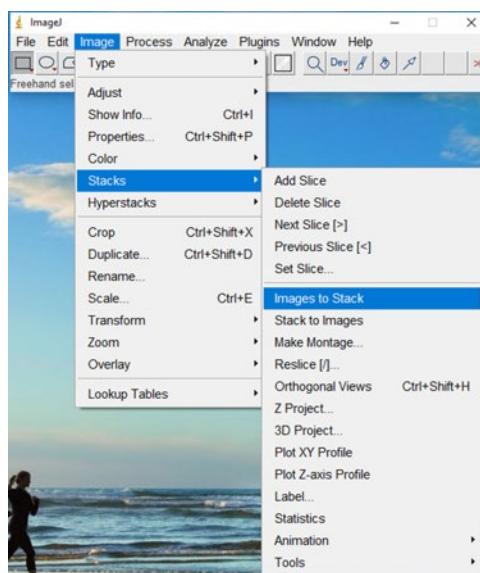


Figure 22. ImageJ menu leading to the “Images to Stack” tool.

ImageJ will generate the video when saving the stack with the “save as” option and selecting .AVI as the file extension. A menu will be shown to select the frame rate and image compression used to generate the video, as shown in Figure 23.

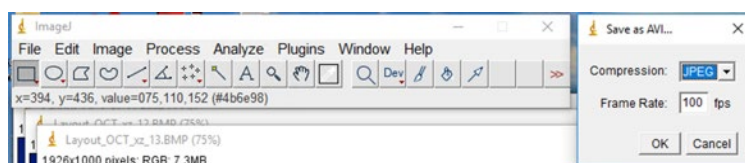


Figure 23. ImageJ menu leading to select the image compression and frame rate when saving .AVI files.

As an example, the models in the folder “models for visualization” inside the folder

Research/Barton/Projects/Grants/Salpingoscope/Journal papers files/2019 OSA Biophotonics/

are used to generate the videos saved in the same folder. The video “picsForVideo_X-Z view.mp4” shows a visualization of the illumination fiber moving and changing the ray traces to generate an accurate representation of the scanning system while used in the reflectance mode.

The different files inside the “models for visualization” have slightly different configurations to generate the desired video. For example, the tissue was modeled in different ways depending on the imaging technique. For OCT, the tissue was modeled as a mirror. The OCT model assumes that all the light is reflected at the surface of the tissue. The tissue curvature was adjusted to allow for the majority of the light to reflect at this boundary. The video for this change is “picsForVideo_OCT.mp4”.

The MPM system models the tissue changing its volume physics properties with an angle scattering model. The parameters were: Mean path $1e-6$ and angle 350, assuming it will scatter anywhere between 0 to 350 degrees. Then a wavelength shift was introduced to model the SHG, THG, 2PEF, and 3PEF. It is imperative to understand that this model does not work for accurate MPM optical modeling since it does not evaluate the needed conditions for SHG and THG. This modality is for visuals only. The resulting video for this modality is “picsForVideo_MPMisometric.mp4” and “picsForVideo_MPM_XZplane.mp4”.

APPENDIX B: Proximal supporting system for co-registered multimodal imaging designed for reflectance, multiphoton, and optical coherence microscopy.

This appendix includes all supplemental material for the multimodal proximal system design and implementation phase of the project, including a proceeding manuscript submitted and accepted in the SPIE Proceedings Volume 11634 SPIE BIOS - Multimodal Biomedical Imaging XVI, the method to wire the electronics of custom PMT detection systems, and two Standard Operating Procedures (SOP) for multiphoton microscope and spectrometer alignment.

B.1 Accepted Manuscript: A co-registered multimodal imaging system for reflectance, multiphoton, and optical coherence microscopy.

The following proceeding manuscript was published March 5, 2020, by the SPIE BIOS - Multimodal Biomedical Imaging XVI proceedings.

<https://doi.org/10.1117/12.2576954>

David Vega, Jennifer K. Barton, Dominique Galvez, Steven Paul Santaniello, Zuzana Adams, Nancy Y. Pham, Kelli Kiekens, Ricky Cordova, Jenna Montague, "A co-registered multimodal imaging system for reflectance, multiphoton, and optical coherence microscopy," Proc. SPIE 11634, Multimodal Biomedical Imaging XVI, 116340Q (5 March 2021).

A co-registered multimodal imaging system for reflectance, multiphoton, and optical coherence microscopy.

David Vega¹, Dominique Galvez¹, Zuzana Adams¹, Steven Paul Santaniello¹, Nancy Y. Pham², Kelli Kiekens¹, Ricky Cordova², Jenna Montague¹, and Jennifer K. Barton^{1,2}.

¹ College of Optical Sciences, University of Arizona, Tucson, AZ,

² Department of Biomedical Engineering, University of Arizona, Tucson, AZ

ABSTRACT

Multimodal imaging is an advantageous method to increase the accuracy of disease classification. As an example, we and others have shown that optical coherence tomography images and fluorescence spectroscopy contain complementary information that can increase the sensitivity and specificity for cancer detection. A common challenge in multimodal imaging is image co-registration. The different images are often taken with separate imaging setups, making it challenging to precisely image the same tissue area or co-register the images computationally. To solve this problem, we have developed a co-registered multimodal imaging system that images the same tissue location with reflectance, multi-photon, and optical coherence microscopy. The co-registration mechanism is a dual-clad fiber that integrates with a scanning microscope or scanning endoscope, collecting all three signals using the same optical path. In the current implementation, optical coherence tomography utilizes a 1300 nm super luminescent diode, multi-photon signals are excited by a custom femtosecond 1400 nm fiber laser producing two- and three-photon signals in the 460-900 nm band, and reflectance imaging operates at 561 nm. The system separates the different signals using fiber wavelength division multiplexers, a dual-clad fiber coupler, and dichroic mirrors to deliver the different signals to the corresponding detector. This wavelength selection enables the system to work passively, meaning that there is no need for devices such as filter wheels. Using the scanning microscope configuration, we have obtained multimodal images of *ex-vivo* ovine ovary tissue.

1. Background

Ovarian cancer (OC) is the deadliest gynecological cancer, with an estimated ~22,000 cases in the United States^{1,2}. OC causes more deaths than any other cancer of the female reproductive system¹. The statistics suggest OC has a very low survival rate due to late diagnosis³. Proper diagnosis is often delayed due to the lack of technology to diagnose it at early stages, the non-specific symptoms, and the desire to avoid invasive laparoscopy procedures used to detect OC. There has been limited success in developing a screening method for OC, motivating the development of new methods to detect OC at early stages. A successful early detection technique could improve affected patients' outcomes since OC detected at the localized stage has a five-year survival rate of 93%, whereas the rate at the distant stage is only 31%¹.

Optical imaging modalities have been shown to effectively detect OC^{4,5,6,7,8,9}. Multiple modalities may provide improved classification accuracy¹⁰. Research teams, including ours, have been developing novel multimodal imaging endoscopes that feature optical coherence tomography (OCT) and other imaging modalities such as fluorescence wide-field imaging or multiphoton microscopy (MPM)^{11,12,13,14}. A multimodal endoscope capable of reaching the ovaries and fallopian tubes might be able to detect OC in the early stages. For example, an endoscope using a transvaginal approach could navigate through the peritoneal cavity using wide-field reflectance imaging. When a suspicious area is observed, the same endoscope could obtain high-resolution images of the area using imaging modalities such as OCT or MPM. Current multimodal imaging systems usually utilize different optical channels to generate each image, complicating the images' co-registration.

To allow easy co-registration, we have previously presented a miniature multimodal optical objective that can obtain images with both wide-field low-resolution, low numerical aperture (NA) suitable for reflectance navigation, and high-resolution, high NA suitable for MPM and optical coherence microscopy (OCM)¹⁵, which is OCT with high lateral resolution. MPM and OCT have complementary mechanisms of contrast and have both been shown to yield excellent correct ovarian cancer classification^{16,17}. The endoscope objective can be utilized with a scanning fiber to illuminate the sample and collect remitted light as shown previously¹⁸, but with a dual-clad fiber (DCF). The core of the DCF carries the illumination light for all modalities and the OCM collection light. The first cladding provides a more efficient collection of MPM or reflectance light. With this simple arrangement, the DCF becomes the co-registration mechanism for the multiple modalities.

2. Multimodal Proximal System Overview

A multi-modality endoscope has to be supported by a proximal system capable of simultaneously acquiring, separating, and displaying multiple signals and images. Based on previous work¹⁹, we designed such a proximal system. The system is versatile enough to be used with an endoscope delivery system or with other implementations, such as a scanning microscope, as long as the microscope's input mechanism is a fiber. In this manuscript, we present a proximal multimodal system with images obtained from a scanning microscope.

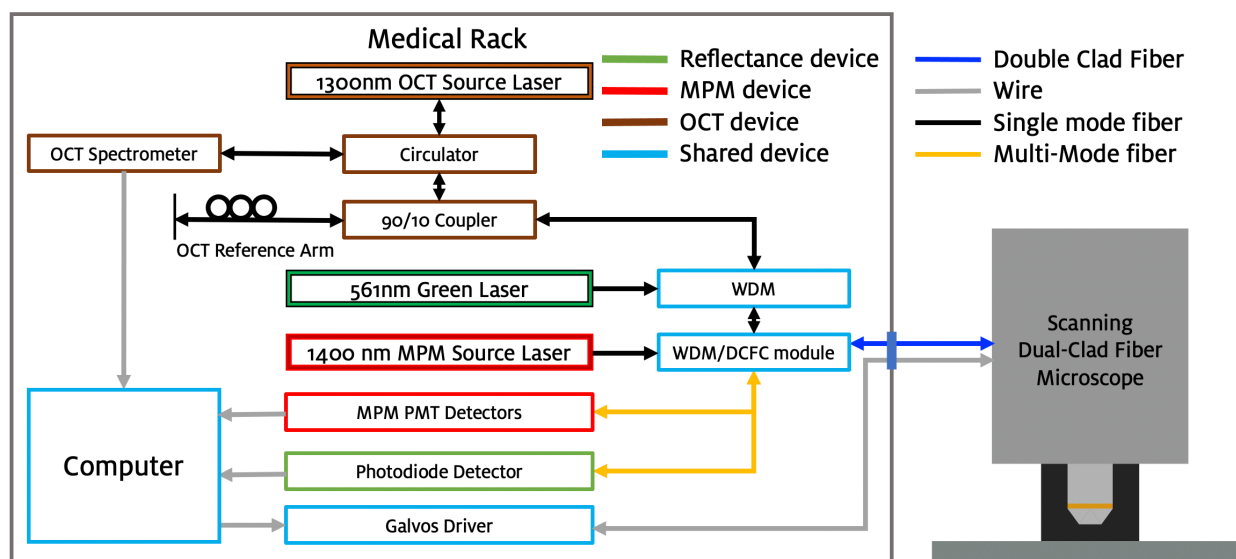


Figure 1. Diagram for the multimodal proximal system (medical rack) connected to the scanning dual-clad fiber microscope. Note that all the major components are listed and are color-coded by optical modality. Devices in brown correspond to the OCT/OCM imaging modality. Devices in red correspond to the MPM imaging modality. Devices in green correspond to the reflectance imaging modality. Devices in blue are shared among all imaging modalities.

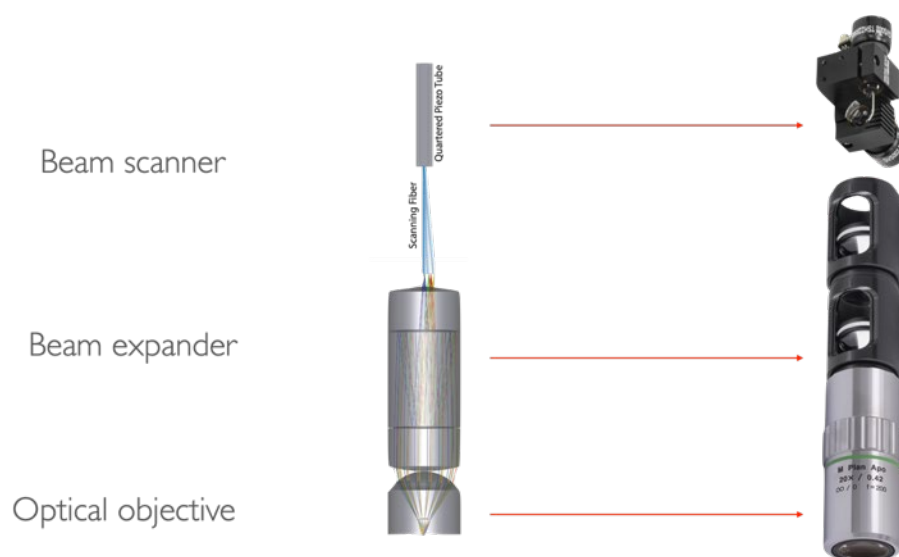


Figure 2. Analogies between an endoscopic optical system (left) and a scanning microscope (right) are shown. The endoscope components include a scanning piezo (PI, MA, USA) and custom optics (Optics Technology, Inc. NY, USA) with custom embedded coatings (Blue Ridge Optics, VA, USA). The scanning microscope components include scanning galvos (included in GVSM002-EC, Thorlabs, NJ, USA), beam expander (SM1L20C slotted lens tubes Thorlabs, NJ, USA, 62-599-INK, and 62-605-INK, Edmund Optics, NJ, USA), and objective (MY20X-804, Mitutoyo, Kanagawa, Japan).

The diagram for the medical rack connected to the scanning dual-clad fiber microscope is presented in Figure 1. This diagram shows the major components that are described in the following sections. The advantage of using the proximal system with a tabletop scanning microscope is that we can perform co-registered multimodal optical imaging to analyze *ex-vivo* samples, *in vitro* cultures, and small animals.

This proximal system can control scanning and obtain signals from either an endoscope or a scanning microscope because, in principle, they are akin to each other. For example, the proximal system can supply voltage outputs to a quartered tube piezoelectric actuator with a cantilevered fiber to produce scanning motion within the endoscope. Similarly, the proximal system can control a galvo scanning system using voltage outputs to define the galvos' scanning angles. The beam diameter in both systems is expanded optically. In the endoscope, the diverging light from the DCF is further expanded using a triplet with dichroic surfaces embedded in the lenses¹⁵. In the tabletop microscope, the light from the DCF is collimated before the scanning galvos, then a simple beam expander composed of two lenses increases the beam diameter. The endoscope's final lens functions as an optical objective that focuses the light at the sample plane, analogous to the microscope objective in the tabletop system. The similarities can be seen in Figure 2.

3. OCT Subsystem Components.

Figure 3 shows the OCT subsystem's isolated components, and Table 1 shows the manufacturers and part numbers of the components used in the spectral domain OCT subsystem. The OCT light source is a super luminescent diode (SLD) centered at 1300 nm with ~75 nm FWHM. Light is coupled to a circulator and then split at the 90-10 coupler to direct light to the scanning

microscope (90%) and the reference arm (10%). The light travels through a custom wavelength division multiplexer (WDM) (used to couple in the reflectance subsystem's green light source, discussed later) and a custom combined WDM/dual-clad fiber coupler (WDM/DCFC), used to couple in the MPM source, discussed later, and couple all light into the core of the DCF). Light is delivered to the scanning microscope using a DCF. Remitted light collected from the sample travels through the same path back to the circulator to be delivered to the custom-made spectrometer. The interference pattern created by light reflected from the reference arm and sample arm (microscope arm) is captured with a line sensor camera in the spectrometer.

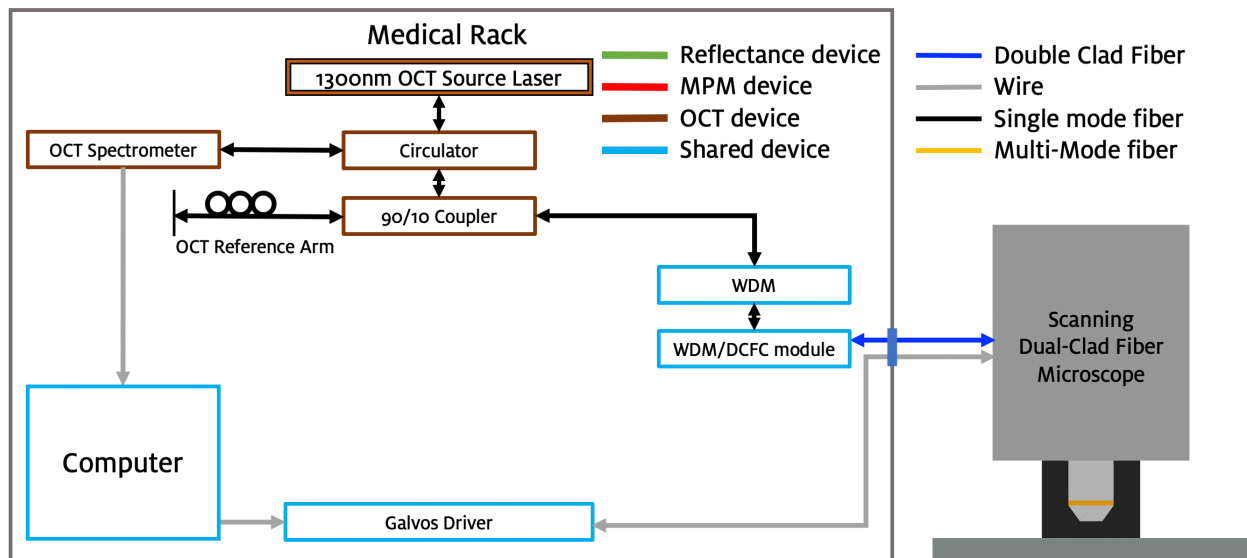


Figure 3. OCT subsystem diagram.

The data acquisition process and image reconstruction are controlled by a computer utilizing a frame grabber (PCIe-1433) to read the spectrometer's camera and a multipurpose DAQ (PCIe-6321) to provide control waveforms to the scanning galvos in the tabletop microscope. Custom-made software, described in a later section, controls the scanning and data acquisition from the camera.

Table 1. OCT subsystem components. Standard optomechanics have been excluded from this table.

Part Name	Manufacturer	Manufacturer Part Number
Laser		
OCT source	Superlum	Driver PILOT-3-2 with 2x2BBC SLD
Spectrometer		
Line sensor camera	Sensors Unlimited	GL2048L
Optical grating	Thorlabs	GR25-0613
Lens	Thorlabs	AC254-300-C
Collimator (fiber input)	Thorlabs	MPD124-M01
Fiber Components		
Circulator	OZ optics	37474 FOC-12N-11
90/10 fiber coupler	Precision Micro-optics	FUSC-280125223
Custom WDM	OZ optics	WDM-12P-111-532/1210:1410-9/125-SSS-40-3A3A3A-3-1-SP
Custom WDM/DCFC	Castor Optics Inc	DBM-1300-200901
Reference Arm		
Collimator (fiber input)	OZ optics	HPUCO-23A-1300/1550-S-11AS
Mirror	Thorlabs	PF10-03-P01
Polarization Disks	Generic	Ø 2" ,3-Paddle polarization controller
Computer system		
Camera Link cable	National Instruments	1 199745-05
Computer	Dell	Precision Tower 7810 XCTO
Software	Intaq	Custom
Frame grabber	National Instruments	NI PCIe-1433
Multipurpose DAQ	National Instruments	PCIe-6321
Terminal Block for PCIe-6321	National Instruments	SCB-68

3.1 OCT considerations and custom-made components

OCT components were chosen to achieve desired high performance. The SLD was chosen to be centered at 1300 nm to take advantage of low scattering in tissue at this wavelength.

Additionally, light sources and photonic components are widely available at 1300 nm. The ~75 nm full width half maximum spectral width of this source provides an axial resolution of ~10 μm , which is sufficient to resolve tissue layer thickening. The 90-10 coupler directs more power towards the sample since a lower remitted signal from the sample is expected than from the reference arm mirror, thus providing better fringe contrast at the spectrometer camera. The

circulator redirects light from going back into the source to the spectrometer, providing more power to the spectrometer. Therefore, we can use a shorter camera integration time (typically 9.1 μ s) to avoid interferometric fringe washout due to vibrations or sample motion. The custom WDM is used to introduce the reflectance subsystem laser passively and does not affect the OCT system except for the laser insertion losses due to this additional fiber component. The WDM/DCFC merges the combined OCT/reflectance light with the MPM laser source and couples them into the core of the DCF going to the scanning microscope.

The reference arm uses standard polarization paddles to match the polarization state of the light in the reference and sample arm, to maximize the fringe contrast at the spectrometer camera plane. Light from the fiber optic is collimated and directed to a standard 1" mirror that serves as the 0 mm optical path difference reference. The reflected light is recoupled into the fiber and travels to the spectrometer via the 90/10 coupler and the circulator.

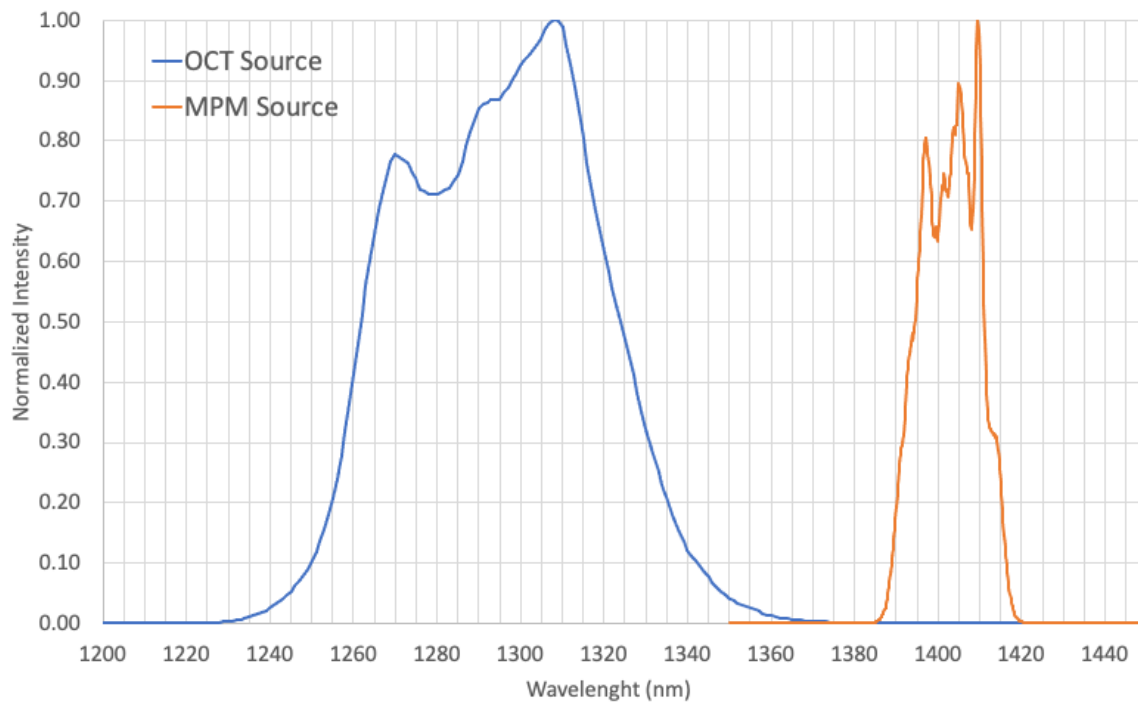


Figure 4. Normalized spectrum of the OCT and MPM sources.

The spectrometer must have sufficient spectral resolution to provide OCT images with the desired depth of imaging. Calculation of the spectrometer requirements has been previously presented²⁰. Since we expect a penetration depth (z_{\max}) in our highly scattering tissues of no more than 2 mm, the spectral resolution should be better than 0.211 nm/pixel as calculated with equation 1.

$$\delta\lambda \leq \frac{1}{4} \frac{\lambda_0^2}{z_{\max}} \quad (1)$$

If only the ~75 nm FWHM spectral width was mapped to the detector, and only 2 mm depth was required to be imaged, the detector only needs to have 355 pixels. The 2048 pixels in the GL2048L line camera are well above this requirement, allowing us to image up to ~6 mm depth and map the full SLD spectral width of ~140 nm spanning from 1370 nm to 1230 nm, as seen in Figure 4. Under these conditions, the spectral bandwidth on each pixel is ~0.068 nm/pixel, and the optimum axial resolution of 9.9 μm is maintained. To choose the lens for the spectrometer and map the entire spectral width, we used equation 2.

$$f_{\text{lens}} = \frac{\text{detector length}}{2\tan(\Delta\theta_G)} \quad (2)$$

$\Delta\theta_G$ is the $\frac{1}{2}$ angle spread of the spectrum due to the grating in the spectrometer. The detector length is 2048 pixels \times 10 μm = 20.48 mm. Using the grating equation, we obtain $\Delta\theta_G \sim 2$ degrees. Therefore, we need a lens with a focal length of ~291 mm; we choose the Thorlabs AC254-300-C lens with an $f_{\text{lens}} = 300$ mm.

To ensure a full angle spread of 4 degrees with enough resolution to spread the spectrum at the camera plane, a sufficiently large area with a specific number of grooves (N) of the grating must be illuminated. The light incident on the grating comes from the circulator output, which is collimated by an all reflective parabola of focal length $f_{\text{collimator}}$. We chose the Thorlabs GR25-

0613 grating due to its spectral qualities and used equation 3 to obtain the N that need to be illuminated when working the first diffraction order $m=1$.

$$\frac{\lambda_{\text{central}}}{\delta\lambda} = mN \quad (3)$$

N needs to be ~ 3893 lines. Using equation 4, we calculated the Gaussian 1/e beam diameter needed.

$$\text{Gaussian Beam Diameter} = \frac{N}{G} \cos \theta_i \sqrt{\frac{\ln(100)}{\ln(2)}} \quad (4)$$

G is the grating density set at 600 ln/mm for the GR25-0613 grating and θ_i is ~ 48 degrees as obtained from the grating equation¹⁹. The Gaussian beam diameter should be ~ 11.2 mm. The system needs a $f_{\text{collimator}} \geq 39.6$ mm as calculated using equation 5 and the fiber NA of 0.14.

$$f_{\text{collimator}} \geq \frac{\text{Beam Diameter}}{2 \tan(\sin^{-1} \text{NA})} \quad (5)$$

We chose a parabolic off-axis mirror collimator with an $f_{\text{collimator}} = 50.8$ mm to have a single element with minimal aberrations and to exceed the calculated minimum beam diameter at the grating. A picture of the custom spectrometer is shown in Figure 5.

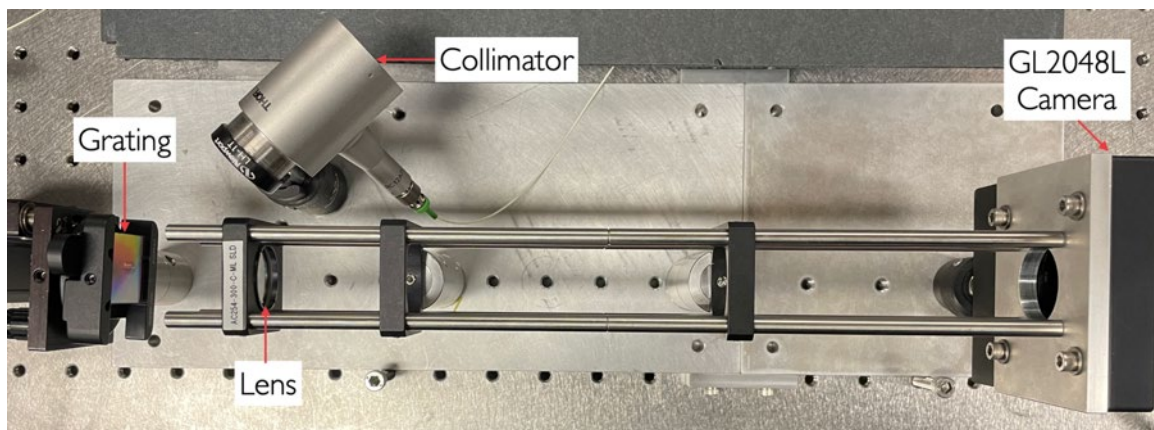


Figure 5. Custom-made spectrometer.

4. MPM Subsystem Components

Figure 6 shows the isolated components of the MPM subsystem, and Table 2 shows the manufacturers and part numbers of the components used. The laser we use is custom-made, centered at 1400 nm, with a pulse duration of about 100 fs at the laser output. The MPM source laser spectrum is shown in Figure 4. The repetition rate is 45 MHz, and the average power is $\sim 160 \text{ mW}^{21}$. The 100 fs pulse is delivered to a pulse compensator grating pair to pre-chirp the pulse and account for fiber and glass dispersion between the laser and the sample. After the pre-chirp, laser light is coupled into the WDM/DCFC module that combines this laser light with the OCT and reflectance sources into the core of the DCF connected to the scanning microscope. A pulse duration of $\sim 82 \text{ fs}$ was measured at the sample plane utilizing a Femtochrome FR-103XL autocorrelator. The microscope optics collect the emitted light from the sample and couple the collected light to the DCF's first cladding. The WDM/DCFC directs the light in the cladding to a multimode fiber that delivers it to the custom photomultiplier tube (PMT) assembly.

In the PMT assembly, the multimode fiber connects to an all-reflective collimator to avoid chromatic aberrations. Collimated light is directed towards a set of dichroic mirrors and filters that separate the light into wavelength bands corresponding to Second Harmonic Generation (SHG), Third Harmonic Generation (THG), 2-Photon Excited Fluorescence (2PEF), and 3-Photon Excited Fluorescence (3PEF). A different PMT then detects each signal. Each PMT is connected to a PMT amplifier, which is connected to the multipurpose DAQ board (PCIe-6374). A low-pass filter is connected between the amplifier and the DAQ board to reduce PMT white noise.

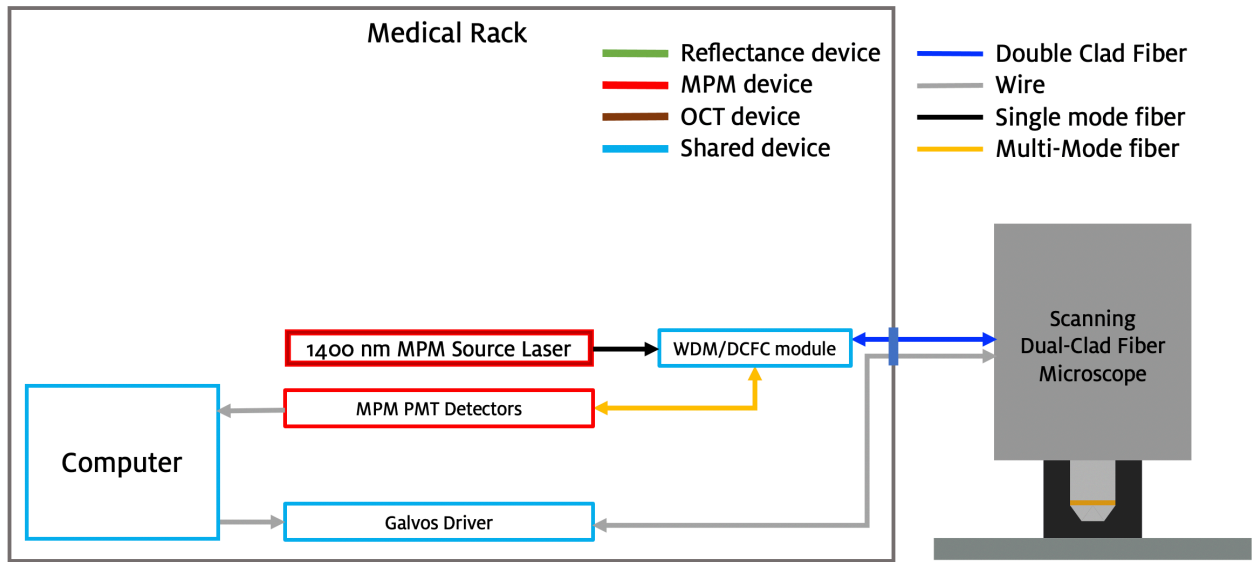


Figure 6. MPM subsystem diagram.

The same computer used by the OCT subsystem also performs the MPM data acquisition and controls scanning. The same multipurpose DAQ board (PCIe-6321) provides control waveforms to the tabletop microscope scanning galvos, just as in OCT mode, but a separate, four analog input channel, synchronous multipurpose DAQ board (PCIe-6374) is used to read amplifier voltages. The custom software also supports the MPM modality and synchronizes the scanning with the data acquisition routine to reconstruct images point-by-point.

4.1 MPM custom-made components

A custom PMT assembly was slightly modified from previous work¹⁹ to accommodate a source laser with a center wavelength at ~ 1400 nm and $1/e$ spectral width of ~ 35 nm²¹ (the previous version was designed for a laser with spectrum centered at ~ 1350 nm). Table 3 includes the wavelength ranges expected from various MPM signals with this new laser.

A diagram of the dichroic mirror and filter setup, and a picture of the PMT assembly, are shown in Figure 7. To ensure that each signal is separated as expected, we tested the assembly by coupling light from an incandescent lamp (MI-I150, Edmund Optics) to a multimode fiber connected to the collimator's entry port. Then, we used a separate multimode fiber to capture a portion of the filtered light at the PMT location for each signal. The multimode fiber was connected to a spectrometer (USB2000+, OceanOptics) to obtain the spectrum.

The theoretical transmission was taken from Kiekens et al¹⁹ and is overlaid upon the measured transmission in Figure 8. The measured transmission bands show their respective cutoffs near the theoretical cutoffs. The expected center wavelengths for SHG and THG are shown with a yellow and blue line, respectively. The center wavelengths of both harmonic generation signals are directed to the appropriate PMTs even with the laser center wavelength change. Note that cross-contamination of SHG and 2PEF signals can occur due to both filters transmitting between approximately 680 nm and 745 nm, as seen in Figure 8. There is also a probability of 3PEF contaminating SHG if the given fluorophore emits above 600 nm. As the harmonic generation signals have a finite spectral bandwidth (about 15 nm for SHG and 10 nm for THG), the probability of contamination of harmonic signals into their respective fluorescence channels is greater.

PMT4-V3 transimpedance amplifiers (Advanced Research Instruments) were selected because they provided the needed gain as well as frequency response for use in this system.

Table 2. MPM subsystem components. Standard optomechanics have been excluded from this table. Parts common with the OCT system (Table 1) are not duplicated in this table.

Part Name	Manufacturer	Manufacturer Part Number
Laser		
MPM Laser	Custom made	100 fs pulse duration, 45 MHz pulse repetition rate, and 160 mW average power ²¹ .
PMT box		
3x PMT SHG, 2PEF, 3PEF	Hamamatsu	H10721-20
1x PMT THG	Hamamatsu	H10721-110
Filter 1	Semrock	FF01-890/SP
Dichroic filter 1	Semrock	FF605-Di02-25x36
Dichroic filter 2	Semrock	FF725-SDi01-25x36x3.5
Dichroic filter 3	Semrock	FF484-FDi01-25x36
Filter 2	Semrock	FF01-850/310-25
Filter 3	Semrock	FF01-550/200-25
Filter 4	Semrock	FF01-770/SP-25
Collimator (fiber input)	Thorlabs	RC02FC-P01
PMT voltage monitor	MakerFocus	B077ZQQQFC
PMT potentiometer	Generic	10k Ω variable resistor.
Electronic breadboard	Adafruit	1214
Electrical 4 pins interface connector	Hillitchi	B07F5B5LLX
BNC interface coupler	QMseller	B07VY3KKJJ
Power Supply	Keysight	E3631A
Amplifiers	Advanced Research Instruments Corp.	PMT4-V3
Electronic filter	KROHN-HITE	3945 Multichannel Filter
Computer system		
Multipurpose DAQ – Four inputs	National Instruments	PCIe-6374
Analog to digital converter for PCIe-6374	National Instruments	185124H-01L

Table 3. The expected spectral range of multiphoton processes with the 1400nm center wavelength MPM laser.

MPM Signal	Wavelength Range
SHG	690-710 nm
2PEF	710-900 nm
THG	460-474nm
3PEF	474-660 nm

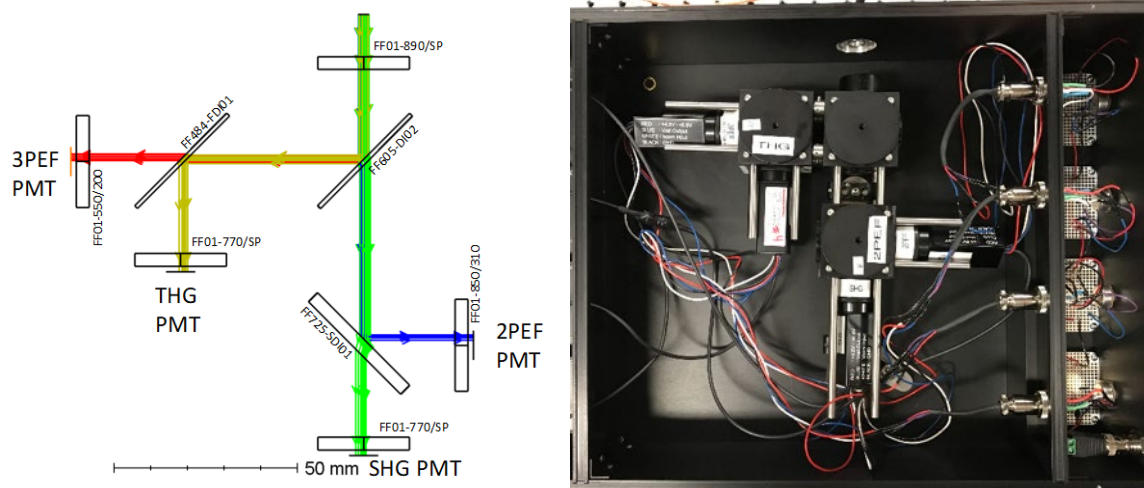


Figure 7. Left, Labeled diagram for PMT dichroic mirrors and filters arrangement. Right, photograph of PMT assembly, with variable gain potentiometers at the right compartment.

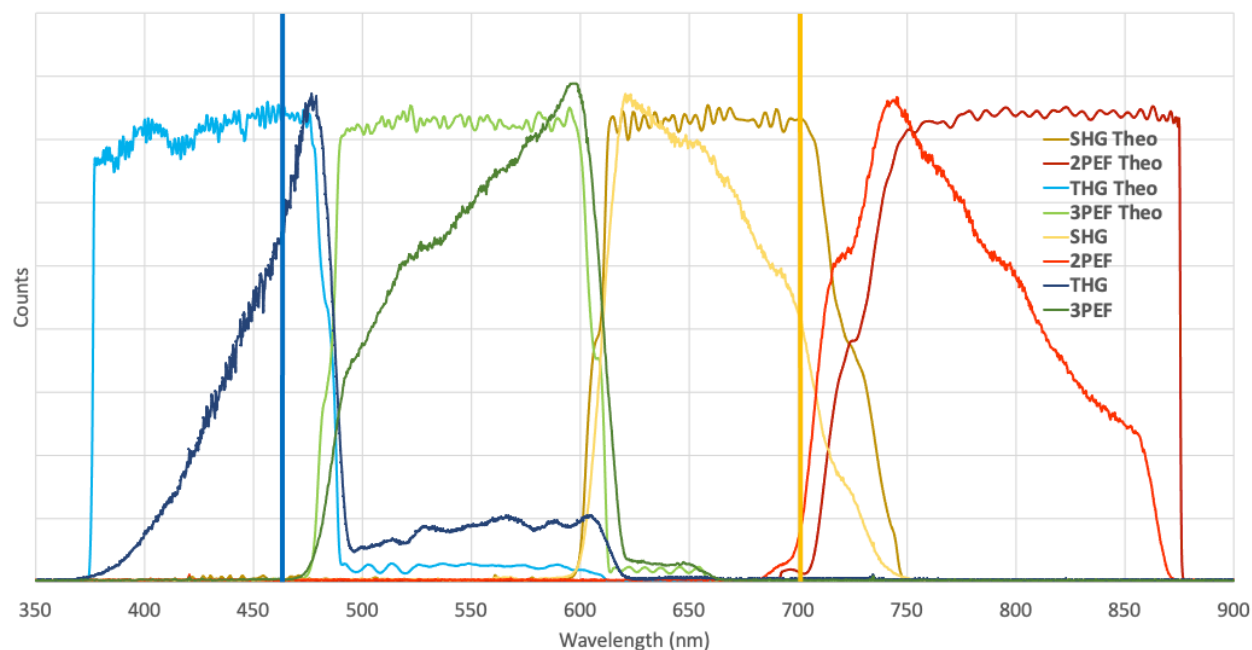


Figure 8. Theoretical wavelength transmission of a uniform spectral emitter through the PMT assembly to each MPM signal PMT is overlaid in the same graph with scaled spectra measured using an incandescent source. Expected wavelength cutoffs are near their theoretical positions. The vertical blue line marks the center wavelength of THG, and the yellow line marks the center wavelength of SHG using our laser source. The nonuniformity of the measured transmission is due to the incandescent lamp spectrum.

5. Reflectance Subsystem Components

Figure 9 shows the isolated components of the reflectance subsystem, and Table 4 shows the manufacturers and part numbers of the components used in this imaging modality. Our source is

a continuous-wave laser centered at 561 nm. This wavelength was chosen because it is well absorbed by hemoglobin, providing contrast in most tissues. This laser is coupled into the system through the custom-made WDM. The WDM/DCFC further couples this laser into the core of the DCF and to the tabletop scanning microscope. Backscattered light is captured by the microscope optics and coupled to the DCF's first cladding. The WDM/DCFC directs the light in the cladding to a multimode fiber that is connected to a photodiode.

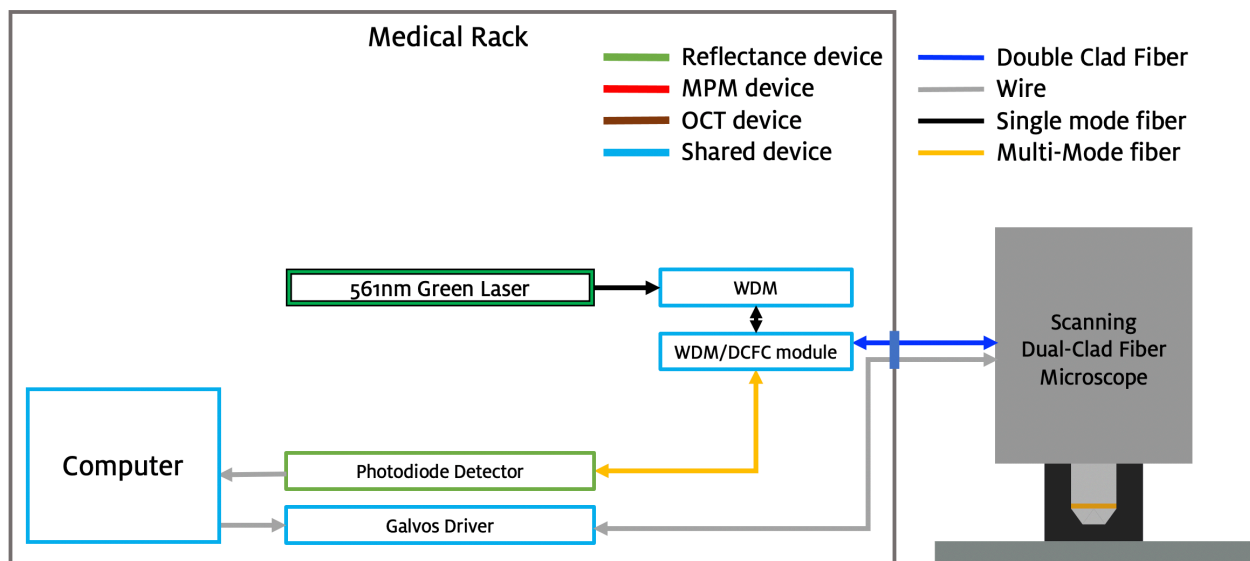


Figure 9. Reflectance subsystem diagram.

This fiber is the same multimode fiber used in MPM to deliver the light to the PMT custom setup. During the design phase, it was decided that the fiber would be disconnected and connected to the right detector when used with the tabletop microscope. Therefore, the fiber is connected to the PMTs when the system is being used in the MPM mode, and the fiber is connected to the photodiode when the system is being used in the reflectance mode. This method avoids any losses in the collected signal that would be incurred from adding a WDM for the green laser. Additionally, a WDM would be difficult to manufacture since the spectral signal for

3PEF includes the 561 nm wavelength. This problem can be avoided by using a separate collection path for the reflected light. For example, we have built an endoscope with 12 multimode, high numerical aperture (NA) collection fibers for the reflectance subsystem. Regardless, it is critical that the green laser not be activated while the PMTs are energized. An interlock prevents this occurrence. The photodiode is read by the software using the same algorithm for MPM. Therefore, the photodiode is also connected to the high-speed multipurpose DAQ board (PCIE-6374) for data acquisition. As this DAQ board has only four analog input channels, one of the MPM PMT amplifiers must be disconnected to acquire the reflectance signal. The same multipurpose DAQ board (PCIE-6321) provides control signals to the scanning galvos.

Table 4. Reflectance subsystem components. Standard optomechanics have been excluded from this table. Parts common with the OCT system (Table 1) or MPM system (Table 2) are not duplicated in this table.

Part Name	Manufacturer	Manufacturer Part Number
Laser		
Green 35mW 561nm laser	LaserGlow Technologies	R560503FX
Photodiode		
Photodiode	MKS (aka Newport)	2107-FC-M

6. Software

The computer synchronizes the data acquisition with the scanning galvo control signals using a custom-made LabView (National Instruments, TX, USA) program. Currently, the software allows for the acquisition of one modality at a time. The user interface for the OCT mode is shown in Figure 10.

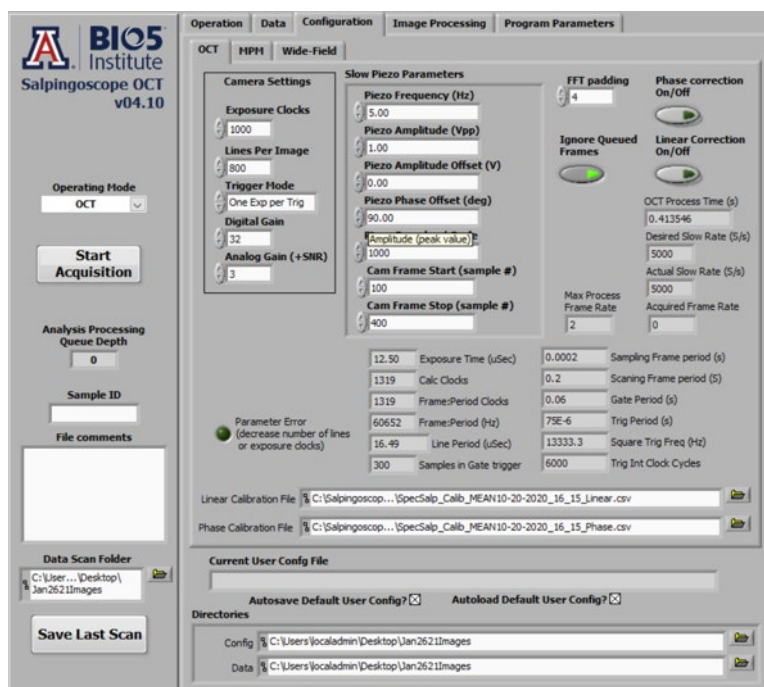


Figure 10. User interface for custom-made LabView software synchronizing the scanning and data acquisition of the multimodal system.

The multipurpose DAQ board outputs analog signals that control the motion of the galvos and data acquisition triggers to synchronize the data acquisition. These outputs are calculated using the sampling parameters set by the user, the characteristics of the tabletop microscope optics, and the detectors to define the image's physical size and the number of pixels. The choice of data acquisition board with an onboard Field Programmable Gate Array (FPGA) allows the program to capture images at video-rate speeds of 30-40 Hz since the computer's processing resources are not being used to generate the output signals. Depending upon image size and extent of processing required for the modality (especially the wavelength-to-wavenumber resampling and the Fourier transform calculations required for OCT), the computer may be unable to display images as rapidly as the data is acquired. In that case, the software contains an option to ignore queued frames resulting in a video feed at a slower rate but without lag in the video feed due to frame processing.

7. Multimodal Imaging Test

We obtained initial images with the reflectance, MPM, and OCT modalities using *ex-vivo* ovine ovarian tissue, shown in Figure 11 and Figure 12. The tissue used was free of labeling or contrast agents. Note that the tissue surface was not flat, resulting in a reflectance image that is not in focus over the entire image. However, as seen in Figure 11, the reflectance image shows the tissue topology with excellent contrast. As limited tissue two-photon autofluorescence would be expected with our 1400nm center wavelength source, likely, most of the signal in the 2PEF image is SHG generated by tissue collagen; however, longer wavelength fluorophores such as porphyrin may also contribute. 3PEF images likely show fluorescence emission from various endogenous fluorophores, including collagen, NADH, and FAD, and may also include THG contamination from step index of refraction changes. The OCT image shown in Figure 12 shows a cross-sectional view of the tissue morphology along a horizontal line in the center of the field of view. All images correspond to the same location on the tissue, and all *en face* images have the same $\sim 300 \times 300 \mu\text{m}$ field of view.

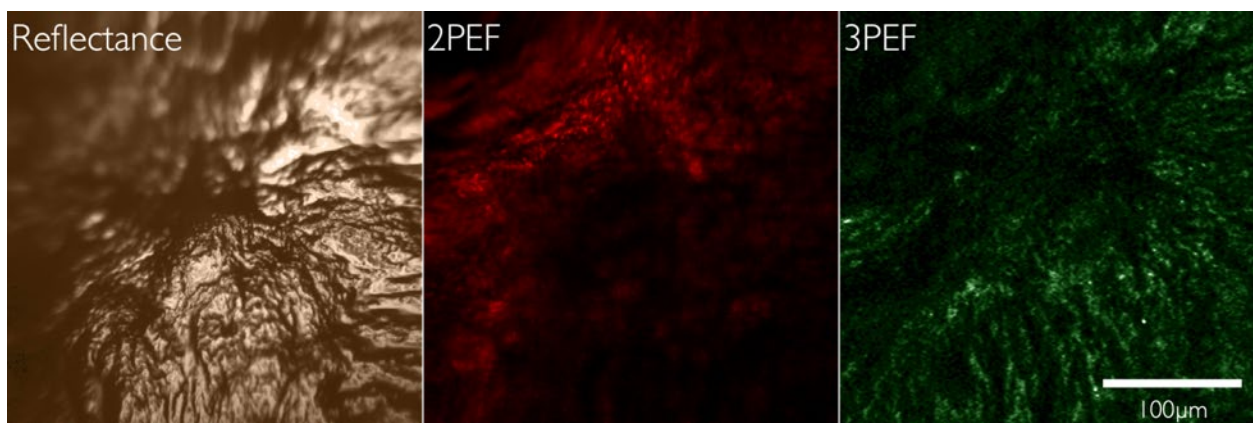


Figure 11. Co-registered reflectance (left), 2PEF (middle), and 3PEF (right) of ovine ovarian tissue.

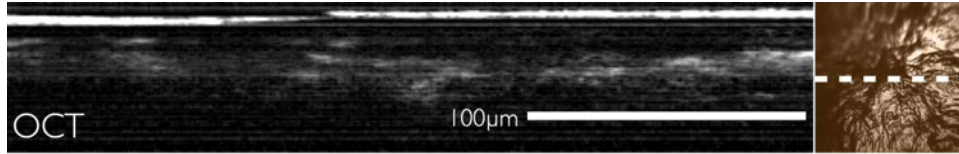


Figure 12. The OCT image (left) was obtained by scanning along a horizontal line at the center of the reflectance and MPM field of view (right).

8. Future Work

The multimodal imaging proximal system is functional at this stage but still needs some calibration and performance adjustments to improve imaging quality when used with the tabletop microscope. Future work includes fiber length adjustments, improved dispersion control, and improvements to software control of the scanning galvos with bi-directional scanning in OCT mode to enable 3D OCM imaging and *en face* images as are typical in OCM. Once the ovarian imaging endoscope is ready to be tested, the proximal system will be utilized in conjunction with the endoscope for an *in-vivo* ovarian imaging study in sheep.

Acknowledgements

We want to acknowledge the support provided by several teams. The Ultrafast Fiber Lasers and Nonlinear Optics group, led by Professor Khanh Kieu, provided us with their 1400 nm custom-made pulsed laser. INTAQ supplied the expertise needed to program the FPGA allowing the program to achieve software performance. Finally, Castor Optics tailored a custom solution to build the WDM/DCFC.

Funding

Research reported in this publication was supported by National Institute of Biomedical Imaging and Bioengineering of the National Institutes of Health under award number 1R01EB020605.

This material is based upon work supported by the National Science Foundation Graduate Research Fellowship Program under Grant No. DGE-1746060. Any opinions, findings, and conclusions or recommendations expressed in this material are those of the author(s) and do not necessarily reflect the views of the National Science Foundation.

REFERENCES

- [1] American Cancer Society, Inc., “Ovarian Cancer,” cancer.org, 17th, January 2021, <http://www.cancer.org/cancer/ovariancancer/index>
- [2] Torre, Lindsey A, Trabert, Britton, DeSantis, Carol E, Miller, Kimberly D, Samimi, Goli, Runowicz, Carolyn D, . . . Siegel, Rebecca L. (2018). Ovarian cancer statistics, 2018. *CA: A Cancer Journal for Clinicians*, 68(4), 284-296.
- [3] Cronin, Kathleen A, Lake, Andrew J, Scott, Susan, Sherman, Recinda L, Noone, Anne-Michelle, Howlander, Nadia, . . . Jemal, Ahmedin. (2018). Annual Report to the Nation on the Status of Cancer, part I: National cancer statistics. *Cancer*, 124(13), 2785-2800.
- [4] Hariri, Lida P, Bonnema, Garret T, Schmidt, Kathy, Winkler, Amy M, Korde, Vrushali, Hatch, Kenneth D, . . . Barton, Jennifer K. (2009). Laparoscopic optical coherence tomography imaging of human ovarian cancer. *Gynecologic Oncology*, 114(2), 188-194.
- [5] Nathaniel D. Kirkpatrick, Molly A. Brewer, & Urs Utzinger. (2007). Endogenous Optical Biomarkers of Ovarian Cancer Evaluated with Multiphoton Microscopy. *Cancer Epidemiology, Biomarkers & Prevention*, 16(10), 2048-2057.
- [6] Wang, Tianheng, Brewer, Molly, & Zhu, Quing. (2015). An overview of optical coherence tomography for ovarian tissue imaging and characterization. *Wiley Interdisciplinary Reviews. Nanomedicine and Nanobiotechnology*, 7(1), 1-16.
- [7] Williams, Rebecca M, Flesken-Nikitin, Andrea, Ellenson, Lora Hedrick, Connolly, Denise C, Hamilton, Thomas C, Nikitin, Alexander Yu, & Zipfel, Warren R. (2010). Strategies for High Resolution Imaging of Epithelial Ovarian Cancer by Laparoscopic Nonlinear Microscopy. *Translational Oncology*, 3(3), 181-194.
- [8] Rentchler, Eric C, Gant, Kristal L, Drapkin, Ronny, Patankar, Manish, & J Campagnola, Paul. (2019). Imaging Collagen Alterations in STICs and High Grade Ovarian Cancers in the Fallopian Tubes by Second Harmonic Generation Microscopy. *Cancers*, 11(11), 1805.
- [9] Tate T, Baggett B, Rice PS, Watson Koevary J, Orsinger, GV, Nymeyer AC, Welge WA, Saboda K, Roe DJ, Hatch KD, Chambers SK, Utzinger U, Barton JK, “Multispectral fluorescence imaging of human ovarian and fallopian tube tissue for early stage cancer detection,” *J. Biomed. Opt.* 21(5), 056005, 2016.
- [10] Sawyer, Travis W, Koevary, Jennifer W, Howard, Caitlin C, Austin, Olivia J, Rice, Photini F. S, Hutchens, Gabrielle V, . . . Barton, Jennifer K. (2020). Fluorescence and Multiphoton Imaging for Tissue Characterization of a Model of Postmenopausal Ovarian Cancer. *Lasers in Surgery and Medicine*, 52(10), 993-1009.
- [11] A. R. Tumlinson, B. Považay, L. P. Hariri, J. B. McNally, A. Unterhuber, B. M. Hermann, H. Sattmann, W. Drexler, and J. K. Barton, “In vivo ultrahigh-resolution optical coherence tomography of mouse colon with an achromatized endoscope,” *J. Biomed. Opt.* 11, 064003 (2006).
- [12] Y. Li, J. Jing, J. Yu, B. Zhang, T. Huo, Q. Yang, and Z. Chen, “Multimodality endoscopic optical coherence tomography and fluorescence imaging technology for visualization of layered architecture and subsurface microvasculature,” *Opt. Lett.* 43, 2074–2077 (2018).
- [13] D. Lorenser, B. C. Quirk, M. Auger, W.-J. Madore, R. W. Kirk, N. Godbout, D. D. Sampson, C. Boudoux, and R. A. McLaughlin, “Dual- modality needle probe for combined fluorescence imaging and three-dimensional optical coherence tomography,” *Opt. Lett.* 38, 266–268 (2013).

- [14] H. Yoo, J. W. Kim, M. Shishkov, E. Namati, T. Morse, R. Shubochkin, J. R. McCarthy, V. Ntziachristos, B. E. Bouma, F. A. Jaffer, and G. J. Tearney, "Intra-arterial catheter for simultaneous microstructural and molecular imaging in vivo," *Nat. Med.* 17, 1680–1684 (2011).
- [15] Vega, David, Sawyer, Travis W, Pham, Nancy Y, & Barton, Jennifer K. (2020). Use of embedded and patterned dichroic surfaces with reflective optical power to enable multiple optical paths in a micro-objective. *Applied Optics* (2004), 59(22), G71-G78.
- [16] Sawyer, Travis W, et al. "Three-Dimensional Texture Analysis of Optical Coherence Tomography Images of Ovarian Tissue." *Physics in Medicine & Biology*, 2019, pp. Physics in Medicine & Biology.
- [17] Sawyer, Travis W, et al. "Quantification of Multiphoton and Fluorescence Images of Reproductive Tissues from a Mouse Ovarian Cancer Model Shows Promise for Early Disease Detection." *Journal of Biomedical Optics*, vol. 24, no. 9, 2019, p. 096010.
- [18] Lee, C. M., Engelbrecht, C. J., Soper, T. D., Helmchen, F., & Seibel, E. J. "Scanning fiber endoscopy with highly flexible, 1-mm catheterscopes for wide-field, full-color imaging," *Journal of Biophotonics*, 3(5-6), 385–407. (2010).
- [19] Kiekens, Kelli C, Talarico, Olivia, & Barton, Jennifer K. (2018). Proximal Design for a Multimodality Endoscope with Multiphoton Microscopy, Optical Coherence Microscopy and Visual Modalities, 10501, 1050119-1050119-14.
- [20] Fujimoto, James G ; Drexler, Wolfgang. (n.d.). *Optical Coherence Tomography* (2nd ed. 2015 ed.). Cham: Springer International Publishing.
- [21] Qin, Yukun, et al. "Watt-Level All-Fiber Optical Parametric Chirped-Pulse Amplifier Working at 1300 Nm." *Optics Letters*, vol. 44, no. 14, 2019, pp. 3422–3425.

B.1.1 Files Storage Location

All the files associated with this publication are stored in the following directories:

/Volumes/Research/Barton/Projects/Grants/Salpingoscope/Journal papers files/2021 Photonics West

Within the folder, the images included in the original manuscript are available in a Keynote file and a PowerPoint pptx file. Both files are named “21-2-12 DVega PW2021” but have different extensions. The laser spectrum data and the dichroic system transmission data used to make the manuscript graphs are stored in the “DataFiles” folder in an excel xlsx file named “PMT_Dichroics&LaserData.”

The raw CSV and configuration files for the reflectance, multiphoton, and OCT files are stored in the “DataFiles/OvarianTissue” folder. The processed images are also within this folder in PNG format. The theoretical transmission and the raw data for the MPM dichroic measurements are also stored in the “DataFiles/MPMSetup” folder. This data is combined in the “PMT_Dichroics&LaserData” file.

Additionally, a video describing how to image in the OCT mode has been included in the “DataFiles/OCT Tabletop imaging video” folder.

B.2 Electronics for Systems with Multiple Photomultiplier Tubes

A light-tight box containing 4 PMTs and their associated amplifiers, as well as all the filters shown in Figure 7 of the previous section was constructed. The box is designed to fit into the salpingoscope instrument rack, and to provide convenience for connecting to the input optical fiber, changing the amplifier gain, and connecting the output signals to the DAQ terminal block. The photomultiplier tubes' (PMT) amplification systems were originally designed with a resistor that limited the PMT gains to about half of their entire range. The limited gain precluded the detection of fainter signals. Therefore, the box was enhanced by modifying the circuit using a 10 k Ω potentiometer and adding a digital voltmeter to monitor the gain for each independent PMT (B077ZQQFC, MakerFocus, USA). The electronics diagram is shown in Figure 1. Each PMT has five wires attached to its internal circuits. One wire is terminated with an SMA connector connected to a transimpedance amplifier (current to voltage amplifier) to amplify the optical signal detected by the PMT. The other four wires are color-coded:

- The red wire connects to a 5.0 V power supply positive port.
- The black wire connects to the power supply negative port.
- The blue wire connects to the positive side of the potentiometer and provides 1.1V positive voltage with respect to the power supply negative port. This voltage is used as gain reference but does not influence the PMT gain.
- The white wire connects to the potentiometer variable resistance and provides meanings to control the PMT gain voltage that ranges from 0 V to the reference 1.1 V provided by the blue wire.

The potentiometer negative side is connected to the negative power supply terminal to close the gain circuit.

The manufacturer recommends ensuring the voltage does not exceed +1.1 V when adjusting the potentiometer. Therefore, all voltages were tested for each PMT once they were all connected to the circuit. The input voltage and the gain voltage of each PMT were tested individually. The power supply maintained the provided voltage at 5.0V. It is recommended not to exceed an input voltage of 5.4 V as it can damage the PMTs. The reference voltage in the blue wires measured 1.052 V on average. The gain voltage in the white wires changed from 0 to 1.051 on average.

The voltage measurements are included in the excel file

“/Volumes/Research/Barton/Projects/Grants/Salpingoscope/Salpingoscope Excel File”

Once the file is open, the “PMT circuit voltages” tab must be selected to display the voltages.

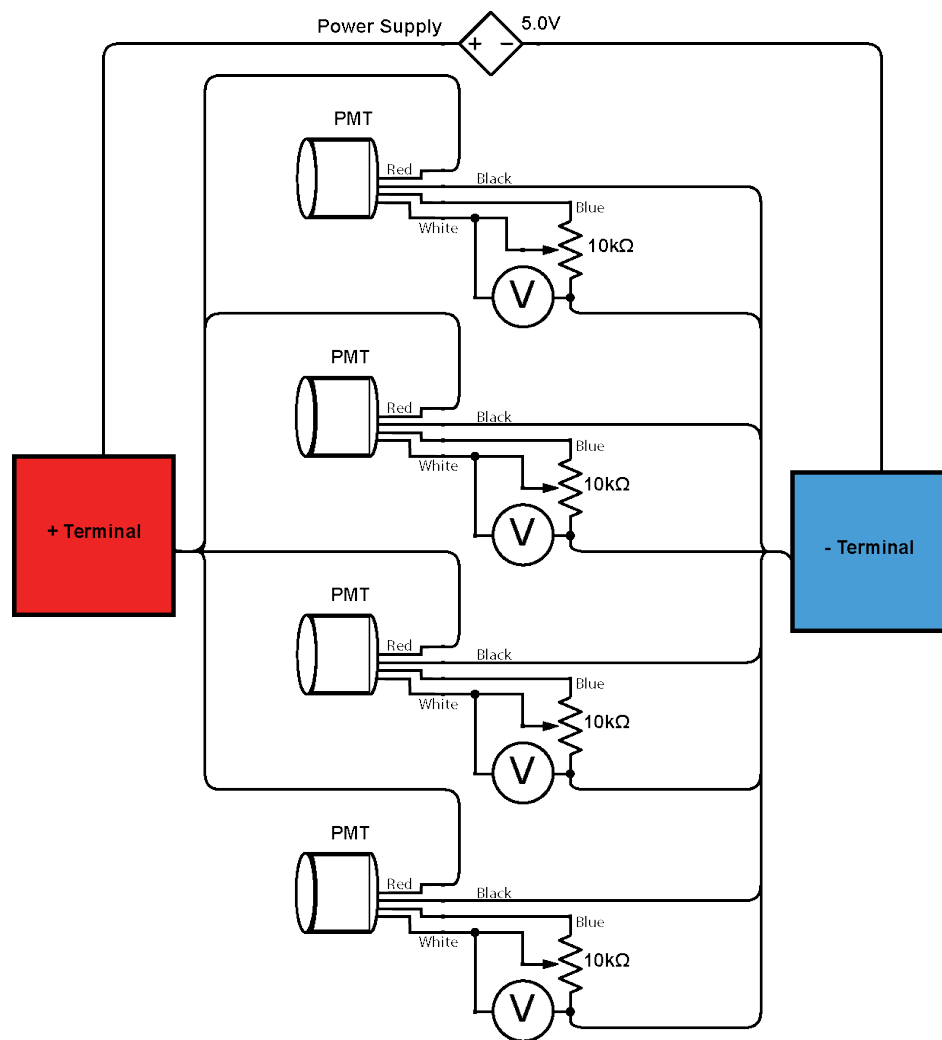


Figure 1. PMT electronic diagram. An additional cable from the PMT that connects to the amplifier is not shown for clarity.

B.3 Standard Operating Procedure B02-021b: Alignment & Assembly Procedure of Optical Components for the Multiphoton Microscope

For this project a tabletop multiphoton microscope was developed to support image testing and future studies. The following standard operating procedure (SOP) was developed according to laboratory protocol and serves as a support for alignment maintenance of the instrument.

Standard Operating Procedures University of Arizona Biomedical Engineering Program

SOP # B02-021	Title: Alignment & Assembly Procedure of Optical Components for the Multiphoton Microscope
Origin Date: 03/30/20 Revision Date: 08/17/20 Rev. 2	Approval: Date Approved:

Equipment:

General Equipment

- Posts: https://www.thorlabs.com/newgrouppage9.cfm?objectgroup_ID=1266



- Post holders: https://www.thorlabs.com/newgrouppage9.cfm?objectgroup_id=4124



- Screws and washers, as needed
- Red laser: FTEC2635-050SF0
- WinCamD-LCM – 1" CMOS Beam Profiler and filters (ND-1, ND-2, and ND-4)
 - <https://www.dataray.com/products/wincamd-lcm-cmos-beam-profiler>



Beam Expander Alignment

- Beam Expander Lens 1: Edmund Optics #62-599-INK (25.4mm Dia. x 25.4mm FL, VIS-NIR, Inked, Plano-Convex Lens)
 - <https://www.edmundoptics.com/p/254mm-dia-x-254mm-fl-vis-nir-inked-plano-convex-lens/17242/>
- Beam Expander Lens 2: Edmund Optics #62-605-INK (25.4mm Dia. x 101.6mm FL, VIS-NIR, Inked, Plano-Convex Lens)
 - <https://www.edmundoptics.com/p/254mm-dia-x-1016mm-fl-vis-nir-inked-plano-convex-lens/17254/>
- SM1L30C Slotted Lens tube, 2 count
 - <https://www.thorlabs.com/thorproduct.cfm?partnumber=SM1L20C>



- SM1L20/SM1L30 solid lens tube, 1 count
 - https://www.thorlabs.com/newgrouppage9.cfm?objectgroup_id=3307



- Thorlabs Imperial 1" TravelMax Stage with Micrometer Drive (LNR25M) with Base Mounting Plate for LNR25 Stage (LNR25P1).
 - https://www.thorlabs.com/newgrouppage9.cfm?objectgroup_id=4551



- 1" clear aperture threaded cage plates, 2 count
 - https://www.thorlabs.com/newgrouppage9.cfm?objectgroup_id=2273



- CB02 cage mount bracket, 2 count.
 - <https://www.thorlabs.com/thorproduct.cfm?partnumber=CP02B>



- Cage rod about 12-18" long. 4 count.
 - https://www.thorlabs.com/newgrouppage9.cfm?objectgroup_id=4124



- Thorlabs VRC4CPT: 30 mm Cage System Alignment Plate with IR Disk, or similar alignment tool
 - <https://www.thorlabs.com/thorproduct.cfm?partnumber=VRC4CPT#ad-image-0>



Laser Collimator Alignment

- Collimator: Thorlabs RC02APC-P01
 - <https://www.thorlabs.com/thorproduct.cfm?partnumber=RC02APC-P01>



- 8" square breadboard, 1 count
 - <https://www.newport.com/c/optical-breadboards>
- Thermal compound: Arctic MX-4
 - https://www.amazon.com/ARCTIC-MX-4-Compound-Micro-particles-Durability/dp/B0795DP124/ref=sr_1_3?keywords=thermal+paste&qid=1583251359&sr=8-3&pldnSite=1
- Galvo kit: GVS002 series (Thorlabs)
 - Galvo 1: TSH232169-X
 - Galvo 2: TSH232170-Y
 - Heatsink: GHS003
 - Galvo holder
 - https://www.thorlabs.com/newgrouppage9.cfm?objectgroup_id=3770



- Newport kinematic mount: Mirror Mount, ULTIMA®, Clear Edge, 0.5 in., (3) 80-TPI Allen-Keys. Model U50-A
 - <https://www.newport.com/p/U50-A>



Galvo Alignment

- Assembled galvo holder from laser collimator alignment

Lens Tube Alignment w/ Galvos

- Newport 340-RC rod clamps, 2 count
 - <https://www.newport.com/p/340-RC>



- 24" long 1.5" wide post, 1 count

Objective Alignment with the Rest of the System

- Ruler, or other rigid measuring instrument.
- Objective: 20X Mitutoyo Plan Apo Infinity Corrected Long WD Objective
 - <https://www.edmundoptics.com/p/20x-mitutoyo-plan-apo-infinity-corrected-long-wd-objective/6625/>



Procedure

This document is intended to provide a detailed explanation of the alignment and assembly procedures for the optical components in the multiphoton microscope.

Overview:

1. Beam Expander Alignment
2. Laser Collimator Alignment
3. Galvo Alignment
4. Lens Tube Alignment with Galvos
5. Objective Alignment with the Rest of the System

Beam Expander Alignment:

1. The first lens in the beam expander, lens 1, will face the laser collimator (Fig. 1). To place the lens as close as possible to the collimator, it will be installed in a 1" cage plate between two retaining rings (Fig. 2). First, install the first retaining ring in the cage plate, ensuring that it is flush with the outside surface of the cage plate. Then, carefully place lens 1 in the cage plate such that its curved edge is making contact with the retaining ring, and the flat edge of the lens is inside the cage plate. The curved edge of lens 1 should jut out from one side of the cage plate (Fig. 2). Install the second retaining ring on the flat side of lens 1. Now, attach a SM1L30C slotted lens tube to the cage plate, near the flat side of lens 1.

Note: After this point, be mindful of lens 1, as it is easy to touch or scratch accidentally.

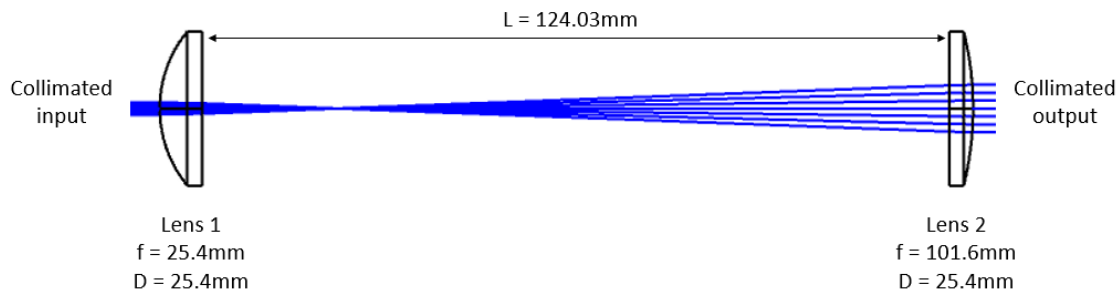


Figure 1: Optical layout of beam expander.

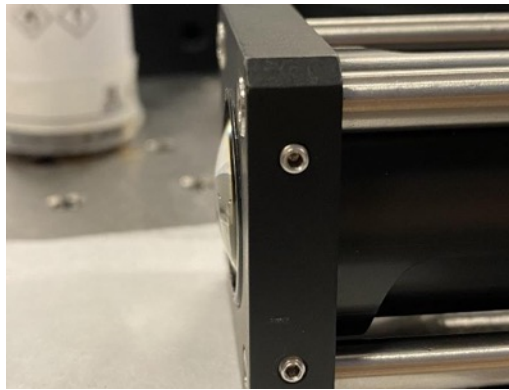


Figure 2: Lens 1 should protrude from the cage plate.

2. Attach another SM1L30C tube to the first tube. Set a caliper to the appropriate tube length: $L = 124.03\text{mm}$, vertex to vertex (Fig. 1). This will be the distance between the plano surface of lens 1 and the first retaining ring for lens 2. After placing the retaining ring at the appropriate location, carefully place lens 2 in the tube, with the flat side making contact with the retaining ring (see figure 1 for appropriate lens orientation). Secure lens 2 with another retaining ring. Attach a 2" solid lens tube (the length may be adjusted later when adding the objective) to the slotted lens tube setup on the right-hand side to add length (Fig. 3). Cover the tube slots using the tube covers to prevent dust/dirt collection in the lenses.

3. Mount the lens tube on a linear translation stage. To do this, first attach the translation stage to the optical table. Then, thread four cage rods through the lens 1 cage plate (Fig.

Note: It may be necessary to attach a few rods together for length. Use as few as possible, since using multiple rods will decrease stability.

4. Screw post holders onto the linear translation stage in the locations where two cage mount brackets will make contact with the lens tube. Then, slide the bottom two cage rods surrounding the lens tube through the brackets. Slide the brackets into the post holders, and secure with the post holder screw (Fig. 3). Attach another cage plate on this side of the lens tube for stability.

Note: It is advisable to ensure that the lens tube is level, as this will help with alignment later.

Note: Use the type of post holder that will only push on the post when you screw it in. This will help with alignment. Try to avoid the usage of the type of post holder that pushes on the post (Fig. 3)

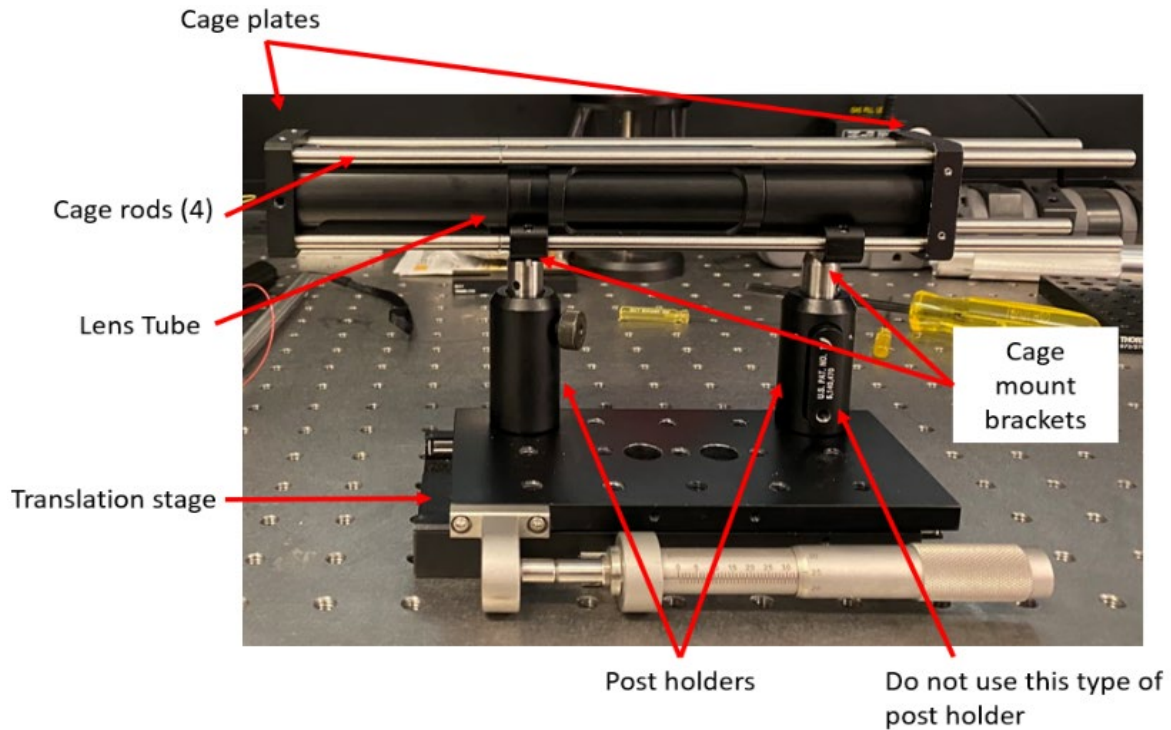


Figure 3: Completed lens tube setup on the linear translation stage.

5. Mount the laser collimator onto a post onto the optical table, facing the lens tube on the linear translation stage at about the same height as the lens tube.
6. Insert a fiber into the laser collimator (ThorLabs RC02APC-P01). The ideal fiber input NA is 0.13. Using a different NA will change the diameter of the beam that is the object for the beam expander. However, the magnification should still be around 4 since it is independent from the laser collimator.

Note: In order to properly insert the fiber, first line up the fiber notch with the notch in the collimator, then screw in. Doing this incorrectly will cause incorrect alignment.

7. Use the linear translation stage, collimator height and tip and tilt adjustments of the collimator mount to center the laser beam on lens 1 and lens 2. Verify using the cage

system alignment plate by placing it on the top cage rods at the back of the cage plate (Fig. 4).

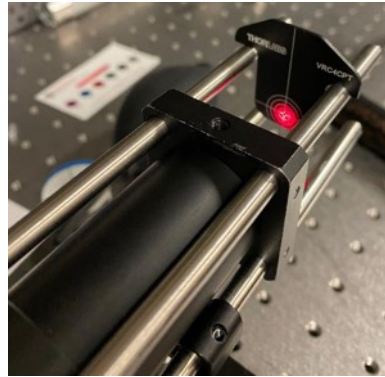


Figure 4: Utilizing the cage system alignment plate to ensure that the laser is centered.

8. Verify the collimation and the magnification of the output beam from the beam expander using the WinCam beam profiler. First, attach 4 post holders at distances along the optical axis up to 1 meter (one at the output of the collimator [A], one near the beam expander output [B], one >1m away [D], and one in between B and D [C]) (Fig. 5). Then, attach a ½” post to the camera and place it in one of the post holders. Plug the WinCamD-LCM -- 1” CMOS Beam Profiler into the computer and launch the DataRay software (it may be necessary to run as administrator).

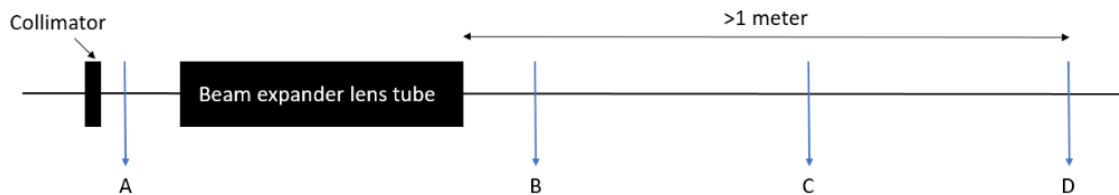


Figure 5: Optical diagram of the collimation test setup. Post holders are placed at locations A, B, C, and D, and will hold the camera.

9. The beam diameter is characterized by the $1/e^2$ Gaussian beam criteria, which is the same as defining the edges of the beam where the intensity is 13.5% of the maximum. To do this in the software, double click on “Clip[a]” and “Clip[b]” on the left side of

the screen, and set the clip levels to 13.5% (do not let the software pick the clip levels automatically) (Fig. 6).

Note: Another option may be to characterize the edges of the beam with full width/half max (FWHM), in which case the clip level can be set to 50%.

Note: If the beam looks very asymmetrical (like in figure 6), ensure that the orientation of the fiber is not affecting the beam shape. If this is an issue, secure the fiber with tape or another adhesive to hold it in one place.

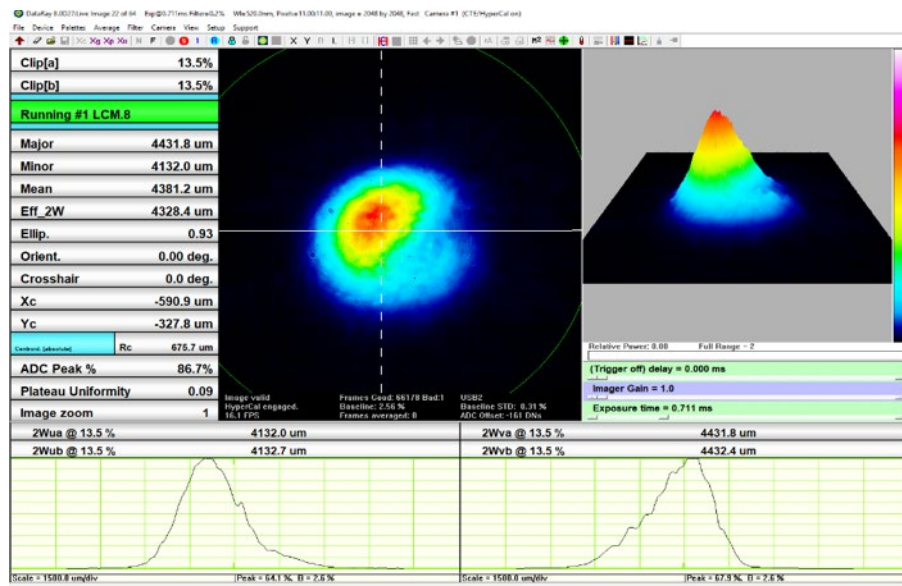


Figure 6: DataRay user interface.

- Measure and record the mean diameter of the beam at the 4 different post locations (A, B, C, and D). It is likely that the beam will be slightly elliptical, giving it different values for the major and minor axis. The mean diameter is a weighted average of the major and minor axes. When measuring the diameter at B, C, and D, lock the exposure time (on the right-hand side of the screen). Using a different exposure time changes the measured diameter of the beam.

Note: The recommended camera filters are ND-4 for the collimator output, and ND-2 for the beam expander output. This may vary depending on the power of the alignment laser.

11. Adjust the location of lens 2 as needed to have a collimated output from the beam expander. The diameter of the beam is allowed to vary within $<1\%$ over 1 meter (This is approximately 50 microns, but will vary based on fiber NA. In this case, a 0.12 NA fiber was used). This tolerance is to ensure proper illumination to the Mitutoyo objective. Lens 2 may need to be adjusted several times.
12. Check that the magnification is about 4 by taking the ratio of the beam diameter before and after the beam expander. Previously, the magnification has been approximately 3.7. One way to check is to compare magnification during the collimation iterations (Step #11) and check for consistency.
13. Do not disassemble the setup of posts and post holders B, C, and D installed on the optical table. These will be useful in the next step.

Laser Collimator Alignment

1. The laser collimator height will depend on the height of the galvos. The galvo holder will need to be attached to a heat sink to help disperse heat produced by the galvos. To assemble the galvo holder and heat sink, first apply a small amount of thermal compound to the part of the galvo holder that will make contact with the heat sink (Fig. 7). Do not apply too much thermal compound, as excess can damage optics. Then, screw the heat sink into the galvo holder (Fig. 7). Carefully remove any excess thermal compound using ethanol or acetone. Be sure to avoid contamination of any other area (especially optics) by the thermal compound.



Figure 7: Attaching the galvo holder to the heat sink.

2. The laser collimator needs to be aligned to the table. Mount the laser collimator on the square breadboard using a post and post holder. Secure the breadboard to the optical table with at least two screws. Adjust the laser collimator height by using the galvos and beam expander as reference (Fig. 8). Alignment targets may be helpful in this step. The height of the collimator in reference to the breadboard will be around 10cm, but can vary.

Note: The collimator should be aligned with the taller hole on the galvo holder.

Do not worry about aligning in x, just make sure the collimator is at an appropriate height.

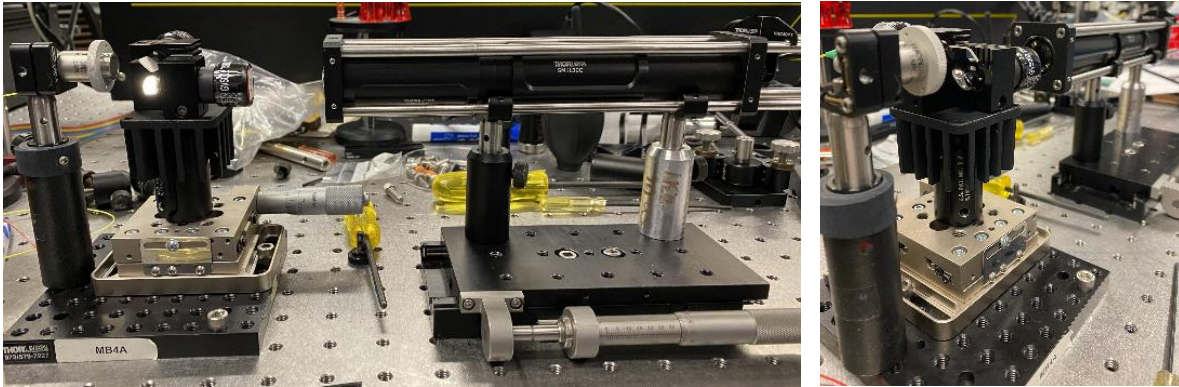


Figure 8: Use the galvo holder and beam expander to coarsely adjust the laser collimator to the correct height.

3. Remove the galvo holder and the beam expander. Set them aside for later.

4. Attach the WinCam to post location B from the previous beam expander alignment step (Fig. 5). To ensure that the camera is not tilted in the x and y direction, create an alignment tool using a cage plate and cage rails (Fig. 9). To do this, attach a cage plate to a post and post holder. Then, add and secure cage rails at the approximate length between the cage plate and the camera. Next, remove this cage plate alignment tool from the optical table and place on a flat surface with the rails facing down (Fig. 10). Using a level, adjust the length of each cage rod until the alignment tool is level.



Figure 9: Setting up the alignment tool that will keep the camera from tilting about the y-axis.

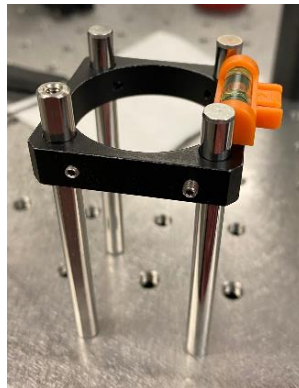


Figure 10: Fine adjustment of the cage plate alignment tool.

5. The cage plate alignment tool will reduce camera tilt about the y-axis. To ensure that the camera is in the same y position for all measurements, mark the cage rod contact locations on tape on the back of the camera (Fig. 11). They can be arbitrary, as long as they are consistent between measurements. Every time the camera is moved to a new location, set the height of the camera by matching up these markings with the cage plate alignment tool.

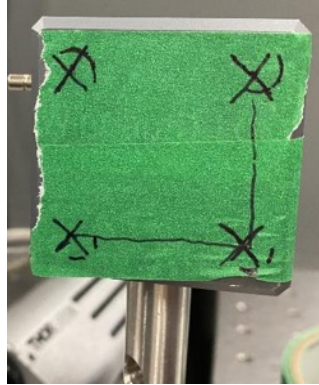


Figure 11: Markings on the back of the camera will designate the appropriate camera height

6. Move the camera to post location B (Fig. 5), then adjust the laser collimator in its post holder to the desired height by adjusting the post length and post screws. Record the position of the spot on the camera (X_c and Y_c on the left side of the interface).
7. Move the camera to post location D ($>1\text{m}$ from the collimator). Use the cage plate alignment tool every time the camera moves from now on. Move the entire tool, including the post holder, to keep its height consistent. Also, check that the cage plate alignment tool is level (Fig. 10) every time it is moved. Sometimes the cage rods can slip and become misaligned.
8. There are 3 screws on the back of the collimator, in the shape of an L. The screws on the ends of the “L” control tip/tilt in x and y independently, while the middle screw moves the beam diagonally. Use these screws to adjust its tip/tilt to bring the spot back to the coordinates on the camera measured in step #3.

9. Move the camera back to post location B and repeat adjusting the post length and post screws to bring the spot back to the proper position. It may be useful to utilize post location C as an intermediate point.

10. Iterate through steps 4-6 until the spot maintains a constant XY position on the camera for all positions of the camera at the three test points. The tolerance for this alignment is 1mrad half-angle. This corresponds to a beam displacement tolerance of 1mm over 1m in any direction, using the tangent of the angle.

Note: The XY position does not need to be equal to the starting position, as long as it is consistent at all post locations within the tolerance.

11. Once the collimator is aligned, make sure it is well secured in its post holder. The collimator will not need to be adjusted again.

Galvo Alignment

1. Remove the fiber from the collimator. Without misaligning the collimator, remove the screws from the optical breadboard, rotate it 90 degrees counterclockwise (so that once the galvos are in place, the beam will propagate along the camera measurement axis from previous steps), and reattach the breadboard with screws. Attach the LNR25M linear translation stage with the LNR25P1 baseplate to the optical breadboard with at least two screws. Make sure that the baseplate adjustment is in the x direction, and the micrometer adjustment is in the y direction (Fig. 12). Verify by eye (or with the camera if there is space) that the collimator is still aligned.

2. Attach the galvo holder to the linear translation stage with a post and post holder, such that the beam will exit the galvo holder in the same direction and along the same axis as the camera testing setup used in previous steps (Fig. 12). Install the galvos.

Note: Be sure to include the paper that sits in between the galvo cylinder and the holder. The paper holds the galvos in place and allows for more rotation control during alignment. Additionally, do not neglect the spacer that goes in between the galvo and the galvo holder. This will ensure that galvo 1 and galvo 2 are at their appropriate (and respective) distances. Galvo 1 and galvo 2 have differently sized spacers.

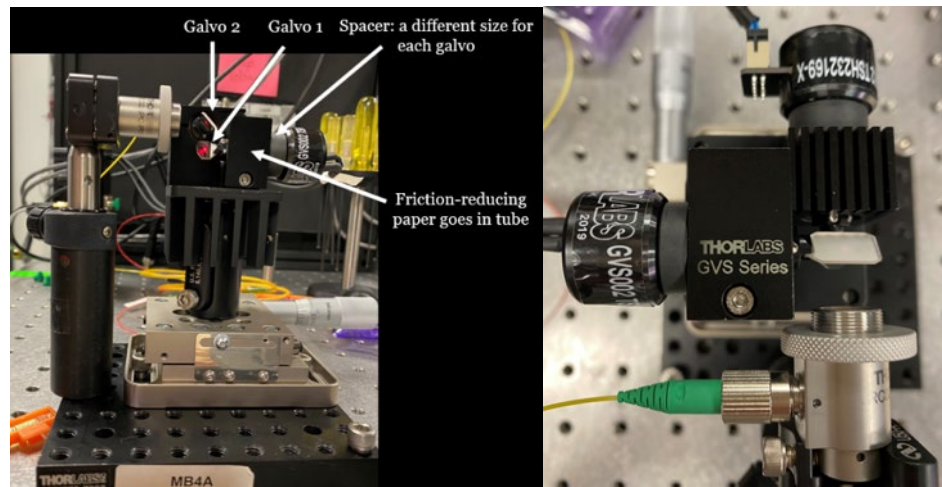


Figure 12: Galvo configuration in the galvo holder

3. Adjust the post height and the z coordinate of the linear translation stage until the laser beam spot on each galvo is centered with the galvo's rotation axis. The beam spot should roughly be in the center of each mirror (Fig. 13).

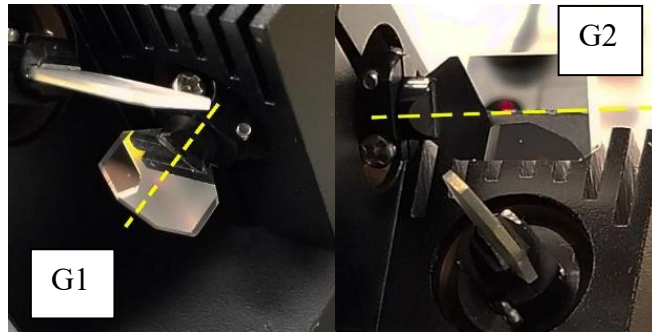


Figure 13: Line up the beam on each galvo's axis of rotation

4. When the beams are centered on both mirrors, secure the galvo holder by tightening the screws holding it in the post holder. Make sure it is secure before proceeding to the next steps.

5. For this step, **be sure to plug each galvo into the correct controller**. Plug the galvos into their controllers and turn on the power supply. This will rotate the mirrors and hold them in their zero position. **The galvos must be powered on for the rest of the microscope alignment.** Without the power supply turned on, the mirrors will slip due to gravity. Galvo 1 (G1) controls the Y scanning of the spot and Galvo 2 (G2) controls the X scanning of the spot.

6. Loosen both screws securing the galvos in place. They should be loosened enough that you can manually rotate them by hand, but tight enough that they do not slip from position when not being actively rotated by hand. It may take some trial and error to find the appropriate looseness.

7. The height difference between the laser collimator and the galvo output beam is ~10mm according to Thorlabs' galvo specifications. To account for this, mark the

back of the camera at a point 10mm above the original markings. Align the camera with the new markings when using the cage plate alignment tool (Fig. 14).

Note: This beam displacement measurement will likely be approximate, and the camera height may need to be adjusted again.

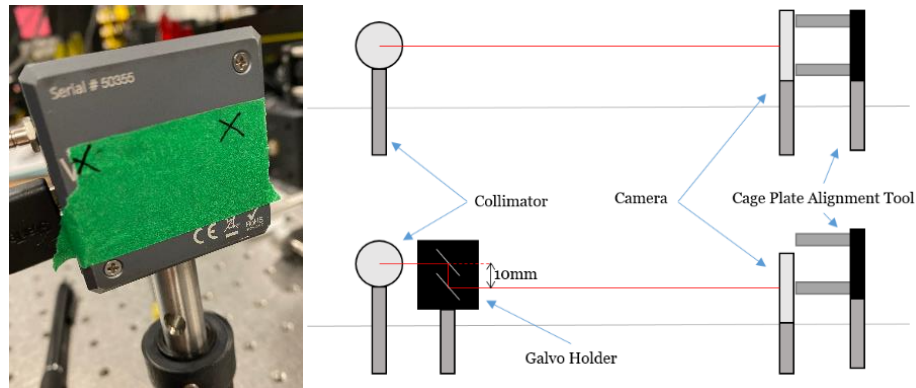


Figure 14: Continue to use the cage plate alignment tool, adjusting the height when necessary.

8. Move the winCam to post location B. Adjust G1 and G2 until the beam coordinates (X_c , Y_c) on the camera approximately match the coordinates from the laser collimator alignment. This is the starting point, the x and y coordinates will likely be different after alignment.
9. Move the alignment target to post location D. Adjust G1 and G2, similarly to the laser collimator, to account for tip and tilt. Iterate until there is less than 1mm displacement over 1m (between post location B and D).
10. Use the socket wrench to tightly secure the galvo in place while holding it in the correct position. If a displacement is noted as a result of tightening the screw, loosen and readjust the galvos to account for this displacement.

11. Adjust the linear translation stage in the x direction. Note the location of the y coordinate on both sides of the edge of the camera field. The change in y coordinate should be within the measured displacement of the y coordinate between post location B and D. For example, if the y coordinate changed by 0.6mm from B to D, the y coordinate should not change more than 0.6mm when the linear translation stage is adjusted from side to side, across the entire camera.
12. Test the alignment in the x and y direction. Moving the galvo setup in x should produce the same displacement in the x direction, and no displacement in the y direction. Start by recording X_c and Y_c with the camera in position D, and the position of the linear translation stage. Then, using the linear translation stage, move the galvo setup in x to one edge of the camera. Measure X_c , Y_c , and the linear translation stage position. (Fig. 15).
 - Displacement in x in the camera plane should match the displacement of the linear translation stage, within the tolerance measured previously. For example, if the x coordinate changed by 0.3mm from B to D, the maximum allowable discrepancy between the camera plane displacement and the linear translation stage displacement is 0.3mm.
 - Displacement in y in the camera plane should not exceed the tolerance measured previously, similarly to the x tolerance. For example, if the y coordinate changed by 0.6mm from B to D, the maximum allowable discrepancy between Y_c at the center and the edge of the camera is 0.6mm.

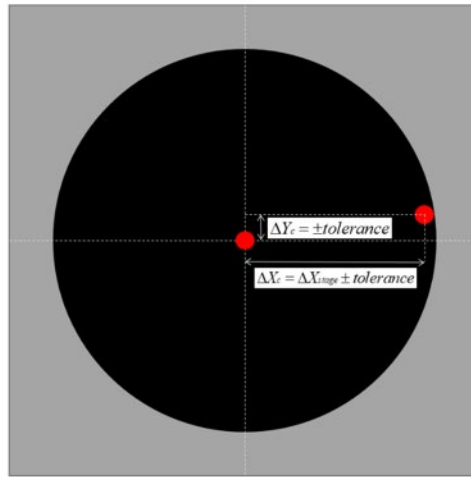


Figure 15: Testing the galvo alignment in the x and y direction by adjusting the position of the linear translation stage.

13. Repeat for the other edge of the camera.

14. Once the galvos are secured, carefully unscrew the square breadboard from the optical table and mount it on a post clamp. Secure the post clamp on the main assembly after adding another clamp below it to hold the cage system containing the beam expander (Fig. 16).

Note: Make sure that the collimator/galvos assembly is mounted at an appropriate height that will allow 120 mm of distance between the microscope objective and the base of the setup when the microscope is fully assembled.

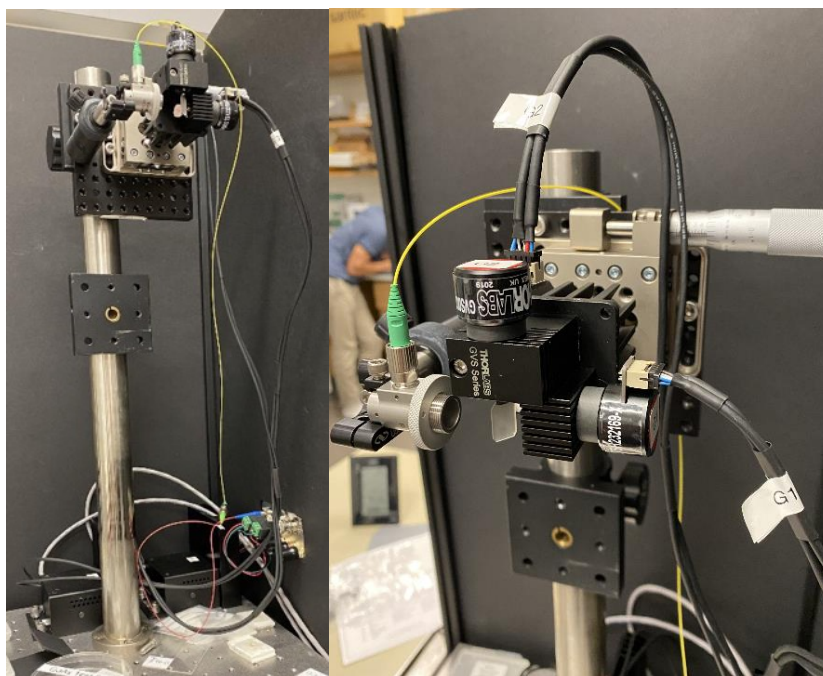


Figure 16: Attaching the front end of the microscope to the post.

Lens Tube Alignment with Galvos

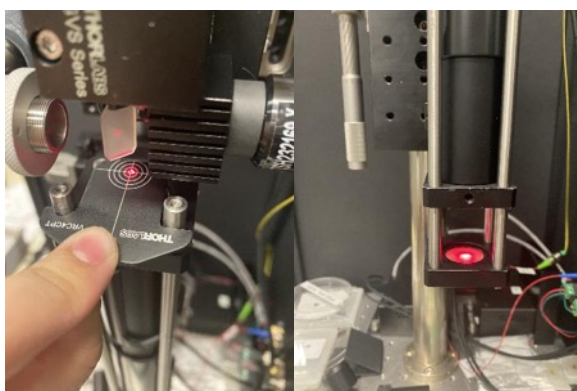


Figure 17: Alignment of the lens tube using the cage system alignment plate and a 1" alignment target.

1. Adjust the cage rods on the lens tube so that the two rods on top protrude past lens 1. This will allow the usage of the cage system alignment plate in between the galvos and the lens tube without touching Lens 1(Fig. 17).

2. Remove the lens tube from the post holders on its linear translation stage. Attach the stage to the 1" post in the same way as the collimator/galvo setup. Once the translation stage is secure, replace the lens tube on its post holders.

Note: When attaching the translation stage to the post clamp, ensure that the screws are very tight. This will keep the stage from moving once it is aligned.

3. Adjust the position of the translation stage (and if necessary, the post clamp) until lens 1 is close to the galvos. Be careful to avoid scratching the lens, and leave some room for the cage system alignment plate (Fig. 17).
4. Mount an 1" alignment target on a 1" cage plate. Slide this alignment target onto the cage system (Fig. 17).
5. With the galvos powered on, use the linear translation stage of the galvo assembly to center the beam on lens 1 (using the cage system alignment plate) and on the 1" alignment target (the lens tube's linear translation stage angle may need to be adjusted for this step). Then adjust the beam position in the perpendicular axis by adjusting the cage system in its post holders to center the beam.
6. Repeat step 5 until the beam is both centered on the cage system alignment plate and on the alignment target at the same time (Fig. 17).

7. When the beam is correctly centered on the alignment target, secure the post holder set screws. Lock both the galvo translation stage and the cage system translation stage.
8. Verify that the system is aligned by moving the translation stage up and down, observing if the beam moves on the optical table below.

Objective Alignment with the Rest of the System

1. For each rotating galvo, there will be a position along the optical axis where the output beam is stationary. This would ideally be the position where the back pupil of the Mitutoyo objective should be placed. Since there are two galvos, the objective will be placed at a midpoint between these two points. The placement of the microscope objective is important for capturing the most light in order to use the full NA of the microscope objective.
2. Remove the solid lens tube from the back end of the lens tube. Once the ideal objective location is determined, a solid lens tube that is closest to the desired length between the beam expander and the objective will be attached.
3. Mount a ruler or similar rigid measurement instrument adjacent to the cage system at which the lens tube and the microscope objective will be mounted on (Fig. 18).

Note: The measurements in this step do not need to be extremely precise-- the limiting factor will be the available lengths of solid lens tube to add onto the beam expander.

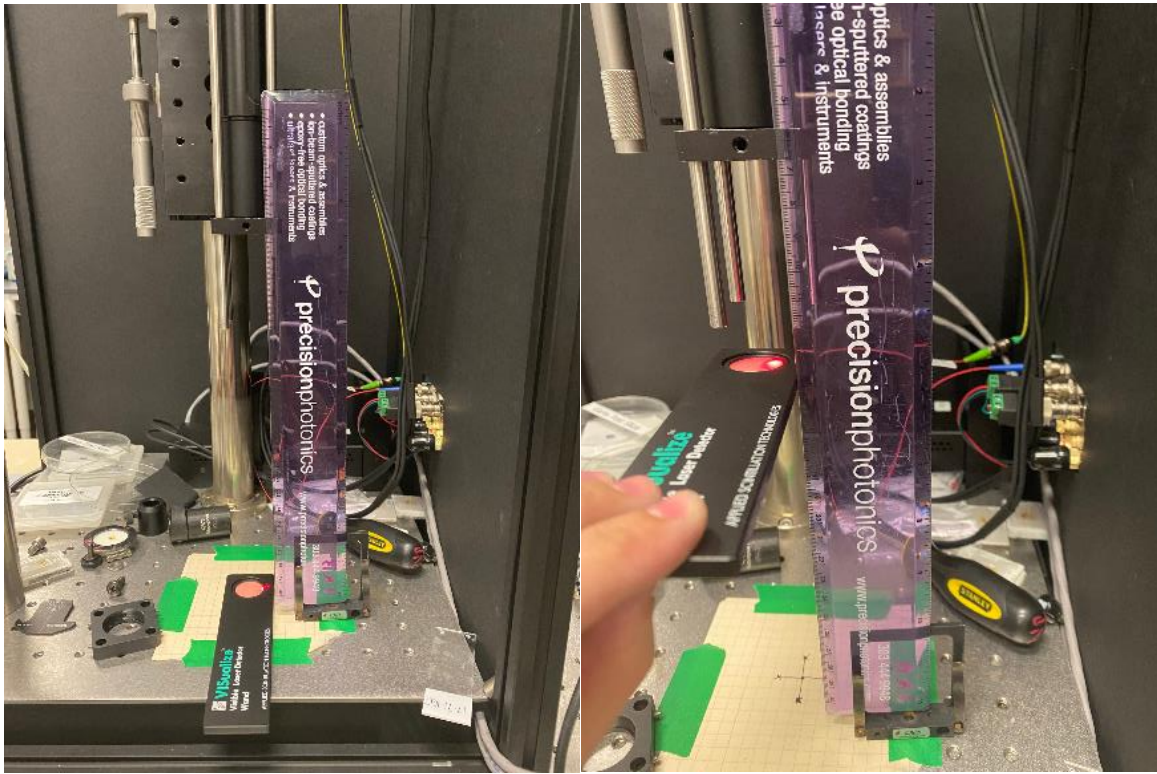


Figure 18: Using alignment tools to determine the ideal objective placement for each galvo.

4. Connect a sine wave function generator to the input of G1. The function generator will provide the command for the galvo to move. Make sure the function generator is not providing more voltage/frequency than the galvos can handle (do not exceed 10V or 350Hz at any time during this process). There are two options for finding the ideal objective placement for each galvo:
 - Observing motion: set the function generator output to a sine wave with a frequency of $\sim 5\text{Hz}$ and a voltage of $\sim 2\text{-}5\text{V}$. The ideal objective placement is the location on the optical axis where no motion of the beam is observed after the lens tube.
 - Observing shape: set the function generator output to a sine wave with a frequency of $\sim 50\text{Hz}$ and a voltage of $\sim 2\text{-}5\text{V}$. A line where the galvo is scanning

can be observed. The ideal objective placement is the location on the optical axis where the line converges to a circle.

5. At the ideal objective placement for G1, secure the target in place and record the position of the cage plate.
6. Repeat steps 3-4 for galvo 2.
7. The midpoint between the positions recorded in steps 4 and 5 will be the position where the objective lens should be mounted.
8. Measure the distance between the lens tube and the position where the objective lens will be mounted. Determine the appropriate length of solid lens tubing that will be needed to cover this distance. Screw the solid tube to the end of the lens tube system.
9. Remove the cage plate containing the alignment target. Mount the objective lens onto a 1" threaded cage plate, then place the cage plate containing the objective at the correct position in the cage system and secure it. At this point all optical components of the system should be assembled and aligned (Fig. 19).

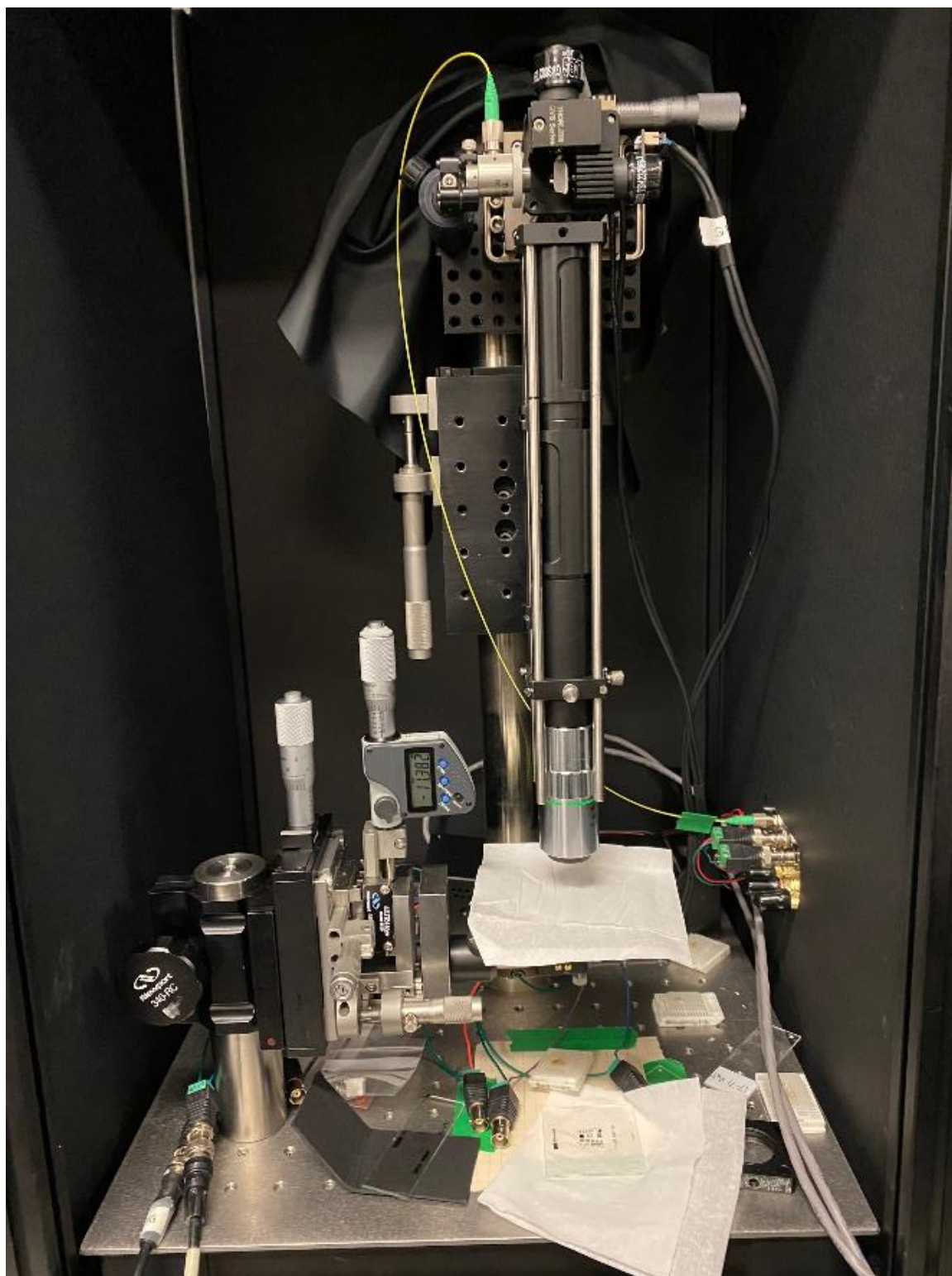


Figure 19: Fully assembled tabletop microscope

B.4 Standard Operating Procedure B02-022: Salpingoscope Spectrometer Alignment

The following standard operating procedure (SOP) was developed according to laboratory protocol and serves as a support for alignment maintenance of the OCT spectrometer.

Standard Operating Procedures

University of Arizona Biomedical Engineering Program

SOP # B02-022	Title: Salpingoscope Spectrometer Alignment
Origin Date: 02/21/20 Revision Date:	Approval: Date Approved:

Supplies:

- Kim Wipes
- Black electrical tape folded in half so neither side is sticky

Equipment:

- SLD laser source
- SMF-28 fiber patch cable
- Thorlabs RC12APC-P01 - Protected Silver Reflective Collimator (off-axis parabolic mirror in tube mount)
- 1" retaining ring
- Thorlabs GR25-0613 - Ruled Reflective Diffraction Grating
- Tip/tilt mount for square optics
- Thorlabs AC254-300-C-ML lens (achromatic doublet)

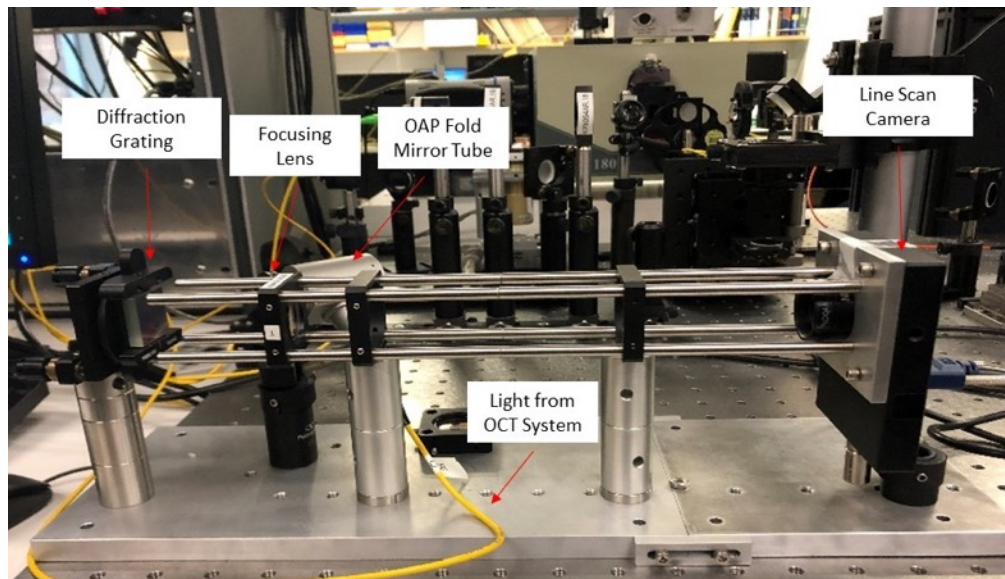
- Cage system mounting equipment
- Optical mounting posts
- Line scan camera mount
- Sensors Unlimited GL2048L InGaAs Linescan Camera by UTC Aerospace Systems (now Collins Aerospace)

Procedure:

In this procedure the salpingoscope spectrometer is assembled, aligned, and fringes from a spectral domain OCT system are acquired.

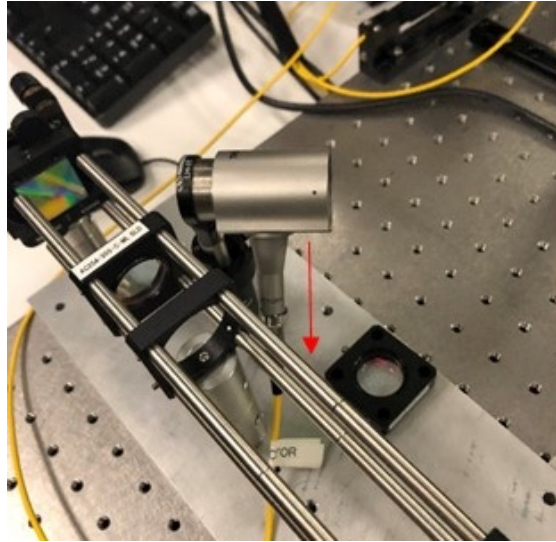
Assemble and Align Spectrometer:

1. The photo below shows a layout of the spectrometer.

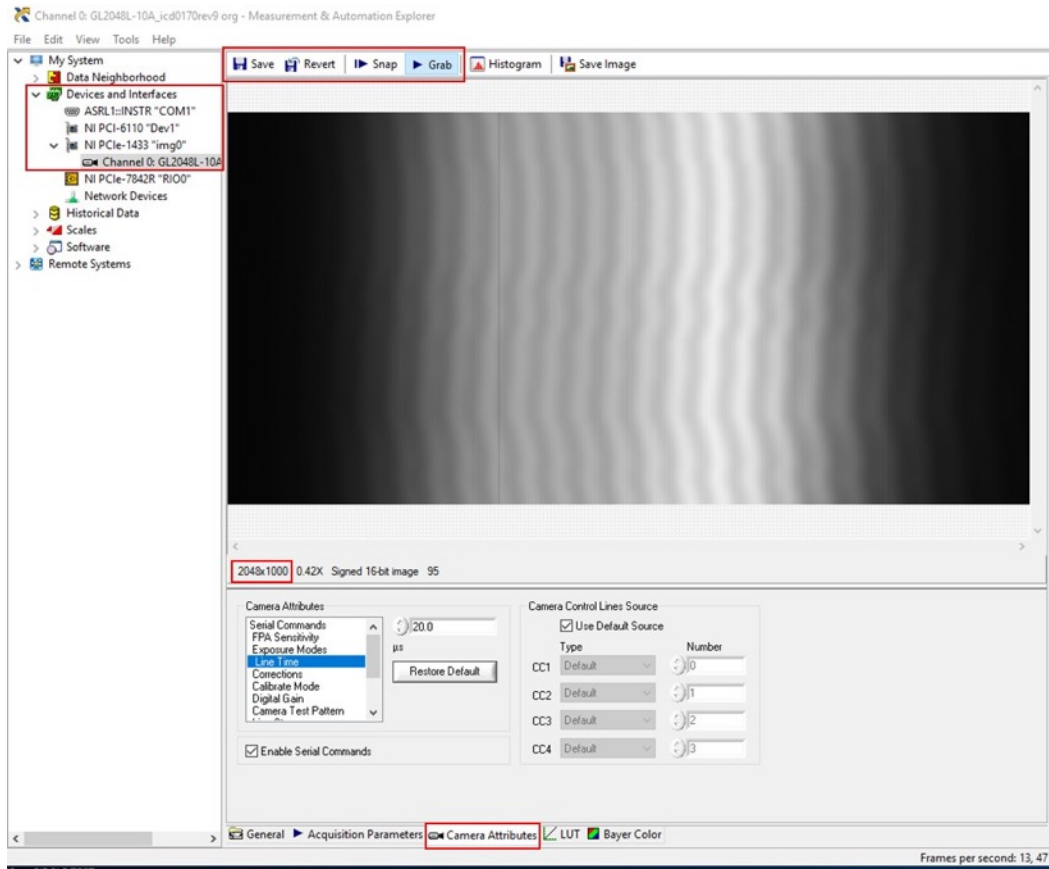


2. Connect the camera to the computer with the SDR-MDR cable going into the Camera Link Port 0 in the NI PCIe-1433 National Instruments acquisition board, and connect its power cord.

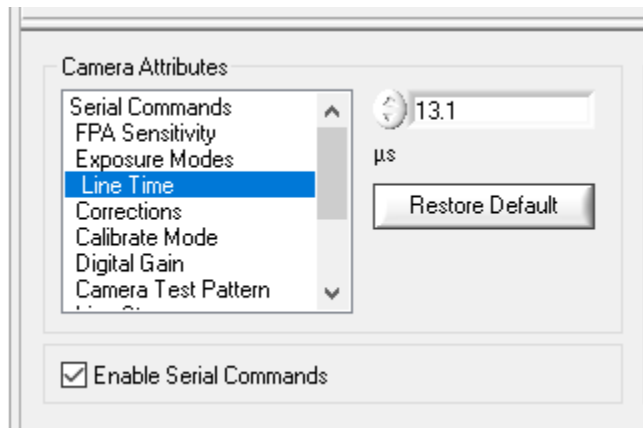
3. Connect the superluminescent diode (SLD) directly into the spectrometer via the tube mount. The tube mount tail should be facing downward so there is enough room for the spectrometer and fiber on the salpingoscope spectrometer shelf. Screw a 1" retaining ring into the threaded part of the tube mount to act as a stop to keep the tail in this orientation. Point the collimated beam towards the center of the diffraction grating.



4. Open the National Instruments software, "NI MAX." On the left side of the screen, in the "Devices and Interfaces" drop down menu expand "NI PCIe-1433" and double-click on "Channel 0." Use the Grab, Snap, and Histogram buttons to view what the camera is capturing. Right-click on the image, select "Viewer Tools" and then "Zoom to Fit" to get a full field of view of the camera.



5. In “Camera Attributes” make sure to select “Line Time.” In order to not saturate the camera, make sure the camera is running at a line time between 13.1 and 20 μs to avoid saturation. “Digital Gain” should be set to 1.0.



6. Use an IR viewing card to track the light, specifically the various diffraction modes, through the spectrometer system.

7. Make sure the light hitting the detector is coming from the 0th order diffraction mode since 90% of the light is concentrated in this mode.

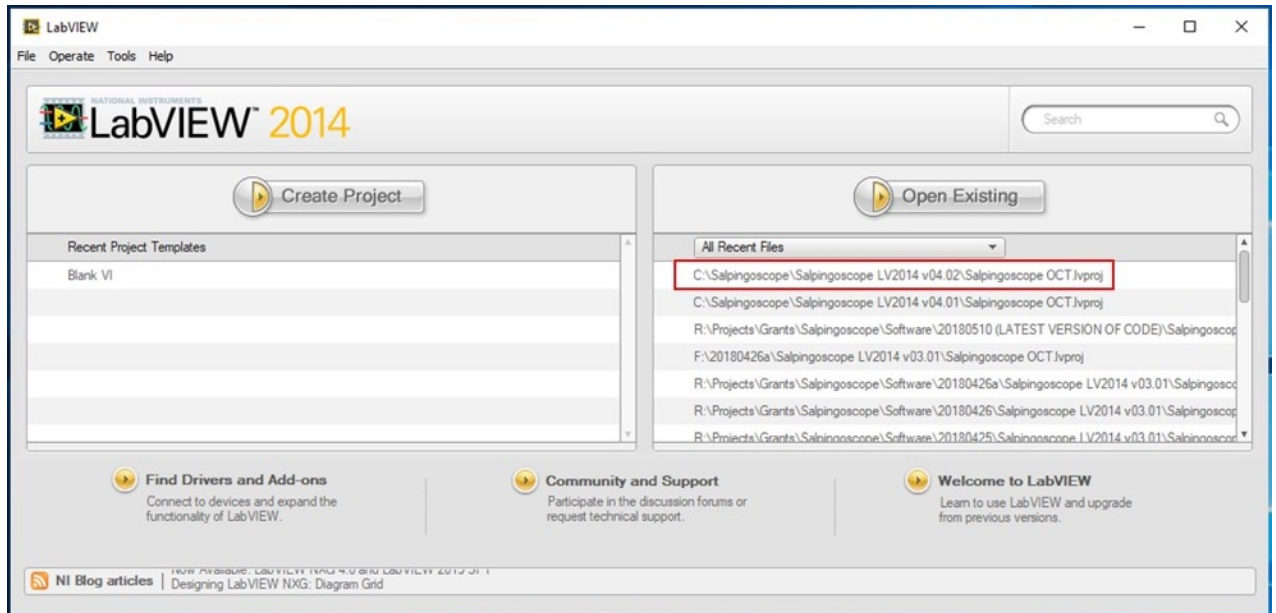


8. Rotate the diffraction grating tip/tilt mount on its post in order to get the 0th order mode generally hitting the detector. Use the fine tip/tilt adjustment knobs to make sure the light is coming through the spectrometer in a straight line. If alignment is acceptable, the camera software should show the following pattern.

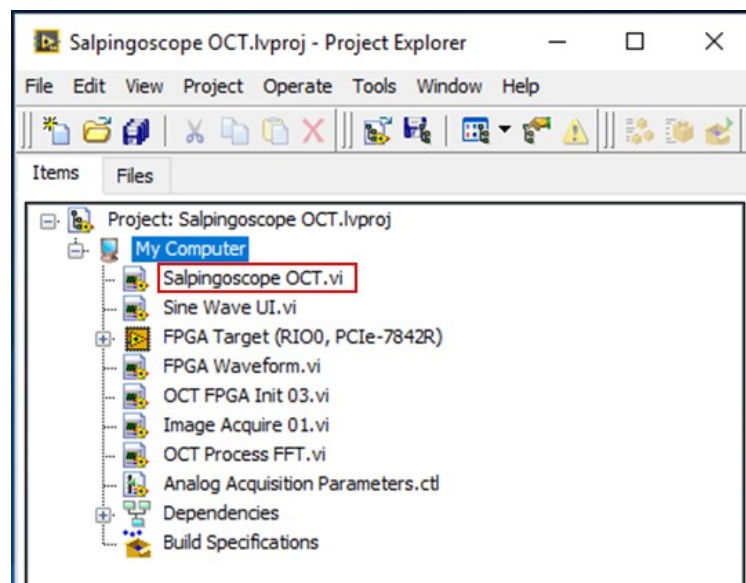


Obtaining Fringes:

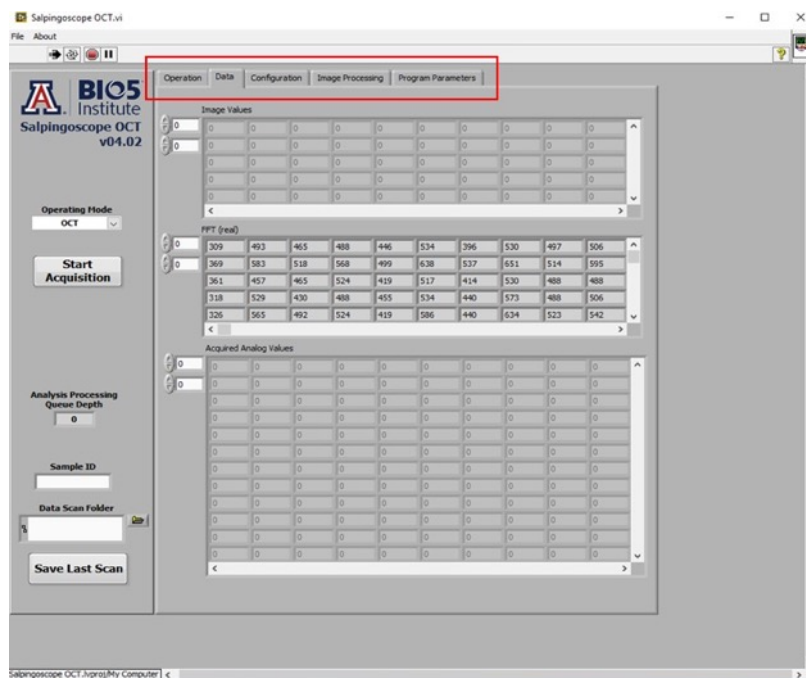
1. Connect the spectrometer to an aligned spectral domain OCT system with the same SLD.
2. Open Salpingoscope LabVIEW software by opening National Instruments LabVIEW 2014. Double-click on the 4.02 version of the Salpingoscope software.



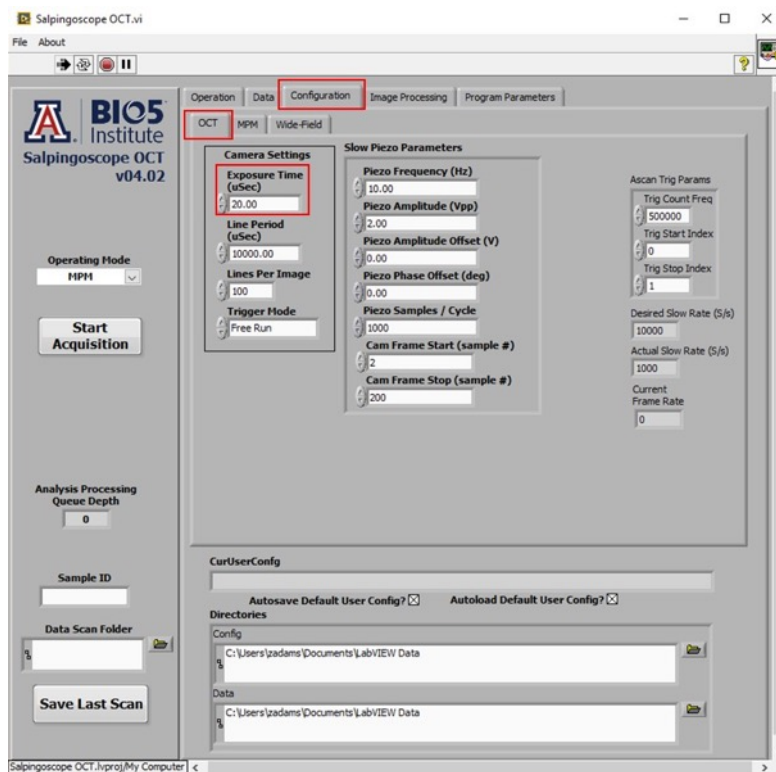
3. This window will open, double-click on “Salpingoscope OCT.vi.” The other open windows may be closed.



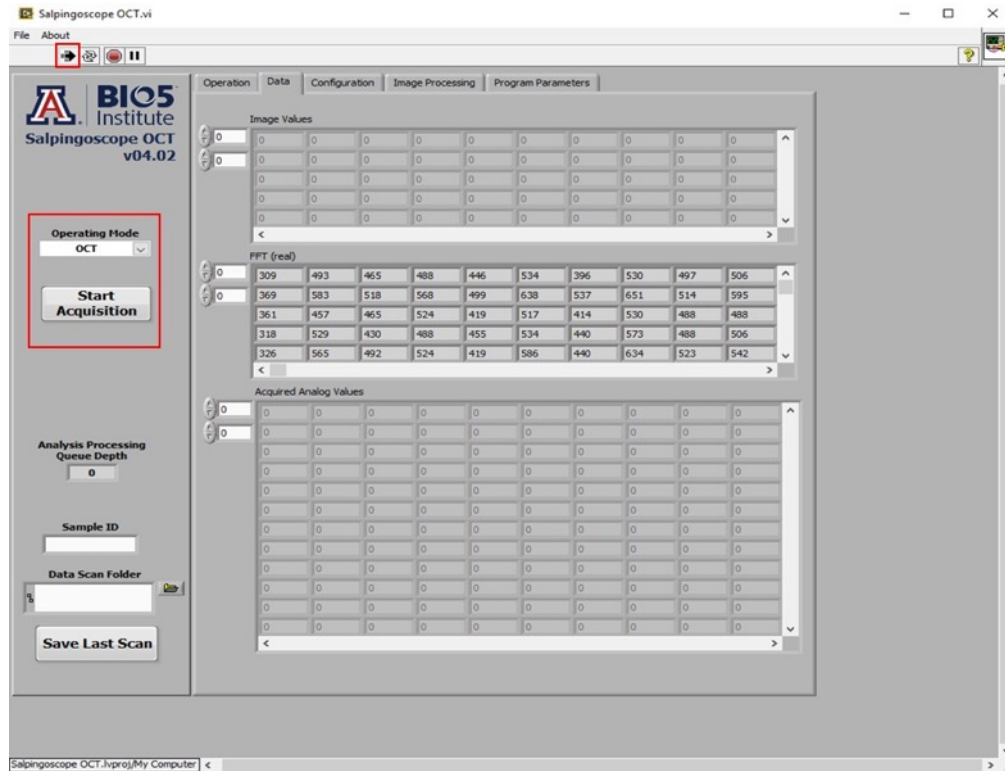
4. This is the home screen of the Salpingoscope LabVIEW software. The “Data” tab shows the intensity values of the A-scans. At this point the array should be empty.



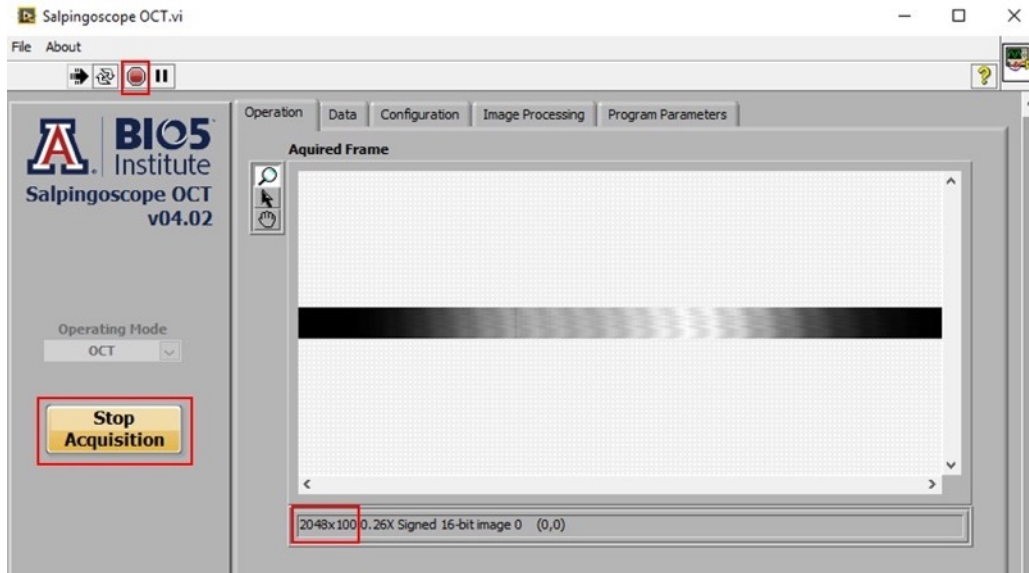
5. If any changes are made in the “Configuration” tab, do not save them, just document the changes made to produce results (ie exposure time).



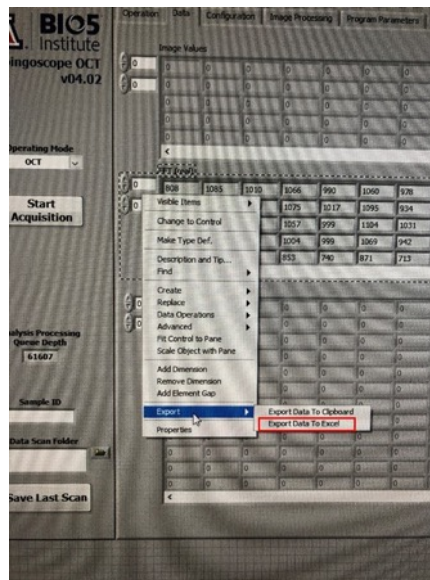
6. To start taking an A-scan, click the arrow in the upper left-hand part of the screen, make sure the operating mode is set to “OCT”, and then click “Start Acquisition.”



7. To stop taking an A-scan select “Stop Acquisition” then click the red stop button in the left hand corner of the screen. This photo also shows how the fringes from the A-scan can be viewed in the “Operation” tab. **NOTE:** Fringes can be seen far more clearly with the NI MAX software. The LabVIEW image is 2048x100 while the NI MAX image is 2048x1000. The LabVIEW software and NI MAX software cannot run at the same time because they will both attempt to connect to the camera. Make sure to close out of NI MAX while running LabVIEW. LabVIEW does not need to be completely closed when running NI MAX, but it must be stopped.



8. Right-click between the two zeros next to the FFT box. In the drop down export the A-scan values to Excel and use Excel to save them as a CSV file so they can be used in ImageJ and/or MATLAB.



9. Cover the camera sensor with black electrical tape or a Kim Wipe to protect it from dust.
10. In order to see fringes on the NI MAX or LabVIEW software, the optical path lengths (OPL) between the sample and reference arm in the OCT system need to be matched. This is the same concept as matching the OPLs of a test and reference beam on a Michelson Interferometer to get fringes on a detector.

APPENDIX C: Triple modality co-registered endoscope.

This appendix includes all supplemental material for the integration of the salpingoscope optical system with the proximal tower, including a manuscript for future submission as a journal paper, seven standard operating procedures (SOPs) that instruct how to assemble the salpingoscope optical system and handle, how to sterilize the instrument, and how to calibrate the spectrometer to be used with the salpingoscope or any other instrument such as the tabletop microscope.

C.1 Manuscript: Triple-modality co-registered endoscope featuring wide-field reflectance imaging, and high-resolution multiphoton and optical coherence microscopy.

The following manuscript is written following OSA guidelines for future submission as a journal paper.

Triple-modality co-registered endoscope featuring wide-field reflectance imaging, and high-resolution multiphoton and optical coherence microscopy

David Vega¹, Dominique Galvez¹, Gabriella Romano², Nancy Y. Pham², John Heusinkveld³, Ricky Cordova², Makenna Aitken², Sartanee Suebka¹, and Jennifer K. Barton^{1,2}.

¹The University of Arizona, The James C Wyant College of Optical Sciences, The University of Arizona, Tucson, AZ, USA, 85721

²University of Arizona, Biomedical Engineering, The University of Arizona, Tucson, AZ, USA, 85721

³University of Arizona, Department of Obstetrics and Gynecology, College of Medicine, The University of Arizona, Tucson, AZ, USA, 85721

Abstract

We present the design and feasibility testing of a multimodal co-registered endoscope based on a dual-path optical system integrated with a scanning piezo. This endoscope incorporates three different imaging modalities. A large field of view reflectance imaging system enables visualization of objects several millimeters in front of the endoscope, while optical coherence microscopy and multiphoton microscopy are employed in contact with tissue to further analyze suspicious areas. The optical system allows multiple different imaging modalities by employing a dual optical path. One path features a low numerical aperture and wide field of view to allow reflectance imaging of distant objects. The other path features a high numerical aperture and short working distance to allow microscopy techniques such as optical coherence microscopy and multiphoton microscopy. Images of test targets were obtained with each imaging modality to verify and characterize the imaging capabilities of the endoscope. The reflectance modality was demonstrated with a 561 nm laser to allow high contrast with blood vessels. It achieved a lateral resolution of 24.8 μm at 5 mm and a working distance from 5 mm to 30 mm. Optical coherence microscopy (OCM) was performed with a 1300 nm super-luminescent diode since this wavelength experiences low relative scattering to allow for deeper tissue imaging. Measured OCM lateral and axial resolution was 4.0 μm and 14.2 μm , respectively. Multiphoton

microscopy (MPM) was performed with a custom 1400 nm femtosecond fiber laser, a wavelength suitable for exciting multiple exogenous and some endogenous fluorophores, as well as providing information on tissue composition through harmonic generation processes. A 4.0 μm MPM lateral resolution was measured.

1. Introduction

It is estimated that cancer affects about 450 per 100,000 people in the United States alone¹. Cancer detection at early stages is critical to a patient's outcome since cancer is localized and is most responsive to treatment at the early stages. Unfortunately, detecting localized early-stage cancer is difficult due to the lack of symptoms and the microscopic size of early neoplastic lesions. Making a definitive diagnosis with histology requires a destructive surgical biopsy that can miss the affected tissue area. Therefore, a faster and less invasive detection method that can survey more tissue is desired to make the process efficient and accurate. Optical imaging has been proven to detect several types of early cancer effectively. Furthermore, multimodal optical imaging may provide improved classification accuracy². Research teams, including ours, have been developing novel endoscopes that feature dual-modality imaging to reach internal organs³⁻⁶. A multimodal endoscope might detect cancer and reduce unnecessary biopsies.

Optical imaging methods

Optical imaging techniques including reflectance and fluorescence imaging, confocal microscopy, multiphoton microscopy (MPM), and optical coherence tomography (OCT) have proven to be sensitive and specific methods of detection for different cancers⁷⁻¹⁸. A wide-field imaging technique, such as reflectance or fluorescence imaging, can first be used to identify suspicious areas of tissue that may contain cancer. These areas can then be further investigated

using a high-resolution technique such as MPM, OCT, or optical coherence microscopy (OCM). Our endoscope combines the three modalities: wide-field narrow-band reflectance imaging, MPM, and OCM.

Reflectance imaging obtains contrast from tissue scatterers and absorbers, particularly hemoglobin. Narrow-band illumination in the blue or green wavelength region enables the identification of regions with increased vascularity, a hallmark of cancer¹⁹. OCM provides depth-resolved, micron-scale resolution images of tissue microstructure using reflected near-infrared (NIR) light. OCM uses a high numerical aperture (NA) objective to achieve high lateral resolution while sacrificing the extended depth of focus typically achieved with OCT.

Two multiphoton processes of interest in MPM are two-photon excited fluorescence (2PEF) and second harmonic generation (SHG). 2PEF occurs when multiple photons are absorbed nearly simultaneously by a molecule. This molecule then emits a single photon at a wavelength shorter than the incident light yet longer than half the incident wavelength. Fluorescent molecules, including some with excitation or emission in the near infrared such as lipopigments and porphyrins, are known to be altered in cancerous tissue. SHG is generated by non-centrosymmetric molecules, such as collagen, which emit light at exactly half the excitation light wavelength. Therefore, combining reflectance, OCM, and MPM in an endoscope may provide a highly sensitive and specific tool for the *in-vivo* detection of cancer in its early stages. As such, it could serve as a minimally invasive alternative to surgical biopsy and histology. Additionally, the co-registered imaging of known features of cancerous tissue, such as increased vascularity, modified tissue and cellular microstructure, altered collagen structure, and changes in

biomolecule concentration, can potentially provide additional information about the health of the tissue, further increasing the sensitivity and specificity over a single-modality system.

Goals of this study

With the intent of providing a tool to detect abnormal cells and tissue indicative of early-stage cancer, we designed a rigid endoscope that can perform co-registered visible light reflectance imaging for navigation, and OCM and MPM for detailed tissue interrogation. For operational functionality, two additional channels are included in the endoscope, one for irrigation and another for biopsy forceps or other small-diameter tool use. This triple-modality endoscope is small enough for minimally invasive imaging a could be used as an optical screening method for various cancers in the future. For example, it can be utilized as a transvaginal salpingoscope to screen women at high risk for ovarian cancer. It could also be used during surgical laparoscopy to locate cancer margins or metastases. The endoscope is designed so that the narrow-band, wide-field navigation modality can be used to safely insert the device and navigate into the peritoneal cavity and identify suspicious areas. Once a suspicious area is identified, the front face of the endoscope can be placed in contact with the tissue to perform high-resolution imaging with OCM or MPM.

2. Requirements

Functional and physical requirements

In cooperation with our physician collaborators, a set of functional and physical requirements was derived for the endoscope. These requirements are summarized in Table 3. The endoscope requires a forward-viewing reflected-light modality with a wide field of view (FOV) to enable

insertion, navigation to the tissue of interest, and rapid identification of abnormalities. Tissue suspected to be abnormal would then be imaged at high resolution with OCM and MPM to confirm findings. Ideally, the navigation and high-resolution modalities should be co-registered. Additional requirements for clinical utility include an irrigation channel that can either deliver saline for cleaning the optics at the distal tip of the endoscope or deliver exogenous contrast agents for improved labeling of pathological tissue. Additionally, an accessory channel for biopsy tools enables the collection of a small tissue sample for conventional methods of diagnosis.

The ability to reach organs of interest, such as the ovary, dictates the physical requirements for both the insertable distal section and the non-insertable proximal section (handle). For the insertable portion, we established basic requirements for rigidity, diameter, length, biocompatibility, and sterilizability. We chose to make the distal section completely rigid for familiarity and allow the physician to have an explicit reference for the endoscope's location. Therapeutic endoscopes with diameters as large as 7 mm are often utilized. However, for diagnostic purposes, diameters of less than 4 mm are preferred to minimize tissue trauma. This diameter is large enough to encapsulate the optics and the irrigation and biopsy accessory channels. The length of the insertable section should be large enough for the tip to reach the tissues of interest in a variety of patient anatomies. It was estimated that an insertable length of approximately 25 cm would be sufficient for imaging of ovaries and fallopian tubes. All exposed components must be made from biocompatible materials and be sterilizable without losing performance.

Table 3. Requirements for the endoscope.

Functional requirements	
Requirement	Specification
Navigation / Reflectance imaging	Wide-field low-resolution
OCM imaging	High lateral and axial resolution
MPM imaging	High lateral resolution
Irrigation port	>0.5 mm diameter
Accessory channel	>1.2 mm diameter
Rigidity (hypotube)	Completely rigid
Endoscope outer diameter	$\leq 4\text{mm}$
Insertable length	$\geq 25\text{ cm}$
Sterilizability	Hydrogen peroxide

Optical requirements

Clinically relevant requirements for FOV, working distance, resolution, imaging speed, illumination wavelength, and power were established for all of the optical modalities. A summary of the optical requirements is presented in Table 4.

Reflected light modality (navigation) optical requirements

The FOV for the navigation modality should be sufficient to identify the target tissue and avoid damage to adjacent tissues, ideally 60° full FOV, with 25° considered adequate. Working distance should be at least 5-20 mm, with a lateral resolution of better than $50\text{ }\mu\text{m}$ at 5 mm distance at the center of the field. These requirements allow adequate navigation to identify focal areas of disease that are abnormal clusters of 10 or more cells²⁰. Video-rate (i.e., 30 images/second) imaging speed is required to reduce motion artifacts. The illumination source should provide high contrast for navigation purposes. For monochrome imaging, blue to green wavelengths are preferred to enhance blood contrast. Laser safety standards should comply as per ANSI Z136.1 standard.

Table 4. Summary of optical requirements. Irradiance values were calculated following the ANSI Z136.1 standard.

Optical requirements	
Requirement	Specification
Forward viewing reflectance	
FOV	25 to 60 Degrees
Working Distance	5-20 mm
Resolution	50 μm @ 5 mm WD
Imaging speed	> 30 fps
Illumination wavelength	400-700 nm
Optical coherence microscopy	
FOV	$\geq 100 \mu\text{m}$
Focal Distance	50 μm
Lateral resolution	$\leq 2 \mu\text{m}$
Axial resolution	$\leq 10 \mu\text{m}$
Imaging speed	> 30 fps
Illumination wavelength	1300 nm
Multiphoton microscopy	
FOV	>100 μm
Working Distance	50 μm
Lateral resolution	$\leq 2 \mu\text{m}$
Imaging speed	> 30 fps
Illumination wavelength	$\geq 1200 \text{ nm}$ and $\leq 1500 \text{ nm}$

High-resolution modalities optical requirements

The FOV of the high-resolution modalities should be sufficient to image a representative amount of tissue (e.g., at least ten cell diameters or about 100 μm). The high-resolution mode is utilized when the endoscope is near or in contact with the tissue. A focal distance of $\sim 50 \mu\text{m}$ enables visualization of simple epithelia and acceptable tissue attenuation. Cellular resolution (lateral $\leq 2 \mu\text{m}$, and axial $\leq 10 \mu\text{m}$) is necessary to identify pathology. Although having the endoscope in contact with tissue mitigates motion artifact, rapid imaging, ideally at video rate, is still desired. For OCM and MPM imaging modalities, illumination wavelengths in the NIR range are

preferred due to relatively low attenuation and significant penetration for tissue imaging. An OCT source with a 1300 nm center wavelength is ideal for tissue penetration and availability of photonic components. A bandwidth of at least 70 nm is desired to achieve 10 μm axial resolution. A variety of wavelengths of MPM lasers are useful, with wavelengths between 1200 nm and 1500 nm providing advantages of low tissue attenuation as well as ability to excite near-infrared endogenous fluorophores or exogenous dyes. The MPM source must also provide short pulses with durations in the 100-200 fs range to achieve high excitation efficiency but minimize non-linear processes in fiber while maintaining a high repetition rate for rapid image acquisition and should comply with the ANSI Z136.1 standard.

Data acquisition requirements

MPM and OCM are techniques in which the image is reconstructed by scanning the FOV point by point or column by column, respectively. Navigation imaging could be performed with either point-by-point reconstruction or a two-dimensional snapshot. However, the former technique was chosen to maintain compatibility with MPM and OCM. As such, a distal two-dimensional scanning system is necessary. Given the need for fiber deliver of light through the endoscope, we have chosen to use a quartered piezo scanning system with cantilevered fiber, described in detail later.

A sufficiently fast detector and data acquisition method must be implemented to meet imaging sampling and speed requirements. Video-rate of 100x100 pixels images in reflectance and MPM modalities requires a sensor with a bandwidth of 1MHz or greater. Variable gain is useful to account for differing signal strengths. Photomultiplier tubes (PMT) and associated amplifiers used for detecting MPM signals must be highly sensitive in the red to NIR wavelengths and have

gain-bandwidth products sufficient for handling weak high-speed signals. Preferably, both MPM signals should be detected and digitized synchronously to ensure co-registered imaging. Since we implemented spectral domain configuration for OCM, the associated line scan camera must be capable of readout speeds in the kHz.

Table 5. Summary of acquisition requirements

Data acquisition requirements	
Requirement	Specification
Forward-viewing reflectance	
Reflectance sensor bandwidth	≥ 1 MHz
Spectral response wavelengths	400-700 nm
Reflectance sensor gain	Variable
Data acquisition board sampling rate	≥ 2 MHz
Optical coherence microscopy	
OCM line scan camera readout rate	≥ 6 kHz
Spectral response wavelengths	1300 nm \pm 38 nm
OCM line scan camera exposure time	Variable
Frame grabber acquisition rate	Lines at ≥ 6 kHz
Multiphoton microscopy	
PMT/amplifier gain-bandwidth product	≥ 1 MHz at $\geq 10^6$ gain
Spectral response wavelengths	650-850 nm
Data acquisition board sampling rate	≥ 2 MHz
Proximal system	
Equipment rack	Portable
Graphic user interface	Yes
Electrical power safety	Per IEC 60601-1 Part 1, third edition, Part 1, section 8.7.3d
Laser safety	Per ANSI Z136.1

An equipment rack should enclose all sources, detectors, and computational equipment. It should also be portable and comply with electrical and laser safety requirements. The software interface

should control imaging parameters and display images to the user. Table 5 summarizes the acquisition requirements.

3. Multimodal system design

Figure 2 shows a diagram for the multimodal endoscope system designed and built to meet the requirements in section 2. The system can be divided into the handheld endoscope and the instrument rack. The endoscope consists of the insertable portion, the handle, and the long flexible tubing relaying light and power between the handle and rack, while the instrument rack contains of the optical and photonic components as well as the computer.

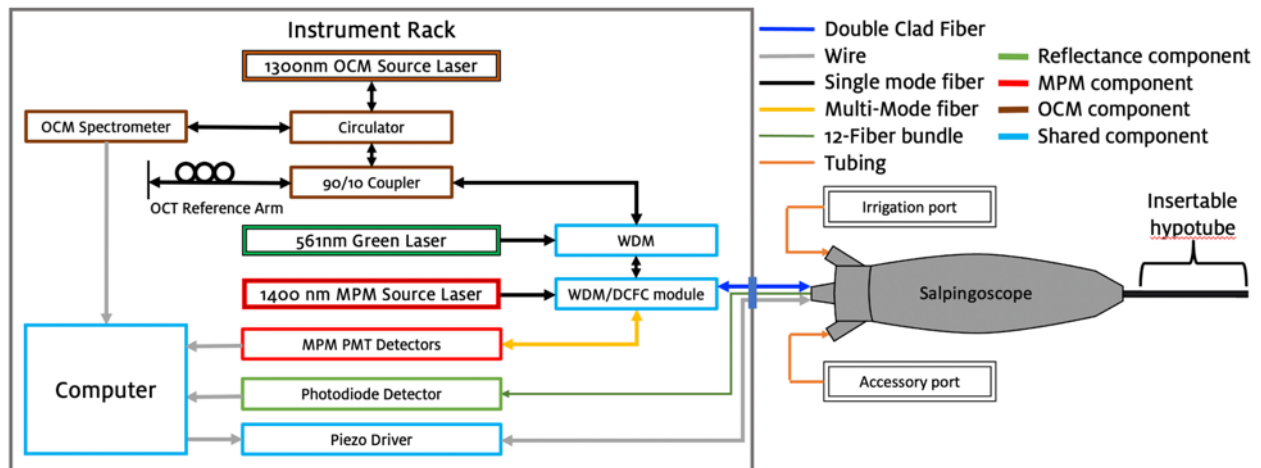


Figure 2. Endoscope system diagram. Green outlined components are for navigation. Red outlined components are for MPM imaging. Brown outlined components are for OCM imaging. Components outlined in blue are shared by two or more modalities. Various fiber types, electrical wire, and tubing are color coded as shown in figure.

4. Endoscope design

A photograph of the endoscope is shown in Figure 3. The insertable portion consists of a rigid hypotube protecting the fibers, electrical wires, and accessory channel tubing and contains a distal ferrule that holds the imaging optics, the quartered piezo scanning system, light collection fibers, and tubing for the irrigation and accessory channels. The hypotube is made of medical-

grade stainless steel (304H09XX, MicroGroup (Medway), MA, USA), custom-cut to set the insertable section's length at 30 cm with an outer diameter of 3.733 mm and a wall thickness of 178 μm . The non-insertable ergonomic handle is 3D-printed from rigid VeroBlack (Stratasys, MN, USA) material. It contains the irrigation and accessory ports as well as channels for the fibers and piezo control wires.

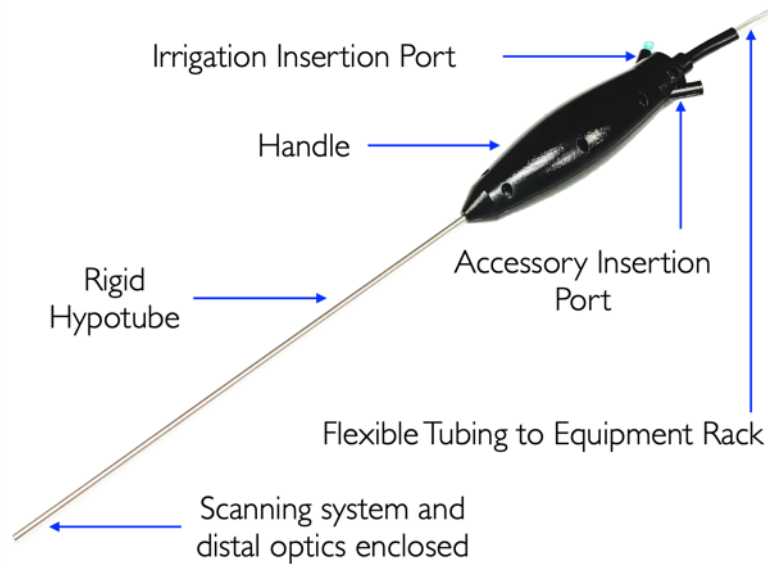


Figure 3. Photograph of the endoscope prototype, with major components labeled.

Distal tip configuration

A diagram and photograph of the components housed within the distal ferrule (no protective hypotube), and a distal tip end view of the completed endoscope, are shown in Figure 4 and Figure 5, respectively.

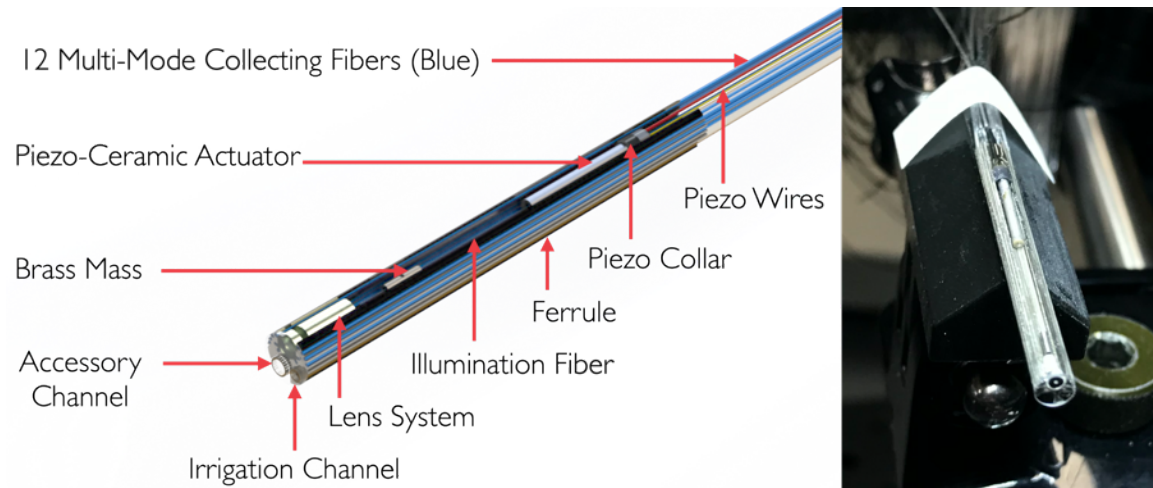


Figure 4. (Left) Rendering, and (right) photograph, of the endoscope distal assembly under construction. The protective hypotubing is not yet installed.

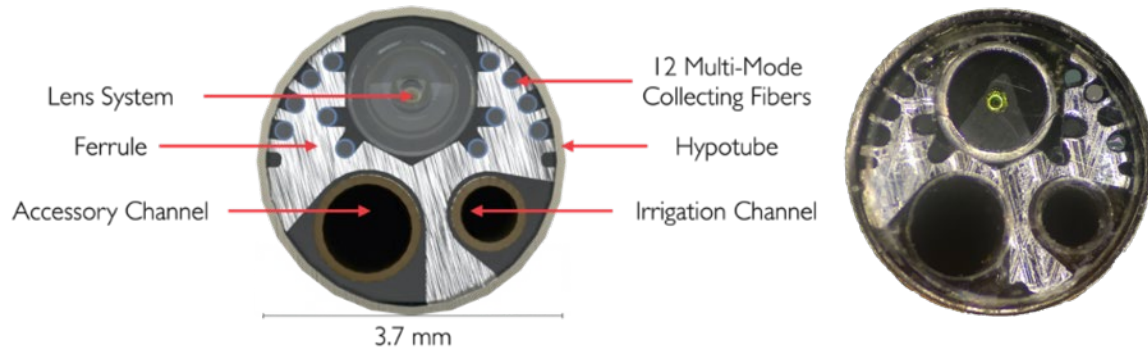


Figure 5. Distal tip end-view rendering (left) and (right) photograph of the completed endoscope.

The custom ferrule (Majer Precision Engineering, Inc, AZ, USA) is made of medical-grade stainless steel and was designed to hold all the optical components, the scanning system, and the irrigation and accessory channel tubing in a rigid configuration. It has a small outer diameter of 3.3 mm, which fits inside the hypotubing of the insertable portion. The ferrule's complex shape was achieved using fine wire electrical discharge machining (EDM). Within the ferrule, the largest cutout (1.52 mm diameter) holds the quartered piezo scanning system and a lens system, used for illumination in all three imaging modalities (navigation, OCM, and MPM) and collection of remitted light for OCM and MPM. Twelve small cutouts hold collection fibers for the remitted navigation light. A 1.35 mm diameter cutout holds the polyimide accessory channel

tubing (480-II, MicroLumen, FL, USA), which has a 1.34 mm outer diameter and 0.06 mm wall thickness. The resulting 1.22 mm clear channel is sufficiently large to pass accessories such as biopsy forceps (SpyBite, M00546270, Boston Scientific Corporation, Natick, MA, USA). The final 0.97 mm diameter cutout holds smaller diameter tubing (335-II, MicroLumen, FL, USA) with an outer diameter of 0.96 mm and a 0.05 mm wall thickness. This tubing is used for irrigation with saline and the delivery of contrast agents. The latter two functionalities are shown in Figure 6.



Figure 6. (Left) Biopsy forceps (SpyBite) inserted through the accessory channel. (Right) Water being flushed through the irrigation channel.

Optical and scanning system configuration

All three optical modalities utilize a common double-clad fiber (DCF) (DCF13, Thorlabs, NY, USA), scanning system, and lens system. All modalities utilize the single-mode core of the DCF for illumination. Based on the requirements in section 2, the specified illumination wavelength, remitted signal wavelength, illumination spot size (resolution), illumination FOV, and collection mechanism for the three modalities are specified in Table 6.

An illumination wavelength of 561 nm was chosen for navigation based on laser availability and optical tissue properties. This wavelength provides high contrast when imaging blood vessels due to the oxy- and deoxy-hemoglobin absorption peaks near this wavelength²¹. A laser diode with 35 mW power output was used (R560503FX, LaserGlow Technologies, Toronto, Canada).

For OCM, a dual-superluminescent diode with a center wavelength of 1300 nm, 70 nm full-width-half-maximum bandwidth, and 8 mW power was chosen (Broadlighter 1300, SuperLum, Co. Cork, Ireland). For MPM, a custom ~100 fs, 40 MHz pulsed laser centered at 1400 nm with 160 mW output power was utilized²². The power output measurements at the distal tip of the endoscope were lower than the source outputs, and they were confirmed to meet ANSI Z136.1 standard for permissible laser exposure.

Table 6. Illumination and collection mechanisms for the different optical modalities

	Reflectance	OCM	MPM
Illumination wavelength	561 nm	1300 \pm 38 nm	1400 \pm 10 nm
Illumination mechanism	Fiber core	Fiber core	Fiber core
FOV	25°	100 μ m	100 μ m
Signal wavelength	561 nm	1300 \pm 38 nm	~ 695 - 870 nm
Collection mechanism	12 multimode collection fibers	Fiber core	Fiber first cladding
Resolution	50 μ m at 5 mm	2 μ m lateral, 10 μ m axial	2 μ m lateral

The differing illumination spot sizes and FOVs of the reflectance system compared to those of the OCM/MPM system are made possible by the novel lens system previously described²³. In brief, the lens system contains a triplet with two dichroic coatings at the distal and proximal inner surfaces in the shape of a dot and a ring, respectively. The coatings are arranged similar to the primary and secondary mirrors of a telescope. The coatings transmit light at visible wavelengths so that the final objective lens weakly focuses the light into a low 0.007 numerical aperture (NA) beam with a depth of focus from 5 to 22 mm and a central spot size of 10.98 μ m at best focus. The reflectance signal from the illuminated spot is collected with twelve 0.5 NA multi-mode fibers held by the ferrule, enabling good light collection efficiency. At NIR wavelengths, the coatings reflect light in a telescope-like configuration to expand the beam, and the final objective lens strongly focuses them to a high 0.44 NA beam with a 50 μ m front focal distance and a ~ 2 μ m spot size. The OCM light is collected back into the single-mode core of

the DCF, as required for this interferometric technique. The MPM signal is collected in the .2 NA first cladding of the DCF, which enables increased light collection over utilizing the core only. Note that MPM only captures the central portion of the collected light since the wavelengths generated by the nonlinear effects are not affected by the dichroic surfaces. The optical paths used are illustrated in Figure 7.

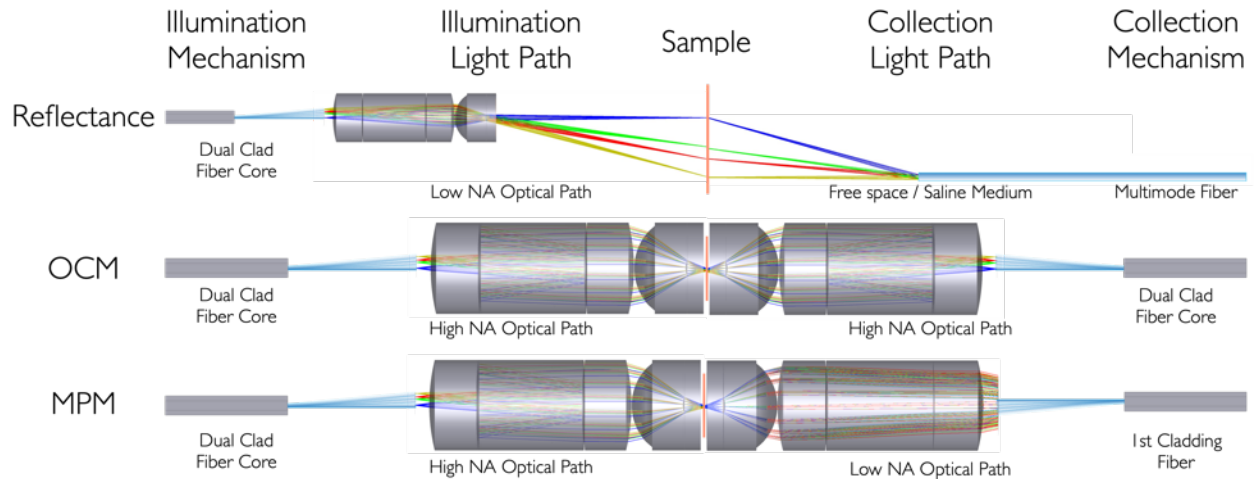


Figure 7. Tunnel diagrams, where light propagates from left to right including reflected light, for the Illumination, optical paths, and collection mechanisms for the different optical modalities. The sample is represented with an orange line.

The quartered-piezo (piezo) scanning assembly with a cantilevered DCF and fiber mass is shown in Figure 8. Scanning endoscopes have been demonstrated before using Lissajous and spiral scanning patterns²⁴. Our endoscope works with a raster pattern since relatively slow (tens of Hz) scanning is required for OCM, and relatively fast (thousands of Hz) scanning is required for video-rate *en face* navigation and MPM imaging. Raster scanning can also ease image reconstruction because it is acquired in a more intuitive sequence than spiral or Lissajous scanning. However, image calibration adjustment is still needed due to the sinusoidal motion of the piezo. Raster scanning at slow and fast frequencies can be achieved by utilizing multiple vibrational resonance frequencies (e.g., first and third) that can be adjusted by tuning the fiber length and utilizing fiber-mounted masses²².

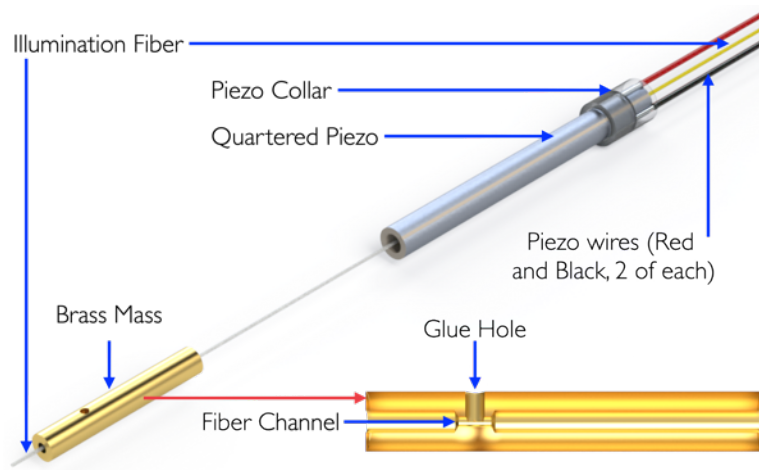


Figure 8. Quartered piezo scanning assembly including the quartered piezo tube, fiber, wires, collar, and brass mass. The brass mass is shown sectioned through the middle to show the internal “bow-tie” shape, the fiber channel, and the hole used to glue the mass to the fiber.

The scanning system shown in Figure 8 utilizes a custom piezo with 1.0 mm outer diameter, 0.2 mm wall thickness, 11 mm length, 4 longitudinal outer electrodes (electrically isolated quadrants at 90 degrees), and PIC255 material (PI, Auburn, MA, USA). A custom polyether ether ketone (PEEK) piezo collar (Optics Technology, Pittsford, NY, USA) holds the proximal piezo stationary and centered inside the ferrule cutout while allowing the distal piezo end and the cantilevered fiber to oscillate with relative freedom. Additionally, the collar protects the exposed leads that apply voltage to the piezo electrodes. Desired resonant frequencies of ~ 38 Hz first resonance and ~ 3800 Hz third resonance were achieved using 16 mm long cantilevered fiber with a custom brass mass (Optics Technology). The mass shape is cylindrical to maximize its weight in the 1.52 mm ferrule cutout while allowing a tip deflection amplitude of up to $400\ \mu\text{m}$ peak-to-peak. The cylinder's inner diameter was shaped in a “bow-tie” fashion and glued to the fiber at one point only, through a hole on the side of the mass. Thus, the fiber is free to bend and oscillate as required at third resonance. The mass is placed such that the center of mass sits at a location between 75-80% of the fiber's length, aiming for the third resonance distal nodal point. The mass, placed as described, lowers the first harmonic frequency while keeping the third

harmonic frequency relatively unchanged²², allowing for a 100X difference in the two frequencies for raster scanning. The ratio of scanning frequencies limits the number of pixels in one dimension of the image, in this case to 100.

Endoscope handle

The fibers, piezo control wires, and irrigation and accessory tubing are carried through the hypotube to the 3D-printed handle, where they are separated into three different channels, as shown in Figure 9. The center channel contains the 12 multimode collection fibers, the dual-clad fiber, and the four piezo control wires. A curved side-channel houses the accessory channel tubing with a 1.22 mm inner diameter. The tapered entrance allows the tool to be inserted smoothly. A second side-channel holds the Luer lock tip of a 21G hypodermic needle with a shortened cannula (EXEL, CA, USA) which is mated with and glued into the irrigation channel tubing. This Luer lock connector provides an attachment point that allows for the introduction of saline or contrast agents with a standard Luer lock syringe.



Figure 9, (Left) Open handle showing the internal channels guiding the different components. (Right) Handle with components installed.

Proximal to the handle, the fibers and piezo control wires are protected with a 2.0 m long, 3/16" outer diameter vinyl tube (4027470, ACE, USA). The tubing is glued to the handle and protected with a separate heat shrink tubing at the handle interface (MT5000-1/2-0-SP, TE Connectivity, Schaffhausen, Switzerland). Components exit the vinyl tube's proximal end and lead into three

connectors that attach the handheld endoscope to the instrument rack. A standard FC/APC connector is used for the DCF, a standard SMA connector is used for all twelve multimode fibers combined into a single 900 μm lumen, and a 4-pin connector is used for the piezo control wires (SP13-4pin, SZJELEN, China). A complete prototype of the handheld endoscope is shown in Figure 10.

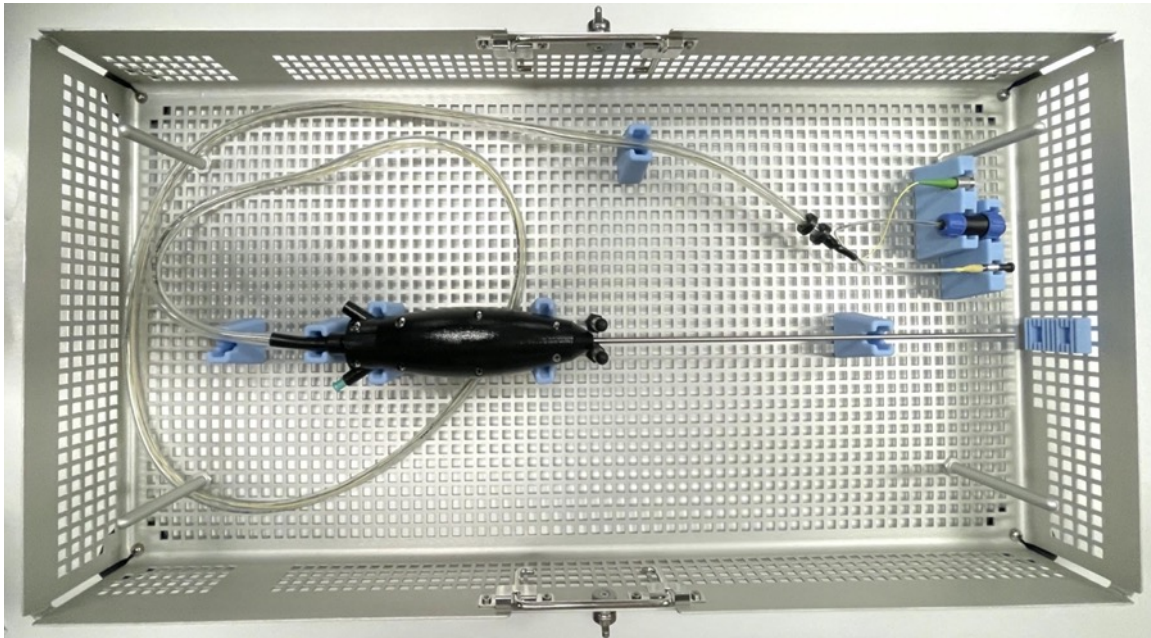


Figure 10. Endoscope prototype in sterilization box.

All exposed materials were carefully selected to ensure compatibility and sterilizability of the endoscope. The hypotube is made of 304 stainless steel, and a custom cover glass is made of fused silica (W-SIO2UVE-RS0003, Bern Optics, MA, USA). The irrigation and accessory tubing is made of polyimide. The gaps between the cover glass and the hypotube and the gaps between the inner irrigation and accessory tubing and the cover glass are sealed with a medical-grade epoxy (EP42HT-2MED Clear, Masterbond, NJ, USA). Gaps between components such as the handle-hypotube interface are further sealed with medical-grade adhesive (Loctite 4013, Henkel Adhesives, Düsseldorf, Germany). The 3D-printed handle material (VeroBlack) and the

vinyl tubing are not biocompatible, but they can be covered with a sterile ultrasound sheath during clinical use. Sterilizability of the entire handheld endoscope was confirmed with deliberate contamination, then swabs for common pathogens after hydrogen peroxide sterilization. All tests revealed that no pathogens were present after sterilization.

5. Instrumentation rack systems

The rack contains all source, detector, and computational components needed to operate the endoscope²⁵. The rack contains an electrical power isolator (IS1800HG, Tripplite, IL, USA) and conforms to leakage current safety requirements [IEC 60601-1 Part 1, third edition, Part 1, section 8.7.3d].

Navigation components

Referring to the system diagram in Figure 1, the 561 nm laser is connected to a custom wavelength division multiplexer (WDM) (OZ optics, Canada) optimized for combining this wavelength with the 1300 nm OCM source. The WDM output then enters a custom WDM/Dual Clad Fiber Coupler (DCFC) (DBM-1300-200901, CASTOR, Canada) which adds in the 1400 nm MPM source and directs all wavelengths into the core of the DCF that runs through the endoscope. The single 900 μm lumen SMA connector containing light reflected from the sample is mated to an SMA connector containing a single 1500 μm core fiber at the instrument rack interface (M93L01, Thorlabs, NJ, USA). This fiber is coupled to an SMA-adapted silicon detector (New Focus 2107-FC-M, MKS | Newport, CA, USA) with a 6 MHz bandwidth at the 3×10^2 gain used during testing.

OCM components

The 1300 nm OCM source is coupled into a fiber interferometer containing a circulator (37474 FOC-12N-11, OZ Optics, Canada) and a 90:10 fiber coupler (FUSC-280125223, Precision Micro-optics, MA, USA). Ten percent of the power is directed into a reference arm with dispersion matching, polarization control, and an optical path length adjustable to match the endoscope. The remaining 90% of the power is directed into the WDMs for passage through the DCFC and output through the DCF core. Light reflected by the tissue into the DCF core follows the same return path, where it is recombined with reference arm light and directed by the circulator to the spectrometer. The spectrometer is equipped with a reflective collimator (MPD124-M01, Thorlabs, NJ, USA), 300 mm focal length custom-made lens (AC254-300-C-ML, Thorlabs, NJ, USA), reflective grating (GR25-0613, Thorlabs, NJ, USA), and a 2048 pixel linear array (GL2048L, Sensors Unlimited, NJ, USA). This camera was chosen due to its high quantum efficiency (60%-70%), user-controlled exposure, high dynamic range ($>1200:1$), and appropriate read rate of up to 76,000 lines per second.

MPM components

MPM source light from the custom 1400 nm femtosecond laser is combined with the other wavelengths into the DCF core via the second WDM and DCFC. Remitted light in the DCF inner cladding is delivered via the multimode arm of the DCF to a custom-made PMT enclosure. A reflective collimator (RC02FC-P01, Thorlabs, NJ, USA) delivers the light to a series of dichroic mirrors that separate SHG and 2PEF (FF01-890/SP, FF725-SDi01-25x36x3.5, FF01-850/310-25, FF01-770/SP-25, Semrock, NY, USA) and direct the signals to PMTs (H10721-20, Hamamatsu, Iwata, Japan). Transimpedance amplifiers (PMT-4V3, Advanced Research

Instruments Corp. OR, USA) provide variable gain with a 2 MHz bandwidth at the 1×10^6 gain used in testing. A programmable filter (3945, Krohn-Hite, MA, USA) can be used to remove high-frequency noise.

Data acquisition, software, and display

To generate piezo control signals, acquire detector/camera data, and reconstruct and display images, a custom LabView program was written in collaboration with INTAQ (Arizona, USA). Based on user input image dimensions and image rate, piezo control signals for each axis are generated and output through a multipurpose data acquisition (DAQ) board (PCIe-6321, National Instruments, Austin, TX). The control signals are further amplified at the piezo driver (TD250, Piezo Drive, Shortland, Australia). One-dimensional slow-axis scanning is used for OCM imaging, and two-dimensional fast- and slow-axis raster scanning is used for reflectance and MPM modes. Piezo control signals are synchronized with data acquisition. Reflectance and MPM signals are acquired with the same multipurpose DAQ board, capable of up to four synchronous analog input channels at up to 3.5 MHz each (PCIe-6374, National Instruments, Austin, TX). Due to limitations in the current software only acquiring on one side of the sinusoidal piezo movement, the number of pixels in the slow scanning imaging dimension is limited to 50. The number of pixels in the fast scanning dimension is only limited by the sampling rate of the DAQ board and the piezo fast scan frequency, and could be up to 460. OCM line scan camera signals are acquired with a frame grabber (PCIe-1433, National Instruments, Austin, TX). The number of A-scans (line scan camera reads) per image is limited by the camera line rate and the piezo slow scan frequency and could be up to 950.

The software enables the acquisition and the display of navigation, OCM, or MPM images. Navigation and MPM images are displayed in real-time in their as-acquired form, which is distorted due to the scanning system's sinusoidal movement, piezo scanning axes that may not be perfectly perpendicular, and minor stable whirling of the fiber. In practice, typically 10% of data points at each image edge are excluded, as the fiber movement at these locations is so slow as to cause significant distortion and provide limited additional FOV. Therefore the number of pixels in the slow scanning imaging dimension is normally 40. A calibration obtained from imaging a grid pattern can be applied to process images into their true dimensions.

OCM camera reads are processed by applying calibration files created using published methods²⁶ and taking the Fourier transform of each A-scan. B-scan images are constructed by combining processed A-scans. Acquired raw data, processed data, and configuration files are saved upon request.

6. Results

Reflectance test

The endoscopic optical system was tested in a tabletop configuration without the hypotube to allow for alignment of the components. Reflectance modality images of a black on white paper USAF resolution target were analyzed (#53-715, Edmund Optics, NJ, USA) to evaluate FOV and lateral resolution. At a working distance of 5.0 mm, up to a 2.5 FOV could be imaged, which equates to a 28° FOV. To evaluate lateral resolution, the FOV was reduced to $\sim 0.25 \times 0.25$ mm by controlling the piezo oscillation amplitude voltage. The reduction of the FOV resulted in ~ 6 μm distance between pixels when a square image of 40 x 40 pixels was obtained. The contrast

was calculated utilizing the grayscale values of the images, and the resolving criterion was set to a contrast of .01 or greater using:

$$\text{Contrast} = \frac{I_{\max} - I_{\min}}{I_{\max} + I_{\min}}$$

Grayscale values were read from a line traced through the horizontal or vertical bars of the respective element. An I_{\max} or I_{\min} was taken at each line's inflection points, and four contrast values were calculated, one for each adjacent I_{\max} and I_{\min} values, using the contrast equation. The average of these contrast values is the reported value. Figure 11 shows reflectance images of the USAF resolution target. The smallest element with contrast above the threshold is group 4 element 3, equivalent to a lateral resolution of 24.80 μm or 20.16 lines per millimeter. Vertical lines displayed a contrast of $\sim.024$, and horizontal lines displayed a contrast of $\sim.011$.

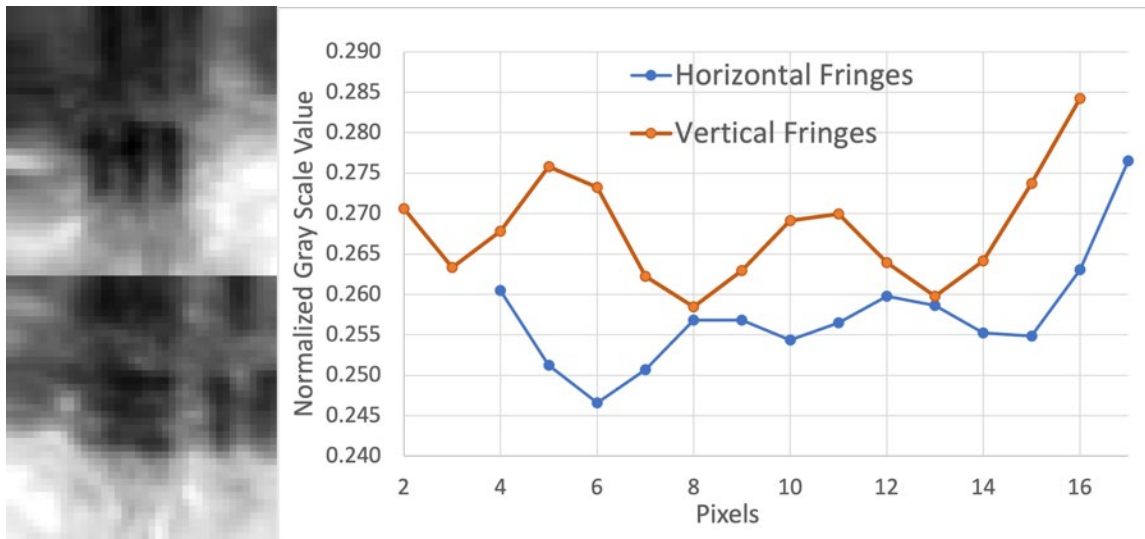


Figure 11. (Left) Reflectance images of a USAF target showing the vertical (top) and horizontal (bottom) lines for group 4 element 3. The contrast and brightness of these images were digitally adjusted for clarity. (Right) Grayscale values extracted from the red lines traced over the horizontal and vertical patterns shown on the left side.

The differences in contrast between the horizontal and vertical fringes seen in Figure 11 may be attributable to the suboptimal alignment of the lenses causing astigmatism.

To further test the capability of reflectance imaging, and to measure the working distance range, images of a reflectance target were obtained at 5 mm, 10 mm, 15 mm, and 30 mm from the endoscope distal cover glass. The target consists of a surface coated with Spectralon (Labsphere, Inc, NH, USA) and geometrical shapes made of Fineshut KIWAMI (Koyo Orient Japan Co. LTD, Saitama, Japan). These materials provide some of the highest and lowest, respectively, reflectance values obtainable, thus providing higher contrast than the USAF target. The reflectance images and the target white light image can be seen in Figure 12. The finite thickness of the Fineshut material causes some artifacts, especially at close range. The reflectance images show that the shapes are visualized over the entire range. At 30 mm the low collection efficiency of the reflected signal results in a noisier image.

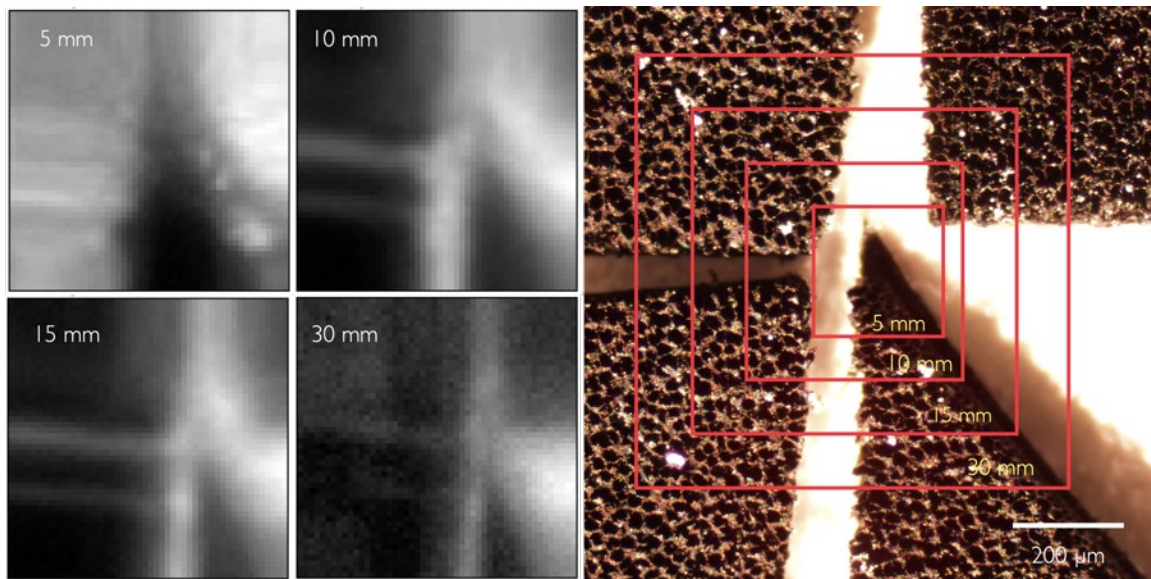


Figure 12. Images of a reflectance target in white light and reflectance at 5 mm, 10 mm, 15 mm, and 30 mm from the endoscope distal cover glass. The white light image has been labeled for the approximate location of the scans.

OCM test

To test OCM, the lateral FOV was reduced to $\sim 50 \mu\text{m}$ by controlling the piezo oscillation amplitude voltage. The reduction of the FOV resulted in $\sim 0.3 \mu\text{m}$ distance between A-scans with a total of 166 lines per frame. The best focus was found to be at $\sim 60 \mu\text{m}$ from the distal

cover glass. A variable line grating test target (R1L3S6P, Thorlabs, NJ USA) was imaged to test OCM lateral resolution. The OCM image is shown in Figure 13. This test was performed as a simple pass/fail test for OCM since the system's lateral resolution is theoretically $2\text{ }\mu\text{m}$, but the smallest pattern in the target is $4\text{ }\mu\text{m}$. The image shows excellent contrast between the lines in the lateral direction.

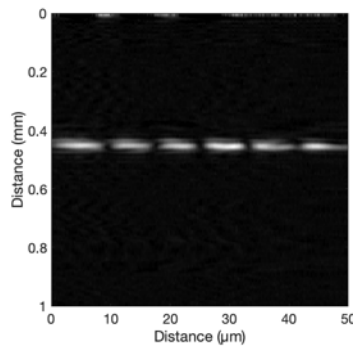


Figure 13. OCM image of a variable line grating test target (R1L3S6P, Thorlabs, NJ USA).

The $14.2\text{ }\mu\text{m}$ FWHM of the line in the axial direction (vertical on the image) is significantly degraded from the theoretical axial resolution of $\sim 9\text{ }\mu\text{m}$. We attribute the discrepancy to suboptimal calibration of the spectrometer.

MPM test

The broken edge of a Gallium Arsenide (GaAs) sample was imaged to test the MPM modality due to the strong emission of 2PEF at the edge. The FOV was reduced to $\sim 50 \times 50\text{ }\mu\text{m}$ by controlling the piezo oscillation amplitude voltage. The reduction of the FOV resulted in $\sim 1.25\text{ }\mu\text{m}$ distance between pixels when a square image of 40×40 pixels was obtained. The best focus was found to be at $\sim 60\text{ }\mu\text{m}$ from the distal cover glass. The multiphoton image obtained by averaging 32 frames is shown in Figure 14. The edge image allows us to use a nonlinear

technique to characterize lateral resolution²⁷. This technique consists of fitting the edge profile using

$$g(x) = \frac{a}{2} \left(1 - \operatorname{erf} \left[\frac{\sqrt{2}(x - b)}{c} \right] \right)$$

where x is lateral displacement of the scanning sampling, and a , b , and c are fitting coefficients.

The resolution of the system is given by multiplying the fitting coefficient c by 1.17. A simple MATLAB code was generated to perform this task.

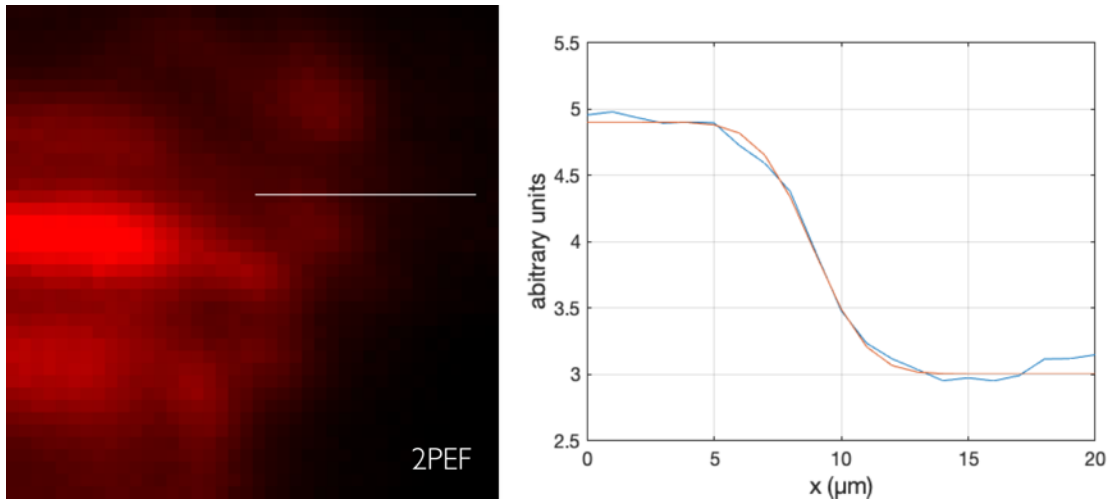


Figure 14. 2PEF image of a GaAs edge. The profile was taken from the white line in the image.

The resolution computed by this technique is $3.97 \mu\text{m}$. Additionally, an image of a computer chip was acquired to further test the MPM capability. The image can be seen in Figure 15, showing two wires that are used to connect the chip's internal components. Chip materials such as silicon doped hafnium oxide and metals are likely the SHG and 2PEF sources.

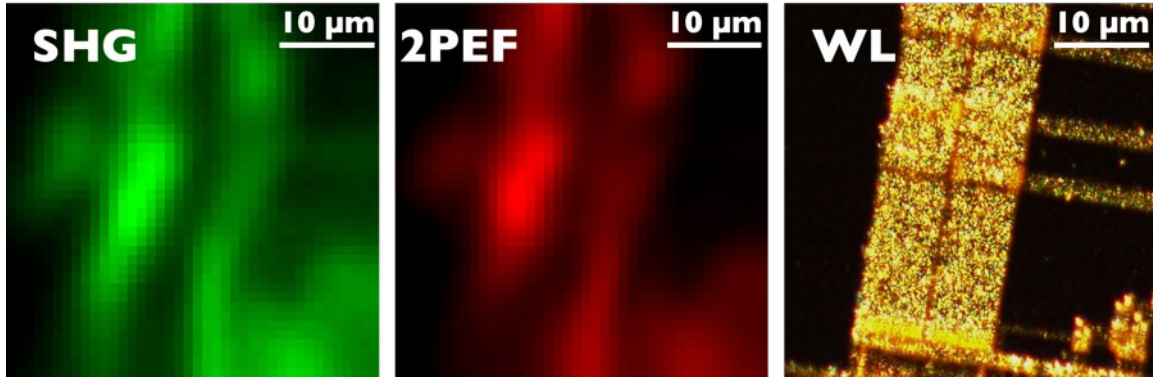


Figure 15. SHG, 2PEF, and White Light images of computer chip. The red square in the white light image indicates where the SHG and 2PEF images were taken. The long vertical strands in the center are wires that connect the internal components of the chip.

7. Discussion and future work

We present an endoscope that enables three optical imaging modalities through the same optical system. The endoscope requirements (as taken from Tables 1, 2, and 3) and their results are summarized in Table 7. All functional, data acquisition, and safety requirements were met, as were most optical requirements. Measurements of lateral resolution from reflectance (low NA) and MPM (high NA) images were poorer than those predicted by optical modeling software. Nonetheless, the lateral resolution of the reflectance modality was still within the required range. Axial resolution for OCM could likely be improved by better calibration, and lateral resolution of MPM by better optical alignment and tighter tolerances on optics manufacturing. Future plans include increasing system performance. For example, the piezo harmonic frequencies limit the number of rows that an image can have. By utilizing the first and fourth resonance, the number of pixels in the slow scanning dimension of reflectance and MPM images could be increased. A drawback of using the 4th resonance is that at higher harmonics, the deflection amplitude decreases, requiring higher voltages to increase the amplitude and possibly impairing the ability to scan the entire field of view. A simpler change would be to acquire signals on both sides of the fast sinusoidal scan, doubling the number of pixels in the slow scanning dimension. Image adjustment to reverse-order every other line would need to be

implemented, as well as better calibration to accommodate the minor stable whirling of the fiber, which leads to the fiber tracing an ellipse rather than a line. Simultaneous acquisition of OCM and MPM images is possible but not currently implemented in software.

Significant losses occur for high NA modalities at the optical system dichroic filter obscuration. Together with other system losses, the power on the sample is only .9 mW for OCM and 17 mW for MPM. A higher efficiency optical system, or simply higher power sources would improve the signal-to-noise ratio for both imaging modalities.

The current system could also provide additional functionality. By replacing the reflectance modality photodiode with a filter and PMT, the same low-NA optical path combined with raster scanning and the 12 multi-mode optical collection fibers could be used for single photon fluorescence imaging. Since the triplet dichroic filters have a cut-on at ~ 900 nm, OCT could be performed by changing out the 1300 nm superluminescent diode for one in the 800 nm range. The WDMs would also need to be swapped for ones that worked at this wavelength. The OCT system would then work through the low-NA optical path, providing a larger FOV and depth of focus but worse lateral resolution.

Next steps include fully packaging and sterilizing the endoscope and demonstrating its use for imaging of the ovaries and fallopian tubes in an ewe model and in human volunteers already undergoing a laparoscopic procedure. This endoscope could also be used for other purposes. Most organs that can be reached with a rigid endoscope represent a potential site of use. For example, modification of the endoscope with a shorter hypotube could enable oral cancer screening.

Table 7. Summary of the requirements along with the results and if the performance passes or fails the criteria.

Functional requirements			
Requirement	Specification	Measurement	Pass or Fail
Navigation / Reflectance imaging	Wide-field low-resolution	Functional	Pass
OCM imaging	High lateral and axial resolution	Functional	Pass
MPM imaging	High lateral resolution	Functional	Pass
Irrigation port	>0.5 mm diameter	0.86 mm	Pass
Accessory channel	>1.2 mm diameter	1.22 mm	Pass
Rigidity (hypotube)	Completely rigid	Yes	Pass
Endoscope outer diameter	$\leq 4\text{ mm}$	3.73 mm	Pass
Insertable length	$\geq 25\text{ cm}$	$\sim 30\text{ cm}$	Pass
Sterilizability	Hydrogen peroxide	Yes	Pass
Optical requirements			
Forward viewing reflectance			
FOV	25 to 60 Degrees	25 Degrees	Pass
Working Distance	5-20 mm	5-30 mm	Pass
Resolution	50 μm @ 5 mm WD	24.8 μm	Pass
Imaging speed	> 30 fps	38 Fps	Pass
Illumination wavelength	400-700 nm	561 nm	Pass
Optical coherence microscopy			
FOV	$\geq 100\text{ }\mu\text{m}$	$\sim 100\text{ }\mu\text{m}$	Pass
Focal Distance	50 μm	60 μm	Pass
Lateral resolution	$\leq 2\text{ }\mu\text{m}$	<4 μm	Unknown
Axial resolution	$\leq 10\text{ }\mu\text{m}$	14.2 μm	Fail
Imaging speed	> 30 fps	38 Fps	Pass
Illumination wavelength	1300 nm	1300 nm	Pass
Multiphoton microscopy			
FOV	>100 μm	$\sim 100\text{ }\mu\text{m}$	Pass
Working Distance	50 μm	60 μm	Pass
Lateral resolution	$\leq 2\text{ }\mu\text{m}$	3.97 μm	Fail
Imaging speed	> 30 fps	38 Fps	Pass
Illumination wavelength	$\geq 1200\text{ nm}$ and $\leq 1500\text{ nm}$	1400 nm	Pass
Data acquisition requirements			
Forward-viewing reflectance			
Reflectance sensor bandwidth	$\geq 1\text{ MHz}$	12 MHz	Pass
Spectral response wavelengths	400-700 nm	350-1000 nm	Pass
Reflectance sensor gain	Variable	Yes	Pass
Data acquisition board sampling rate	$\geq 2\text{ MHz}$	6 MHz	Pass

Optical coherence microscopy			
OCM line scan camera readout rate	≥ 6 kHz	72 kHz	Pass
Spectral response wavelengths	1300 nm \pm 38 nm	1100-1600 nm	Pass
OCM line scan camera exposure time	Variable	6 μ s - 10ms	Pass
Frame grabber acquisition rate	Lines at ≥ 6 kHz	2 MHz	Pass
Multiphoton microscopy			
PMT/amplifier gain-bandwidth product	≥ 1 MHz at $\geq 10^6$ gain	2Mhz 2 MHz at 10^6 gain	Pass
Spectral response wavelengths	650-850 nm	611-875 nm	Pass
Data acquisition board sampling rate	≥ 2 MHz	3.5 MHz	Pass
Proximal system			
Equipment rack	Portable	Yes	Pass
Graphic user interface	Yes	Yes	Pass
Electrical power safety	Per IEC 60601-1 Part 1, third edition, Part 1, section 8.7.3d	Yes	Pass
Laser safety	Per ANSI Z136.1	Yes	Pass

Funding

Research reported in this publication was supported by National Institute of Biomedical Imaging and Bioengineering of the National Institutes of Health under award number 1R01EB020605

This material is based upon work supported by the National Science Foundation Graduate Research Fellowship Program under Grant No. DGE-1746060. Any opinions, findings, and conclusions or recommendations expressed in this material are those of the author(s) and do not necessarily reflect the views of the National Science Foundation.

Acknowledgments

The authors want to acknowledge the support provided by several teams. The Ultrafast Fiber Lasers and Nonlinear Optics group, led by Professor Khanh Kieu, built the 1400 nm custom-made

pulsed laser. INTAQ supplied the expertise needed to program the FPGA allowing the program to achieve software performance. Castor Optics tailored a custom solution to build the WDM/DCFC. Kelli Kiekens, Zuzana Adams, Steven Santaniello, and Harrison Thurgood completed work that served as a precursor or support for this project.

Disclosures

The authors declare no conflicts of interest.

References

- [1] Cronin, Kathleen A, Lake, Andrew J, Scott, Susan, Sherman, Recinda L, Noone, Anne-Michelle, Howlander, Nadia, . . . Jemal, Ahmedin. (2018). Annual Report to the Nation on the Status of Cancer, part I: National cancer statistics. *Cancer*, 124(13), 2785-2800.
- [2] Sawyer, Travis W, Koevary, Jennifer W, Howard, Caitlin C, Austin, Olivia J, Rice, Photini F. S, Hutchens, Gabrielle V, . . . Barton, Jennifer K. (2020). Fluorescence and Multiphoton Imaging for Tissue Characterization of a Model of Postmenopausal Ovarian Cancer. *Lasers in Surgery and Medicine*, 52(10), 993-1009.
- [3] A. R. Tumlinson, B. Považay, L. P. Hariri, J. B. McNally, A. Unterhuber, B. M. Hermann, H. Sattmann, W. Drexler, and J. K. Barton, "In vivo ultrahigh-resolution optical coherence tomography of mouse colon with an achromatized endoscope," *J. Biomed. Opt.* 11, 064003 (2006).
- [4] Y. Li, J. Jing, J. Yu, B. Zhang, T. Huo, Q. Yang, and Z. Chen, "Multimodality endoscopic optical coherence tomography and fluorescence imaging technology for visualization of layered architecture and subsurface microvasculature," *Opt. Lett.* 43, 2074–2077 (2018).
- [5] D. Lorensen, B. C. Quirk, M. Auger, W.-J. Madore, R. W. Kirk, N. Godbout, D. D. Sampson, C. Boudoux, and R. A. McLaughlin, "Dual- modality needle probe for combined fluorescence imaging and three-dimensional optical coherence tomography," *Opt. Lett.* 38, 266–268 (2013).
- [6] H. Yoo, J. W. Kim, M. Shishkov, E. Namati, T. Morse, R. Shubochkin, J. R. McCarthy, V. Ntziachristos, B. E. Bouma, F. A. Jaffer, and G. J. Tearney, "Intra-arterial catheter for simultaneous microstructural and molecular imaging in vivo," *Nat. Med.* 17, 1680–1684 (2011).
- [7] Nadiarnykh, Oleg, LaComb, Ronald B, Brewer, Molly A, and Campagnola, Paul J. "Alterations of the Extracellular Matrix in Ovarian Cancer Studied by Second Harmonic Generation Imaging Microscopy." *BMC Cancer* 10.1 (2010): 94. Web.
- [8] Watson, Jennifer M, Marion, Samuel L, Rice, Photini F, Utzinger, Urs, Brewer, Molly A, Hoyer, Patricia B, and Barton, Jennifer K. "Two-photon Excited Fluorescence Imaging of Endogenous Contrast in a Mouse Model of Ovarian Cancer." *Lasers in Surgery and Medicine* 45.3 (2013): 155-66.
- [9] Watson, Jennifer M, Marion, Samuel L, Rice, Photini F, Bentley, David L, Besselsen, David G, Utzinger, Urs, Hoyer, Patricia B, and Barton, Jennifer K. "In Vivo Time-serial Multi-modality Optical Imaging in a Mouse Model of Ovarian Tumorigenesis." *Cancer Biology & Therapy* 15.1 (2014): 42-60.
- [10] Hariri, Lida P, Liebmman, Erica R, Marion, Samuel L, Hoyer, Patricia B, Davis, John R, Brewer, Molly A, and Barton, Jennifer K. "Simultaneous Optical Coherence Tomography and Laser Induced Fluorescence Imaging in Rat Model of Ovarian Carcinogenesis." *Cancer Biology & Therapy* 10.5 (2010): 438-47.

- [11] Kirillin, Mikhail, Panteleeva, Olga, Yunusova, Ekaterina, Donchenko, Ekaterina, and Shakhova, Natalia. "Criteria for Pathology Recognition in Optical Coherence Tomography of Fallopian Tubes." *Journal of Biomedical Optics* 17.8 (2012): 081413-81411.
- [12] Wang, Tianheng, Brewer, Molly, and Zhu, Qing. "An Overview of Optical Coherence Tomography for Ovarian Tissue Imaging and Characterization." *Wiley Interdisciplinary Reviews. Nanomedicine and Nanobiotechnology* 7.1 (2015): 1-16.
- [13] Sawyer, Travis W, Koevary, Jennifer W, Rice, Faith P S, Howard, Caitlin C, Austin, Olivia J, Connolly, Denise C, Cai, Kathy Q, Barton, Jennifer K, and Univ Arizona, Dept Biomed Engr. "Quantification of Multiphoton and Fluorescence Images of Reproductive Tissues from a Mouse Ovarian Cancer Model Shows Promise for Early Disease Detection." *Journal of Biomedical Optics* (2019): Journal of Biomedical Optics.
- [14] Sawyer, Travis W, Chandra, Swati, Rice, Photini F S, Koevary, Jennifer W, Barton, Jennifer K, and Univ Arizona, Coll Opt Sci. "Three-dimensional Texture Analysis of Optical Coherence Tomography Images of Ovarian Tissue." *Physics in Medicine & Biology* (2019): Physics in Medicine & Biology.
- [15] Peters, Inge T A, Stegehuis, Paulien L, Peek, Ronald, Boer, Florine L, Van Zwet, Erik W, Eggermont, Jeroen, Westphal, Johan R, Kuppen, Peter J K, Trimbos, J Baptist, Hilders, Carina G J M, Lelieveldt, Boudewijn P F, Van De Velde, Cornelis J H, Bosse, Tjalling, Dijkstra, Jouke, and Vahrmeijer, Alexander L. "Noninvasive Detection of Metastases and Follicle Density in Ovarian Tissue Using Full-Field Optical Coherence Tomography." *Clinical Cancer Research* 22.22 (2016): 5506-513.
- [16] Zipfel, Warren R, Williams, Rebecca M, and Webb, Watt W. "Nonlinear Magic: Multiphoton Microscopy in the Biosciences." *Nature Biotechnology* 21.11 (2003): 1369-377.
- [17] Williams, Rebecca M, Flesken-Nikitin, Andrea, Ellenson, Lora Hedrick, Connolly, Denise C, Hamilton, Thomas C, Nikitin, Alexander Yu, and Zipfel, Warren R. "Strategies for High Resolution Imaging of Epithelial Ovarian Cancer by Laparoscopic Nonlinear Microscopy." *Translational Oncology* 3.3 (2010): 181-94.
- [18] Tanbakuchi, Anthony A., PhD, Udovich, Joshua A., PhD, Rouse, Andrew R., PhD, Hatch, Kenneth D., MD, and Gmitro, Arthur F., PhD. "In Vivo Imaging of Ovarian Tissue Using a Novel Confocal Microlaparoscope." *American Journal of Obstetrics and Gynecology* 202.1 (2010): 90.e1-0.e9. Web.
- [19] Hanahan, D, & Weinberg, R A. (2000). The hallmarks of cancer. *Cell (Cambridge)*, 100(1), 57.
- [20] Visvanathan, Kala, Vang, Russell, Shaw, Patricia, Gross, Amy, Soslow, Robert, Parkash, Vinita, and Kurman, Robert J. "Diagnosis of Serous Tubal Intraepithelial Carcinoma Based on Morphologic and Immunohistochemical Features: A Reproducibility Study." *The American Journal of Surgical Pathology* 35.12 (2011): 1766-775.
- [21] Hemmer, Eva, Benayas, Antonio, Légaré, François, and Vetrone, Fiorenzo. "Exploiting the Biological Windows: Current Perspectives on Fluorescent Bioprobes Emitting above 1000 Nm." *Nanoscale Horizons* 1.3 (2016): 168-84.
- [22] Kiekens, Kelli, Vega, David, Thurgood, Harrison, Galvez, Dominique, McGregor, Davis, Sawyer, Travis, and Barton, Jennifer. "Effect of an Added Mass On the Vibration Characteristics for Raster Scanning of a Cantilevered Optical Fiber." *Journal of Engineering and Science in Medical Diagnostics and Therapy* (2021): Journal of Engineering and Science in Medical Diagnostics and Therapy, 2021-03-31.
- [23] Vega, David, Sawyer, Travis W, Pham, Nancy Y, & Barton, Jennifer K. (2020). Use of embedded and patterned dichroic surfaces with reflective optical power to enable multiple optical paths in a micro-objective. *Applied Optics* (2004), 59(22), G71-G78.
- [24] Lee, Cameron M, Engelbrecht, Christoph J, Soper, Timothy D, Helmchen, Fritjof, and Seibel, Eric J. "Scanning Fiber Endoscopy with Highly Flexible, 1 Mm Catheterscopes for Wide-field, Full-color Imaging." *Journal of Biophotonics* 3.5-6 (2010): 385-407.
- [25] David Vega, Jennifer K. Barton, Dominique B. Galvez, Steven P. Santaniello, Zuzana Adams, Nancy Y. Pham, Kelli Kiekens, Ricky Cordova, Jenna Montague, "A coregistered multimodal imaging system for reflectance, multiphoton, and optical coherence microscopy," Proc. SPIE 11634, Multimodal Biomedical Imaging XVI, 116340Q (5 March 2021)

- [26] Attendu, Xavier, Ruis, Roosje M, Boudoux, Caroline, Van Leeuwen, Ton G, and Faber, Dirk J. "Simple and Robust Calibration Procedure for K-linearization and Dispersion Compensation in Optical Coherence Tomography." *Journal of Biomedical Optics* 24.5 (2019): 1-11.
- [27] Mehravar, Soroush, Cromeey, Benjamin, and Kieu, Khanh. "Characterization of Multiphoton Microscopes by the Nonlinear Knife-edge Technique." *Applied Optics (2004)* 59.22 (2020): G219-224.

C.1.1 Files Storage Location

All the files associated with this manuscript are stored in the following directories:

/Volumes/Research/Barton/Projects/Grants/Salpingoscope/Journal papers files/Salpingoscope system

Within the folder, the images included in the manuscript are available in a Keynote file and a PowerPoint pptx file. Both files are named “FiguresSalpingoscopeSystem” but have different extensions. In the folder named “images”, the raw and processed data can be found. The 2PEFRowData folder includes all the edge analysis and figures to evaluate the resolution of the system. The reflectance contrast graphs were obtained following the processes described in Appendix A, section A.1.1.

The processed images are also within this folder in TIFF and PNG format. Additionally a copy of the bill of materials is stored in this folder for completeness.

C.2 Standard Operating Procedure B16-011: Salpingoscope Fiber Gluing

This SOP guides a technician through the 12 optical fibers gluing process onto a ferrule. The reflectance system utilizes the fibers in the Salpingoscope. The fibers collect the scattered light from a sample and direct this signal to a photodiode. The following standard operating procedure (SOP) was developed according to laboratory protocol.

Standard Operating Procedures University of Arizona Biomedical Engineering Program

SOP # B16-011	Title: Placement of Salpingoscope Fibers in Ferrule
Origin Date: 09/25/18 Revision Date: 01/27/2020	Approval: Date Approved:

Supplies:

- Salpingoscope Ferrule Mount (3D printed, part file: Ferrule Mount.sldpt)
- Salpingoscope Ferrule (3.3mm OD, Majer Precision)
- 3x Salpingoscope Fiber Clip (3D printed, part file: Clip_Final.sldpt)
- Optical Fiber (Thorlabs – FP200URT, 200um Core, 225um Cladding, 0.50NA)
- Norland 68 Optical Glue (Norland)
- Kim Wipes
- Optical cleaning alcohol (ethanol, isopropanol, etc.)
- 2x Glass Microscope Slide
- BD Insulin Syringe with 31 gauge, 8 mm needle
- Un-Powdered Latex Gloves
- Electrical Tape
- Razor Blade

- First Contact (Photonic Cleaning Solutions, WI)
- Measuring Tape
- Optical Q-Tips
- Expired Nylon Surgical Suture
- Scissors

Equipment:

- Surgical Microscope
- Optical Breadboard
- CT-30 or CT-08 High Precision Cleaver (Fujikura)
- Side Viewing Microscope
- UV Epoxy Curing Gun
- UV safety glasses
- Modified Go Pro Mount

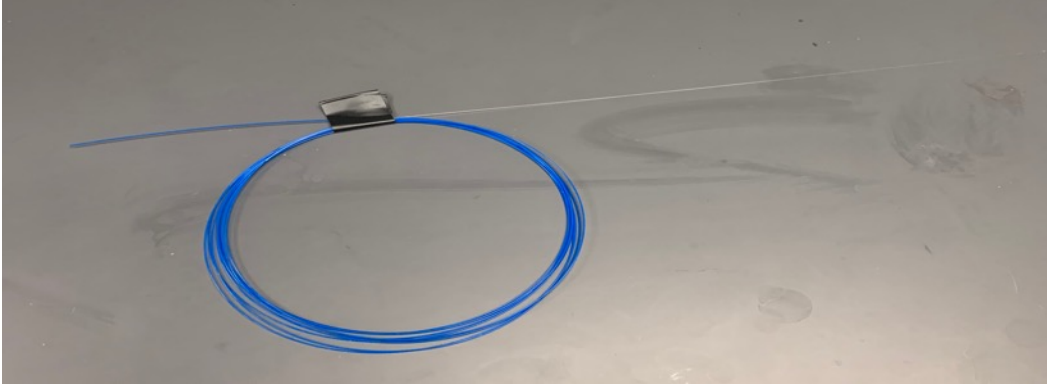
Procedure:

In this procedure the technician prepares and glues into place the 12 optical fibers utilized in the Salpingoscope assembly for visible navigation. Make sure to wear gloves throughout.

Fiber Preparation

9. Measure 3.25m of the custom drawn optical fiber and cut using fiber stripper.
10. Strip fiber jacket back exposing ~40cm of fiber (~length of hypotube + ferrule). Note:
allot ~10 min per fiber to strip.

11. Cut a piece ~20 cm piece of electrical tape, to cut into smaller pieces later.
12. Individually unthread a single piece of fiber and wrap it up into a small circle (~8 cm diameter). Tie this wrap together with the electrical tape and place it in a safe place.



13. Repeat this to all fibers until a large amount of individually wrapped fibers has been accumulated.

Ferrule Preparation and Setup:

11. Prior to gluing in any optical fibers, it is important to ensure that the ferrule is absent of all other endoscopic components and free of any leftover glue residue (if reusing a ferrule). If glue remains, or there are other components from a prior attempt glued in the ferrule, remove them by following the SOP for ferrule cleaning.
12. Check to see channels are not damaged (clear and unbent for easy fiber threading).
Correct with needle as needed.
13. Once the ferrule is free of glue residue and components, clean the ferrule one more time with optical cleaning alcohol and a green optical Q-Tip.

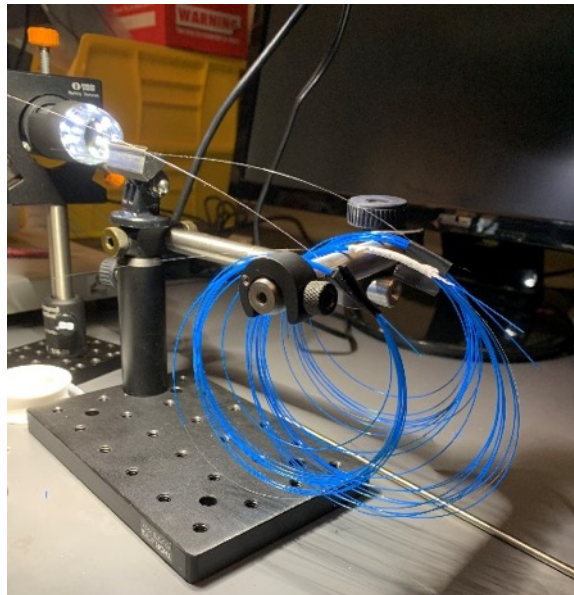


14. A jig should be constructed with the 3D printed ferrule mount.



15. Place the ferrule in the ferrule mount and set up the surgical microscope such that you can see the top of the ferrule closest to the face.

16. Set up the side view microscope such that you can view the front face of the ferrule



Fiber Gluing Procedure:

The fiber gluing procedure is completed by gluing in three fibers at a time. The ferrule itself has four sets of three fibers clearly separated. There are two sets of three fibers located on the inside of the ferrule and two sets of three fibers on the outer edges of the ferrule (refer to diagrams below). Due to the configuration of our setup, you may need to rotate the assembly between

sides in order to have better visualization while gluing. In order to maintain fiber organization, it is recommended that you start gluing in the fibers from one of the outer sides, then the inner sides, then the last outer side.

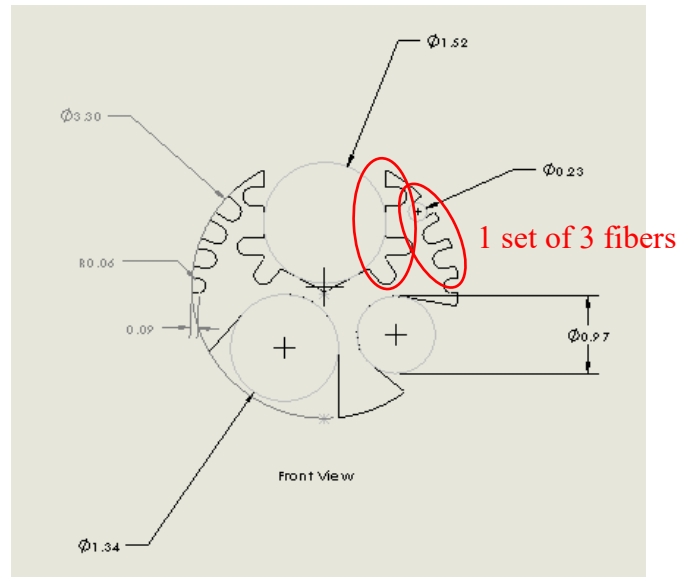


Fig. 1. One set of three fibers indicated by single red oval.

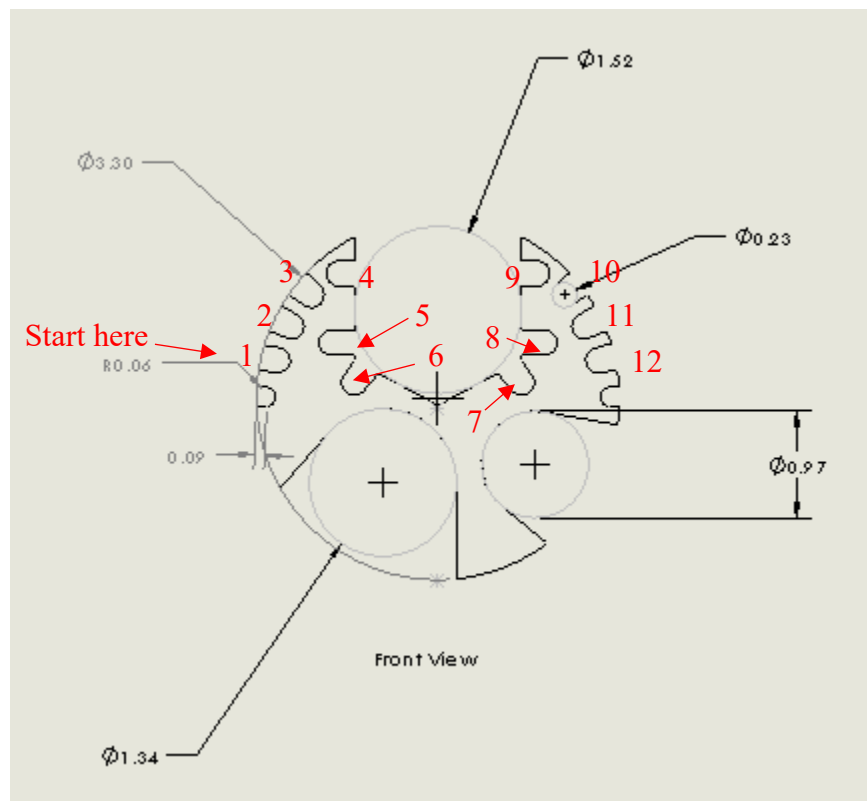
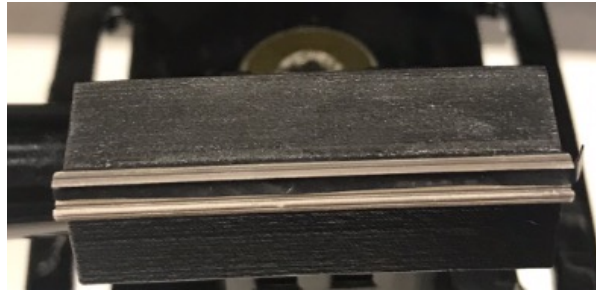
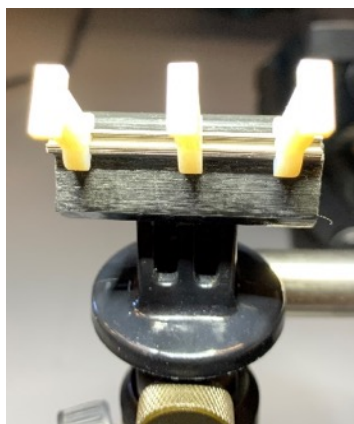


Fig. 2. Sample fiber installation order. Note: can be completed starting from the other outside set of fibers

1. Rotate the ferrule mount 90 degrees (with respect to the post) such that the outside of the ferrule on one of the sides is parallel with the table.
2. Using a razor blade, cut a very thin strip of electrical tape and place it on over top of the V-Groove to prevent glue from getting where it should not. Be careful not to cover the fiber channel closest to this groove (see picture). (this practice is up to the user's preference).



3. Grab three rolled pieces of custom fiber and set them aside.
4. Carefully open the wrapped fiber and unwrap one side by one revolution to leave the fiber with one short end and one longer end. Do this for all three fibers.
5. Place two fiber clips approximately 2mm from the distal and proximal faces of the ferrule. Place the final fiber clip on the center of the ferrule. The three clips help hold the fibers in place and reduces the chance of gluing two fibers into one channel.



6. Carefully place the three prepared fibers into one of the three open channels located on the ferrule. This can be done by placing the rolled portion of the fiber on the jig's horizontal bar, while carefully taking the longer end of the fiber spool and threading it underneath the fiber clip such that it sits in a channel. Add fibers in order from furthest channel to closest channel as outlined in Fig. 2.

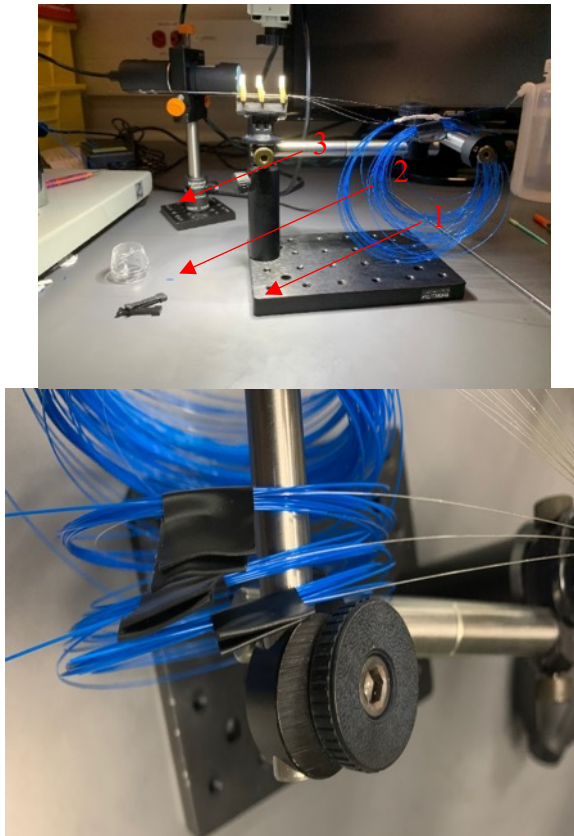
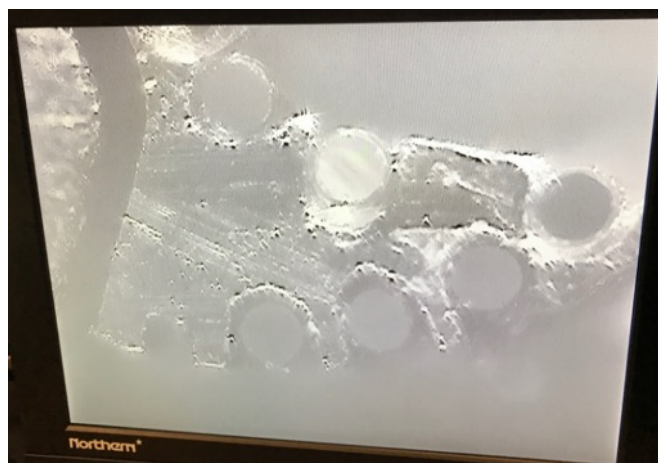


Fig. 3. Placement of fibers on horizontal jig bar in accordance with installation order (refer to Fig. 2)

7. Pull the fibers until approximately 3-4 inches of fiber is sticking out from the distal ferrule face. Clean the fiber using a Kim Wipe and optical cleaning alcohol (isopropanol, methanol, etc.).
8. Then cleave the fiber with the cleaver.



9. Repeat steps 7-8 for the remaining two fibers, make sure to be careful of the already cleaved faces. Also make sure there is a single fiber per channel, do not glue two fibers into the same channel.
10. Now, carefully pull back the fibers such that their face sits just inside the ferrule (~50 μm or less)
11. Check to make sure the fiber faces are well cleaved and undamaged utilizing the side viewing microscope.

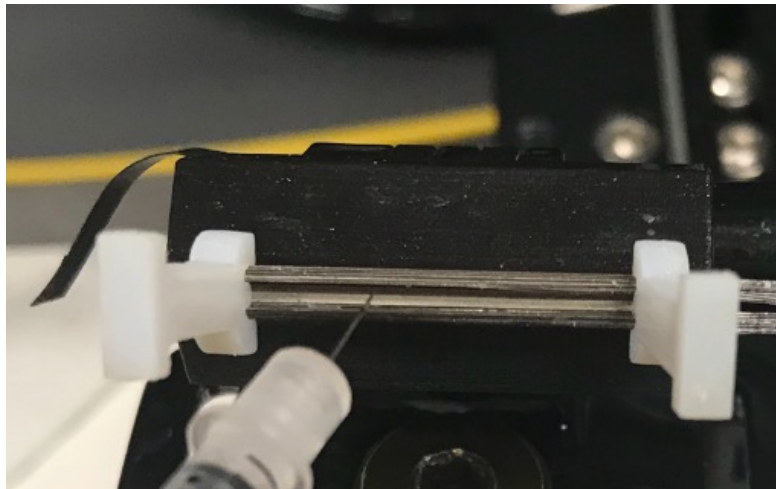


Some Notes on Gluing the Fibers in:

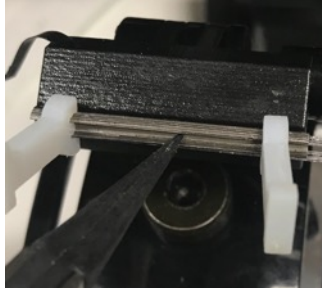
How to apply: Place a single drop of NOA 68 glue on a microscope slide. Use Insulin Syringe to carefully pick up a droplet of glue. Touch the needle tip to the desired location in the ferrule to apply the glue. Be mindful of your glue droplet size, as the glue will spread due to its low viscosity, so a large drop could quickly become a mess. Keep glue at least 5 mm away from the fiber faces and 2 mm away from the back of the ferrule.

How to cure: The NOA 68 glue is cured by the UV gun. Set the lamp to 60 seconds, if not set already, and aim the light at the desired cure location. Be sure to allow the lamp to cool in between 60 second rounds to prevent machine overheating. The internal fan will automatically shut off when ready for another round.

How to secure: Glue in ~ 1 cm lengths of the fiber starting at the distal end. Securing the fiber faces at the distal end first will prevent them sliding around and getting misaligned during further gluing. While curing, use the needle to gently press the fibers into the correct channels if they are not in the correct positions.



12. Using the needle, apply pressure across the fibers to push the glue down into the channels and pick up some of the excess. Apply glue to the distal section of the fibers so that the fiber face positions are held in place.



13. After the distal end has been cured, apply more glue down the rest of the ferrule/fibers.

Cure the rest of the glue repeating the curing process a few more times once the whole ferrule is secured.



14. Once the first three fibers have cured, the ferrule can be rotated such that the inner side of the ferrule on the same side is facing you and is tilted slightly upward.



15. Repeat steps 3-13 of the fiber gluing procedure to glue in the remaining three fibers on this side of the ferrule.

16. Once all six fibers have been glued in on one half of the ferrule, very carefully rotate the entire assembly 180 degrees taking care not to break any of the fibers. This is done so that the empty fiber channels on the opposite side can be as easily accessible.
17. Once rotated, repeat steps 3-16 for the remaining six fibers.

C.3 Standard Operating Procedure B02-024: Salpingoscope Stop-Objective Lens Gluing

This SOP guides a technician through the installation of an optical that is fixed to a ZnS lens.

The following standard operating procedure (SOP) was developed according to laboratory protocol.

**Standard Operating Procedures
University of Arizona
Biomedical Engineering Program**

SOP # B02-024	Title: Salpingoscope Stop-Objective Lens gluing
Origin Date: 07/31/19 Revision Date: 07/31/19 Rev. 1	Approval: Date Approved:

Supplies:

- Salpingoscope ZnS Lens Mount (3D printed, part file: Mount for lenses_Update 8-1_ZNS_objective holder_wChafer.SLDPRT)
- Salpingoscope Objective Lens (1.5 mm OD, UofA Precision Freeform Optics Design, Fabrication and Testing Facility)
- Stop aperture (1.3 mm OD with .264 inner aperture, Gateway Laser Services)

Glues:

- Norland 68 optical UV adhesive (Norland)

Miscellaneous:

- Kim Wipes
- Cleaning alcohol (ethanol, isopropanol, etc.)

- BD insulin syringe (31-gauge, 8 mm)
- Un-Powdered latex gloves
- Glass microscope slides
- Plastic tipped tweezers
- First Contact Cleaner in a BD insulin syringe to facilitate application.

Equipment:

- Surgical microscope
- Optical breadboard (English)
- UV epoxy curing gun
- UV safety glasses
- 1x ½" diameter optical post (1" long)
- 1x ½" diameter optical post base (2" long)
- 1x 90° ½ optical post holders
- Lens paper
- Edmund Optics (EO) MI-150 illumination lamp

Procedure:

In this procedure the technician installs and fixes the aperture stop on the ZNS objective lens used in the salpingoscope. This includes: cleaning the ZnS objective lens (ZOL), prepare Norland 68 to fix the aperture stop, center the aperture stop, pre-fixing the aperture stop, finalize the fixation of the aperture stop, and store the lens to prevent dust contamination. Make sure to wear gloves or finger covers throughout the procedure.

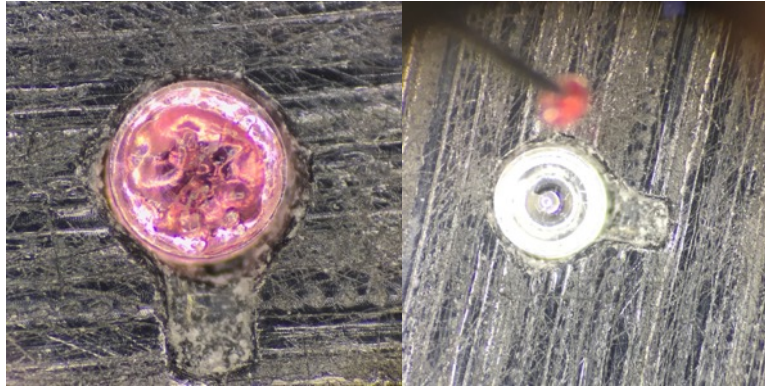
Placing ZnS Objective (ZOL) lens in the lens holder

1. In order to center and glue the stop in the ZOL, a jig must be constructed that holds the ZOL to facilitate the installation of the stop. The jig will ensure the technician has a top down view of the lens and the lens is held in place at all times. The jig is an aid for holding the lens in place and make the process easier. After construction the jig, the lens can be placed in the 3D printed lens holder. This jig is constructed utilizing the following equipment:

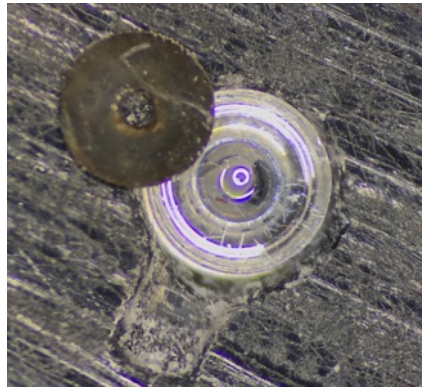
- 2x ½” diameter optical post (2” long)
- 90° ½ optical post holders
- ½” diameter optical post base (4” long)
- Optical breadboard or optical base



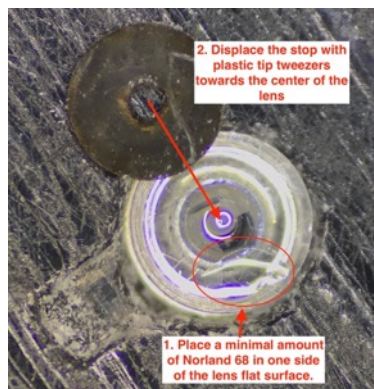
2. Place a drop of First Contact cleaner with an insulin syringe. Wait 20 minutes, and then remove it with a clean insulin syringe. Inspect using both: bright field illumination and dark field illumination to ensure the surface is free of dust. Evaluate scratches since ZnS is not a hard material.



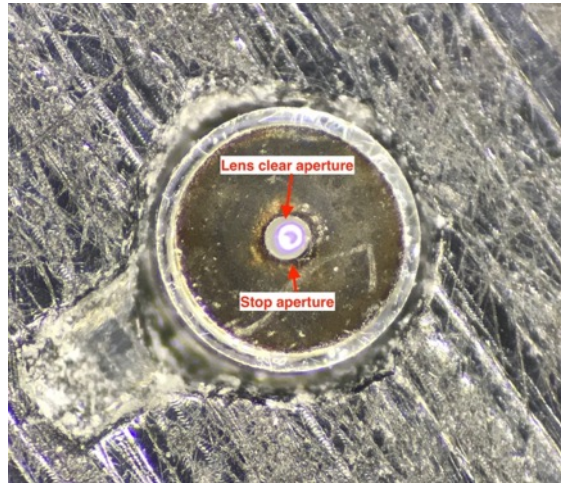
3. Place the stop next to the lens overlapping about 1/3 of the diameter of the stop.



4. Place a minimal amount of Norland 68 and displace the stop towards the center of the lens very slowly.



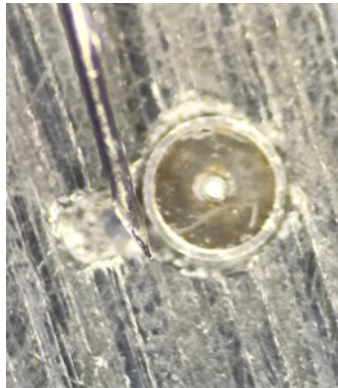
5. Center the stop aperture to the lens. The guide is the center aperture and the lens' clear aperture. A good guide is the edge of the clear aperture matching with the edge of the stop aperture.



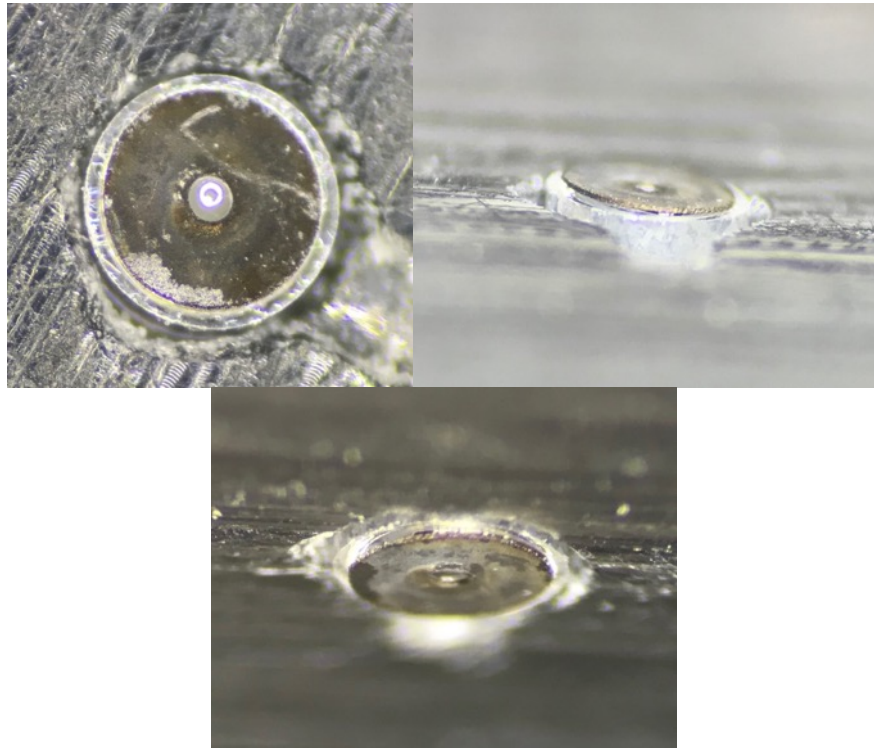
6. Push the stop down very carefully without moving the alignment. Readjust cocentrartion if needed and pre-fix the stop by curing Norland 68 with a UV curing lamp. Rotate the lens every 1 minute during 5 minutes exposure to make sure Norland 68 gets enough curing time and angles.



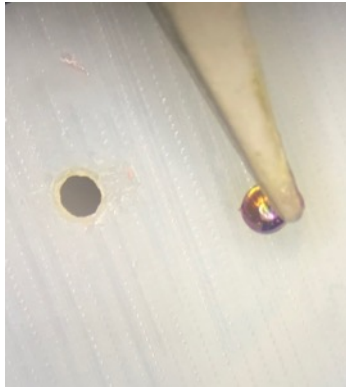
7. Double check for contraption. If the stop is not centered. Used methylin Chloride to dissolve Norland 68 and restart the process. If the stop is still centered, use capillary forces to insert Norland 68 in two more areas different than the initial cured Norland 68. This is accomplished by getting a small amount of Norland 68 in a side of the syringe needle and placing the needle sideways with the glue towards the lens on top of the lens just at the edge of the stop.



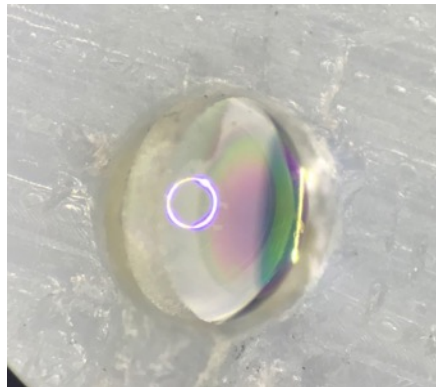
8. Inspect for centration and stop angle of stop. If centration is acceptable and the stop is mostly flat it should be usable.



9. Clean the back of the lens by holding it with tweezers and apply First Contact cleaner with the syringe. The lens may stick to the tweezer, but that is not a problem since it can be used later to remove the cleaner.



10. After the cleaner has dried then use the hole of the lens holder to hold the lens and peel the side of the cleaner. The results are really good.



11. Cover the lens with the lens bag to protect it from dust or other contaminants.



12. The Lens with the stop is ready to be installed in the ferrule.

C.4 Standard Operating Procedure B16-014: Salpingoscope Ferrule Construction

This document guides the technician through the steps to construct the salpingoscope ferrule assembly. The installation of the cover plate, objective, triplet, piezo scanning system, and working channel tubing are included in these instructions. The following standard operating procedure (SOP) was developed according to laboratory protocol

Standard Operating Procedures University of Arizona Biomedical Engineering Program

SOP # B16-014	Title: Construction of Salpingoscope Ferrule Assembly
Origin Date: 07/12/19 Revision Date: 07/12/19 Rev. 1	Approval: Date Approved:

Supplies:

- Salpingoscope Ferrule Mount (3D printed, part file: Ferrule Mount.sldpt)
- Salpingoscope Ferrule with 12 collecting fibers (3.3mm OD, Majer Precision) See SOP B02-14
- Salpingoscope Piezo assembly (1.0 mm OD, PI) See SOP B02-13
- Salpingoscope Objective Lens with Stop (1.5 mm OD, UofA Precision Freeform Optics Design, Fabrication and Testing Facility) See SOP B02-019
- Triplet lens (1.5 mm OD Optics Technologies Inc.)
- Cover plate (3.3mm OD, Bern's Optics [no working channels] or Rayotek [if working channels will be installed])

- Working channel tubing [if working channels will be installed] (335-II Polyimide w/ PTFE Comp ID, MicroLumen)
- Working channel tubing [if working channels will be installed] (480-II Polyimide)

Glues:

- Norland 68 optical UV adhesive (Norland)
- Loctite 4013 (Medical Grade Super Glue)

Miscellaneous:

- Kim Wipes
- Cleaning alcohol (ethanol, isopropanol, etc.)
- BD insulin syringe (31-gauge, 8 mm)
- Un-Powdered latex gloves
- Glass microscope slides
- Expired nylon surgical suture
- Plastic tipped tweezers
- First Contact Cleaner

Equipment:

- Wi-Fi microscope (Max-See)
- Surgical microscope
- Optical breadboard (English)
- UV epoxy curing gun

- UV safety glasses
- 3x ½” diameter optical post (1” long)
- 2x ½” diameter optical post base (2” long)
- 1x ½” diameter optical post base (1” long)
- Spare laptop in lab (Donated by P.S. Rice)
- 2x 90° ½ optical post holders
- Lens paper
- Edmund Optics (EO) MI-150 illumination lamp

Procedure:

In this procedure the technician constructs the ferrule assembly to be used in the Salpingoscope handle. This includes, gluing the cover plate, aligning the objective lens and the triplet and gluing them in place, aligning and gluing of the piezo assembly, gluing the working channels if needed, cleaving/splicing of the fiber, and gluing of the end mass. Make sure to wear gloves or finger covers throughout the procedure.

Placing cover on ferrule

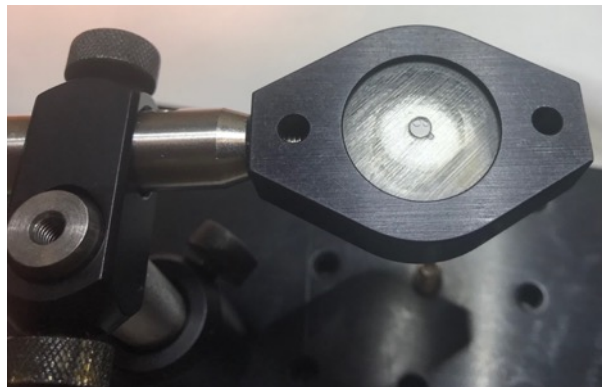
13. In order to center and glue in the cover plate, a jig must be constructed that holds the ferrule face-forward towards the surgical microscope. This will ensure the technician has a top down view of the assembly and can align the ferrule and the cover concentric to each other. The ferrule should be placed on the 3D printed ferrule holder with the fibers suspended by a ½ optical post in the back. This jig is constructed utilizing the following equipment:

- 2x ½” diameter optical post (4” long)
- 90° ½ optical post holders
- ½” diameter optical post base (6” long)

The entire base here the ferrule is at is removed from the current optical post base and is positioned in the 6” post base as seen in the picture utilizing a 90° ½ optical post holders and two ½” diameter optical post that are 4” long. In this picture the cover is already on place.



14. Using the stereoscope, the cover needs to be cleaned before installation. This cleaning is a general cleaning before the final cleaning of the optical area. The cover can be placed in a 3D printed cover holder that fits in a lens assembly as seen in the picture.



The cover side that is going to be exposed is not as important to be clean at this point, but the side that will be facing the ferrule should be as clean as possible to avoid debris inside the endoscope. To clean the cover, follow the next procedure.

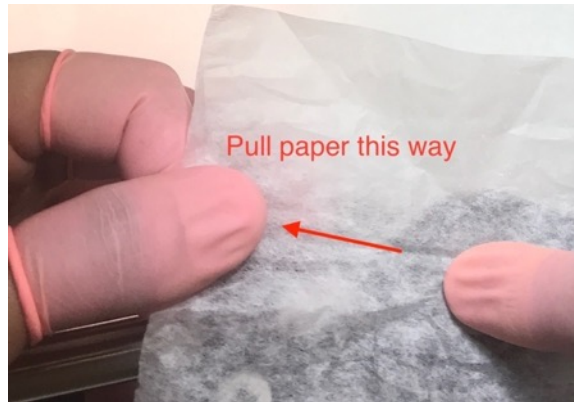
- Grab one sheet of lens paper (not Kim Wipes) and drop 1 or 2 drops of acetone on it.



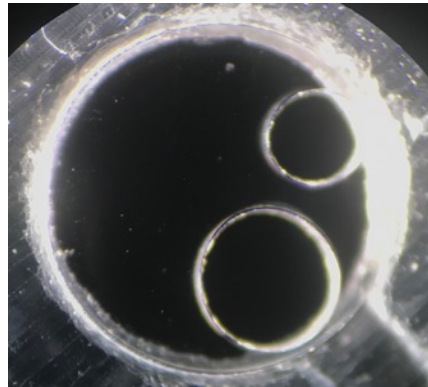
- Wait for the acetone to evaporate almost completely to avoid acetone droplets on the cover surface. Once acetone is almost dried, place the acetone area of the lens paper on top of the cover holding it gently with one finger on top of the cover.



- Gently slide the paper towards the dried side of the lens paper.



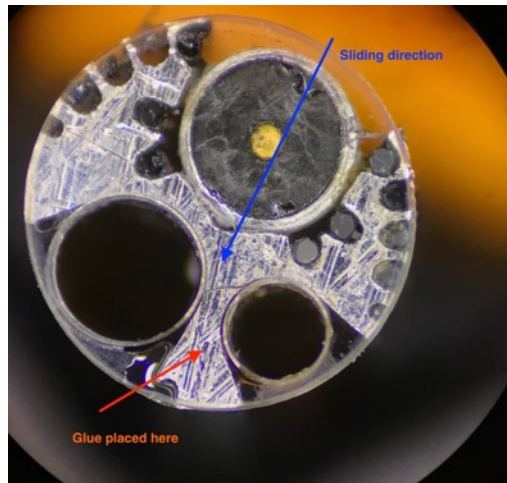
- Repeat the process until the area is seen clean under the stereoscope as seen in the picture.



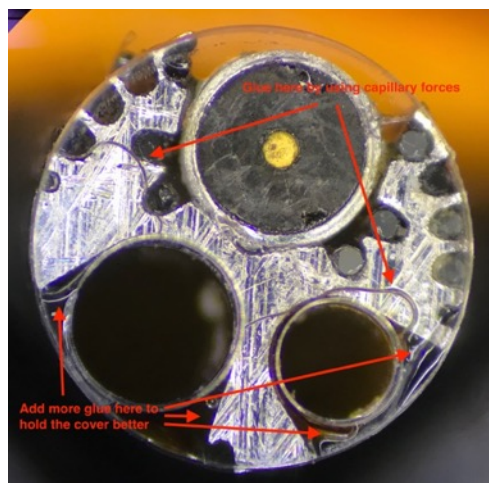
15. The entire assembly holding the ferrule with the 12 fibers is placed under the stereoscope preferably with a cardboard box in case the cover falls from the ferrule or from technician hands.

16. Using the stereoscope, place Norland 68 in the ferrule extension between the working channels and slide the cover into place. Gently adjust the cover position using little finger taps go get it on place. Note that the picture shows the objective for clarity, but the

objective will not be installed at this stage. Cure the Norland 68 with 5 minutes of UV exposure.



17. Using capillary effects glue is placed next to the working channel to hold the cover from both sides. And additional Norland 68 was placed between the ferrule, cover, working channel boundaries to help the cover to stay in place.

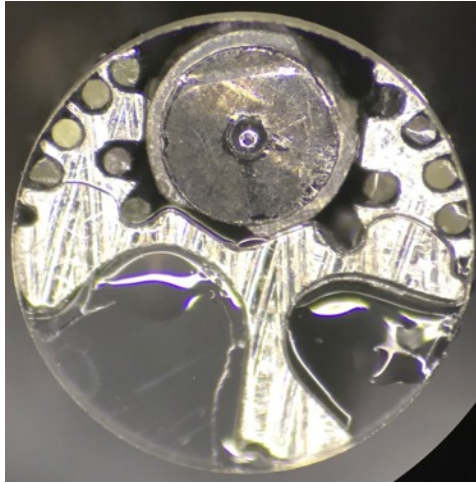


18. Cure at least 6 minutes with UV light since there is a significant quantity of Norland 68

19. Waiting 24 hours for Norland to bond strongly with the cover and metal before continuing will ensure that the cover does not come off in the next steps.

20. The inside of the two working channels should be sealed with the medical grade master bond epoxy during handle assembly construction. Add additional Norland 68 on the

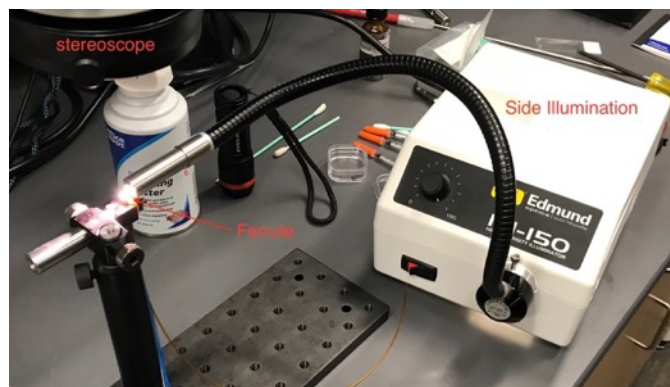
entire T shape to avoid the the risk of contaminating the lenses when assembling to the hypotube. The final footprint of Norland is seen in the picture. Note that the lens assembly will not be installed at this stage but it is shown for clarity.



Cleaning and inspection of cover plate in ferrule

Once the ferrule is installed, it can be inspected using dark field illumination. This technique can be used to inspect the cover at any stages of the process. During installation, after placing the objective lens and at the end of the ferrule assembly procedure. The cover should be cleaned specially at the central aperture on the stop (black disk installed in the objective lens).

1. Place the ferrule under the stereoscope without a cardboard box, and illuminate using the EO MI-150 lamp from a side.



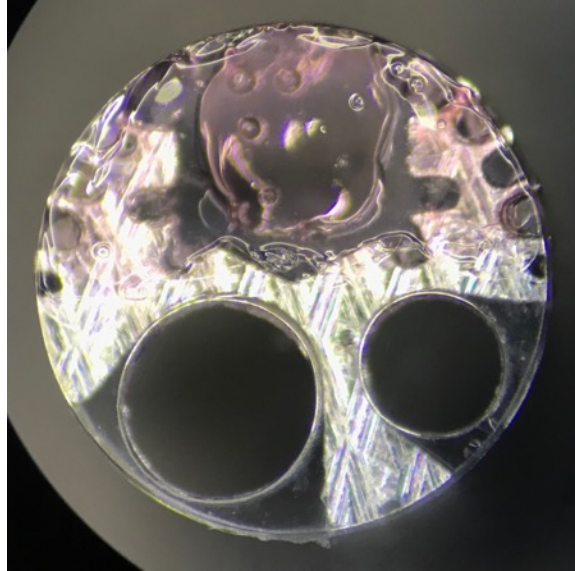
2. Using the stereoscope, inspect the cover plate. You may observe something similar to the following image. Notice that this cover was purposely contaminated to evaluate the cleaning method.



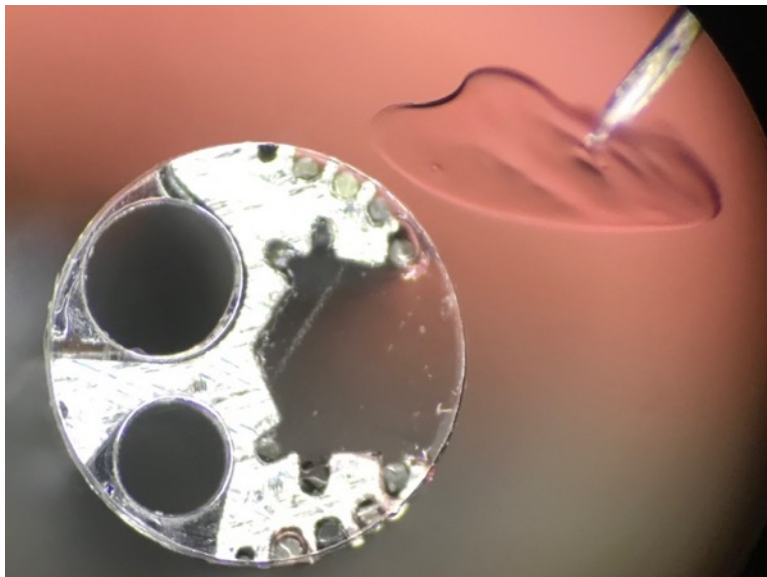
3. Using compressed air (from a safe distance) blow any major particles.



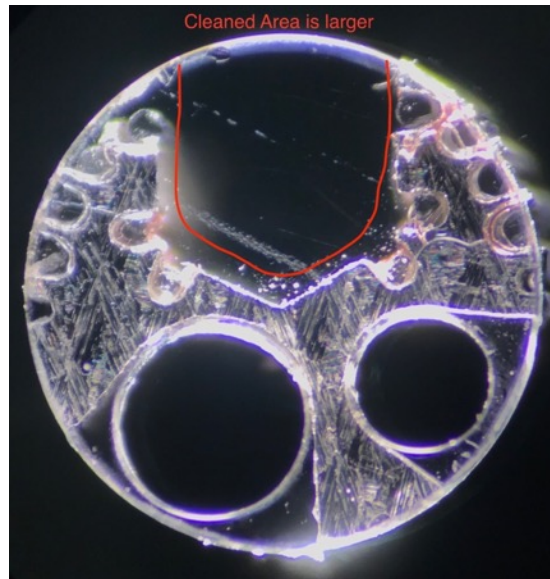
4. Using First Contact cleaner in a syringe, apply the cleaner to the center area of the bottom of the cover. Optionally, also apply to the top area to improve the inspection judgment of the cover. Wait about 30 minutes for the First Contact cleaner to dry.



5. Remove both layers of dried First Contact Cleaner using a syringe. This process should be done very carefully and slowly to avoid any scratches on the cover. Lift one side of the film and from there puncture the film and pull it side to side.



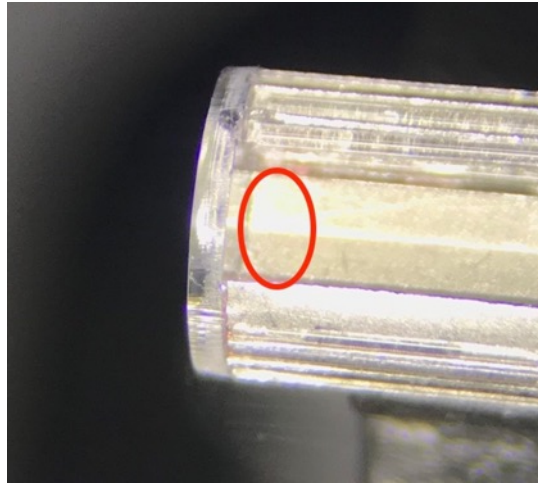
6. Inspect the cover using dark field illumination as explained before for its cleanliness. If the cover has any particles in the area where the objective aperture will be, repeat the process until it has no particles at this place. Note that the cleaned area is larger than the aperture.



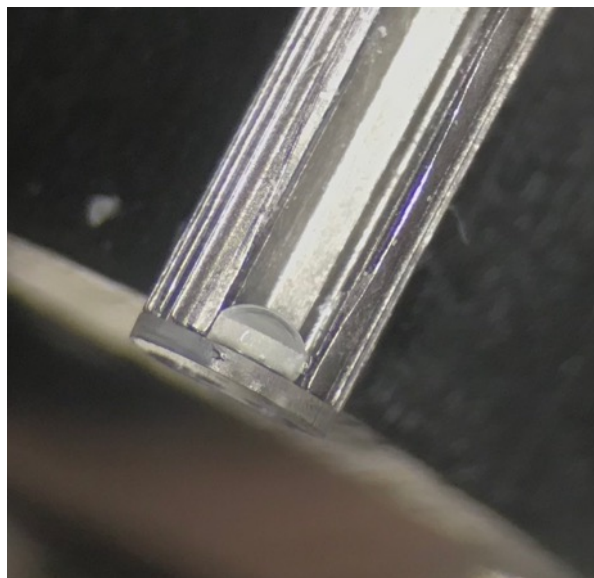
Placing the objective lens, the triplet lens and the piezo assembly in the ferrule (time consuming process that needs to be done the same day to avoid issues with Norland 68)

After following the instructions in SOP B02-019, the objective lens can be installed in the ferrule as follows. At this stage the objective lens should be clean and mounted on a lens holder or stored in a lens safe container. The technician has to be very careful since the only surface available to clean from this lens is the back surface. The stop surface should be kept clean during this process since first contact cannot be used to clean this surface anymore. If needed only alcohol base or acetone cleaner can be used on the stop side of the lens.

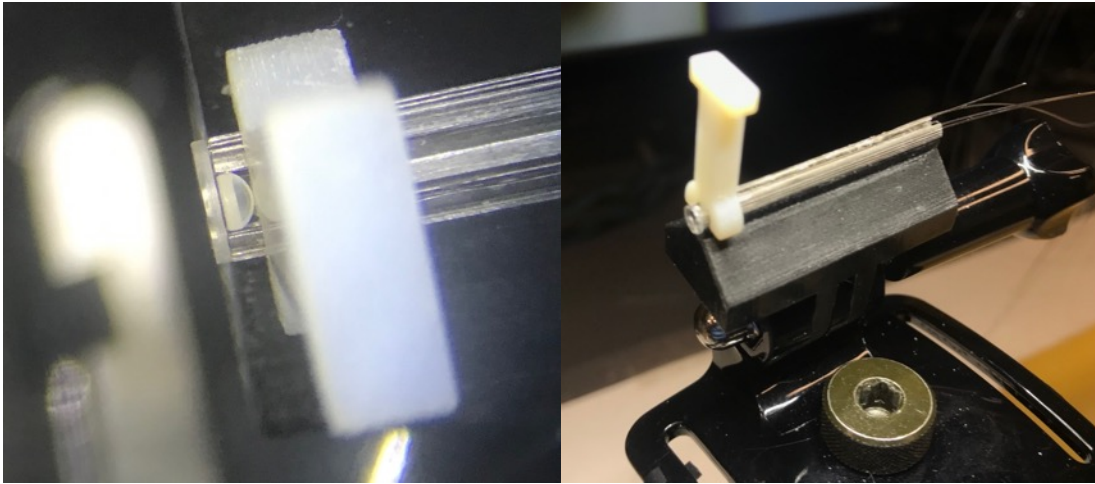
1. Place very little Norland 68 on the V-channel of the ferrule next to the cover but not touching the cover.



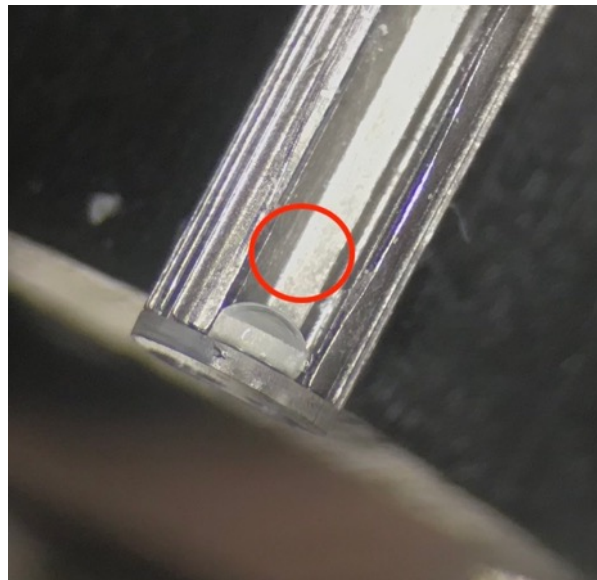
2. This step is challenging since the lens should be placed without contaminating the optical surfaces. Slow and careful movements are recommended here. Remove the objective lens from its current holder or storage and place the stop side of the lens parallel to cover plate. Check for contamination on the cover from the liquid Norland in the bottom of the ferrule. If the cover is contaminated, clean it with ethanol, and then follow the cover cleaning procedure and restart this process. **Do not** cure the Norland 68.



3. If the positioning of the lens is successful, a 3D printed fiber holder can be used to hold the lens in place and to make sure it is flush with the cover.

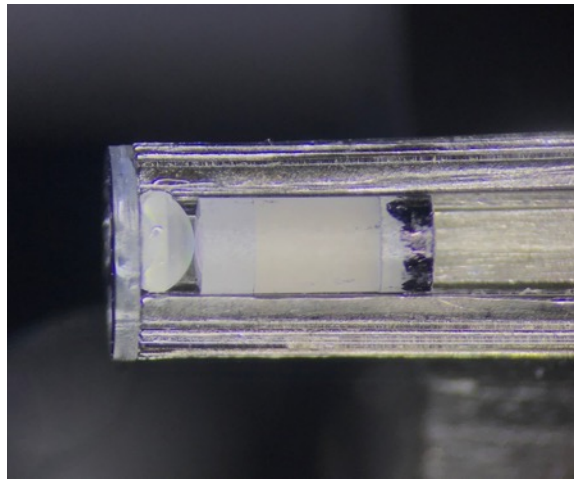


4. Place very little Norland 68 on the V-channel of the ferrule behind the objective lens but not touching the lens. Allow space for the triplet front face curvature (Sag) and the objective lens curvature (sag).

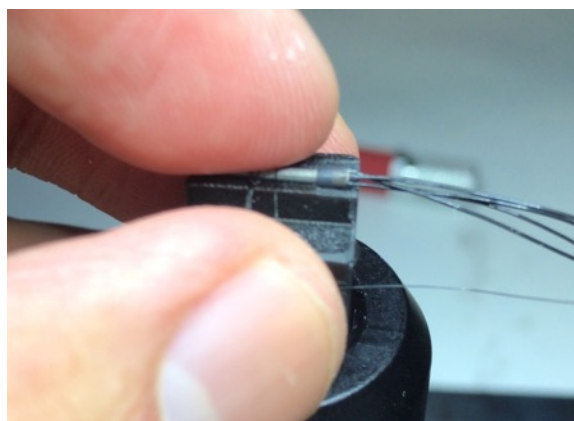


5. Place the triplet. Remove the triplet lens from its current holder or storage and place element 1 (marked in black) facing against the objective lens. Check for contamination

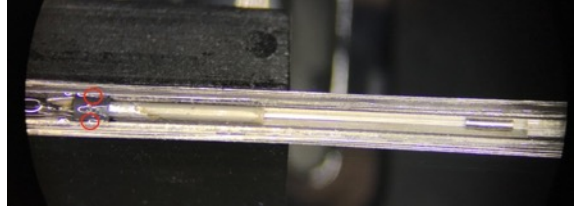
on the cover and interface between objective lens and triplet from the liquid Norland in the bottom of the ferrule. If the cover or the lenses are contaminated, clean it with ethanol, and then follow the cover cleaning procedure and restart this process. **Do not** cure the Norland 68.



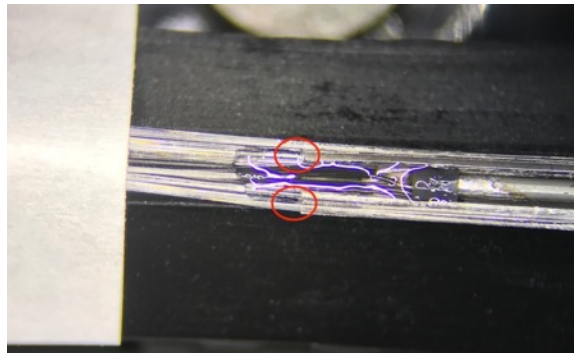
6. Align with reference to the ferrule linear features but **do not** cure the Norland 68 until the piezo assembly is installed and all three components are aligned.
7. Remove the piezo assembly from its current holder. The easiest way is to cut the nylon strings or by pulling to the collar side.



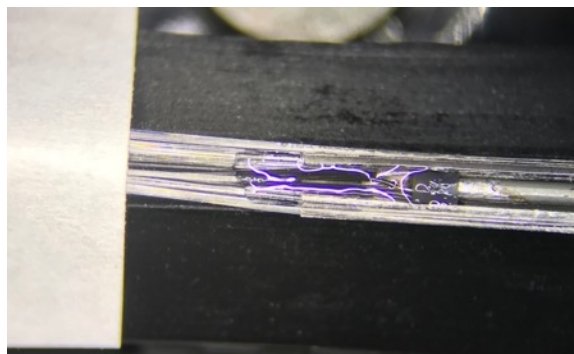
8. Install the piezo in the ferrule, center the fiber and adjust the distance between the fiber tip and the lenses to $\sim 270\mu\text{m}$. Use a small amount of Loctite 4013 to fix the piezo collar in the ferrule as closely aligned as possible.



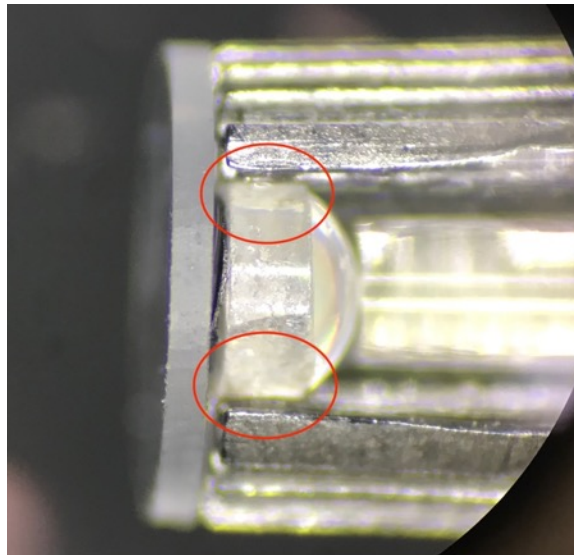
9. Use two drops of Loctite 4013 on the back of the ferrule to protect the wires from braking or detaching from the piezo. This holds the wires really well.



10. Fix piezo cables and fibers by filling up the cavity with Loctite 4013. This protect both the fibers and the piezo cables.



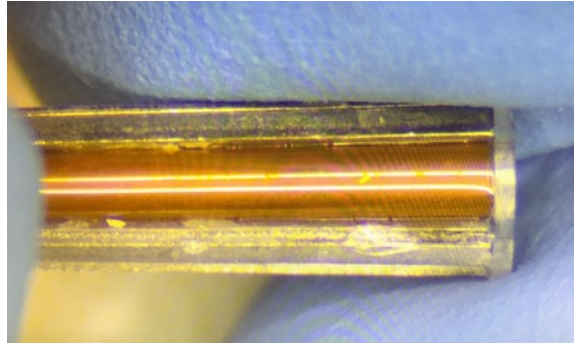
11. Fix objective by adding two drops of Norland 68 between the objective sides and the ferrule. Be careful with capillary forces sucking up Norland between the cover and the objective. Also be aware of keeping the back of the objective lens clean.



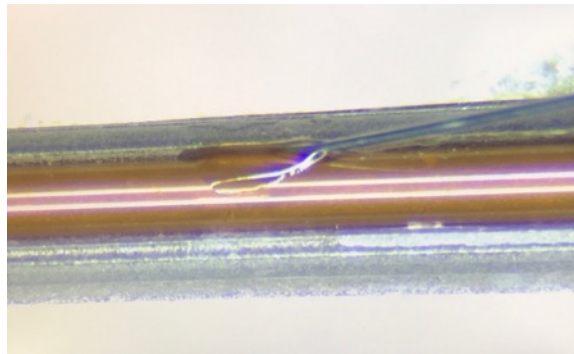
12. Fix triplet following the same process from step 11.

Installing the working channels (optional)

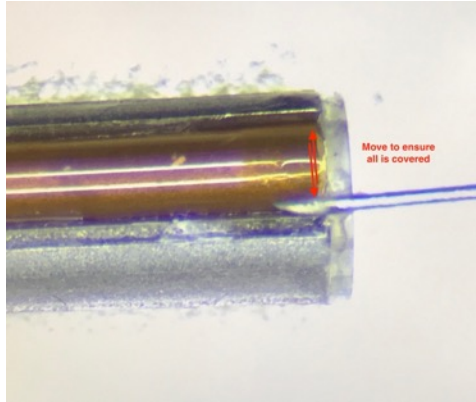
1. Start by making the whiter working channel flush with the ferrule cover and lay down the tubing along the entire length of the ferrule.



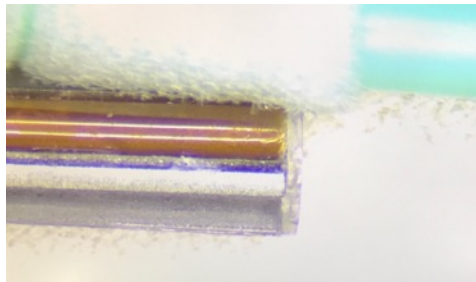
2. Then, grab medical super glue with the tip of a needle, and place the glue along the gap between the tubing and the ferrule. Repeat in the other side of the tubing and on different places along the length of the ferrule. All the time, check that the tubing is flush with the cover plate. If the tubing is not flush, remove the glue with acetone being careful not to contaminate the optical system and start again.



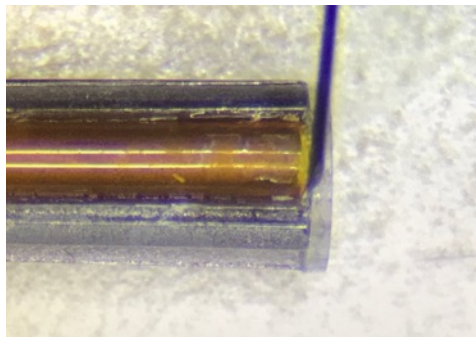
3. Grab medical super glue with the tip of a needle again and place it in the boundary between the glass and the tubing. Move the needle from one side to the other to make sure the entire exposed circumference is covered with medical superglue.



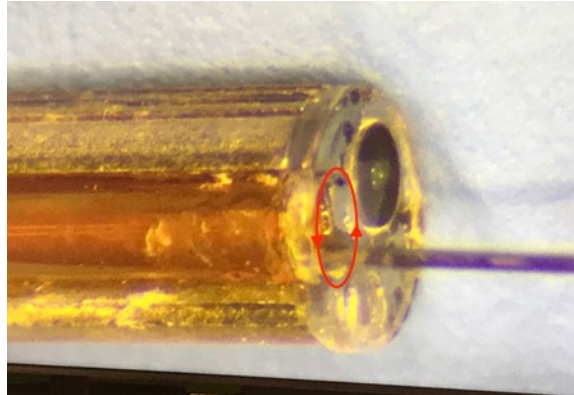
4. Clean any excess at the edge of the cover or ferrule with an optical cleaner.



5. Add more medical supper glue to the corner of the gap and allow the glue to propagate using capillary forces towards the back side. Clean any excess of super glue.



6. Grab more medical grade super glue and seal the interior gap of the tubing-cover interface. Introduce glue to the channel and then move the syringe needle using a circular motion around the edge to cover the entire gap.



7. Repeat the process with the small working channel.

The ferrule is ready to be installed in the Salpingoscope handle following Salpingoscope handle construction.

C.5 Standard Operating Procedure B16-012: Salpingoscope Handle Assembly

This document guides the technician through the steps to construct the salpingoscope handle using the completed ferrule assembly. This process includes preparing the handle, installing the ferrule and sealing the gap between the ferrule and the hypotube, installing the working channels (optional), installing the distal tubing, and sealing the handle. The following standard operating procedure (SOP) was developed according to laboratory protocol.

**Standard Operating Procedures
University of Arizona
Biomedical Engineering Program**

SOP # B16-012	Title: Salpingoscope Handle Assembly
Origin Date: 08/08/19 Revision Date: 08/13/19 Rev. 1.1	Approval: Date Approved:

Supplies:

- Salpingoscope handle (3D printed, part file: 3.4_WorkingChannels_Left.STL and 3.4_WorkingChannels_Right.STL)
- Salpingoscope completed ferrule SOP # B02-018
- 8x M3x0.5 Locking Nuts
- 8x M3x0.5 8mm machine screws
- Hypotube (Microgroup, Inc, MAT-CUT-HYPO, Material No. 97401156)
- Hypodermic needle gauge 21 (EXEL, 12Gx1)
- Shrink tube large (Raychem, MT5000-1/2-0-SP)
- Shrink tube clear (Raychem, CM9833-000)
- Vinyl tube 3/16" diameter (ACE, 4027470)

Glues:

- Loctite 4013 (Medical Grade Super Glue)
- Master Bond EP42HT-2Med (medical grade epoxy)

Miscellaneous:

- Kim Wipes
- Cleaning alcohol (ethanol, isopropanol, etc.)
- 3x BD insulin syringe (31-gauge, 8 mm)
- Un-Powdered latex gloves
- Plastic tipped tweezers
- First Contact Cleaner
- Lens paper
- Sticky labels (preferably paper)

Equipment:

- Surgical microscope
- Optical breadboard (English)
- 1x 4" post base
- 1x 2" post base
- 1x 2" post
- 1x 4" post
- 1x 90° post holder
- 1x small prism holder

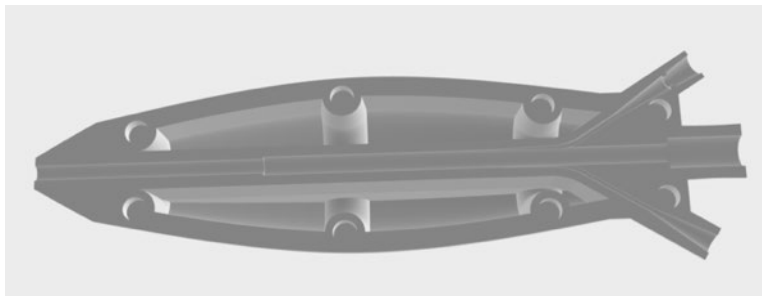
- Table clamp
- Manual hacksaw
- Metal hand file (flat if available)
- Heat gun
- Guide wire (gauge 25 or smaller)

Procedure:

In this procedure the technician constructs the handle assembly using the completed ferrule assembly. The working channels installed in this endoscope are optional depending on the setup being constructed. This process includes, preparing the handle, install the ferrule and seal the gap between the ferrule and the hypotube, install the working channels (optional), install the distal tubing and seal the handle. Make sure to wear gloves or finger covers throughout the procedure when handling abrasive chemicals or glues.

Installing the nuts in the handle for the locking mechanism

1. Clean ALL support material out of handle following B02-3D1 Dissolve Support Material for 3D printed parts.
2. Take the half of the handle that has the larger in diameter non-through hole spaces for the nut/screw locking mechanism (bottom side)



3. Take as single screw and twist it partially into one of the locking nuts, enough to attach the two without falling but not so much that you are completely screwed in.



4. Take the medical grade super glue and apply it to the outer edges of the locking nut



5. Now utilizing the screw as a placement tool press fit the nut into one of the open channels on the handle.



6. Allow about 10-15 seconds in this configuration and then slowly unscrew the bolt from the nut. Leaving only the nut in place. Allow this to dry.



7. Repeat steps 3-6 until all 8 nuts have been glued into place.



8. Glue the hypo tube to the front of this side of the handle. Notice that the hypotube has to be aligned to the edge that is 3D printed onto the handle. Use medical grade super glue.



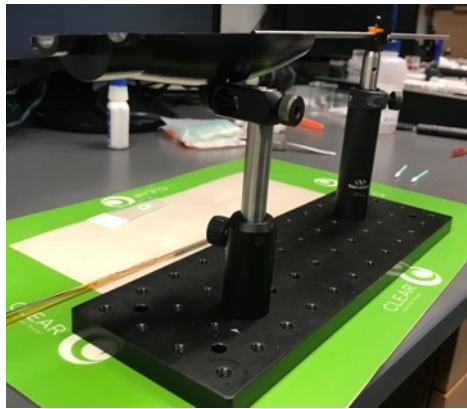
Installing Ferrule in the handle

1. The gig for this task is can be assembled using:

- 1x optical breadboard
- 1x 4" post base
- 1x 2" post base
- 1x 2" post
- 1x 4" post
- 1x 90° post holder
- 1x small prism holder

Lay the handle in one side of the holder and insert the hypo tube in the prism holder.

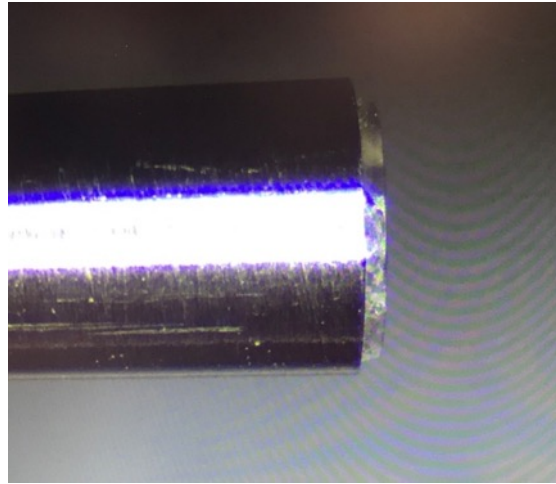
Lock the hypo tube in place to avoid rotation of the handle.



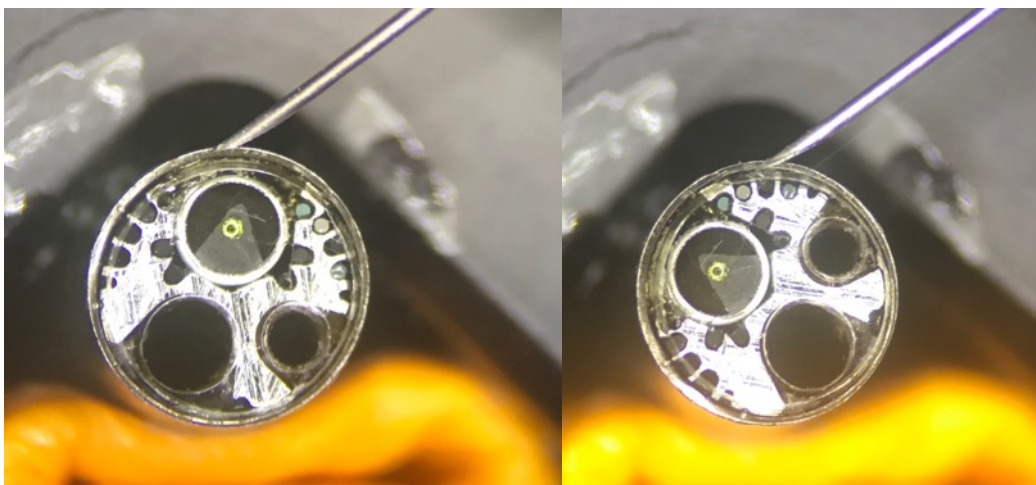
2. Insert the ferrule to the hypo tube through the back and push it until it emerges in the distal end of the hypo tube.



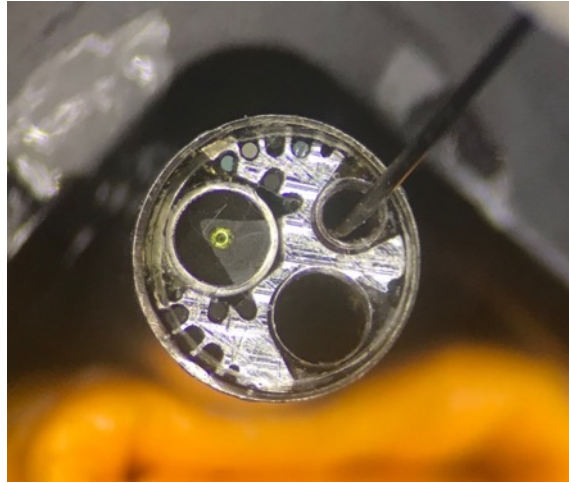
3. Adjust the position of the ferrule, so the hypo tube is only covering half of the thickness of the cover plate.



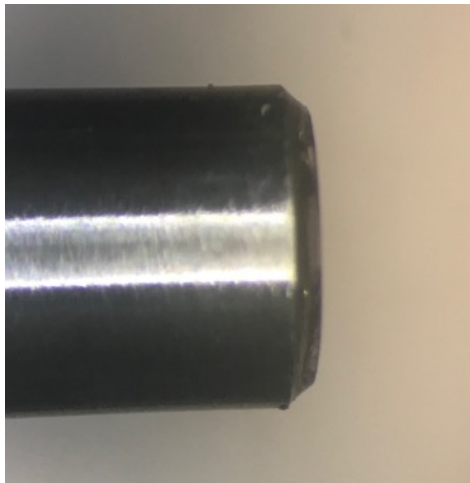
4. Prepare a small amount of Master Bond EP42HT-2Med epoxy and wait about 2.5 hours for precuring. The viscosity will help the epoxy to stay in place and not to drip and contaminate the ferrule or lens assembly. After testing master bond for a tick viscosity, seal the gap between the cover and the hypo tube using the Master Bond EP42HT-2Med epoxy. Using an insulin syringe, grab a small amount of epoxy and place it in the boundary between the hypotube and the cover glass. Be careful about contaminating the front face. Then, rotate the endoscope very carefully and seal the next section.



5. Continue the process until the entire gap is sealed. Inspect for contamination on the lenses. If contaminated evaluate the possibility of restarting the process. If working channels are installed, seal the working channels using epoxy.



6. After waiting for 24 hours and leaving the endoscope facing up while curing, inspect the fully cured epoxy. The epoxy should create a smooth surface between the cover glass and the hypotube.

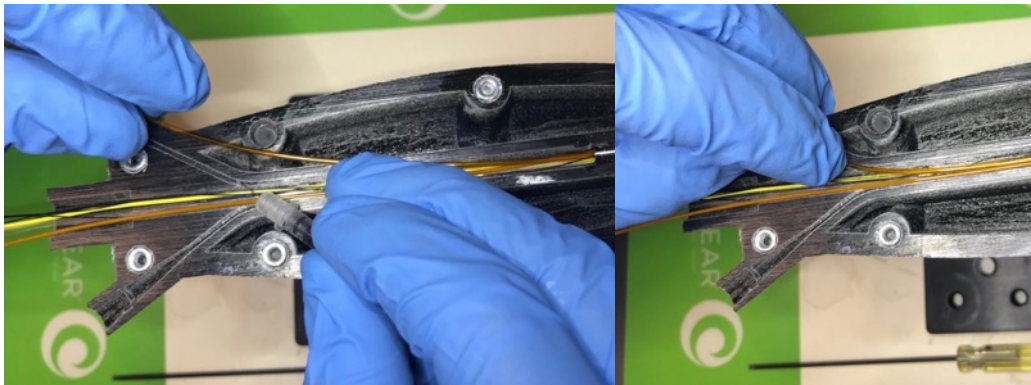


Installing the working channels in the handle (optional)

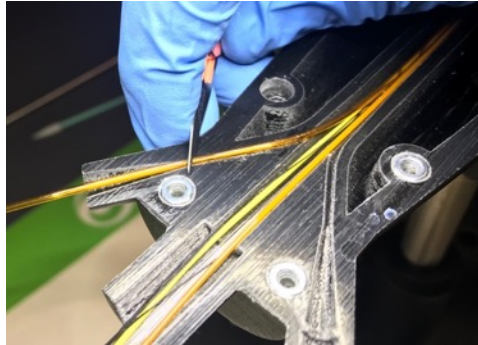
1. When the salpingscope includes working channels, these steps should be followed for proper functioning of the working channels. Note that the working channels are different in outer diameter. Identify the larger and the smaller tubing for the working channels since they should be installed in the matching channel in the 3D printed handle. The thick working channel is installed towards the V-only exit. This exit has no additional features but an enlarged exit.



2. Use medical superglue to fix a small part of the working channel in place. Make sure the channel is fitting well and it is not over bent or stretched.



3. Using a scalpel to remove the extra tubing. The cut should be made at the beginning of the v expansion or before the beginning of the expansion. Make sure that the tubing is not squished after it is cut.



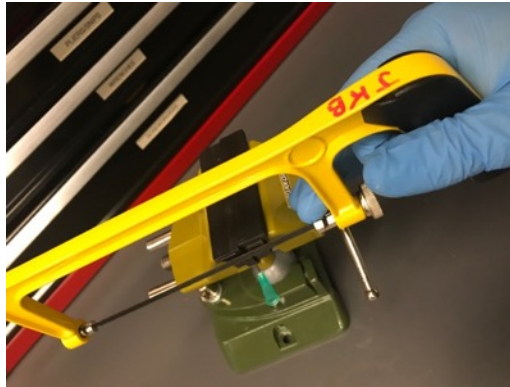
4. Using capillary forces fill up the boundary between the handle and the tubing.



5. The thin working channel is installed towards the V with additional syringe holding features. A needle of gauge 21 is needed to install the thin working channel. In this case we used EXEL hypodermic needle gauge 21.



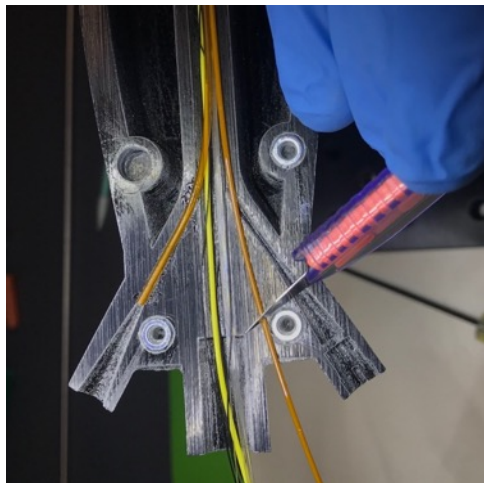
6. First cut about half of the needle using a table clamp and a manual hacksaw.



7. Remove remaining sharp edges with a metal hand file. TIP: use a square hand file since it is easier.



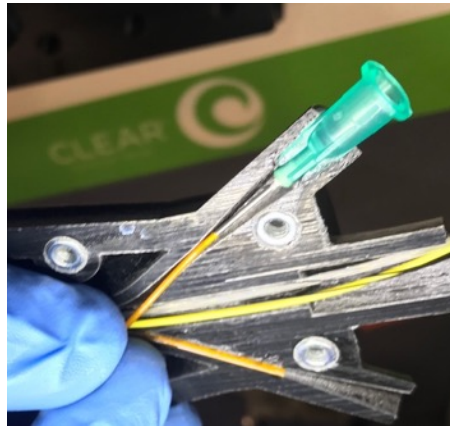
8. Cut the thin tubing about half way of the V shape in the handle.



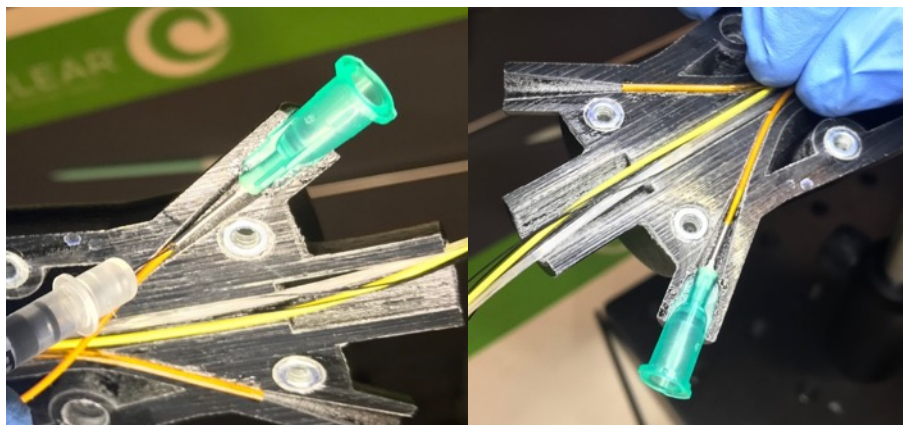
9. Place the syringe needle in the handle making it fit to the shape. It should be held as seen in the picture. Then, fill up the gaps with medical grade super glue. Note, if the needle is too long and no space is left between the needle and the handle it has to be shortened.



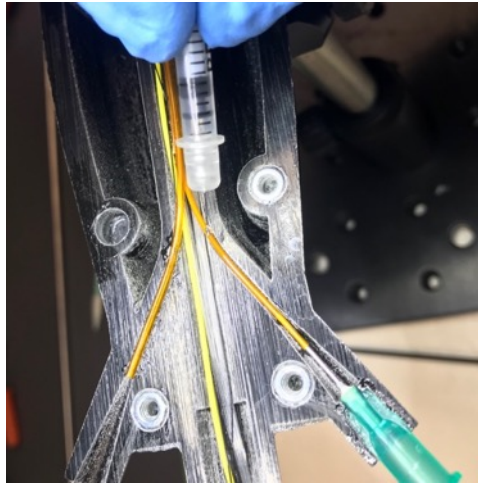
10. Insert the tubing into the initial ~2 mm, but making sure it is not pushed all the way.



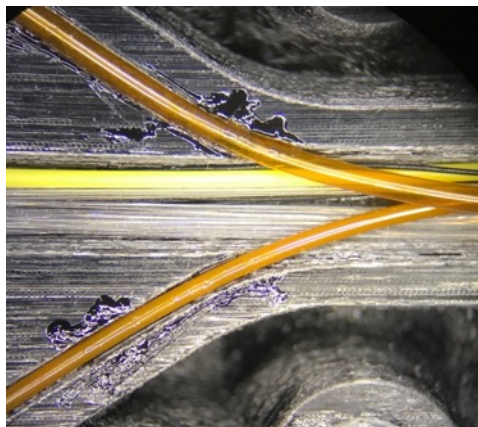
11. Place glue around the needle next to the tubing, and push the tubing, so it gets glued to the needle making sure it falls in the channel printed in the handle.



12. Glue the sides of the tubing to the gap in the 3D printed holder. It is better if it is done through the entire length.



13. Check for any strain or damage to the curved parts of the tubing. A smooth curve will allow for a better insertion of medical tooling.



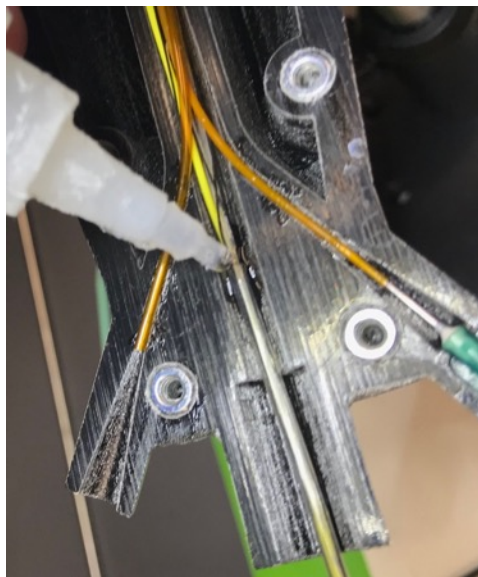
Fixing the fibers and wires to the proximal side of the handle.

1. To ensure that the fibers and wires are not crushed when the handle is closed, they should be glued to the cavity. To begin this process, insert all 12 collecting fibers, 1 dual clad fiber and 4 piezo wires into the CM9833-000 shrink tube. and shrink 1/2 of the tube using

the heat gun in low heat. If high heat is used, the jackets for the double clad and piezo wires may melt.



2. Glue the distal side of the shrink tube to the handle and ensure that all the wires lay almost flat in the handle cavity.



Installing vinyl protective tubing

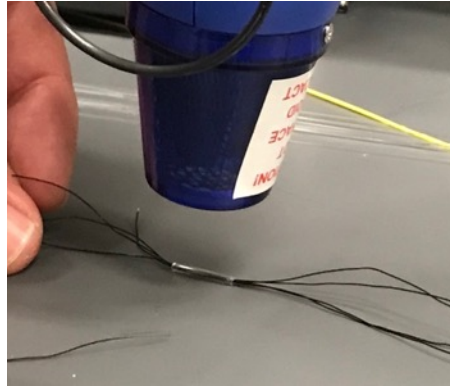
1. The vinyl protective tubing is installed to protect all fibers and wires from the handle to the control and sensors salpingoscope rack. The first step is to extend the fibers and wires along the table.



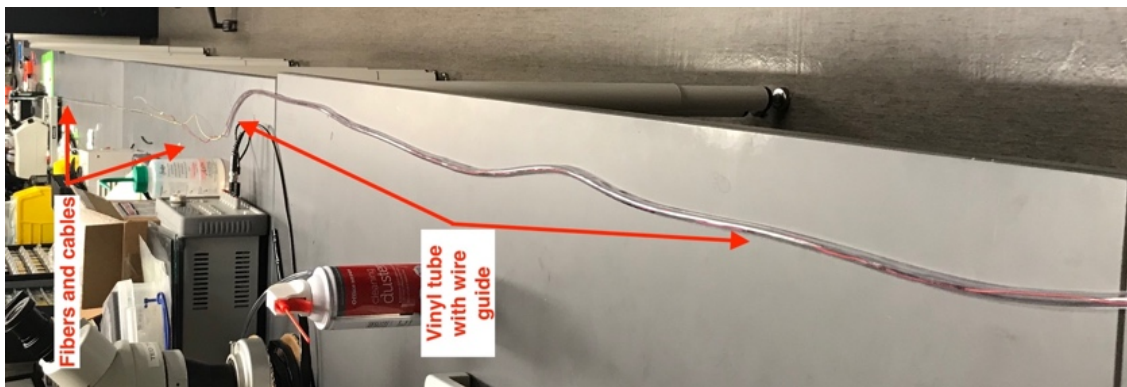
2. Then prepare 2.5 m of 3/16" diameter Vinyl tubing by straighten it. Any curved lengths of the tube will be a difficulty for the fibers at this stage. Therefore, it is recommended that the tube is almost straight before continuing.



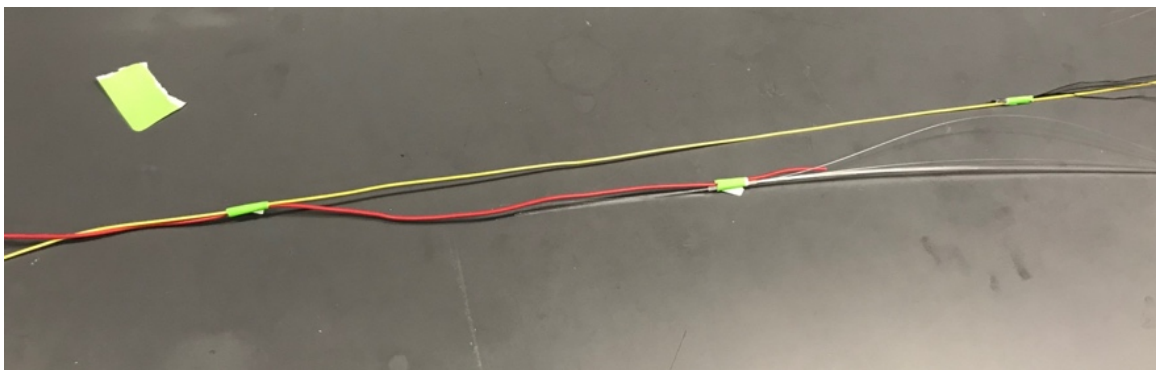
- Using about 1 cm of CM9833-000 shrink tube hold the tips of the 4 piezo cables by shrinking it. Using another 1 cm of CM9833-000 shrink tube hold the tips of all 12 collecting fibers.



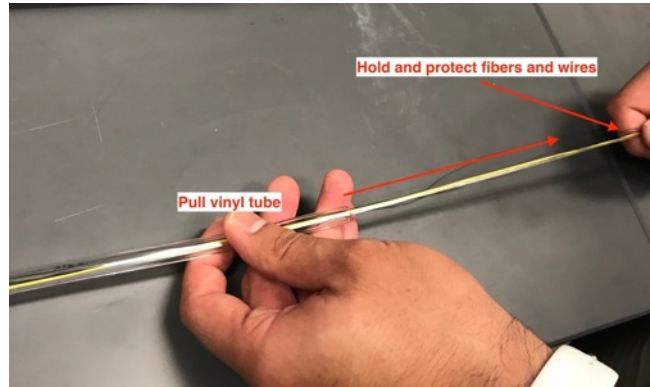
- Pass a wire through the vinyl tubing to be used as a guide for the cables and fibers. And lay the vinyl tubing with the wire flat in the rest of the table.



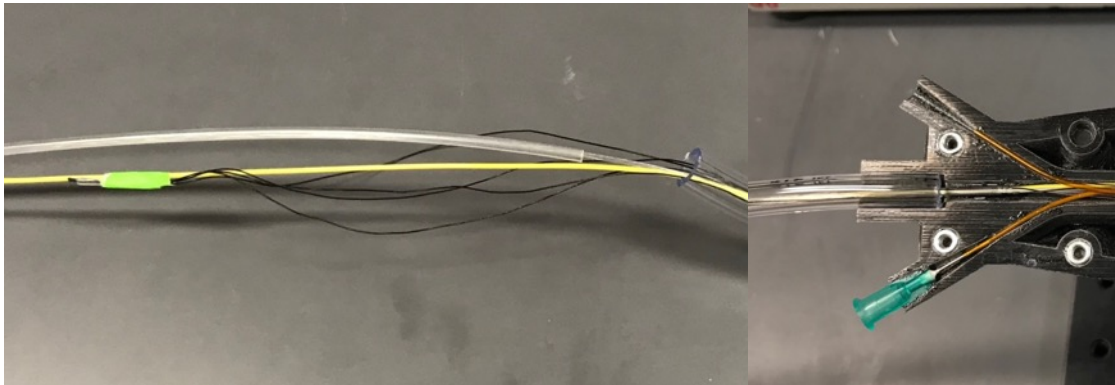
- Attach the larger cable or fiber(s) first to the red wire and continue attaching the next larger cable or fiber(s) until all are attached to the wire guide. Sticky paper labels seem to work better than electrical tape since they have less friction with the vinyl tube.



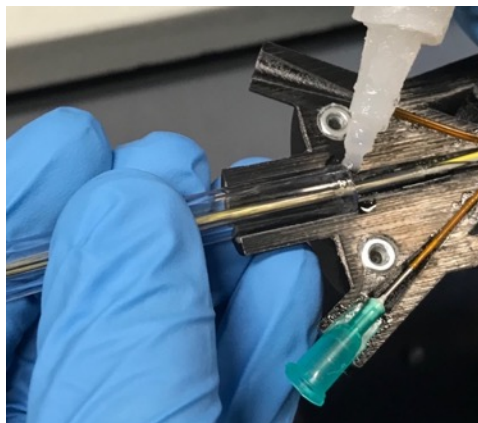
6. Holding the wire guide in place, pull the vinyl tube towards the handle being careful with the fibers. If fibers bend at the end, pull the vinyl tube back and adjust the attachment point to the wire guide. This will prevent breaking any fibers.



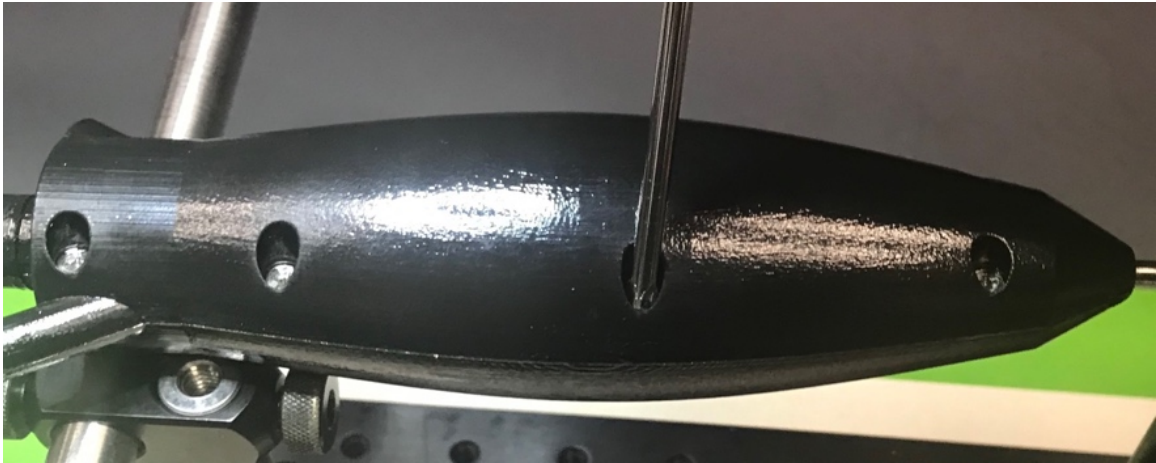
7. Continue until the distal end of the vinyl matches with the handle, and the proximal end has all wires and fibers exposed.



8. Use medical grade super glue to fix the vinyl tube to the handle.



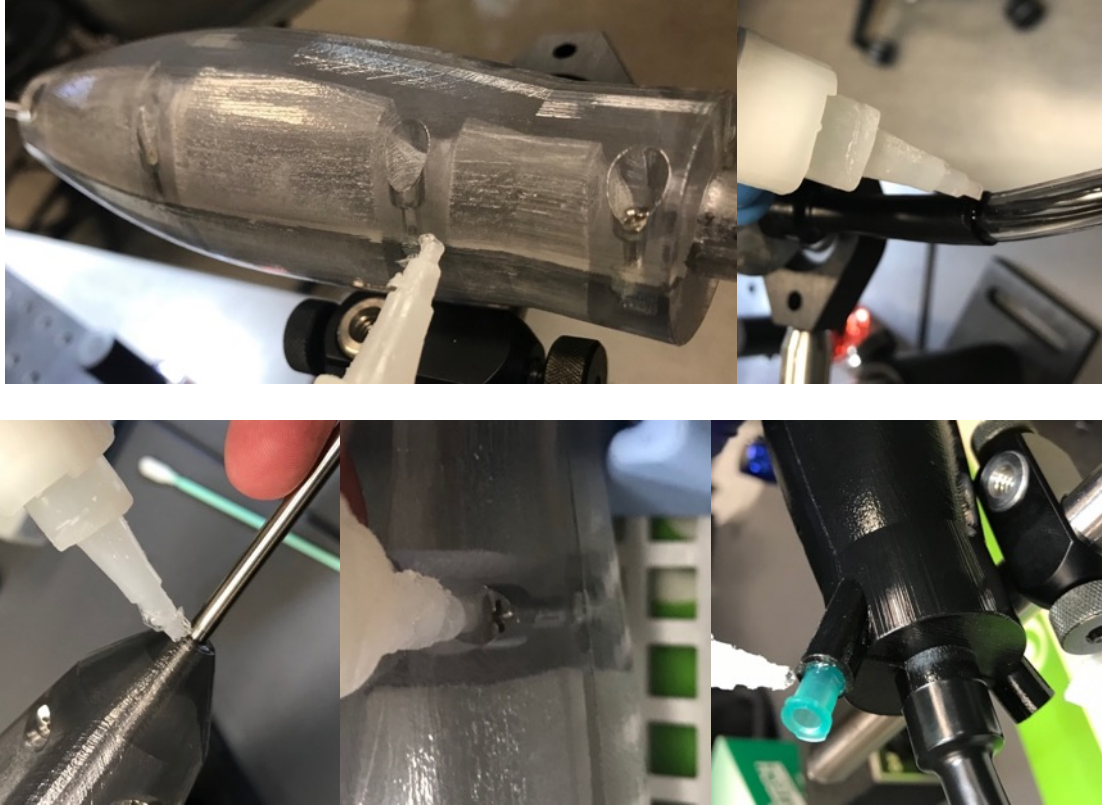
9. Close the handle



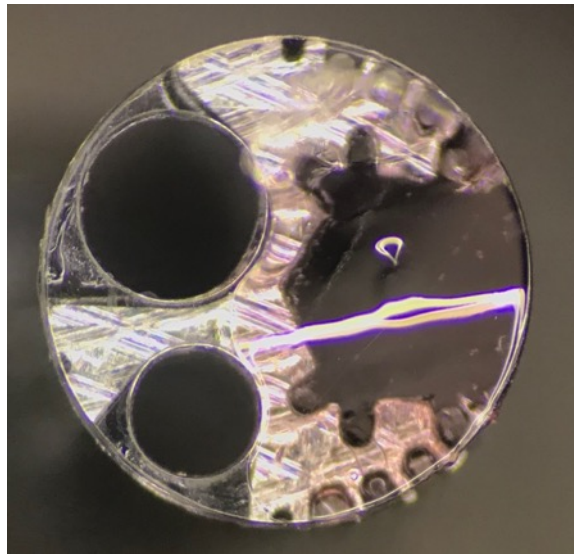
10. Insert a large shrink tube and it around the end of the handle. Shrink the tube with the heat gun ensuring a tight fit.



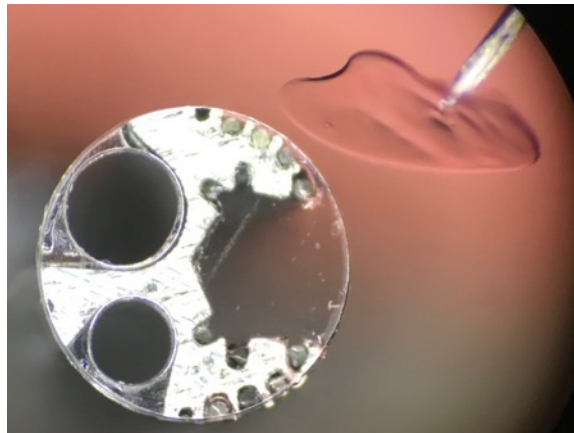
11. Using medical grade super glue, seal the shrunk tube, the junction between the handle pieces, the gap around the syringe needle connector, and the gap around the screws. Note, ensure the distal and the end is well sealed.



12. Using First Contact cleaner in a syringe, apply the cleaner to the top area. Wait about 30 minutes for the First Contact cleaner to dry. Note that picture shown has no objective or other components. This was intended for clarity.



13. Remove the dried First Contact Cleaner using a clean syringe. This process should be done very carefully and slowly to avoid any scratches on the cover. Lift one side of the film and from the lifted part puncture the film and pull it side to side.



C.6 Standard Operating Procedure B02-023: Connectorizing the Salpingoscope

This document guides the technician through the steps to install connectors on the salpingoscope proximal end, including the dual clad fiber, the piezo control wires, and the multimode fibers.

The following standard operating procedure (SOP) was developed according to laboratory protocol.

Standard Operating Procedures University of Arizona Biomedical Engineering Program

SOP # B02-023	Title: Connectorizing the salpingoscope
Origin Date: 08/08/19 Revision Date: 08/11/19 Rev 1.1	Approval: Date Approved:

Supplies:

- Salpingoscope handle with ferrule and vinyl tube finished.
- Shrink tube large (Raychem, MT5000-1/2-0-SP)
- Shrink tube medium (Raychem, MT2000-10.0-0-SP)
- Shrink tube small (Raychem, MT2000-3.0-0-SP)
- Shrink tube clear (Raychem, CM9833-000)
- Fiber single mode connector FC/APC (Thorlabs, 30126A9)
- Fiber multimode connector MM/SMA with 1050 μ m bore diameter (Thorlabs, 11050A)
- Piezo 4 pin connector (SZJELEN, SP13)
- Polishing films grit 30 μ m, 6 μ m, 1 μ m, and .02 μ m (Thorlabs: LFCF, LF1D, LF6D, and LF30D)
- 3D printed rack holders.

Glues:

- Loctite 4013 (Medical Grade Super Glue)
- Loctite Silicon (Medical Grade Silicon) UV Cure.

Miscellaneous:

- Kim Wipes
- Cleaning alcohol (ethanol, isopropanol, etc.)
- Un-Powdered latex gloves
- Work bench protecting paper
- Flux (Chipquik, RMA591NL)
- Lead solder (Loctite, 97SC C511 3C .38mm .25Kg AM)
- Fiber cleaning kit (Thorlabs, FBC1)

Equipment:

- Surgical microscope
- UV epoxy curing gun
- UV safety glasses
- Edmund Optics (EO) MI-150 illumination lamp
- Multimeter
- Fume extractor
- Flux applicator
- Wire stripping or medical scalpel
- Soldering tools (Hakko FM-203, soldering hand, thin soldering tip, tip cleaner).

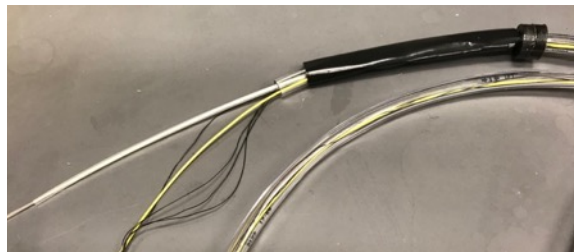
- Wire soldering helpers
- Heat gun
- Polishing pad

Procedure:

In this procedure the technician finishes the assembly of the salpingoscope handle and connectors. This includes, installing all fiber connectors, installing the piezo connector, installing tube protectors and sealing the proximal end of the endoscope. Make sure to wear gloves or finger covers throughout the procedure when handling chemicals, glues or any other abrasive substance.

Placing connectors on fiber ends

1. Insert the vinyl tube rack holders and a medium shrink tube, but don't put it in place or shrink the tube. Insert a CM9833-000 tubing on the 12 collecting fibers but don't shrink it.



2. Before installing fiber connectors, the end of the fibers, 3 shrink tubes have to be inserted. One for the proximal vinyl tube and two for the 12 fibers/SMA boundary. First install a CM9833-000 transparent tubing and then a small shrink black tube.



3. Install a FC/APC fiber connector on the dual clad fiber already with yellow jacket. Wait 24 hours for the epoxy to fully cure.



4. The 12 collecting fibers are being installed in a MM-SMA connector with bore diameter 1050 (Thorlabs 11050A). Note that the strain relief used is not the one provided by Thorlabs with the connector. The same strain relief as the FC/APC is used in this application.

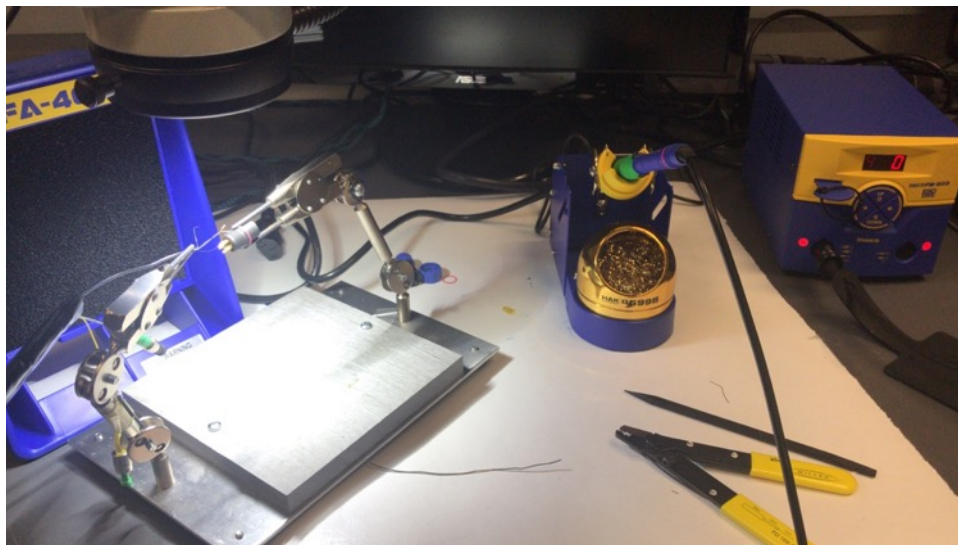


5. Polish fibers by hand and protect the fibers with fiber caps once polished. After polishing, shrink the small black shrink tube around the end of the strain relief of the 12 collecting fibers, but do not shrink all the way to the distal end.

Installing the piezo connector

1. Setup the working bench with the soldering equipment:

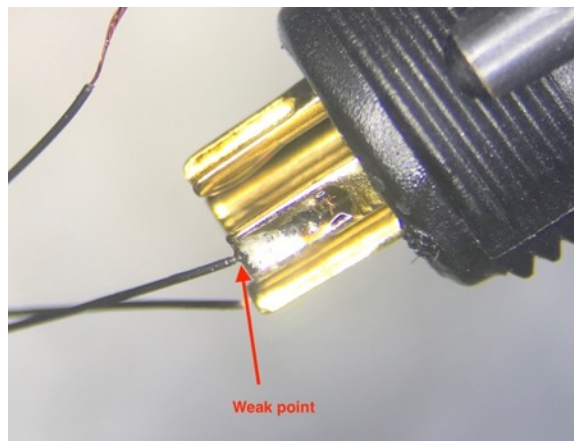
- -Fume extractor
- -Flux (SMD291)
- -Non-Lead solder
- -Flux applicator
- -Wire stripping or medical scalpel
- -Soldering tools (Hakko FM-203, soldering hand, thin soldering tip, tip cleaner.
- -Wire soldering helpers
- -Stereoscope



2. Grab a connector SZJELEN SP13 (4 pins) and separate the cap and pins.

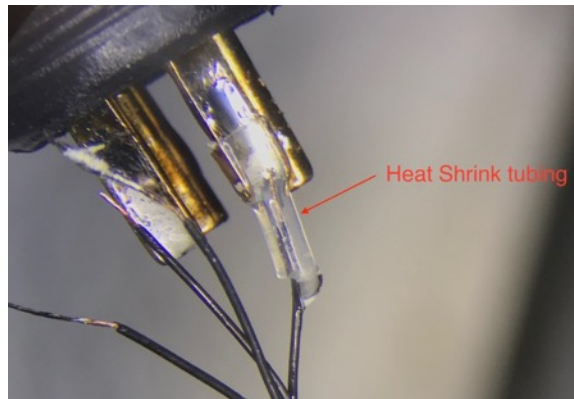


3. Insert the cap of the SZJELEN SP13 connector along the four piezo wires.
4. Cut a piece of CM9833-000 tubing about 10 cm long. Then cut 4 pieces of the same tubing about 5 mm long. Insert the tubing as shown in the picture.
5. Don't solder any wires until this step is read entirely. Be aware that the cable tends to snap at the transition between jacket and exposed wires where the cables get soldered.

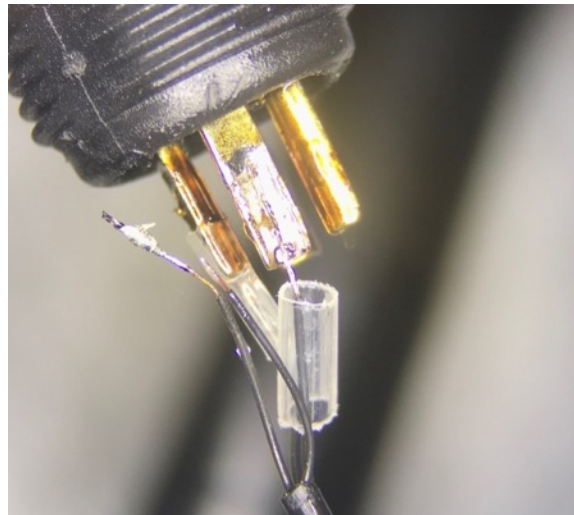


6. The small tubes of about 5 mm long are used to avoid this issue. They are positioned in this interface after soldering the wires to the connector. Additionally, a drop of medical

grade super glue is placed at the wire-tube interface to avoid any movement and protect the wires.



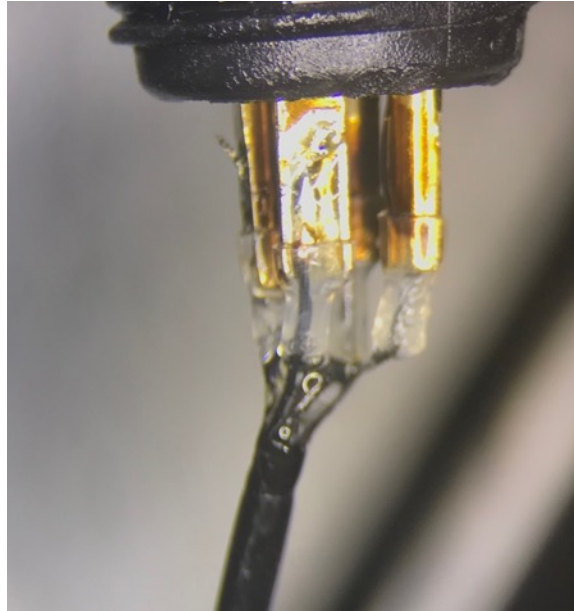
7. To do this, the shrink tube has to be placed before soldering. Then after soldering the cable, it can be put in place and shrunk. After each lead is soldered, medical grade super glue is placed in the back of the tubing and it is absorbed via capillary forces.



8. Solder the 4 wires. It is recommended to place a small amount of flux in the wire and coat it with solder. Also place a small amount of flux in the pin and coat it with solder. Then, place a small amount of flux in the coated pin and solder the wire. At the end inspect for continuity from the wire to the pin with a multimeter.

Take a picture or multiple pictures for clarity

9. Bring the 10 cm shrink tube close to the four small shrink tubes and shrink about half of it starting near the connector. Be aware of not burning the connector. Place medical grade super glue to grab all 4 leads and the long shrink tube.



10. Before closing the connector, place a good amount of medical grade silicon about 1.5 cm from the soldered wires to hold the cap of the connector. If using UV curing silicon, make sure it is fully cured before continuing.



11. Close the connector and seal the back with medical grade superglue for easy removal with acetone if needed.



12. Test the connector using the coupling connection to make sure the pins are not bent.



Sealing the vinyl tube at the proximal end (outdated procedure, update as required)

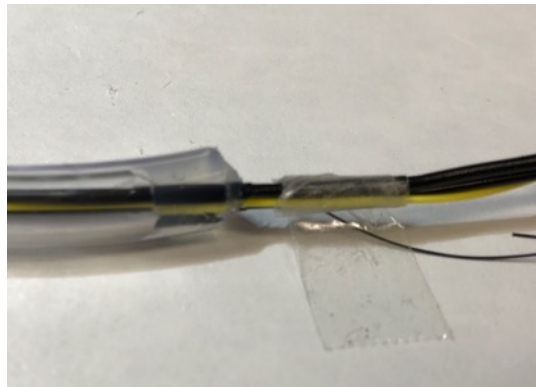
Test the 12 collecting fibers SMA connector by illuminating the proximal end with the Edmund Optics (EO) MI-150 illumination lamp and observing the fibers lighting up at the ferrule.



Test the dual clad fiber by following the same procedure as the 12 illumination fibers.



Attach both the vinyl tube and the connectors to the working table. After they are attached, seal the vinyl tube with medical grade silicon. If UV curing silicon is used, ensure it is fully cured before continuing to the next steps.



Adjust the shrink tube placed in “*Placing connectors on fiber ends*” step 1 to cover the boundary between the fibers/cables and the vinyl tube. Shrink the tube.



Seal the boundary with medical grade super glue in both ends to make sure it is completely sealed.



C.7 Standard Operating Procedure B02-017a: Salpingoscope Cleaning - Sterilization

This document guides the technician through the steps to clean the salpingoscope after a procedure and before gas sterilization. The following standard operating procedure (SOP) was developed according to laboratory protocol.

Standard Operating Procedures University of Arizona Biomedical Engineering Program

SOP # B02-017	Title: Salpingoscope cleaning-sterilization
Origin Date: 4/17/19 Revision Date: 5/20/19	Approval: Date Approved:

Supplies:

- Disinfecting wipes
- Enzymatic Solution
- Sponge
- Distilled Water
- Lint Free Cloth

Equipment:

- Salpingoscope
- Transportation box
- Sterilization box
- Sterilization pouch

Procedure:

SOP for pre-cleaning, decontaminating, disinfecting and sterilization of the Salpingoscope

Use proper PPE at all time when performing this procedure.

Immediately following a procedure perform the following:

1. Remove sterile sleeve from salpingoscope handle and fiber and discard into biohazardous waste.
2. Disconnect the salpingoscope from the main unit.
3. Wipe vinyl tube, handle, and rigid hypotube with a disinfection wipes.
4. Place in transport box with salpingoscope end wrapped with disinfection wipes. Wash within 4 hours.
5. Scrub salpingoscope with an enzymatic solution saturated sponge.
6. Rinse thoroughly with distilled water.
7. Dry with a lint free cloth.
8. Inspect salpingoscope for defects.
9. Mark handle indicating number of uses
10. Place in sterilization box.
11. Place sterilization box in a sterilization pouch for gas sterilization at Banner hospital.
12. When sterilization is complete, pick up unit for the next surgery.

C.8 Standard Operating Procedure B02-027: Multimodal Microscope and Salpingoscope OCT Spectrometer Calibration and Alignment

This document guides the technician through the steps to align the OCT reference arm (tabletop microscope) and take OPD data to generate calibration vectors to use during data acquisition.

The following standard operating procedure (SOP) was developed according to laboratory protocol.

Standard Operating Procedures University of Arizona Biomedical Engineering Program

SOP # B02-027	Title: Multimodal Microscope and Salpingoscope OCT Spectrometer Calibration and alignment
Origin Date: Oct-21-2020 Revision Date: Oct-23-2020	Approval: Date Approved: some day

Supplies:

- Kimwipes

Equipment:

- Salpingoscope spectrometer.
- Salpingoscope Software V04.06 or higher.
- NI MAX software installed in the computer.
- NI PCIe-1433 installed in the computer.
- LabView 2014 installed in the computer.
- Visual Fiber Fault Locator
- IR viewer card

Procedure:

In this procedure the technician aligns the OCT reference arm, takes OPD data for ± 5 mm using a mirror in the sample arm, and generates a calibration vector(s) to use during data acquisition. In specific, the technician should align the OCT reference arm to have a semi steady power where it is maximum at 0mm OPD and equal at ± 5 mm OPD. Ideally the power should be the same during that range of motion, but a variation of -25% is allowed. The technician takes the OPD spectrometer data using the salpingoscope software V04.06 or higher and saves the data in a .csv format and uses this data with the code provided to obtain the calibration vector(s) needed to obtain OCT images during data acquisition.

Aligning the OCT sample arm (microscope).

1. In general, this step does not need to be performed. If misalignment is suspected in the sample arm (the microscope itself) see SOP *B02-021b Alignment & Assembly Procedure of Optical Components for the Multiphoton Microscope*

Upper (Optical Axis) Alignment:

1. Connect a fiber patch cable into the fiber collimator and use the Visible Fault Locator as a source.
2. Place a target on the optical table below the fiber collimator.

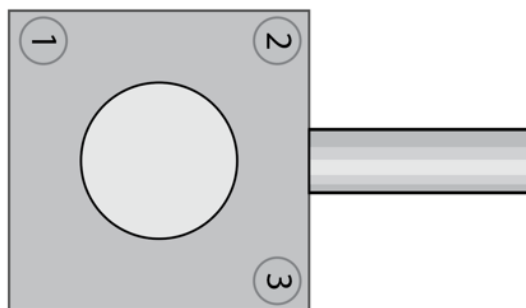
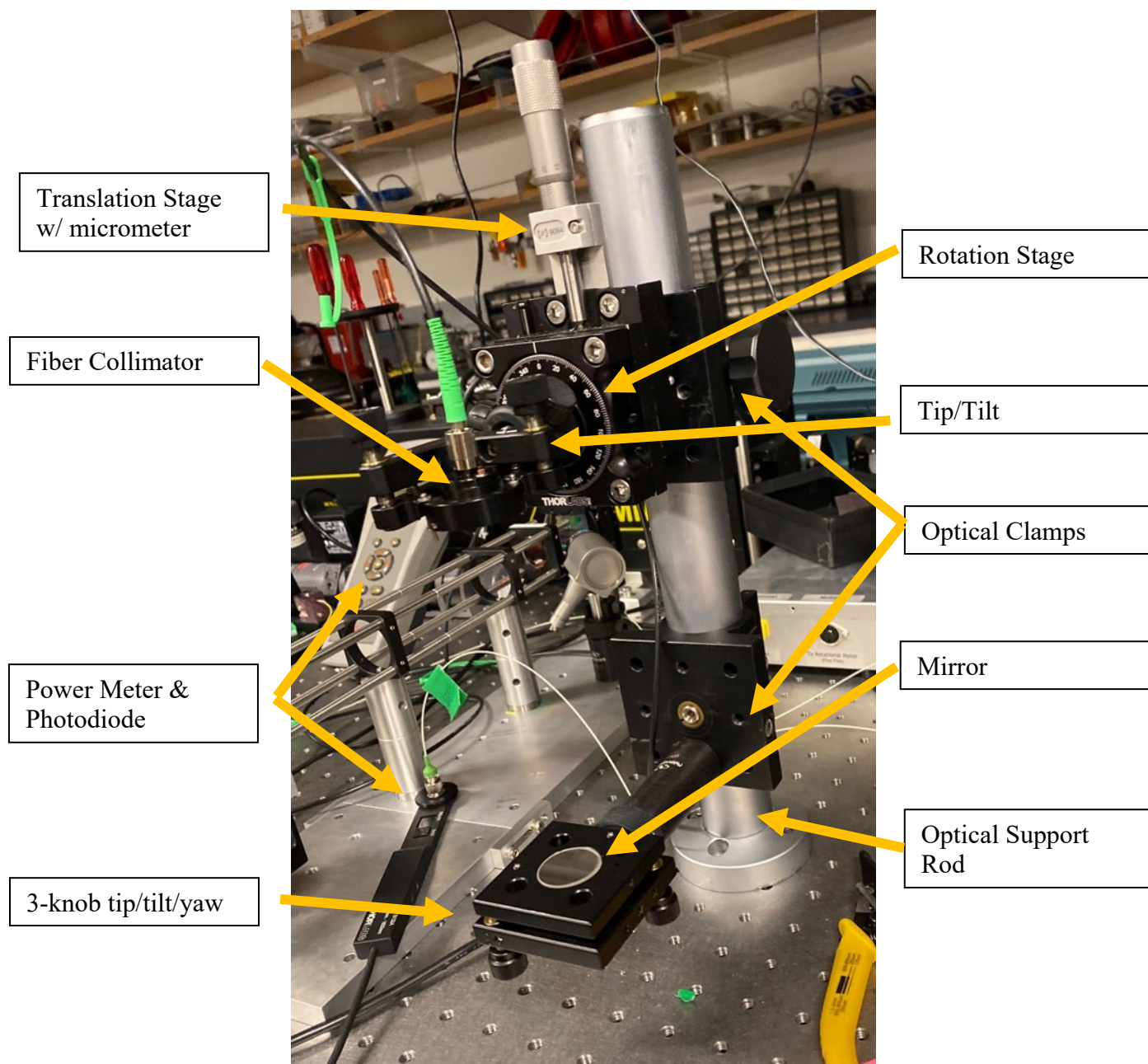
3. Use the micrometer to move the fiber collimator through the micrometer's range to the far distance.
4. Notice if the beam spot has moved off the target. Adjust one of the tip/tilt stage's knobs to be closer to the target spot.
5. Use the micrometer to move the fiber collimator to the other end of the micrometer's range, to the close distance.
6. Notice if the beam has moved off the target. Adjust the other knob of the tip/tilt stage to move the beam closer to the target.
7. Repeat steps 9-12 until the beam stays on-target throughout the entire range of the micrometer. At this point, the optical axis defined by this beam should be perpendicular to the optical table, and the collimator's tip/tilt should no longer be manipulated.
8. Replace the fault finder source with the ~ 1300 nm optical source and verify that the system is still aligned at the wavelength by using an IR viewer card as a target. Leave the micrometer in a middle position, not at the edges of range.

Lower (Mirror) Alignment:

9. Place the mirror unit's optical post into the lower clamp's optical post holder. Do not secure the post into the holder with the side screw yet.
10. View the mirror from the side of the table, adjusting the tip/tilt knobs so that each can begin in a mid-screw state. This will allow adjustments to be made in either direction for each knob.

11. Connect the Thorlabs Power Meter to power and turn it on. Connect the photodiode sensor to the power meter. Screw the 'detector' arm of the Fiber OCT system into the Threaded fiber adapter and place it over the photodiode's sensor area.
12. Using the IR Viewer Card to find and monitor the reflected beam, rotate the optical post inside the optical holder until the reflected beam couples back into the collimator, or is as close as possible to coupling into the collimator.
13. Use the knobs on the mirror's tip/tilt stage to couple light into the collimator. Observe the reading from the power meter to maximize the signal back into the system. For this example, $\sim 500 \mu\text{W}$ was measured out of the collimator, and $\sim 22 \mu\text{W}$ was the maximum signal out of the detector arm.
14. Once aligned at maximum return signal, use the micrometer to move the collimator arm up 5mm. Observe the loss of signal due to this movement.
15. Use knobs 3 to reach a maximum signal, then adjust knob 2 to possible find a greater maximum signal, then repeat the adjustment of these two knobs until a maximum signal is found. The point here is to use knob 3 primarily, and 2 secondarily, because knob 2 has a greater effect on the tip/tilt ruled by knob 1.
16. Use the micrometer to move the collimator down 10 mm, aka 5 mm below the micrometer midpoint.
17. Use only knob 1 to reach a maximum signal at this location.
18. Use the micrometer to move the collimator up 10 mm, and repeat Steps 21-23 a few times.

19. Once this small range is seemingly more aligned, begin increasing the distance away from the midpoint, to eventually up 10 mm and down 10 mm from the midpoint for a maximum range of 20 mm. Repeat through Steps 20-23 until more aligned
20. If not satisfied with the change of signal through the range of the micrometer, switch to a new adjustment pattern like:
 - a. Max range: Adjust knob 3
 - b. Mid range: Adjust knob 2
 - c. Min range: Adjust knob 1
 - d. Mid range: Adjust knob 2
 - e. Repeat



Preparing the laser and the spectrometer for the data acquisition (note that these steps could change with a newer spectrometer).

1. Ensure that the Superlum Broadlighter 1300 is connected to the circulator input FC/APC port. Once properly connected shown in the picture, turn on the switch, wait until the two bottom 'TEC' LEDs are green, and then turn on the 'SLD' LEDs by pushing the black buttons. Note that the top LEDs will turn on to indicate that the laser is on.



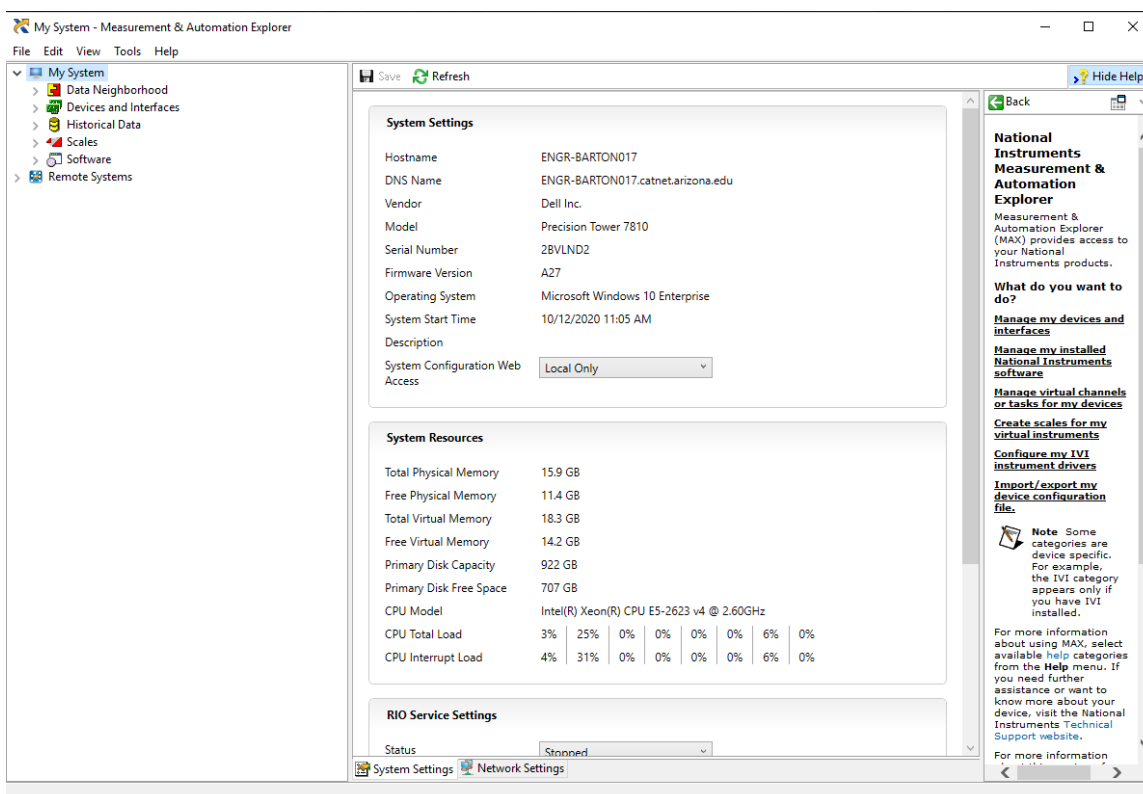
2. If the camera is unplugged, plug in the camera power and wait about 10 seconds. Check that the green LED above the power cable is on. It is recommended to keep the sensor capped to avoid overheating or pixel damage.



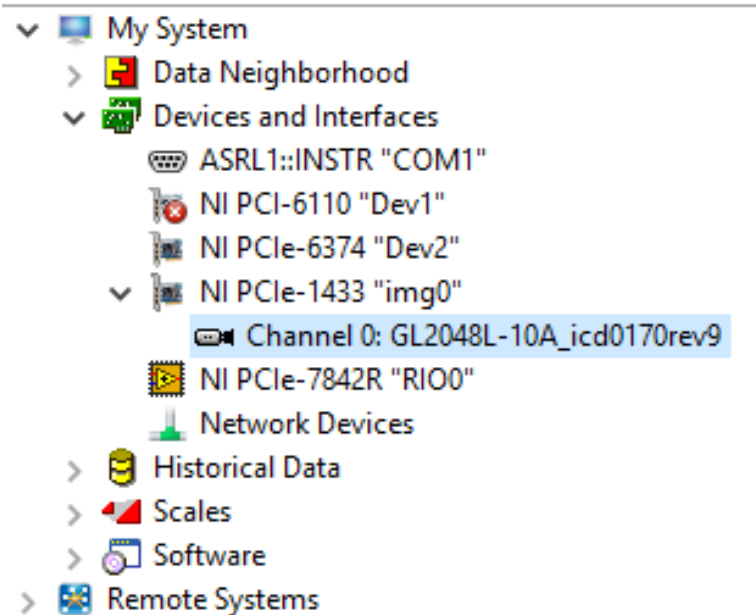
Taking the OCT OPD data for +/-5mm

In this section, the procedure to collect raw data is detailed to ensure proper data is provided to the calibration code. After aligning the OCT reference arm, the returning optical energy from both arms (reference and sample) is more than the spectrometer could collect without being saturated. Saturation of the line detector (GL2048L installed in the salpingoscope spectrometer) should be avoided at all cost since any saturation will affect the calibration fit functions in the code. The GL2047L has a dynamic range from 0 to ~4200 counts, but during this procedure it is recommended that the maximum readout of the camera is <4000 counts. How to avoid saturation is included in the steps below.

1. Open NI MAX and navigate to the camera controls as follows. NI MAX should be located in the start menu under National Instruments folder, open the program. Once open, a window similar to the first figure will be on screen. Navigate to the camera controls by using the NI MAX dropdown tree shown. Click on “Devices and Interfaces”, then click on “NI PCIe-1433 xxx”, and then click on the camera “GL2048L-XXXXXXXXXX”. If another camera with different name is here, right click the camera and change the driver to “GL2048L-10A_icd0170rev9”.

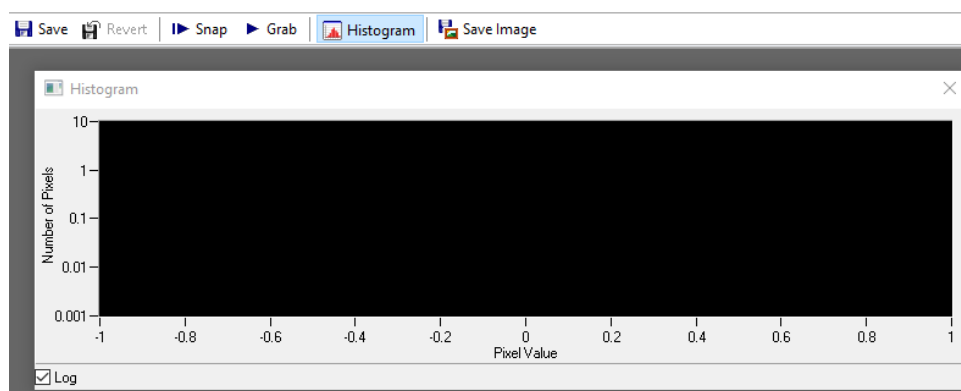


NI MAX window



NI MAX dropdown tree.

- Once you click on the camera the right panel of NI MAX changes and shows a different toolbar at the top. Click Histogram to load the histogram window and click the checkbox that is labeled as Log in the bottom left of the histogram.



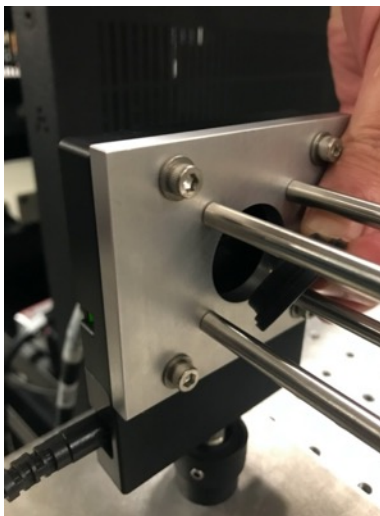
- Check the setting in the camera attributes panel. Note that the FPA sensitivity could be adjusted, but since at this point the sample arm has a mirror, the low setting should be sufficient.

Attribute	Setting
Serial Commands	ON
FPA Sensitivity	Low preferably, it can be adjusted if light is insufficient. Check alignment if low is not sufficient.
Exposure Mode	Line Time 100%
Line Time	13.1 μm
Corrections	On
Calibrate Mode	OFF
Digital Gain	1.0
Camera Test Pattern	OFF

Line Stamp	OFF
Trigger Mode	Fixed Exp
Trigger Polarity	CC1 High
CC1 Trigger Width	4.7
CC1 Trigger Period	20.0 μm

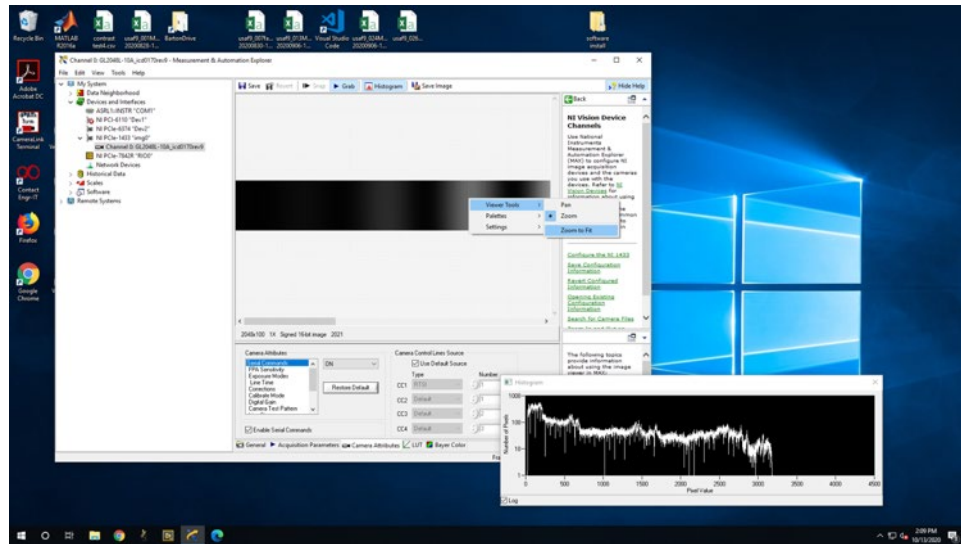
Ensure that the “Enable Serial Commands” check box is checked and “Use Default Source” under Camera Control Lines Source checkbox is checked.

- Once the histogram is loaded and the settings are checked, click “Grab” and uncap the camera to expose the sensor as shown. It is recommended that the camera is kept capped when not acquiring data to avoid pixel overheating.



- At this step you should see data in the histogram and a black and white image. That is the “image” being acquired from the camera. Note that this image is composed by several readouts of the camera line sensor. In this configuration the normal size of the image is

2048x100. By default, the image is not shown completely. Right click on the image, go to viewer tools, and click on “Zoom to Fit” as seen in the figure.



Zoom options to be able to see the entire image.

6. After adjusting the zoom, you should see the entire image and the histogram with data such as in the figure below. Adjust the OPD by moving the translation stage shown until you see 1 fringe (AKA the entire spectrum with no fringes). The 0.0mm OPD is identified by 1 bright fringe. At this point, the exact location of the 0.0 OPD has been identified. If the spectrum disappears all at once that means that you are $\pm \frac{1}{4}$ of a wave away of the 0.0 OPD. Try to determine the half point to the two locations where the spectrum disappears all at once. Note that this step is done as best as possible because due to air, it is difficult to get to 0.0 OPD exactly. Keep adjusting the translation stage of the reference arm until you reach the best possible location of the 0.0mm OPD.

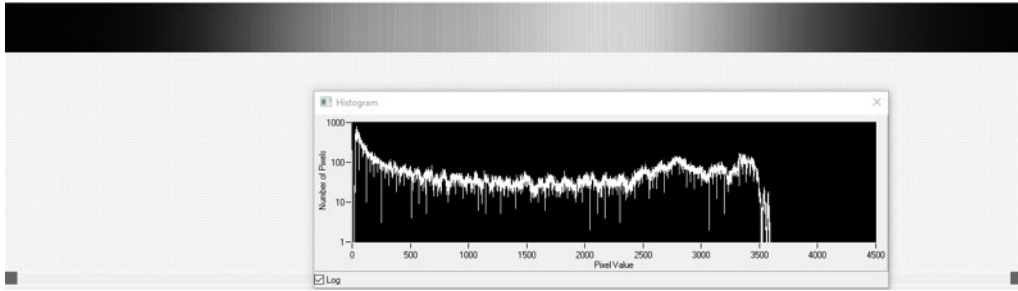


Image showing the 2048 pixels of the sensor and the histogram at OPD=0.0mm



Reference arm translation stage used to modify and adjust the OPD.

7. Write your 0.0mm OPD micrometer location ($0OPD_L$). Use the following formula to calculate the micrometer location (L) for the OPDs needed.

$$L = \frac{OPD}{2} + 0OPD_L$$

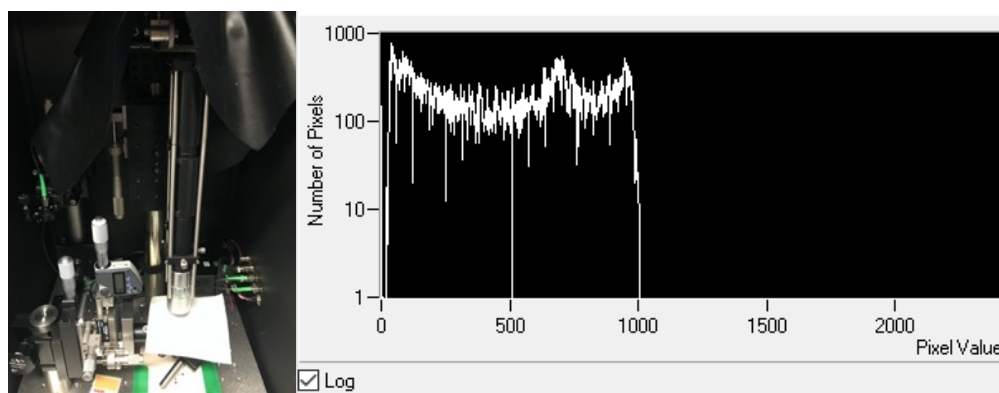
8. Do not take the data in this step. This is a preparation step. It is recommended to use an Excel table to keep track of the locations. +/- OPD data should be taken for at least the intended imaging depth times 2, but it is recommended to take data for the imaging depth +1 mm times 2. For example: if the OCT system is intended to image 2 mm depth, then the minimum OPD data that should be taken is +/- 4.0mm OPD with an interval of

0.1mm OPD in the first 2 mm and then 0.5mm after 2 mm OPD. Ideally, the OPD data that should be taken is ± 6.0 mm OPD with an interval of .1 mm OPD in the first 2 mm and then 0.5mm after 2 mm OPD. See an example in the table below.

OPD	L	OPD2	L'
0.1			-0.1
0.2			-0.2
0.3			-0.3
0.4			-0.4
0.5			-0.5
0.6			-0.6
0.7			-0.7
0.8			-0.8
0.9			-0.9
1.0			-1.0
1.1			-1.1
1.2			-1.2
1.3			-1.3
1.4			-1.4
1.5			-1.5
1.6			-1.6
1.7			-1.7
1.8			-1.8
1.9			-1.9
2.0			-2.0
2.5			-2.5
3.0			-3.0
3.5			-3.5
4.0			-4.0
4.5			-4.5
5.0			-5.0
5.5			-5.5
6.0			-6.0

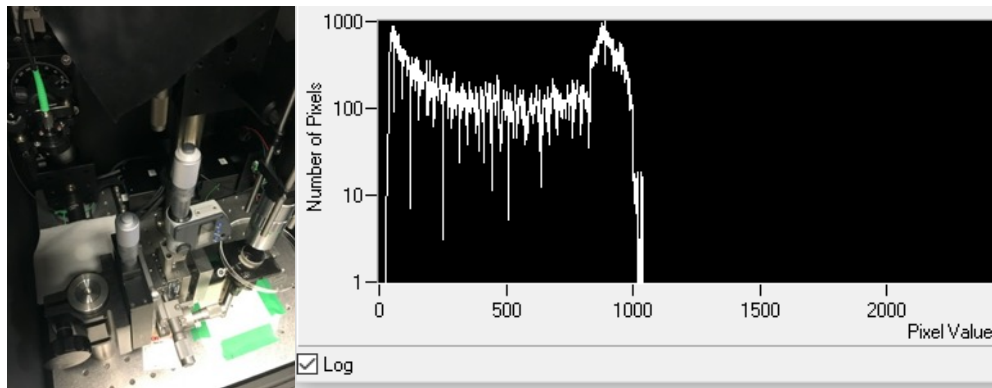
Example table to calculate OPD locations (L) where data needs to be taken.

9. Equate the power in both arms at 0OPD before taking the data. With a Kim wipe, obstruct the mirror in the sample arm as seen in the picture. Adjust the tip OR the tilt (not both) of the mirror at the bottom of the reference arm until the histogram shows pixel values up to about 1000 counts in the x-axis of the histogram.



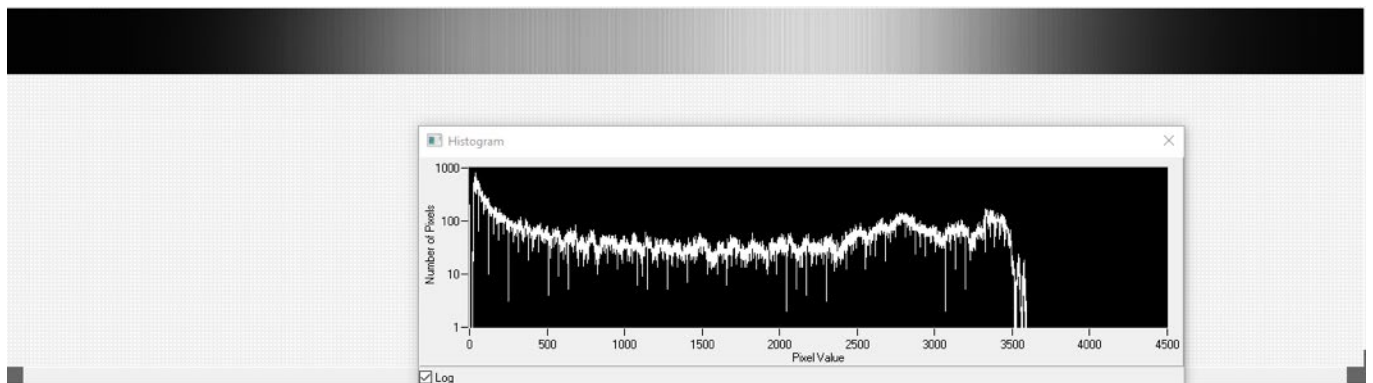
Sample (microscope) arm blocked with a Kim wipe and histogram showing values up to ~1000 counts in the x-axis.

10. Remove the Kim wipe from the sample arm and obstruct mirror in the bottom of the reference arm with the Kim wipe as seen in the picture. Be careful not to bump other components in the sample arm. If any components are bumped repeat step 9.



Reference arm blocked with a Kim wipe and histogram showing values up to ~1000 counts in the x-axis.

11. Remove the Kim wipe and ensure that the histogram reads somewhere between 3000 to 4000 for the highest value at the 0OPD location as seen in the figure. These values usually will help avoiding saturation of the sensor.



0OPD image and histogram showing values in between 3k to 4k.

12. Stop NI MAX by clicking “grab”. This will stop the camera. Cap the camera but do not disconnect the power or connection to the computer. Close NI MAX to free up the camera. If NI MAX prompts to save something click no unless it is intended to save camera settings.
13. Open LabView 2014 to utilize the Salpingoscope software. LabView should be located in the start menu under National Instruments folder, open the program. A similar window to the one shown should load. Open “salpingoscope OCT.lvproj” for any folder of version LV2014 v04.06 or higher. Note that if a newer version is available it may not display the raw data of the camera but will save the data. For calibration, raw data is needed.

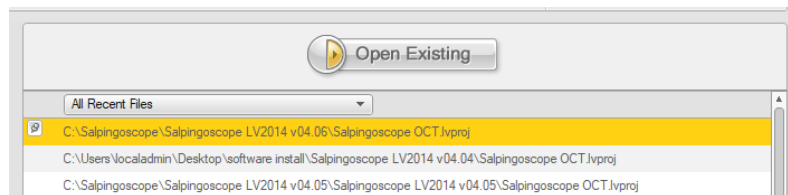
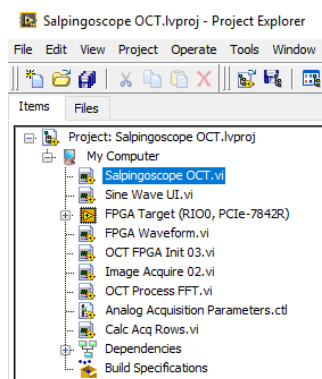


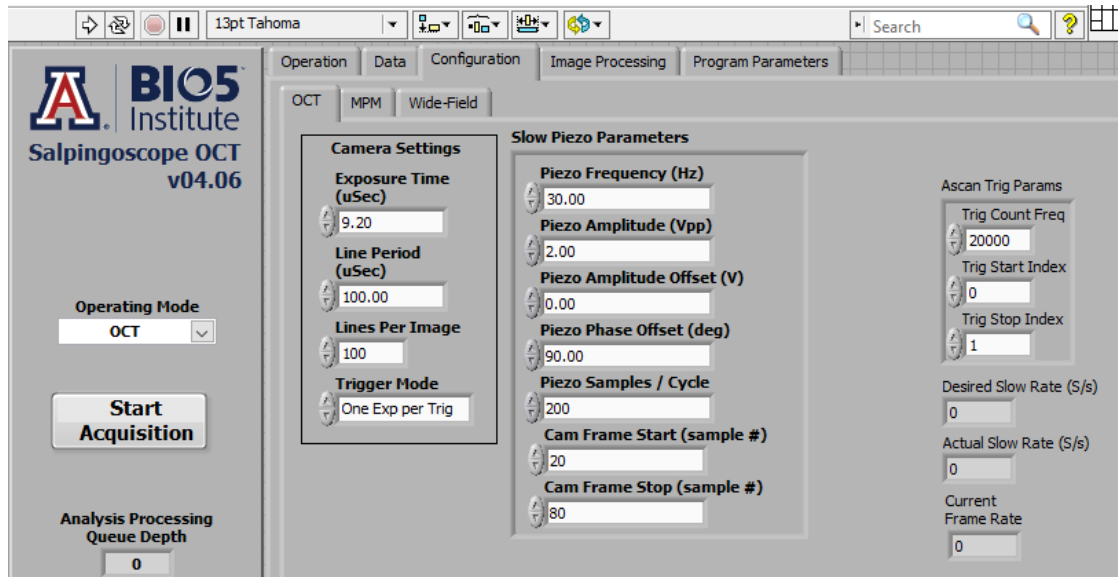
Figure xx, LabView 2014 load window.

14. Double click “Salpingoscope OCT.vi” to load the main Salpingoscope software GUI interface.



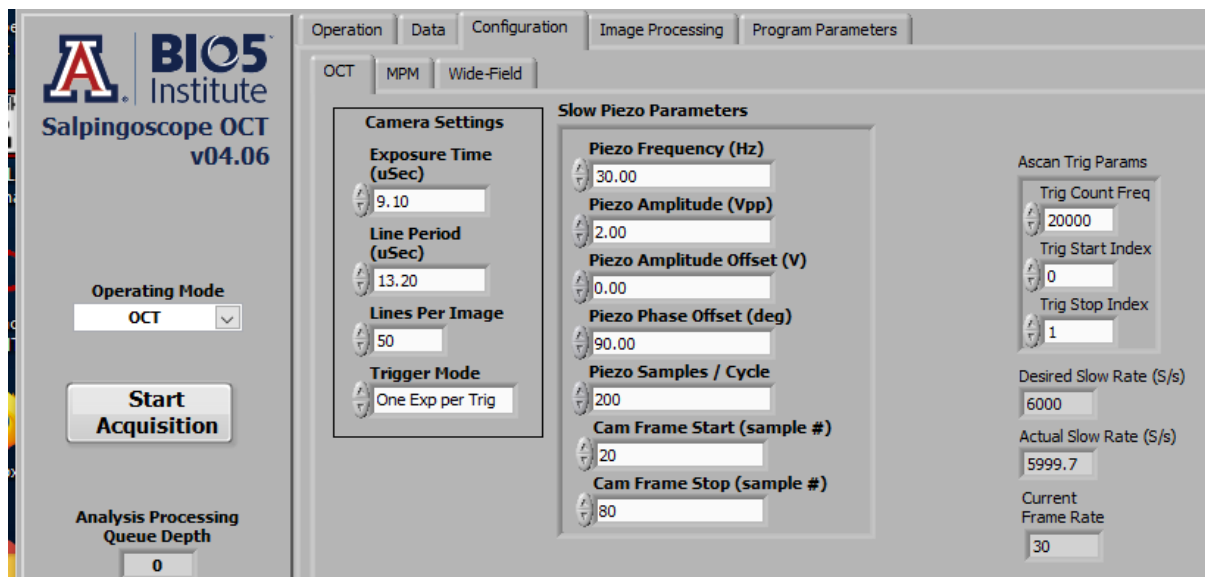
LabView project manager includes the salpingoscope OCT.vi to load the GUI.

15. Click on the right pointed arrow at the top left to run the program and go to the configuration tab, OCT subtab. Also, be sure to set the Operating Mode to “OCT” in the drop down menu in the left panel of the software.



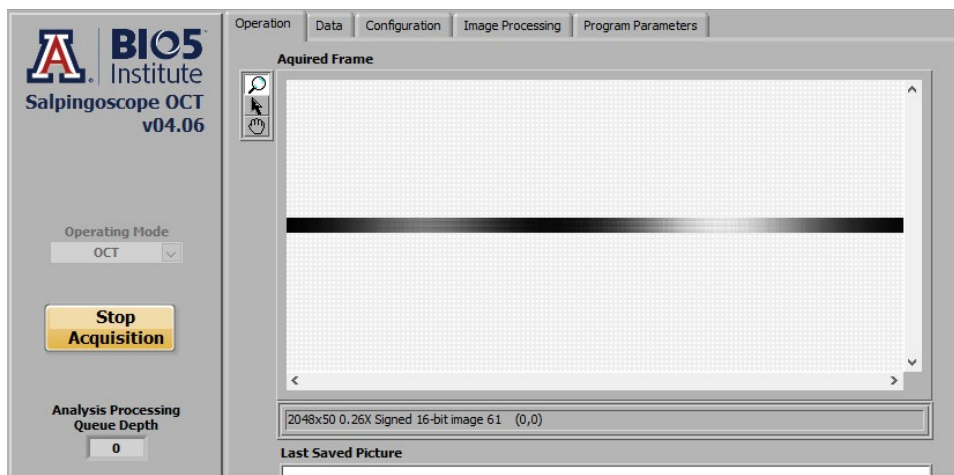
Note that the settings may not be correct before or after running the code. The running arrow at the top left will change from white to black when the code is running.

16. Set the Camera settings to the settings shown in the figure



Camera, piezo, and Ascan Trig Params.

17. Click on “start acquisition” and click on operation to ensure data is showing in the acquired frame. Note that the queue depth starts growing. If the queue starts growing above 10k, the software will become unresponsive. Click “Stop Acquisition” and allow the queue decrease to 0 before starting the next acquisition.



Software windows while acquiring data will show the fringes in the operation tab if the camera is responding to the software.

18. Once data acquisition is verified, move the reference arm to the appropriate location L for the first data point as shown in the figure.



Adjusting the reference arm to the position L for the next OPD data point.

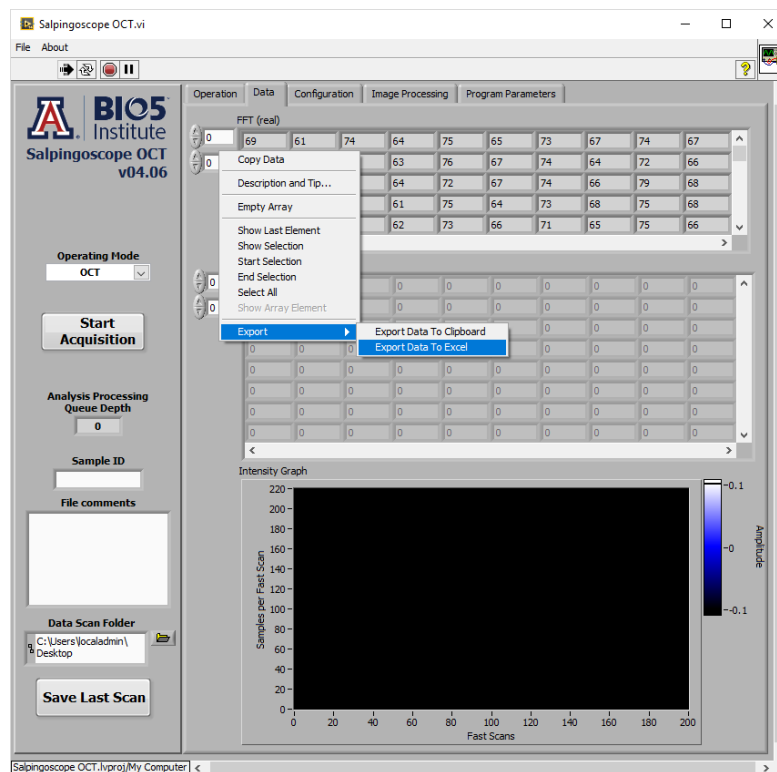
19. (This step has been changed, use the save option in the main GUI) Once the reference arm is at position L, start acquisition and click on the “Data” tab. The data is shown in the FFT (real) array indicator seen in figure xx. Right click in between the indices in the left hand side of the indicator and select Export>Export Data to Excel. Then Stop the Acquisition. After stopping the acquisition, save the excel data as a .csv file with the following format:

For positive OPD files:

“OPD_+X.Xmm_L_X.XXXmm.csv”

For negative OPD files:

“OPD_-X.Xmm_L_X.XXXmm.csv”



Raw camera data being acquired and exported to excel through the LabView Export Data to Excel feature.

20. Move the micrometer of the reference arm to the next position L and repeat step 19 for each data point.

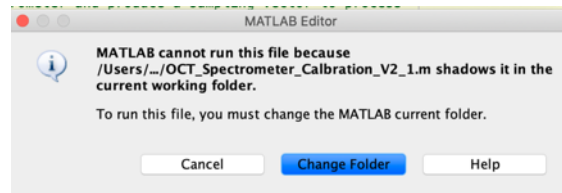
Obtain the calibration vectors for linear sampling and phase correction.

In this section the technician should be able to obtain the calibration vectors with no major issues if the two following statements are true:

- 1) the OPD data is not taken with OPDs larger than 9 mm, and
- 2) the OPD data is not saturated on any of the files.

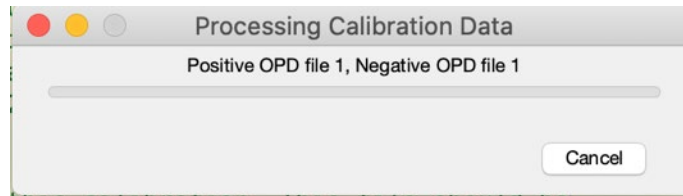
To check saturation use FIJI – ImageJ and plot a horizontal profile. The calibration procedure has been developed such as the code will find for the best calibration. See calibration details in the comments inside the OCT_Spectrometer_Calbration_V2_1.m file.

1. Use an empty/new folder to store the OPD files, the OCT_Spectrometer_Calbration_V2_1.m and the OCT_cal_function.m.
2. Open OCT_Spectrometer_Calbration_V2_1.m with Matlab and run the code with the folder containing the OPD files as the directory. If Matlab asks you to change the current folder, click on “change folder”



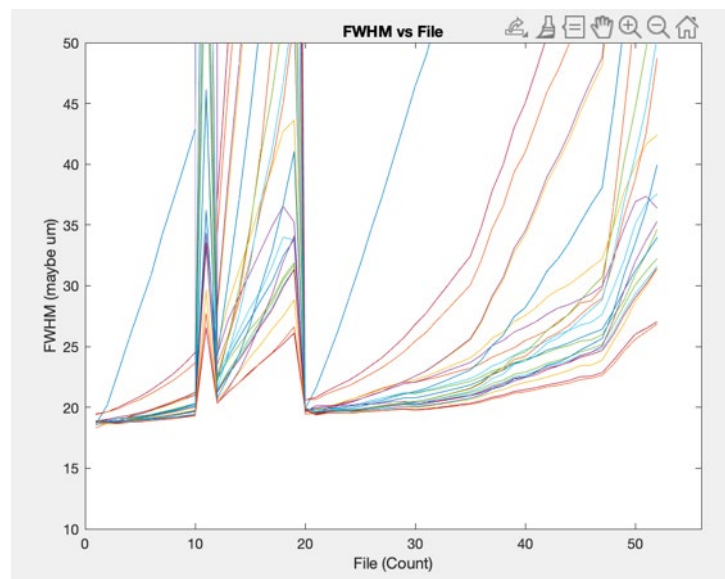
Matlab editor changing current folder.

- Once the code runs, a “Processing Calibration Data” progress bar will appear as in the figure. The bar is for the most part accurate. If at any time the user wishes to cancel the process, click cancel. Read the instructions in the code for more details if any error occurs.



“Processing Calibration Data” waiting bar.

- Every positive and negative OPD calibration combination will be tested and a graph with FWHMs will appear and be updated at every iteration. The graph will look similar to the figure. The code searches for the line with less variation and the line with the best mean. Those two parameters usually result in the best calibration.



FWHM of the processed calibrations in the Matlab code.

5. Halfway through running, the code will report the best calibration(s) obtained. These results will be stored in a text file called “Last_Results.txt”. This file is NOT the calibration. This file only reports what positive and negative OPD combinations obtained the best mean and the lowest variation (STD).
6. Output files to use during imaging (instructions elsewhere for now) are saved in the folder containing the OPD data. If the mean and std sets are different, 4 different vector files will be created. The files terminated with ‘linear’ are intended to be used for the linear correction while the ones terminated with ‘phase’ are intended to process the phase correction while acquiring A-scans.

To use the best mean set vectors use the files that are saved such as:

`'SpecSalp_Calib_MEAN',dateStamp,'_Linear.csv'`

`'SpecSalp_Calib_MEAN',dateStamp,'_Phase.csv'`

To use the best STD set vectors use the files that are saved such as:

`'SpecSalp_Calib_STD',dateStamp,'_Linear.csv'`

`'SpecSalp_Calib_STD',dateStamp,'_Phase.csv'`

If the mean and std sets are the same, 2 different vector files will be created:

`'SpecSalp_Calib_',dateStamp,'_Linear.csv'`

`'SpecSalp_Calib_',dateStamp,'_Phase.csv'`

7. Additionally, the code will process all OPDs to create an image and a .csv file resembling a B-scan of the data sets (ImageJ is better at showing these images than Matlab since Matlab has HUEs that are intended for graphing and not for imaging). Visually inspect these files to ensure that all the lines that are bright have approximately the same FWHM. If they don't, there is something not going well.